TUNING THE MAGNETIC PHASE TRANSITIONS AND THE MAGNETOCALORIC PROPERTIES OF RARE-EARTH MANGANITES FOR MAGNETIC REFRIGERATION APPLICATIONS

THESIS SUBMITTED TO **AcSIR** FOR THE AWARD OF
THE DEGREE OF
DOCTOR OF PHILOSOPHY
IN PHYSICAL SCIENCES

By

ARUN B.

Registration No: 10PP14A39009

Under the guidance of
Dr. M. VASUNDHARA

MATERIALS SCIENCE AND TECHNOLOGY DIVISION
NATIONAL INSTITUTE FOR INTERDISCIPLINARY
SCIENCE AND TECHNOLOGY (CSIR-NIIST)
THIRUVANANTHAPURAM- 695 019
KERALA, INDIA

NOVEMBER 2019

Dedicated to……

My parents, brother, my beloved wife, and my delightful daughter, who wonder what I do all day

The secret of magnetism, now explain that to me!
There is no greater secret, except love and hate

GOETHE from his poem ‘God, Soul and World’

DECLARATION

I hereby declare that the matter embodied in the Ph.D. thesis entitled "**Tuning the magnetic phase transitions and the magnetocaloric properties of rare-earth manganites for magnetic refrigeration applications**" is the result of the investigations carried out by me at the Functional Materials Section, Materials Science and Technology Division, CSIR-National Institute for Interdisciplinary Science and Technology, Thiruvananthapuram, under the supervision of Dr. M. Vasundhara and the same has not been submitted elsewhere for any other degree, diploma or title.

In keeping with the general practice of reporting scientific observations, due acknowledgement has been made wherever the work described is based on the findings of other investigators.

Arun. B

Arun B.

Thiruvananthapuram

NATIONAL INSTITUTE FOR INTERDISCIPLINARY SCIENCE AND TECHNOLOGY
(NIIST)
(Formerly Regional Research Laboratory)
Council of Scientific & Industrial Research (CSIR)
Industrial Estate P.O., Trivandrum – 695 019,
Kerala, INDIA

CERTIFICATE

This is to certify that the work incorporated in this Ph.D. thesis entitled "**Tuning the magnetic phase transitions and the magnetocaloric properties of rare-earth manganites for magnetic refrigeration applications**" submitted by **Mr. Arun B.** to the Academy of Scientific and Innovative Research (AcSIR) in partial fulfilment of the requirements for the award of the **Degree of Doctor of Philosophy in Physical Sciences** embodies original research work carried out by him under my supervision. I further certify that this work has not been submitted to any other University or Institution in part or full for the award of any degree or diploma. Research material obtained from other sources such as text, illustration, table etc. used in the thesis have been duly cited and acknowledged.

Arun 14/11/19

Trivandrum

Arun B.
(Research Scholar)

14/11/19

Dr. M. Vasundhara
(Research supervisor)

Acknowledgements

I present this thesis, in the name of God, the Almighty, who showers his unperturbed blessings undeservingly upon me throughout my life.

It is with great pleasure that I extend my deepest sense of gratitude to Dr. M. Vasundhara, my thesis supervisor, for suggesting me the research problem. Her valuable support, encouragement and guidance throughout the research period have led to the successful completion of this work.

I would like to express my deep sense of gratitude to Dr. M. T. Sebastian (Rtd. Chief Scientist, MSTD, CSIR-NIIST), who encouraged me to take up research as my career.

I am grateful to Dr. A. Ajayaghosh, (Director, CSIR-NIIST) and Dr. Suresh Das and Dr. Gangan Prathap (Former Directors, CSIR-NIIST) for providing the facilities for carrying out the research work. I am deeply indebted to Dr. S. Savithri (Head, MSTD, CSIR-NIIST), Dr. H. Harikrishna Bhat, Dr. M. L. P. Reddy, Dr. U. Syamaprasad (Former Heads, MSTD, NIIST), Dr. C. H. Suresh, Dr. Luxmi Varma and Dr. Mangalam. S. Nair (present and former AcSIR coordinators, CSIR-NIIST).

I would like to express my sincere and heartfelt thanks to Dr. Manoj Raama Varma (Senior Principal Scientist, CSIR-NIIST) for extending the facilities for materials synthesis. I wish to express my sincere thanks to Dr. P. Prabhakar Rao (Rtd. Chief Scientist, MSTD, NIIST) and Dr. U. S. Hareesh (Principal Scientist, CSIR-NIIST) for fruitful scientific discussions and advice during my work.

I would like to express my sincere thanks to Dr. K. Devi Chandrasekhar, Department of Physics, National Sun Yat-Sen University, Taiwan for providing the X-ray absorption spectroscopy studies. Dr. Ajith Kumar Patra and Ms. Shubhra Dash Department of Physics, Central University of Rajasthan, Ajmer is greatly acknowledged for their unconditional help in providing the slow scan X-ray diffraction studies. I would like to express my sincere and heartfelt thanks to Dr. Senoy Thomas (Assistant Professor, Dept. of Physics, CUSAT) for his constant support, encouragement and creative discussions.

It is indeed my pleasure to thank Dr. K.P. Surendran (Senior Scientist, CSIR-NIIST), Dr. S. Ananthakumar (Senior Principal Scientist, CSIR-NIIST), Dr. T.P.D.

Rajan (Principal Scientist, CSIR-NIIST), Dr. V.S. Prasad Principal Technical Officer), Dr. S. Shukla (Principal Scientist, CSIR-NIIST) for fruitful scientific discussions and advice during my work.

Also, I am greatly indebted to Dr. Saju Pillai (Senior Scientist, CSIR-NIIST), and Dr. M. Sundararajan (Senior Scientist, CSIR-NIIST) Mr. A. Peer Mohammed (Sr.Technical Officer), Mr. Kiran Mohan, Mr. M. R. Chandran, Mrs. Lucy Paul, Mr. Prithviraj, Mrs. V. Soumya, Mr. Harish Raj V. for extending various facilities during the course of this work. I would also grateful to the entire NIIST community for their encouragement and support of all the other scientists of NIIST is greatly acknowledged.

I am also grateful to the NIIST administration for extending all the timely help. I am also thankful to all the office staff, specially Geetha aunty, IT lab and library staff at NIIST for their kind cooperation. I would like to thank our technical assistants Ms. Haritha and Mr. Merin for extending their help throughout my research carrier.

I would like to acknowledge and express my deepest sense of gratitude to CSIR for providing the research fellowship to carry out this work. Apart from that, I also wish to acknowledge the funding agencies such as DST and BRNS for financial support during the various stages of my research work.

The creative suggestions, valuable advice and helps given by my seniors Dr. K. S. Deepa, Dr. Savitha Pillai, Dr. P. Nisha, Dr. C. P. Reshmi, Dr. J. Chameswary, Dr. Dhanesh Thomas, Dr. K. M. Manu, Dr. P. Neenu Lekshmi, Dr. Jobin Varghese, Dr. Nina Joseph, Dr. G. R. Raji, Dr. P. Abhilash, Dr. L. K. Namitha and Dr. T. H. Gayathri are greatly acknowledged.

I sincerely acknowledge the contribution and support rendered by Mr. M. V. Suneesh, Ms. Annrose Sunny, Ms. Sudakshina B., Mr. Thanveer T, Mr. Unnikrishnan M. S, Mr. Rajesh R, Mr. Arun S. Pillai, Ms. M. Athira, Ms. Chindu S, Ms. Sumangala Devi, Ms. Aswathy V.S., Dr. Aiswarya R., Ms. Kanakangi S Nair, Ms. Leskhmi D. R., Dr. Angel Mary Joseph, Dr. Induja I., Mr. Rejith R. G., Ms. Jayanthi. S. Panicker, Ms. Vijitha I, Ms. Roshini S Babu, Mr. Akil S. Karun, Ms. Sabitha, Ms. Aparana, Ms. Bhavya, Mr. Adarsh, Ms. Hasna, Ms. Sneha, Ms. Aparna Sathyan, Mr. K. Krishna kumar, Mr. Billu Abraham and all other friends at NIIST family for their help and cooperation.

There are a few people for me in NIIST, to whom I owe a lot. I would like to thank Dr. Akshay V. R, Dr. Vaisakh Sadhasivan, Dr. Dijith K.S., Dr. Bhagya Uthaman, Ms. Aswathi K, Mr. Rojerce Brown Job, Ms. Revathy R, Mr. Vishnu S, Mr. Mukesh. M, Ms. Chinnu Devan, Mr. Shabeer Ali and Mr. Thejas K K for their love and support. I am indebted to many of my lab mates for the support, love and fruitful discussions.

I owe an unlimited debt of gratitude to my parents, my father, Mr. K. Bahuleyan Nair, my mother, Ms. S. Santhakumari, for their unconditional love. Without their support and encouragement, I would not have reached this stage of my life. I am also grateful to my dear wife, Ms. S. Lekshmi Mohan for her love, support, encouragement and understanding, without which I would not have achieved what I have. I am also thankful to my brother Mr. Akil B. for being there for me whenever I need a shoulder to lean. I am also indebted to my Valiyamma, parents-in-law, siblings and grandma for their love, support and understandability throughout these years, which has helped me in the successful and comfortable completion of this work.

Arun B.

CONTENTS

List of Figures

List of Tables

Abbreviations

AC	Alternating current
AFM	Antiferromagnetic
AFMI	Antiferromagnetic insulator
C	Curie constant
CFCs	Chlorofluorocarbons
CG	Cluster glass
C_H	Specific heat capacity at constant field
CW	Curie-Weiss
DC	Direct current
DE	Double exchange
dM/dT	Derivative of magnetization
EDAX	Energy-dispersive X-ray spectroscopy
EDXRF	Energy-dispersive X-ray Fluorescence Spectrometry
ETO	Electrical transport option
FC	Field cooled
FM	Ferromagnetic
FMI	Ferromagnetic insulator
FMM	Ferromagnetic metallic
GKA	Goodenough-Kanamori-Anderson
GSAS	General structure analysis system
H	Magnetic field strength
h	Hour
ΔH	Field change
H_C	Coercivity
HCFCs	Hydrochlorofluorocarbons
HR-TEM	High-resolution transmission electron microscopy
JT	Jahn-Teller
M	Magnetization
MAP	Modified Arrott plot
MCE	Magnetocaloric effect
Mn	Manganese

M_r	Remanent magnetization
M_S	Saturation magnetization
M(T)	Magnetization as function of temperature
O	Oxygen
PM	Paramagnetic
PMI	Paramagnetic insulating
PPMS	Physical property measurement system
RE	Rare-earth elements
R_{exp}	Expected R factor
R_{wp}	R factor
SAED	Selected area diffraction patterns
SE	Superexchange
S_{EL}	Electronic entropy
SEM	Scanning electron microscopy
SG	Spin glass
S_{Lat}	Lattice entropy
S_M	Magnetic entropy
ΔS_M	Isothermal magnetic entropy change
SPM	Superparamagnetic
T	Absolute temperature
ΔT_{ad}	Adiabatic temperature change
T_C	Curie temperature
T_f	Freezing temperature
T_N	Neel temperature
T_P	Metal-insulator transition temperature
Tr	Transition metal
$V^{(a)}$	Anion vacancies
VSM	Vibrating sample magnetometer
XAS	X-ray absorption spectroscopy
XRD	X-ray diffraction
XPS	X-ray photoelectron spectroscopy
ZFC	Zero field cooled

Abstract

Mixed-valent perovskite manganites with general formula $A_{1-x}A'_xMnO_3$ (A= rare-earth and A′= alkaline rare-earth elements) are exotic materials to study the complex interplay of different properties within a system. The discovery of the magnetocaloric effect (MCE) in manganites lead to more studies on perovskite manganites. MCE is the thermal response of the magnetic material to an applied magnetic field and is induced by the coupling of magnetic sublattice with an external magnetic field. It is defined as the reversible change in the magnetic entropy and temperature of a material upon the application or removal of the magnetic field. The A-site cationic size mismatch influences double-exchange mechanism, and thereby leading to change in the magnetic properties. In the present thesis, the magnetic phase transitions and magnetocaloric properties of $Nd_{0.67}Sr_{0.33}MnO_3$ compound is studied. The properties are tuned by substitution of different transition elements at the Mn-site and creating deficiency at the Nd-site, and the compounds are found to be potential candidates for sub-room temperature applications. The creation of deficiency at the A-site of $La_{0.67}Sr_{0.33}MnO_3$ compound helps to tune the transition temperature towards room temperature without compromising the magnetocaloric properties, and the obtained values are more significant than that reported for numerous perovskite manganites. Mixed rare-earth manganites $(RE_{MIX})_{0.67}Sr_{0.33}MnO_3$ are prepared by different combination of precursor oxides (derived from Indian monazite sands and the commercially available one as well), and the compounds are found to be suitable magnetocaloric material for room temperature applications. Some of the compounds reported in this thesis are found as potential candidates for the room temperature magnetic refrigeration applications.

Chapter 1

Prologue

This chapter gives an introduction, motivation that have driven this work, objectives and scope of the thesis work. The organization of the thesis are briefly outlined at the end of the chapter.

1.1. Introduction

Green and sustainable energy is the prime motivation of present-day research. About 15% of the total worldwide energy consumption involves the use of refrigeration, and the most current refrigeration devices operate using the vapour-compression cycle (reverse Carnot cycle). Conventional gas compression based technique is an energy-consuming process and results in the emission of greenhouse gas, which has a profound impact on global warming. Magnetic refrigeration based on magnetocaloric effect (MCE) is a green technology that has aroused great interest to the scientific community because of its rich potential applications. MCE is a magneto-thermodynamic process, in which heating and cooling of a magnetic material take place via magnetization and demagnetization process. During this process, a change in the magnetic entropy (ΔS_M) of the material is observed while removing the magnetic field under the adiabatic condition and this produces a cooling effect in the material. The ΔS_M and adiabatic temperature change (ΔT_{ad}) are the two factors determining the figure of merit for good magnetocaloric material. A giant MCE was found in $Gd_5Si_2Ge_2$, which was considered as a milestone in the field of magnetic refrigeration technology. Since then, there has been a passionate search for identifying new materials with large ΔS_M values. The present thesis is focused on finding potential magnetocaloric materials using rare-earth-based manganites having ABO_3 structure for fulfilling the operational demands at sub-room and room temperatures.

1.2. motivation of the present work

Compounds such as $MnAs_{1-x}Sb_x$, $La(Fe_{1-x}Si_x)$, $MnFe(P_{1-x}Si_x)$, Gd-based amorphous alloys, Ni-Mn-X (X= Ga, In, Sn) Heusler alloys etc. exhibit large ΔS_M values. However, most of these materials show large thermal and field hysteresis, which are the factors considered to be detrimental for an active magnetic refrigerator. Moreover, they contain very expensive as well as toxic elements and have very complicated and costly synthesis routes. In recent years, mixed-valence manganites with general formula $A_{1-x}A'_xMnO_3$ (A= trivalent rare-earth ions such as La^{3+}, Nd^{3+}, Pr^{3+} etc., A′= divalent alkaline earth ions such as Ca^{2+}, Sr^{2+}, Ba^{2+} etc. or tetravalent ions) are perceived as interesting materials due to the rich physics involving charge, spin and orbital degrees of freedom. The mixed-valence manganites can be regarded as solid solutions between the end members such as $AMnO_3$ and $A'MnO_3$ with formal valence states $A^{3+}Mn^{3+}O_3^{2-}$ and $A'^{2+}Mn^{4+}O_3^{2}$, leading to mixed-valence compounds such as $(A_{1-x}^{3+}A'^{2+}_x)(Mn_{1-x}^{3+}Mn_x^{4+})O_3$. Usually, the end members are antiferromagnetic and insulating while the solid solutions with x≈ 0.33 are ferromagnetic and conducting in nature, thus making the particular composition, $A_{0.67}A'_{0.33}MnO_3$ an interesting material. In doped manganites, Mn-ions exist in a mixed valent state of $Mn^{2+}/Mn^{3+}/Mn^{4+}$, which creates ferromagnetism and conduction in these materials. The coupling between Mn^{3+} and Mn^{4+} ions results from the motion of the e_g electron between the two partially filled d- orbitals. Double exchange (DE) interaction, Jahn–Teller effect (JT) and phase separation play a key role in these mixed-valence manganites. The large ΔS_M originates from the considerable variation of magnetization near the transition temperature (T_C) and the strong spin-lattice coupling occurring in the magnetic ordering process play a significant role in magnetic entropy change. Therefore, the main focus in this thesis has been the identification of suitable rare-earth-based manganites especially $A_{0.67}A'_{0.33}MnO_3$ composition (A= La, Nd, mixed rare-earth ions; A′= Sr) and to study their structural, magnetic phase transitions and magnetocaloric properties.

1.3. Objectives and scope of the work

- To develop new magnetocaloric materials based on perovskite-type rare-earth manganites.
- Investigation of crystallographic structure and magnetic phase transitions of the magnetocaloric materials.
- Investigation of MCE by magnetic measurements (ΔS_M) and magnetic-thermal measurements (ΔT_{ad}).
- To develop magnetocaloric materials having T_C near room temperature with maximum ΔS_M for room temperature refrigeration.

1.4. Organization of the thesis

The entire thesis has been divided into **eight chapters**. An introduction to magnetocaloric materials and their recent development, a detailed literature review on perovskite-type mixed-valence manganites and their structural, magnetic and magnetocaloric properties were discussed in the **second-chapter.**

The **third-chapter** deals with the comparative study of magnetic ordering, magnetocaloric and electrical transport behaviour in bulk and nanocrystalline $Nd_{0.67}Sr_{0.33}MnO_3$ manganites. It has been found that the long-range ferromagnetic ordered state becomes unstable upon the reduction of the sample size down to the nanometre scale. AC and DC magnetization studies suggest the frustration of spins in the nanocrystalline system, and thereby it could lead to a cluster glass behaviour. Magnetocaloric properties are found to be detrimental with the reduction in particle size, and thus the bulk $Nd_{0.67}Sr_{0.33}MnO_3$ manganite is better for magnetic refrigeration applications at sub-room temperatures.

The **fourth-chapter** describes the effects of Mn-site substitution by different transition elements in $Nd_{0.67}Sr_{0.33}MnO_3$ manganite. Substitution of 10 at. % of Cr, Fe, Co, Ni and Cu at the Mn-site in $Nd_{0.67}Sr_{0.33}MnO_3$ has broadened the ferromagnetic (FM)-paramagnetic (PM) transition leading to the suppression of magnetocaloric effect. The magnetic ordering, magnetocaloric properties and critical exponent behaviour of the compounds were discussed in detail.

Impact of Nd and Sr-site deficiencies on the structural, magnetic and electrical transport properties in $Nd_{0.67-x}Sr_{0.33}MnO_{3-\delta}$ (x= 0.09, 0.17, 0.25, 0.33) and $Nd_{0.67}Sr_{0.33-y}MnO_{3-\delta}$ (y= 0.09, 0.17) manganites were discussed in the **fifth-chapter**. Among the studied compounds, $Nd_{0.67-x}Sr_{0.33}MnO_{3-\delta}$ (x= 0.17) composition shows the highest T_C with the least value of electrical resistivity and significant enhancement in magnetization than that of the pristine compound. Further, nanocrystalline $Nd_{0.67-x}Sr_{0.33}MnO_{3-\delta}$ (x= 0.17) manganite was synthesized, and the structural, magnetic, magnetocaloric and electrical properties have been systematically studied and compared with that of the bulk counterpart. The bulk compound shows maximum $-\Delta S_M$ value of 1.65 J kg^{-1} K^{-1} and 4.89 J kg^{-1} K^{-1} at 275 K for 10 kOe and 50 KOe field change and it could be a potential candidate for sub-room temperature applications.

The **sixth-chapter** illustrates the effects of La and Sr-site deficiencies on the structural, magnetic and magnetocaloric properties in $La_{0.67}Sr_{0.33}MnO_3$ compound. Among the studied compounds, $La_{0.67}Sr_{0.33-y}MnO_{3-\delta}$ (y = 0.09) composition shows the highest $-\Delta S_M$ of 5.08 J kg^{-1} K^{-1} at 352 K for 50 kOe field and a ΔT_{ad} of 3.48 K, while $La_{0.67}Sr_{0.33}MnO_3$ and $La_{0.67-x}Sr_{0.33}MnO_{3-\delta}$ (x= 0.09) compounds exhibit a $-\Delta S_M$ of 4.78 J kg^{-1} K^{-1} at 364 K and of 4.12 J kg^{-1} K^{-1} at 364 K, respectively. The Sr-site deficient compound shows a promising behaviour of reduction in the T_C towards room temperature, along with an increase in the ΔS_M values. Further, the effects of Sr-site deficiency in $La_{0.67}Sr_{0.33-y}MnO_{3-\delta}$ (y= 0.18 and 0.27) compounds were investigated. A second-order FM-PM transition with an enhancement in magnetization in comparison to the pristine compound ($La_{0.67}Sr_{0.33}MnO_3$) was observed attributed to multiple DE interactions. Significant ΔS_M value (4.61 J kg^{-1} K^{-1}) near room temperature (310 K) was achieved in $La_{0.67}Sr_{0.33-y}MnO_{3-\delta}$ (y= 0.27) compound, which is larger than that reported for numerous perovskite manganites.

A cost-effective precursor material to develop a magnetocaloric material for magnetic refrigeration was proposed in the **seventh-chapter**. A mixed rare earth manganite $(RE_{MIX})_{0.67}Sr_{0.33}MnO_3$ was prepared using a natural mixture of rare earth oxide (RE_2O_3-1), which is a by-product derived from the Indian monazite sand after thorium extraction. The $(RE_{MIX})_{0.67}Sr_{0.33}MnO_3$ compound is found to be ferromagnetic at room temperature and exhibit a $-\Delta S_M$ of 3.28 J $kg^{-1}K^{-1}$ at 310 K under a field change of 50 kOe and makes it a potential candidate for room temperature magnetic refrigeration applications. Further, two different kinds of mixed rare earth oxide (RE_2O_3-2 and RE_2O_3-3) were prepared by commercially available high purity rare earth oxides. The $(RE_{MIX})_{0.67}Sr_{0.33}MnO_3$ composition was prepared by RE_2O_3-2 and RE_2O_3-3 individually, and their structural, magnetic and magnetocaloric properties were studied and compared with that of the pristine compound.

The summary of entire thesis work has been provided in the **eighth-chapter** followed by the scope for the future work.

Chapter 2

Magnetic refrigeration and magnetocaloric materials: Fundamentals and properties of rare-earth manganites

This chapter gives an introduction to magnetic refrigeration and the recent advances in the development of magnetocaloric materials. A detailed literature review on mixed valence manganites and their structural, magnetic and magnetocaloric properties were discussed

2.1. Introduction to magnetic refrigeration

Magnetic refrigeration is a well developed solid-state cooling technology based on the MCE of magnetic materials [1-3]. It is a cost-effective and environmentally sound alternative to the conventional vapour-compression refrigeration system [4, 5]. Under the Montreal Protocol, gases such as chlorofluorocarbons (CFCs) and hydrochlorofluorocarbons (HCFCs) are being phased out because of their ozone layer depletion and global warming effects [6]. However, in the conventional refrigeration technique, CFCs and HCFCs are still used as the refrigerant, and it is clear that this technique is no longer a viable alternative to sustain global needs. In comparison to the conventional method, the magnetic refrigeration system has better energy efficiency, adaptability and does not release any greenhouse gases [1-5]. In the entire process, the magnetocaloric material is subjected to repeated magnetization and demagnetization cycles, and as a result, the magnetic material heats and cools down respectively [7-9]. Even though the magnetic refrigeration is used in practical application to reach hydrogen and helium liquefaction temperatures as well as temperatures below 1 K, there is no commercial technology available for room temperature magnetic refrigeration applications. So, there is a need for developing materials which show strong magnetocaloric properties near room temperatures.

The conventional refrigeration systems consist of a compressor and two heat exchangers (condenser and evaporator). Initially, the refrigerant, which is in the liquid state, picks up heat from the source (space to be refrigerated) and becomes vapour. As the vapour passes through the compressor, its temperature and pressure increases. Then the refrigerant gas emits heat to a sink and becomes liquid. Thus the compressed gas rejects heat to the hot sink, and the expanded gas absorbs heat from the cold source. As the process continuous, hot and cold temperatures produce at the two ends of the system. The magnetization and demagnetization process under controlled magnetic field causes heating and cooling effect in the magnetocaloric material, which is similar to the heating and cooling produced by a refrigerant gas during the compression and expansion cycles in a conventional refrigeration system. The temperature of the refrigerant gas increases during compression and decreases during expansion. However, in magnetic refrigeration, the magnetized magnetocaloric material rejects heat to the sink, and the demagnetized material absorbs heat from the source. A controlled magnetic field is applied in repeated magnetization and demagnetization cycles to the magnetocaloric material, and it creates a temperature gradient in the material [10-12]. The excess heat generated in the system during magnetization is removed using a coolant fluid and the temperature of the magnetocaloric material back down to its original temperature. As the cycles repeated, stabilized hot and cold temperatures are produced in the refrigeration system. Fig. 2.1 shows the comparison of magnetic refrigeration to the conventional vapour-compression refrigeration system. For room-temperature applications, glycol water is used as a coolant fluid to transfer heat between hot and cold sources. Helium gas or liquid hydrogen can be used as coolant fluids at low-temperature, and liquid nitrogen can be used for applications at intermediate temperature. A high energy density permanent magnet is used as a controlled magnetic field at room temperature, and a superconducting magnet can be used for low-temperature applications [13]. The efficiency of a magnetic refrigerator is about 60 % of the Carnot cycle, whereas it is only 40 % in conventional vapour compression refrigeration technique [14]. However, the room temperature magnetic refrigeration is made possible by developing new magnetocaloric materials with large MCE around room temperature.

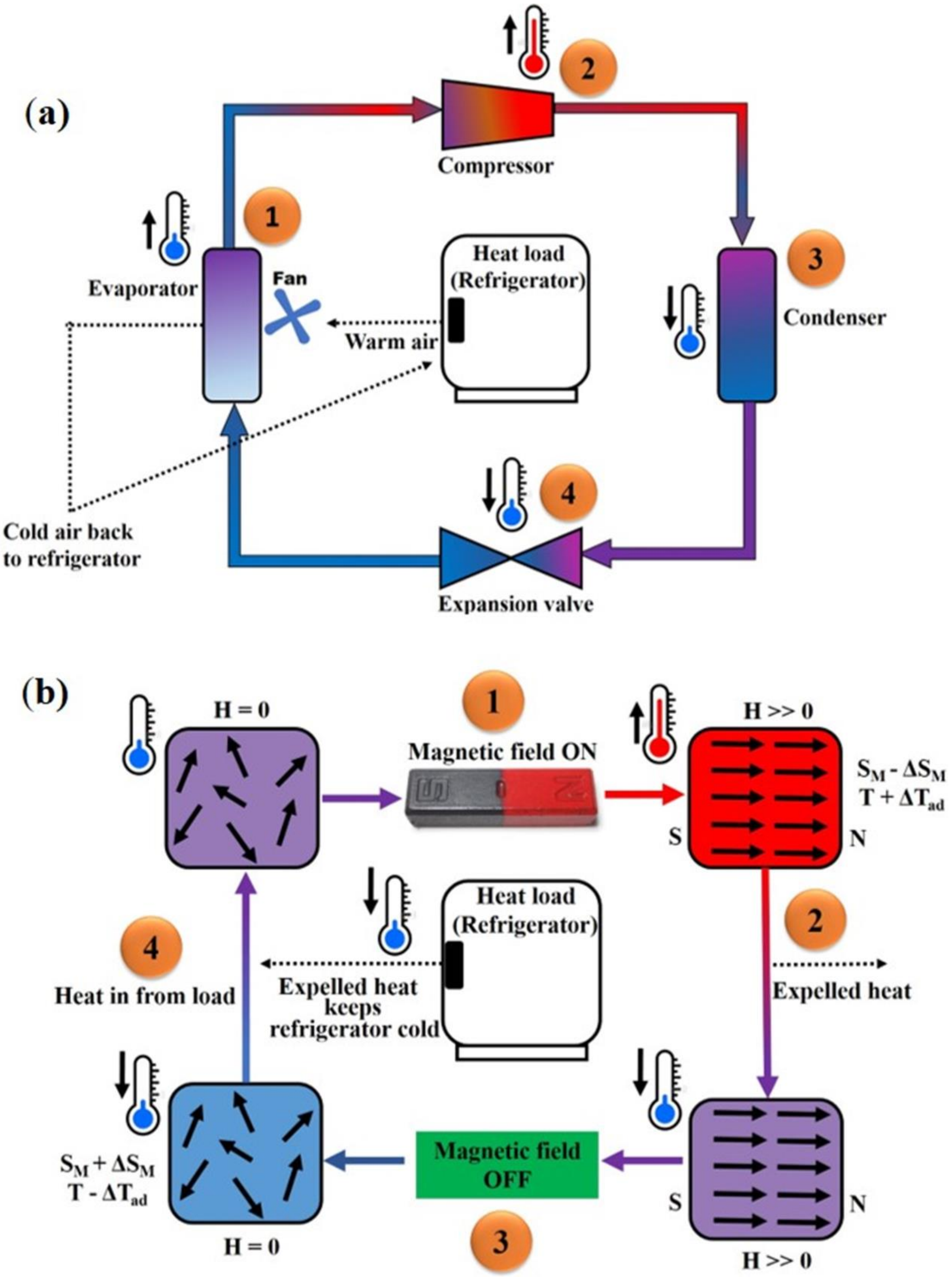

Fig. 2.1. *Comparison of (a) conventional refrigeration to (b) magnetic refrigeration*

2.2. Historical background of MCE

MCE was discovered in 1881 by E. Warburg in iron [15]. But it wasn't experimentally proved until Weiss and Piccard discovered the reversible temperature change in Ni near its Curie temperature in 1917 [16]. The principle of adiabatic demagnetization was demonstrated independently by Debye (1926) and Giauque (1927) and reaches a temperature lower than that of liquid helium, and Giauque got the Nobel Prize for his discovery in 1949 [17, 18]. In 1933, Giauque and MacDougall demonstrated the adiabatic demagnetization process using paramagnetic salt, Gadolinium sulphate ($Gd_2(SO_4)_3 \cdot 8H_2O$) and reaches temperatures of 0.53 K, 0.34 K and 0.25 K starting from 3.4 K, 2.0 K and 1.5 K respectively under a magnetic field of 0.8 T [19]. In 1976, Brown demonstrated a room temperature magnetic refrigeration system using Gadolinium (Gd) as the magnetocaloric material [20]. As a proof of principle, in 1997, Pecharsky and Karl A. Gschneidner of Ames Laboratory, USA demonstrated a giant MCE in $Gd_5(Si_2Ge_2)$ with a potential energy savings of 30 % at room temperature [21]. In 2002 when a group of researchers from the University of Amsterdam, Netherlands demonstrated a giant MCE in MnFe(P, As) alloys [22]. Since then, new magnetocaloric materials and magnetic refrigeration system with various designs and models have been developed [23-33]. Even though the magnetic refrigeration is a promising technology, still there are lots of challenges to be addressed and it is needed to prove that this technology is feasible. The major challenge in this area is the identification of suitable materials with large magnetocaloric properties. So investigations of new materials with large magnetocaloric properties are required for practical applications at sub-room and room temperatures.

2.3. Theoretical background of MCE

MCE is an intrinsic property of a magnetic material. When a magnetic material is subjected to cyclic magnetization and demagnetization process, the material absorbs and emits heat respectively and results in warming and cooling of the material. Magnetocaloric property of a material is related to the magnetic sublattices and its response to the applied magnetic field. The MCE of a material can be quantified in terms of ΔS_M, i.e., the application of magnetic field results in the magnetic entropy change at constant temperature or ΔT_{ad}, i.e., the change in temperature upon application of the magnetic field [34-36]. For temperature greater than that of the Curie temperature (T_C), the material is paramagnetic, and for temperature less than T_C, it becomes ferromagnetic. Thus, in the paramagnetic region, the magnetic moments are oriented in random directions, and the magnetic entropy of the material is reduced. Fig. 2.2 shows the magnetic phase transition of a magnetocaloric material at its T_C and the material shows the maximum magnetocaloric properties at this temperature.

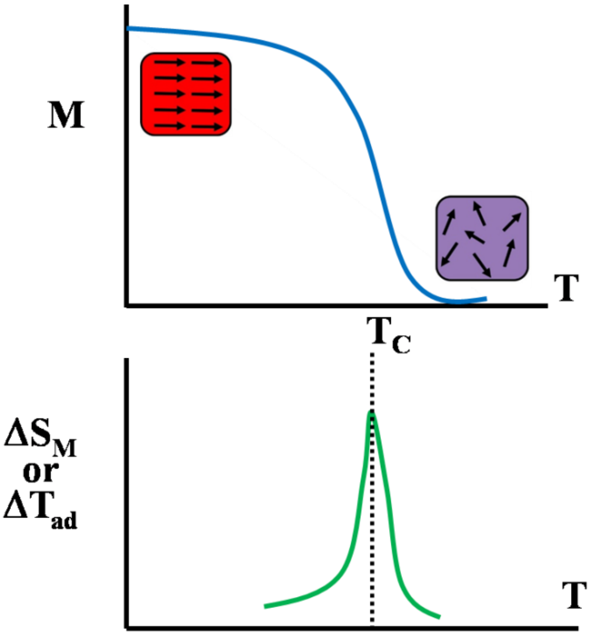

Fig. 2.2. Magnetic phase transition of a magnetocaloric material at its T_C

The total entropy S (T, H) of a ferromagnetic material at constant pressure depends on both the applied magnetic field strength (H), and temperature (T), whose contributions arise from the magnetic entropy (S_M), the lattice entropy (S_{Lat}) and electronic entropy (S_{El})

$$S(T, H) = S_M(T, H) + S_{Lat}(T) + S_{El}(T) \tag{2.1}$$

S_{Lat} and S_{El} entropies are independent of magnetic fields, whereas S_M is lowered due to the ordering of magnetic spins along the field direction. Fig. 2.3 shows the schematic representation of thermal dependence of the entropy of a magnetocaloric material near its T_C. The solid lines represent the S (T, H) at zero magnetic field ($H_0 = 0$) and dotted lines represent at non-zero magnetic fields ($H_1 \neq 0$). The horizontal arrow shows the ΔT, and the vertical arrow shows the ΔS under a field change from H_0 to H_1.

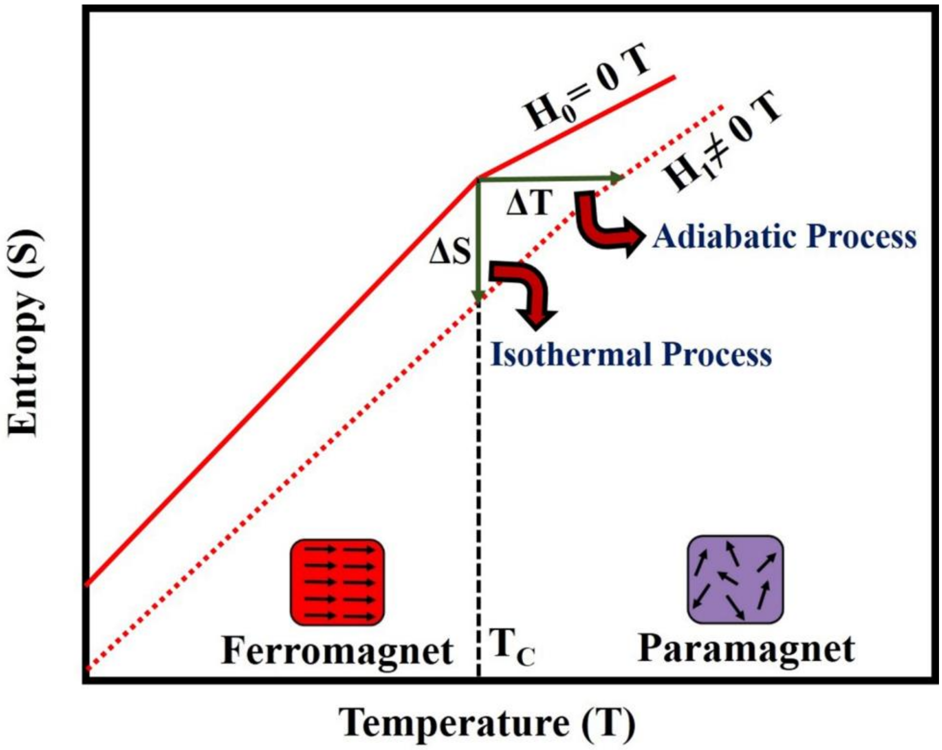

Fig. 2.3. *Schematic representation of thermal dependence of entropy of material near its T_C*

For a magnetocaloric material, S (T, H) remains constant, and the thermodynamics of MCE can be understood from the two magnetic iso-field curves as:

i. When the field is applied adiabatically, the S_M of the material is lowered, and the S_{Lat} is increased because the material is kept isolated from the surroundings. Thus, the increase in S_{Lat} leads to an enhancement in the temperature of the material.

$$S(T_0, H_0) = S(T_1, H_1) \tag{2.2}$$

The difference between the final temperature (T_1) and initial temperature (T_0) gives ΔT_{ad} as

$$\Delta T_{ad} = T_1 - T_0 \tag{2.3}$$

ii. When the field is applied isothermally, the total entropy of the material decreases due to the ordering of magnetic spins and the ΔS_M can be written as

$$\Delta S_M = S(T_0, H_0) - S(T_0, H_1) \tag{2.4}$$

where T_0 represent the temperature at zero field whereas T_1 is the same at a higher field H_1. Hence, when the field is raised, the magnetic entropy of the material decreases due to the ordering of magnetic spins. Therefore, ΔT_{ad} is positive, and ΔS_M is negative, and the magnetic material heats up. When the field is reduced, the magnetic entropy increases (ΔS_M is positive) and giving rise to a cooling effect in the material (ΔT_{ad} is negative).

According to Maxwell's relation [37], at absolute temperature (T), the ΔS_M of a magnetic material can be related to the magnetization (M) and the magnetic field strength (H) as:

$$\left[\frac{\partial S(T,H)}{\partial H}\right]_T = \left[\frac{\partial M(T,H)}{\partial T}\right]_H \tag{2.5}$$

Integrating equation (2.5) for an isothermal and isobaric process gives

$$\Delta S_M(T, \Delta H) = \int_{H_0}^{H_1} \left[\frac{\partial M(T, H)}{\partial T}\right]_H dH \tag{2.6}$$

From the equation (2.6), it is understood that the ΔS_M of a magnetic material is proportional to both the temperature derivative of magnetization at a constant field and the field variation.

For a ferromagnetic material, the absolute value of temperature derivative of magnetization, $\left|\left(\frac{\partial M}{\partial T}\right)\right|_H$ is maximum at T_C; therefore, $\left|\Delta S_M(T)_{\Delta H}\right|$ should show a peak at T_C.

If the magnetic measurements are made at the discrete field and temperature intervals, ΔS_M (T, H) can be related to the M of the material as:

$$\Delta S_M(T, \Delta H) = \sum_i \frac{M_{i+1}(T_{i+1}, H) - M_i(T_i, H)}{T_{i+1} - T_i} \Delta H \tag{2.7}$$

Combining the equation (2.6) with the following thermodynamic relation,

$$C_H = T\left[\frac{\partial S}{\partial T}\right]_H \tag{2.8}$$

where C_H is the specific heat capacity at the constant field.

The infinitesimal adiabatic temperature change of a material is expressed by

$$dT = -\left[\frac{T}{C(T, H)}\right]_H \left[\frac{\partial M(T, H)}{\partial T}\right]_H dH \tag{2.9}$$

Integrating equation (2.9), the MCE of a material can be expressed in terms of ΔT_{ad} as:

$$\Delta T_{ad}(T, \Delta H) = -\int_{H_0}^{H_1} \left[\frac{T}{C\,(T, H)}\right]_H \left[\frac{\partial M(T, H)}{\partial T}\right]_H dH \tag{2.10}$$

From equation (2.10), it can be seen that ΔT_{ad} is proportional to T and inversely proportional to C_H. Since the ferromagnetic material should show a $(\partial M/\partial T)_H$ peak at the T_C, the maximum ΔS_M and ΔT_{ad} are obtained in the vicinity of T_C due to the rapid change in its magnetization values.

2.4. Measurement of MCE

The MCE can be measured either by direct or indirect methods from the magnetization measurements or field dependence of the specific heat capacity [38-40].

2.4.1. Direct measurements

In the direct method, magnetocaloric material is isolated adiabatically, and measurement is carried out either contact or non-contact techniques by placed a temperature sensor on it. In the contact technique, the sensor is in direct thermal contact with the material and non-contact technique, the temperature sensor is not directly connected to the material [41, 42]. In both cases, the sensor measured the initial temperature (T_0) and final temperature (T_1) of the material, when the external magnetic field is swept from H_0 to H_1. Then, ΔT_{ad} is calculated according to the relation,

$$\Delta T_{ad}\,(H_1\text{-}H_0) = T_1\text{-}T_0 \tag{2.11}$$

To perform the direct measurement, the magnetic field is required to change rapidly, and hence the measurements can be performed on immobilized samples by changing the magnetic field, or by mobilized the samples in and out of a uniform magnetic field region [33, 43]. In both the cases, the required field is usually provided by a permanent magnet, electromagnets or superconducting magnets which produce field range of 0.1 to 100 kOe. The time scale required for achieving this field range varies in seconds in an electromagnet to minutes in a superconducting magnet. However, the accuracy of the measurement depends on various factors such as errors in the field arrangements and thermometry, quality of thermal insulation, fluctuation in the reading of the sensor by the magnetic field etc.

2.4.2. Indirect measurements

In the indirect experiments, the ΔS_M and ΔT_{ad} are calculated from the magnetic measurements or field dependence of the specific heat capacity [44, 45]. The specific heat capacity measurements yield both ΔS_M and ΔT_{ad}, while the magnetic measurement gives only

ΔS_M. The accuracy of ΔS_M calculated from the magnetic measurements depends on the accuracy of the magnetic moment measurements with temperature and magnetic field. It is also affected due to the replacement of differentials such as dM, dH and dT by corresponding the measured variations such as ΔM, ΔH and ΔT respectively. Since ΔS_M depends on the small difference between two large entropy values, the error in the measurement can be calculated from equation (2.4) as

$$\sigma\,[\,\Delta S_M\,(T, \Delta H)] = \sigma\,[\,S\,(T, H = 0)] + \sigma\,[\,S\,(T, H \neq 0)] \qquad (2.12)$$

where $\sigma\,[\,S\,(T, H = 0)]$ and $\sigma\,[\,S\,(T, H \neq 0)]$ are the errors at zero field and non-zero field entropy respectively. Pecharsky and Gschneidner have reported that calculation of ΔS_M and ΔT_{ad} using the indirect method is reliable, and the error in the value of ΔS_M lies within the range of 3-10% [46]. However, the error in the ΔT_{ad} is proportional to $\sigma\,[S\,(T, H = 0)]$ and $\sigma\,[S\,(T, H \neq 0)]$, but it is inversely proportional to the temperature derivative of zero field and non-zero field entropy values. In the present thesis work, indirect measurement technique has been used to estimate the values of ΔS_M and ΔT_{ad} from the magnetization measurements and field dependence of the specific heat capacity respectively.

2.5. Magnetocaloric materials

Wide range of magnetocaloric materials show a broad spectrum of T_C with significant ΔS_M and ΔT_{ad} values and the majority of them are based on rare earth (RE) elements and transition metals (Tr). They can be classified into different families based on their crystalline structures. Laves phases, $La[Fe(Si, Al)]_{13}$ family, $Gd_5(Si, Ge)_4$ family, rare-earth manganites etc. belong to rare earth containing groups and Heusler alloys, Mn-Tr-(Si,Ge) and $(Mn,Tr)_5X_3$ compounds, MnAs and MnFe(P, As) family, FeRh alloys etc. are classified under rare earth-free groups.

2.5.1. Magnetocaloric materials containing rare-earth elements

- **Gd metal and its alloys**

The room temperature prototype material Gd metal has been investigated independently by many researchers because it shows ferromagnetic order at 294 K with a $-\Delta S_M$ of 10 J kg^{-1} K^{-1} and a ΔT_{ad} of 5.4 K for a field change (ΔH) of 50 kOe [47]. However, other pure lanthanide metals such as Pr, Nd, Er, Tm etc. show ferromagnetic order and magnetocaloric properties at low-temperature region [48-50]. To improve the properties of Gd, Gd-RE alloys (RE= Tb, Dy, Ho, Er etc.) and Gd-Mn alloys were prepared, and magnetocaloric properties were studied [51-53]. A change in T_C towards lower temperatures without any significant improvement in properties were observed.

- **Laves phases**

Cubic laves phases have a formula of AB_2 (A= RE elements, B= Tr elements) with $MgCu_2$ type crystal structure. In this system, two magnetic sublattices are formed, one due to the magnetic RE atoms and other due to the itinerant electron magnetism generated by the Tr. Ho_2Co exhibit laves phase with $-\Delta S_M$ of 11 J kg^{-1} K^{-1} at 85 K for ΔH= 50 kOe and deuterium induced YF_2, i.e., ($YFe_2D_{4.2}$) shows $-\Delta S_M$ value greater than 10 J kg^{-1} K^{-1} between 90 and 110 K for ΔH= 50 kOe [54, 55]. Among the laves phases, HoCuSi is an interesting composition due to its large $-\Delta S_M$ of 33.1 J kg^{-1} K^{-1} at 7 K for ΔH= 50 kOe [56]. However, due to the transition at 7 K, it is limited to ultra-low temperature applications. Moreover, the low-yield, as well as time-consuming process, restricts the material from practical applications.

- **La[Fe(Si, Al)]$_{13}$ family**

La and Fe together do not form an intermetallic compound because the binary phase is immiscible. However, the addition of small amounts of Si or Al helps to form a ferromagnetic compound of $NaZn_{13}$ type structure [57]. Cubic $LaFe_{11.4}Si_{1.6}$ exhibits a $-\Delta S_M$ of 19.4 J kg^{-1} K^{-1} at 210 K for ΔH= 50 kOe and $La(Fe_{0.98}Co_{0.02})_{11.7}Al_{1.3}$ shows $-\Delta S_M$ of 11 J kg^{-1} K^{-1} at 200 K for ΔH= 50 kOe [7, 58]. However, single-phase La[Fe(Si, Al)]$_{13}$ system is very difficult to obtain due to the formation of α- Fe phase, La- rich phase and other binary phases. Thus, the system is inhomogeneous and need prolonged annealing of several days at high temperature for single-phase formation.

- **$Gd_5(Si, Ge)_4$ family**

$Gd_5(Si,Ge)_4$ family have a general formula of RE_5X_4 formed between two polymorphic orthorhombic Gd_5Si_4 and Gd_5Ge_4 compounds [59]. According to Pecharsky and Gschneidner, the prototype material $Gd_5Si_2Ge_2$ exhibits large $-\Delta S_M$ of 18.5 J kg^{-1} K^{-1} and ΔT_{ad}= 15 K at 276 K for ΔH of 50 kOe [21]. However, a thermal hysteresis of 2-5 K and the presence of antiferromagnetic Gd_5Si_3 secondary phase restricts the material from practical applications. Moreover, the presence of Ge-rich phases shifts the T_C of the material towards the low-temperature and the substitution of other elements such as Ga, Sn, Mn, In etc. instead of Si/Ge destroy the magnetocaloric properties and shifts the T_C towards higher temperatures [60-64]. A lower amount of Gd_5Si_3 secondary phase is found in $Gd_5Si_{1.95}Ge_{1.95}Nb_{0.1}$ and $Gd_{4.95}Zr_{0.05}Si_2Ge_2$ compounds, which exhibits a $-\Delta S_M$ of 9.6 J kg^{-1} K^{-1} at 295 K and 5.5 J kg^{-1} K^{-1} at 292 K respectively for ΔH of 20 kOe [65, 66]. However, higher annealing temperatures and higher cooling rates are needed to ensure the homogeneity of the compounds.

- **Other crystalline compounds**

Pr_2Fe_{17} and Y_2Fe_{17} are found to be good candidates for near room temperature applications and exhibits $-\Delta S_M$ of 6.3 J kg^{-1} K^{-1} at 290 K and nearly 5 J kg^{-1} K^{-1} at 295 K respectively for ΔH= 50 kOe [67, 68]. $Ce_{0.8}Y_{1.2}Fe_{17}$, $Ce_{0.5}Pr_{1.5}Fe_{17}$ and $Ce_{0.85}Dy_{1.15}Fe_{17}$ compounds showed $-\Delta S_M$ values of 4.3 J kg^{-1} K^{-1} at 253 K, 5.3 J kg^{-1} K^{-1} at 264 K and 3.3 J kg^{-1} K^{-1} at 273 K respectively for ΔH= 50 kOe [69]. Gd_3Tr series compounds such as Gd_3Co, Gd_3Ni and Gd_3Rh exhibited the magnetocaloric properties at low-temperatures and their $-\Delta S_M$ values are 11 J kg^{-1} K^{-1} at 128 K, 5 J kg^{-1} K^{-1} at 99 K and 9.2 J kg^{-1} K^{-1} at 112 K respectively for ΔH= 50 kOe [70-72]. $RETr_{12}B_6$ (RE= Nd, Pr; Tr= Fe, Co) series compounds such as $NdFe_{12}B_6$, $NdCo_{12}B_6$ and $PrFe_{12}B_6$ showed the $-\Delta S_M$ values of 8.4 J kg^{-1} K^{-1} at 220 K (for ΔH = 10 kOe), 1.4 J kg^{-1} K^{-1} at 170 K (for ΔH = 10 kOe) and 11.7 J kg^{-1} K^{-1} at 200 K (for ΔH = 20 kOe) respectively [73, 74].

2.5.2. Rare-earth free magnetocaloric materials

- **Heusler alloys**

Heusler alloys have a general formula X_2YZ in which X and Y are 3d transition elements, and Z is III A- V A group elements [75]. Ni-Mn-Ga is the first reported Heusler alloy for magnetocaloric application in which single-crystal $Ni_{52.6}Mn_{23.1}Ga_{24.3}$ showed a $-\Delta S_M$ of 18 J kg^{-1} K^{-1} at 290 K for ΔH= 50 kOe [8]. $Ni_{50}Mn_{50-x}Y_x$ (Y= In, Sn) series of Heusler alloys showed both structural (austenite-martensite) phase transition and magnetic (FM-PM) phase transition. Inverse MCE (positive ΔS_M) occurred at austenite-martensite phase transition region whereas conventional MCE (negative ΔS_M) occurred at the magnetic phase transition region [76, 77]. Compounds such as $Ni_{50}Mn_{50-x}Sn_x$ (x= 13-15) and $Ni_{50}Mn_{35}In_{15}$ showed maximum inverse $+\Delta S_M$ of 18 J kg^{-1} K^{-1} and 35.8 J kg^{-1} K^{-1} for ΔH of 50 kOe near room temperature [9, 78]. However, the structural transformation leads to the occurrence of inhomogeneous magnetic states, and large thermal hysteresis of 20 K (Ni-Mn-Sn) and 10 K (Ni-Co-Mn-In) restricts the compounds from practical applications.

- **Mn-Tr(Si, Ge) and (Mn, Tr)$_5$X$_3$ compounds**

$MnCoGe_{0.98}B_{0.02}$ compound showed a $-\Delta S_M$ of 47.3 J kg^{-1} K^{-1} at 287 K for ΔH= 50 kOe, however, a thermal hysteresis of 14 K testricts the material from practical applications [79]. In $MnCoSi_{1-x}Ge_x$, a maximum inverse $+\Delta S_M$ = 4 J kg^{-1} K^{-1} is observed for ΔH of 10 kOe [80]. However, the compound shows a thermal and field hysteresis of 8 K and 3.5 kOe, respectively. Mn_5Ge_3 and Mn_5PB_2 are reported to be good candidates for room temperature applications and exhibits $-\Delta S_M$ of 9 J kg^{-1} K^{-1} at 296 K and nearly 5 J kg^{-1} K^{-1} at 302 K respectively for ΔH= 50 kOe [81, 82].

- **MnAs and MnFe(P, As) compounds**

MnAs showed a $-\Delta S_M$ of 30 J kg^{-1} K^{-1} at 318 K for 50 kOe field change and showed a large thermal hysteresis [83]. Compounds such as $MnFeP_{0.45}As_{0.35}$, $MnFe(P_{0.63}Si_{0.26})Ge_{0.11}$ and $MnFeP_{0.5}Si_{0.5}$ are reported to have $-\Delta S_M$ values of 15 J kg^{-1} K^{-1} at 300 K, 16 J kg^{-1} K^{-1} at 292 K and 30 J kg^{-1} K^{-1} at 300 K respectively for ΔH = 20 kOe [10, 84, 85]. However, the toxic nature of arsenic and large thermal hysteresis (above 20 K) limits these compounds from practical applications. Moreover, impurity phases such as Fe_2MnSi has also been found in these compounds which reduce the magnetocaloric properties of the compounds.

- **FeRh alloys**

$Fe_{49}Rh_{51}$ and $Fe_{48}Rh_{52}$ were reported to be good candidates for room temperature applications with inverse $+\Delta S_M$ of 22 J kg^{-1} K^{-1} (for 19. 5 kOe) and 12 J kg^{-1} K^{-1} (for 50 kOe) respectively at 300 K [86, 87]. However, the FeRh alloys are limited to practical applications due to

(i) high cost of Rh, (ii) lack of reproducibility and (iii) virgin M-H curves that cause the irreversibility of the magnetocaloric properties.

- **Other crystalline compounds**

$Fe_{79}Pt_{21}$ alloy was reported to show a $-\Delta S_M$ of 31.3 J kg^{-1} K^{-1} at 250 K for 50 kOe field with huge thermal hysteresis of 30-40 K [88]. Perovskite type Mn_3GaC compounds showed an inverse $+\Delta S_M$ of 15 J kg^{-1} K^{-1} at 165 K for 20 kOe field change [89]. Nanocrystalline Ferrite $CoFe_2O_4$ showed an inverse $+\Delta S_M$ of 0.25 J kg^{-1} K^{-1} at 210 K for 13 kOe field [90].

Even though the intermetallic compounds show large ΔS_M and ΔT_{ad} values, they are considered to be detrimental for practical applications due to the following issues.

(i) high manufacturing cost and complicated synthesis routes

(ii) large thermal and field hysteresis

(iii) lack of reproducibility of the initial properties

(iv) presence of toxic elements like As

(v) heat treatments at higher temperatures and for a prolonged time (several days for some cases) are required to ensure the homogeneity

(vi) due to low electrical resistance, Foucault currents produced as a result of rapid change in the magnetic field

2.6. Introduction to Perovskite manganites

The perovskite has the general formula of ABX_3 structure, where A is trivalent rare-earth ions or divalent alkali earth ions, B is 3-d transition elements, and X is an anion, usually oxide or halide [91-93]. In 1839, the mineral $CaTiO_3$ was discovered in the Ural Mountains of Russia by Gustav Rose, and it is named as "perovskite" after the Russian mineralogist Lev Perovski [94]. Later, the name is applied to all class of materials which have the same type of structure as that of $CaTiO_3$ mineral [95]. The crystal structure and tolerance factor of the first synthetic perovskite were described by Victor Goldschmidt in 1926 and later in 1945 Helen Dick Megaw (1945) published the crystal structure of $BaTiO_3$ based on the X-ray diffraction study [96, 97]. Perovskite oxides (ABO_3) with B-site occupied by manganese are usually called perovskite manganites, and the structure can be regarded as a network of corner-sharing MnO_6 octahedra with rare-earth ions or alkali earth ions occupying the interstitial positions between the octahedra [98, 99]. The mixed-valence manganites with formula $A_{1-x}A'_xMnO_3$ ($A = La^{3+}$, Nd^{3+}, Pr^{3+} etc., $A' = Ca^{2+}$, Sr^{2+}, Ba^{2+} etc. or tetravalent ions) can be regarded as solid solutions between the end members such as $AMnO_3$ and $A'MnO_3$ with formal valence states $A^{3+}Mn^{3+}O_3^{2-}$ and $A'^{2+}Mn^{4+}O_3^{2}$, leading to mixed-valence compounds such as $(A_{1-x}^{3+}A'^{2+}_x)(Mn_{1-x}^{3+}Mn_x^{4+})O_3$ [100, 101]. The exchange interactions between Mn^{3+} and Mn^{4+} ions result from the motion of the e_g electrons between the two partially filled d- orbitals and that creates ferromagnetism and conduction [102]. The large ΔS_M is originating from the significant variation of magnetization near the T_C and the strong spin-lattice coupling occurring in the magnetic ordering process.

Some key parameters play significant roles in controlling the physical properties of the mixed-valence manganites. They are

- average A-site cationic radius $<r_A>$

- size variance $\sigma^2 = < r_A^2 > - < r_A >^2$, a factor related to the degree of disorder
- doping concentration (x) of A'- elements, a factor related to Mn^{3+}/Mn^{4+} ratio
- doping of different transition elements at the Mn-site
- cationic deficiency
- enhancement or reduction of oxygen content

Moreover, some important features determining the electronic and magnetic properties of manganites are

2.6.1. Crystal structure and tolerance factor

The ideal perovskite manganites would show the cubic structure, and the crystallographic symmetry of most of them is modified to rhombohedral, orthorhombic, tetragonal etc. due to the buckling and distortion of the MnO_6 octahedra [103]. The Buckling and distortion of MnO_6 octahedra arise due to the ionic radius mismatch between the rare earth and alkaline earth atoms [104]. Thus the cation substitution, cation and anion deficiency etc. can reduce the ideal cubic structure to structures of lower symmetry [105-107]. A schematic diagram of the perovskite manganite is shown in Fig. 2.4.

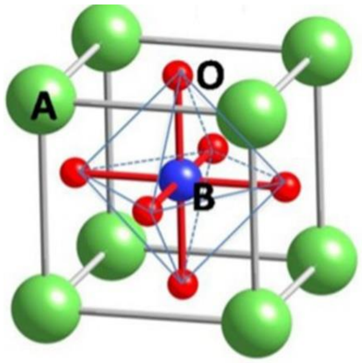

Fig. 2.4. *Crystal structure of perovskite manganite*

The trivalent rare-earth ions and divalent alkaline earth ions are 12 fold coordinated by oxygen ions and located in corners at position (0, 0, 0). The Mn^{3+}/Mn^{4+} ions occupy the body centre position (½, ½, ½), and the oxygen ions are located at the face centre position

(½, ½, 0). The geometric packing within the perovskite structure can be described by the structural factor, called the tolerance factor, defined as [108]

$$\tau = \frac{r_A + r_O}{\sqrt{2}(r_B + r_O)} \tag{2.13}$$

where r_A, r_B and r_O are the average radii of the A- sites, B-sites and oxygen respectively. For an ideal cubic structure, $\tau = 1$ and any deviation from this value is an indication of a distorted cubic structure [109]. For rhombohedral distortions, τ values exist between 0.96 and 1, and for $t < 0.96$, the distortions are orthorhombic [110]. For $\tau > 1$, the perovskite structure will be destroyed, and a hexagonal close packing formed [110]. A reduction in the $\langle r_A \rangle$ leads to the decrease in the unit cell volume, which in turn decreases the τ value. Consequently, the crystal structure distorts from the ideal cubic structure and transform into rhombohedral/orthorhombic/hexagonal close packing. Moreover, change in $\langle r_A \rangle$ results in the Mn–O bond length and Mn–O–Mn bond angle, which strongly affects the electron hopping process between Mn^{3+} and Mn^{4+} ions [111]. Since the magnetic behaviour of manganites strongly depends on the strength of the DE interaction between Mn^{3+} and Mn^{4+} ions, the distortion of MnO_6 octahedra severely influences the magnetic properties of the perovskite manganites.

2.6.2. Crystal field splitting

In perovskite manganites, the crystal field splitting plays a significant role in the electronic and magnetic properties [112]. In manganites, the Mn ions are surrounded by nearest-neighbour oxygen octahedra and due to this, the axes of the crystal orient to specific directions. The Mn ions have a partially filled 3d-subshell with five degenerate levels, and to minimize the Coulomb repulsion, the degenerate levels are filled based on the Hund's rule [113]. Thus, the spherical symmetry reduces, and some of the orbital degeneracy is lifted, resulting in crystal field splitting. The crystal field splitting energy difference is calculated by the relation [114]

$$\Delta \propto \frac{<r>^4}{R^5} \qquad (2.14)$$

where ‘r’ is the radius of the orbital and R is the inter-nuclear distance between Mn and oxygen. In the case of highly symmetric ideal cubic structure, the *d*-level splits into two-fold e_g degenerate levels and three-fold t_{2g} degenerate levels. In the presence of crystal field, the Mn^{3+} ion has an electronic configuration of $3d^4$ ($t_{2g}^{3\uparrow}$ $e_g^{\uparrow}$) with S=2 and Mn^{4+} has $3d^3$ ($t_{2g}^{3\uparrow}$) electrons with S=3/2. The Mn^{2+} ion is very stable and has $3d^5$ ($t_{2g}^{3\uparrow}$ $e_g^{2\uparrow}$) configuration with S=5/2. Fig. 2.5 shows the electronic structure of Mn^{3+} ions in the octahedral crystal field. In an octahedral environment, t_{2g} level with d_{xy}, d_{xz}, and d_{yz} orbitals occupy the lower energy state, while e_g level with $d_{x^2-y^2}$ and $d_{3z^2-r^2}$ orbitals occupy the higher energy states.

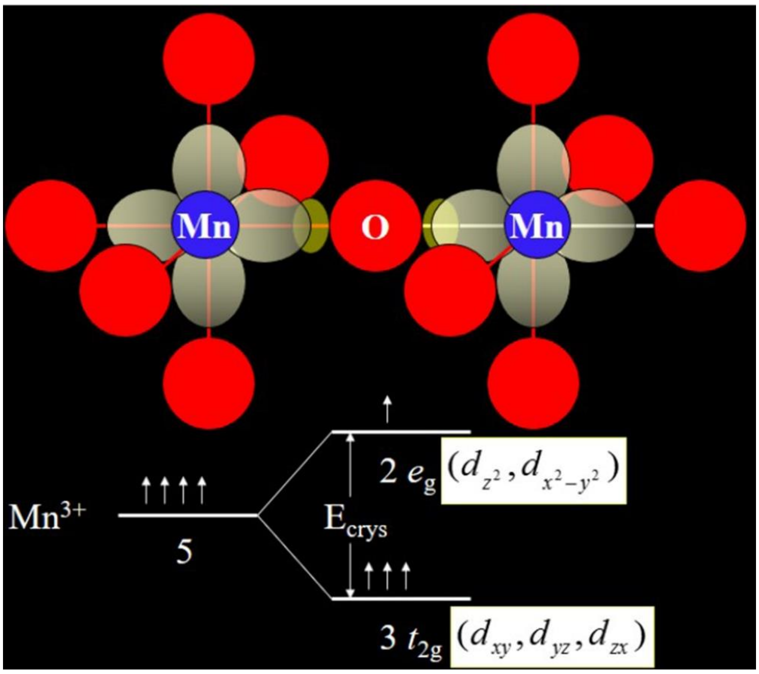

Fig. 2.5. *Electronic structure of* Mn^{3+} *ions in an octahedral crystal field*

The electron density distribution of the d_{xy}, d_{yz} and d_{xz} set of orbitals is farther away from the negative charges of oxygen ions such that t_{2g} electrons of Mn^{3+} ions have lower energy due to lesser Coulomb repulsion from the electrons of the oxygen ions [115]. On the other hand, the two-fold e_g degenerate levels experience more repulsion from the electrons and lead to higher energy states. In comparison to the two-fold e_g orbitals, the three-fold t_{2g} orbitals have less overlap with the 2p orbitals of neighbouring oxygen ions, and therefore, the t_{2g} orbitals are π-bonding and the e_g orbitals are σ-bonding. In case, if the crystal field splitting energy difference is large enough it is more favourable for the electrons to occupy the lower three-fold t_{2g} orbitals and whereas it is more favourable for the electrons to occupy both two-fold e_g orbitals and the three-fold t_{2g} orbitals if the energy difference is small. In doped manganites, the hopping of e_g electrons between the two partially filled d-orbitals of the nearest-neighbour $Mn^{3+}$and Mn^{4+} ions is feasible if the t_{2g} spins of adjacent ions are parallel and that leads to conductivity. However, the electrons in the t_{2g} level tend to be tightly localized due to the strong Coulomb repulsion takes place.

2.6.3. Jahn-Teller effect

Jahn–Teller (JT) effect is a mechanism that describes the geometrical distortion of non-linear molecules [116]. This electronic effect is named after Hermann Arthur Jahn and Edward Teller, who first proved in 1937 about the instability of non-linear degenerate molecules [117]. The theorem states that any nonlinear molecule with a spatially degenerate electronic ground state will be unstable and will undergo a spontaneous symmetry breaking to form a species of lower energy and thereby removing the degeneracy [118]. The strong JT effect is expected in cases having d^9, low-spin d^7 or high-spin d^4 configuration with doubly degenerate ground states. In such situations, the e_g orbitals are occupied by the odd number of electrons, and the orbitals are point directly at the oxygen ions. This leads to a distortion of oxygen octahedra and a large energetic stabilization. However, the effect is weak in situations having

d^1 or d^2 configuration with triply degenerate t_{2g} orbitals, which do not directly point at the oxygen ions due to weak Coulomb repulsion. Fig. 2.6 shows the JT distortion of the MnO_6 octahedra, which lowers the energy of the system when the e_g orbitals have unpaired electrons.

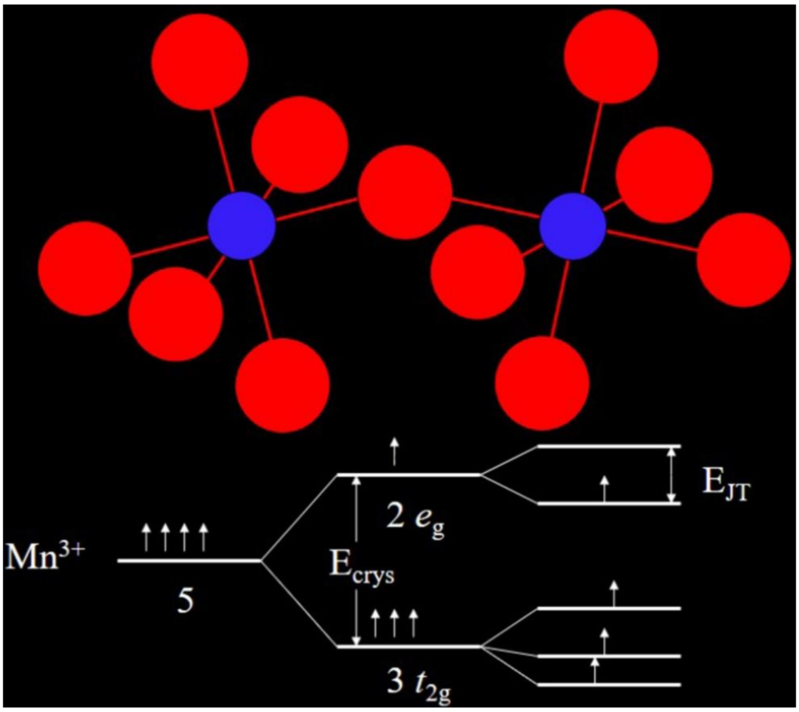

Fig. 2.6. *Jahn-Teller distortion of the* MnO_6 *octahedra*

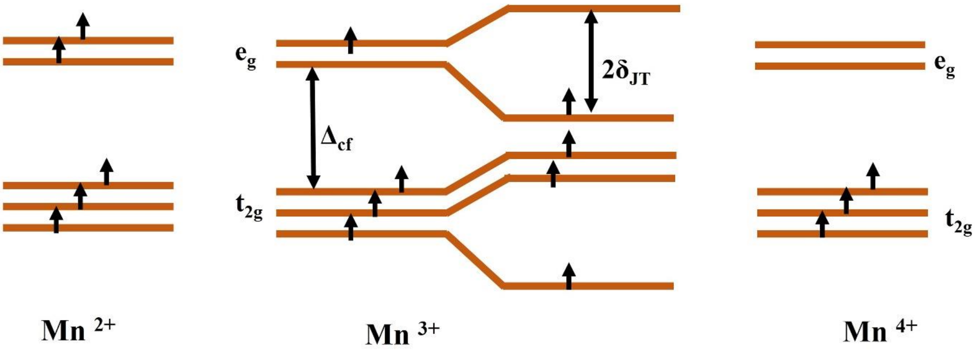

Fig. 2.7. *Electronic structure of* Mn^{2+}, Mn^{3+} *and* Mn^{4+} *ions*

There are two types of JT effect; non- cooperative and cooperative effect [119]. The Mn^{3+} is a JT ion, and it distorts the oxygen octahedra due to the strong JT effect [120]. If Mn^{3+} is present in a host lattice as an impurity, the non- cooperative JT effect takes place in the system. On the other hand, there are too many JT ions present in the lattice, it is known as cooperative JT effect [121]. In manganites, the movement of the oxygen ions from their original position creating an asymmetry between different directions that are further splitting the e_g and t_{2g} levels [122]. Fig. 2.7 shows the electronic structure of Mn^{2+}, Mn^{3+} and Mn^{4+} ions and from the figure, it can be understood that Mn^{2+} and Mn^{4+} are JT inactive and do not tend to distort the oxygen octahedra.

2.6.4. Magnetic exchange interactions

The magnetic order in materials arising because of the cooperative effect between the magnetic moments and it is termed as magnetic exchange interactions. These interactions are responsible for the long-range magnetic order in magnetic systems, and the free energy of the magnetic material is lowered due to these phenomena. The strength of the exchange interaction between the spins is determined from the exchange parameter J_{ij}, and the corresponding exchange Hamiltonian (H_{ex}) is given by [123]

$$H_{ex} = -\frac{1}{2}\sum_{i,j} J_{ij}\, S_i . S_j \qquad (2.15)$$

Where S_i and S_j are the spins located at the lattice site ‘i’ and ‘j’ respectively. When the spins get interacted, the summation in the equation (2.15) extends over all pairs of spins and given the strength of the interaction. The exchange interactions between two spins take place either from electrons of the same atom or two neighbouring atoms. When the two electrons are on the same atom, the exchange integral is positive. This will ensure an asymmetric spatial state due to stabilization of the triplet state, and that will keep the two electrons apart and minimises the Coulomb repulsion between them. When the two electrons are on different atoms, there will be a joint state with a combination of state centred on one atom and a state centred on the other. This ensures a symmetric spatial state of bonding orbital or asymmetric spatial state of anti-bonding orbitals. The anti-bonding orbital has greater kinetic energy and favours the singlet state. Therefore, the exchange integral is likely to be negative. The exchange interactions can be broadly divided into two types. They are direct exchange interactions and indirect exchange interactions.

2.6.4.1. Direct exchange interactions

When the spins of atoms are close enough to have sufficient overlap between the wave function, the direct exchange happens. When the interatomic distance between the two neighbouring atoms is small, electron spent most of their time in between them. This will result in an antiparallel alignment with negative interaction, which favours the antiferromagnetism. If the interatomic distance is large, the electron spent their time away from each other to minimize the Coulomb repulsion and make a parallel alignment with positive exchange interaction, which favours ferromagnetism. Fig. 2.8 shows the direct exchange interactions in which antiparallel alignment favours antiferromagnetism, and parallel alignment favours ferromagnetism.

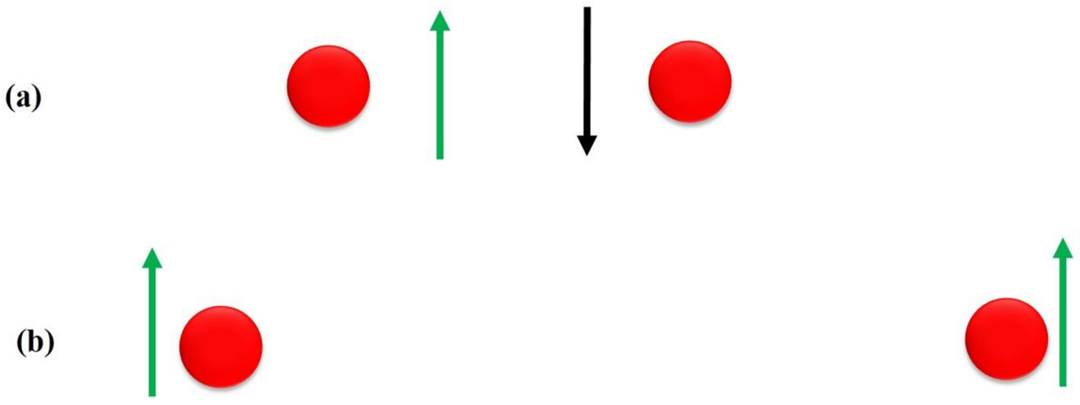

Fig. 2.8. *Direct exchange interactions (a) antiparallel spin alignment and (b) parallel spin alignment*

2.6.4.2. Indirect exchange interactions

The indirect exchange interactions can be classified into two types: they are double exchange interactions and superexchange interactions.

2.6.4.2.1 Double exchange interactions

Double exchange (DE) is a mechanism of electron spin interaction proposed by Zener in 1951 [124]. According to Zener, DE mechanism is responsible for the ferromagnetism and conduction in mixed-valence manganites due to the back and forth travel of an e_g electron between the two Mn ions, as shown in Fig. 2.9.

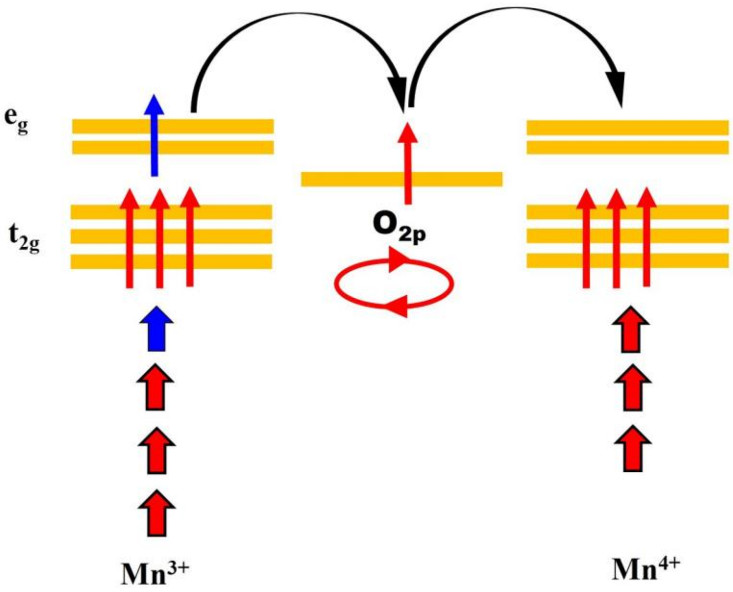

Fig. 2.9. *Double exchange interactions between* Mn^{3+} *and* Mn^{4+} *ions*

The single e_g electron from the $3d_z^2$ orbital of Mn^{3+} can hop to the unoccupied $3d_z^2$ orbitals of Mn^{4+} through O-$2p_z$ orbital of O^{2-}. Since the 2p orbitals of O^{2-} ions are completely filled ($2p^6$), the hopping process has to be accomplished in two steps: transfer of an e_g electron from the $3d_z^2$ orbital of Mn^{3+} to unoccupied oxygen O-$2p_z$ orbital. Simultaneously, one electron from the same O-$2p_z$ orbitals of O^{2-} transfers to the empty e_g orbitals of the Mn^{4+} ion.

Hence, the Mn^{3+} ion becomes Mn^{4+} and vice versa. Due to this simultaneous transfer of electrons through the Mn-O-Mn network is the reason behind the name "double exchange interaction". Due to the strong single-centre exchange interaction between the e_g electron and the t_{2g} electrons, it is required to keep them all aligned in parallel. Hence it is not an energetically favourable condition in which the e_g electron spin will be antiparallel to the t_{2g} electron spins. Thus the ferromagnetic alignment, as well as the transfer of e_g electrons, needed a high spin arrangement between both Mn^{3+} and Mn^{4+} ions and hence the overall energy of the system is saved. The effective hopping of the e_g electron (shown in Fig. 2.10) between neighbouring Mn ions has been evaluated by the equation [125]

$$t = t^0 \cos\left(\frac{\theta}{2}\right) \tag{2.16}$$

where θ is the relative angle between t_{2g} spins located at the two Mn sites and t^0 is the value when $\theta = 0°$.

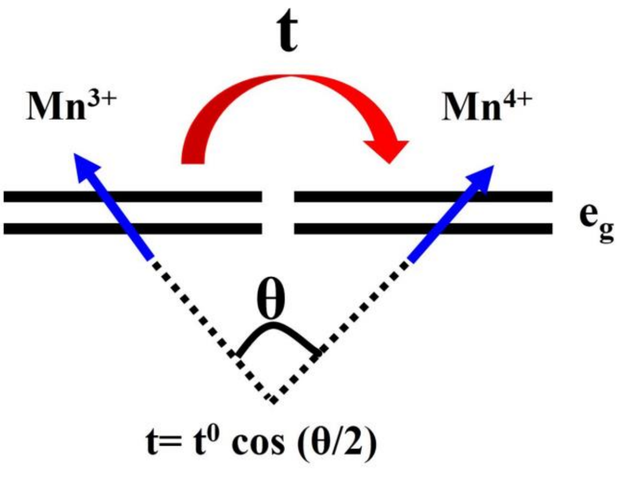

Fig. 2.10. *Hopping of the e_g electrons between neighbouring Mn-ions*

When the temperature is below T_C, all spins of Mn ions have the same direction, and that leads to a ferromagnetic alignment, as shown in Fig. 2.11(a). Thus, the hopping kinetic energy of the conduction elections maximize due to θ= 0°, that results in the hopping of e_g electron of Mn^{3+} back and forth between the neighbour Mn^{4+} ions via the oxygen 2p orbital and hence a ferromagnetic metallic (FMM) ground state emerges. When the temperature is above T_C, all spins are completely disordered, as shown in Fig. 2.11(b) and a paramagnetic insulating (PMI) state emerge. For temperatures near T_C, the spins can be easily aligned by an applied magnetic field, more or less enhancing the hopping of e_g electron between the two Mn ions happens.

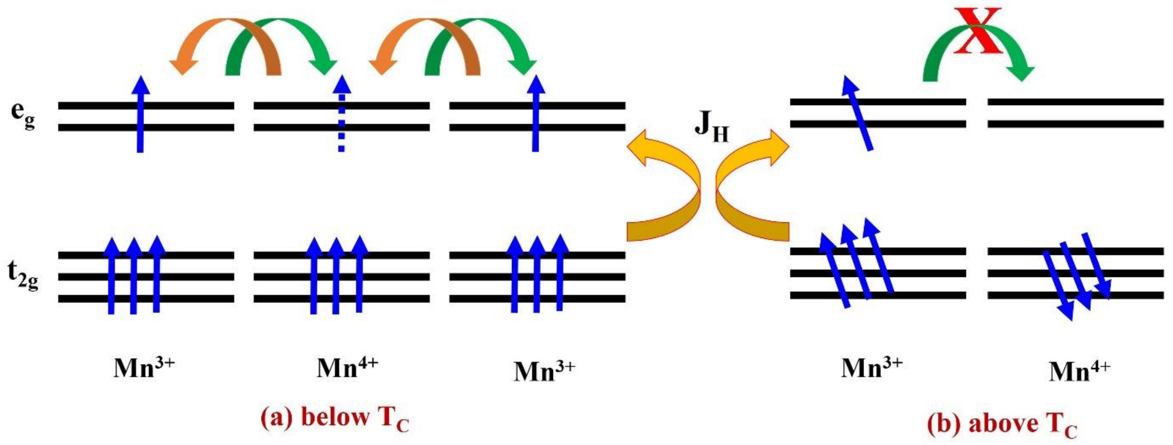

Fig. 2.11. *Illustration of hopping mechanism of the e_g electron between neighbouring Mn-ions (a) below T_C and (b) above T_C. J_H is the FM Hund's coupling between e_g and t_{2g} electrons*

2.6.4.2.2. Super exchange interactions

In superexchange interactions, the interaction between spins on adjacent atoms takes place via the virtual hopping of O-2p electrons to the overlapping e_g orbitals of neighbouring cations, and that leads to the virtual excited states [126]. This virtual excited states leads to a reduction of the total energy depending on the spin direction. This type of interaction is called "super" because it is long-ranged when compared to other interactions. SE interaction depends on the potential exchange and kinetic exchange of the system in which the former is due to the electron repulsion, and the later depends on the degree of overlap of orbitals. According to Goodenough-Kanamori-Anderson (GKA) rules [127-129], the SE interaction between Mn^{3+} and Mn^{4+} ions is FM, between two Mn^{4+} ions is AFM and between two Mn^{3+} ions is FM or AFM. If two Mn^{4+} ions are arranged antiferromagnetically, then the SE interaction takes place due to the hopping of one of the O-2p electrons to the Mn^{4+} ions. The second O-2p electron makes DE interaction with the neighbour Mn^{4+} ion to keep the 2p shell filled. However, the DE interaction is forbidden if the ground state is FM for both Mn^{4+} ions. According to GKA rules, the SE interactions strongly depend on Mn-O-Mn bond angle and vary with the symmetry of electron orbitals and are described below:

The 180° exchange interaction between two half-filled orbitals is highly antiferromagnetic. The virtual hopping of O-2p$_z$ electrons would reduce the total energy only if the spins of the neighbour cations aligned antiparallel, as shown in Fig. 2.12 (a).

The 180° exchange interaction between two empty-filled orbitals is highly antiferromagnetic. The virtual hopping of O-2p$_z$ electrons would reduce the total energy only if the spins of the neighbour cations aligned antiparallel, as shown in Fig. 2.12 (b).

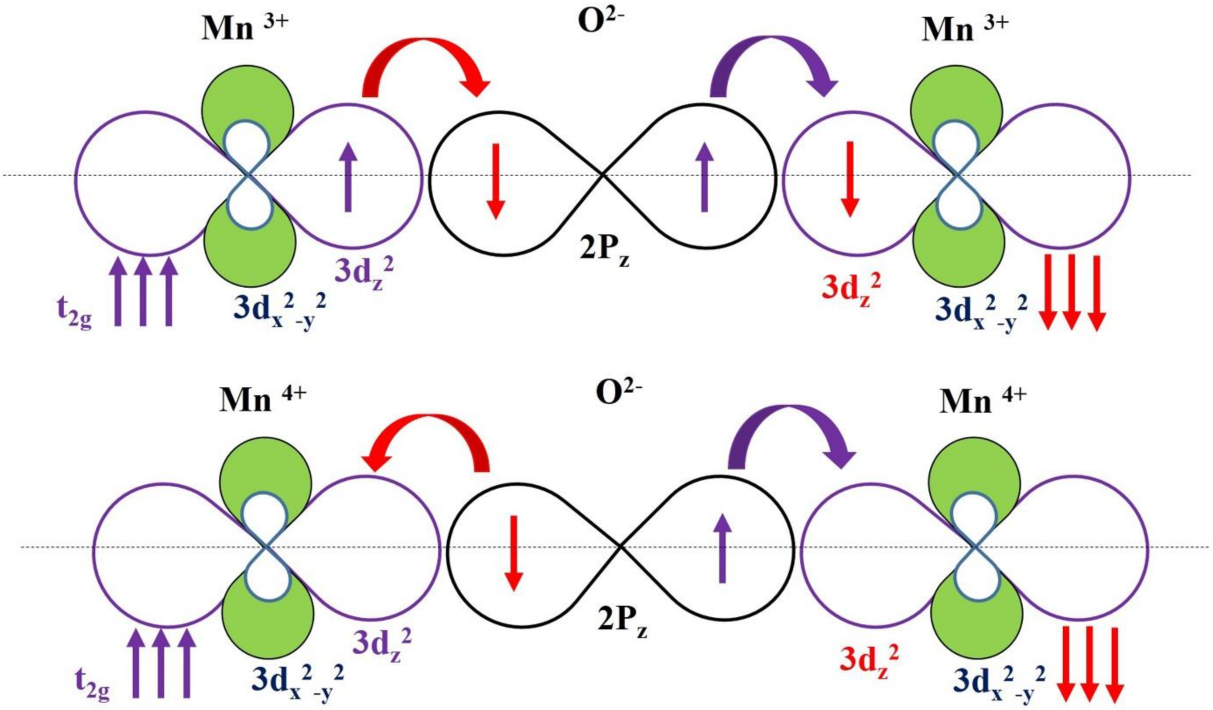

Fig. 2.12. *(a) The 180° exchange interaction between two half-filled orbitals and (b) The 180° exchange interaction between two empty-filled orbitals*

The 180° exchange interaction between one half-filled and one empty-filled orbital is weakly ferromagnetic. The virtual hopping of O-2p_z electrons would reduce the total energy only if the spins of the neighbour cations aligned parallel, as shown in Fig. 2.13 (a).

The 90° exchange interaction between two half-filled orbitals is weakly ferromagnetic. The virtual hopping of one O-2p_z electron and one O-2p_y electron would reduce the total energy only if the spins of the neighbour cations aligned parallel, as shown in Fig. 2.13 (b).

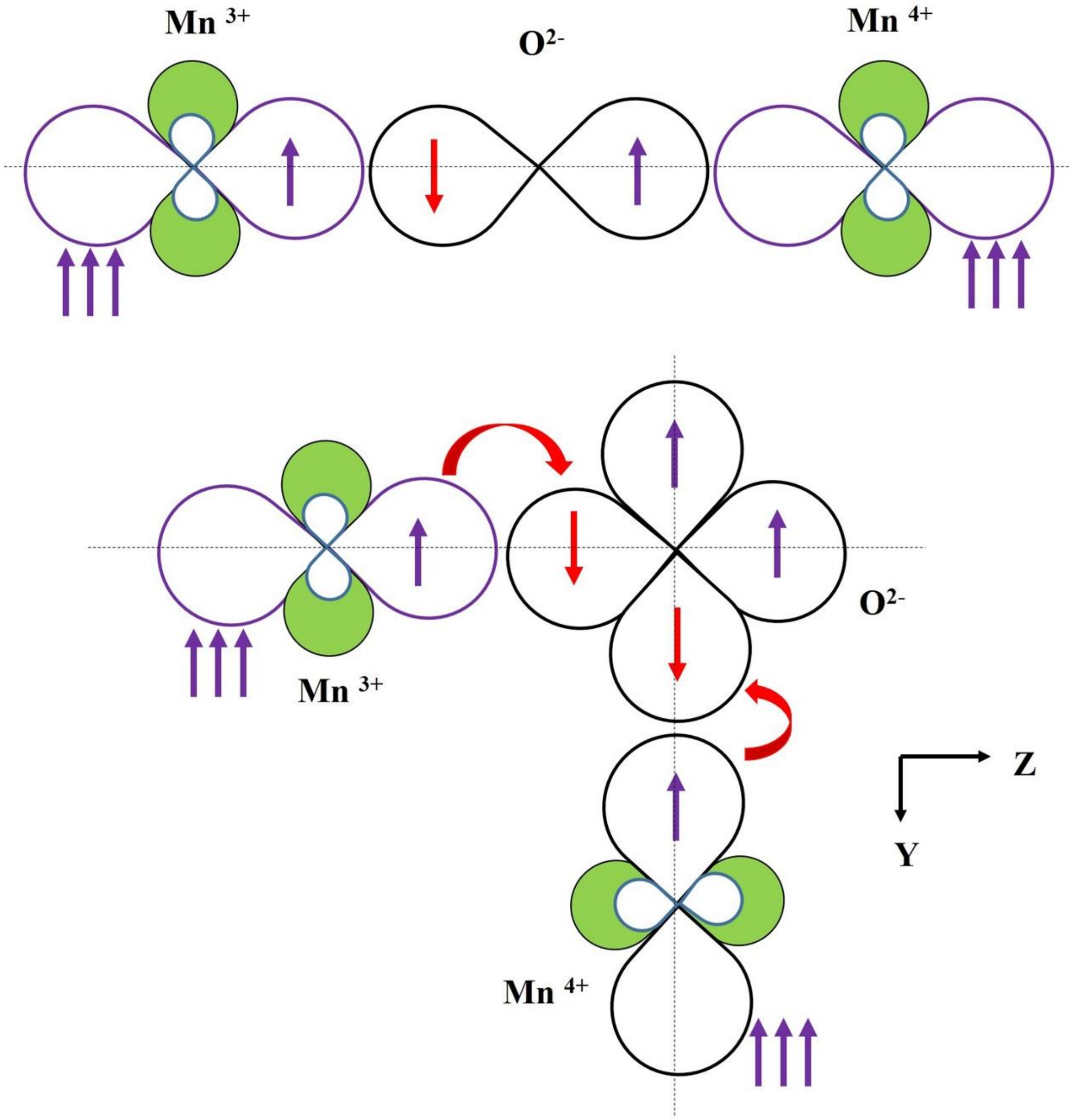

Fig. 2.13. *(a) The 180° exchange interaction between one half-filled and one empty-filled orbital and (b) The 90° exchange interaction between two half-filled orbitals*

2.6.5. Magnetic and magnetocaloric properties of manganites

In 1950, Jonker and Van Santen first reported about the family of manganites and conducted the magnetization studies on $La_{1-x}Ca_xMnO_3$, $La_{1-x}Sr_xMnO_3$ and $La_{1-x}Ba_xMnO_3$ manganites [130]. The authors obtained the respective transition temperature and found the existence of ferromagnetism on the studied materials. Later, they again reported the electrical conductivity and transition temperature anomalies on the same group of materials [131]. In 1954, Volger *et al*. reported the magnetoresistive properties on $La_{0.8}Sr_{0.2}MnO_3$ manganites and found that electrical resistivity decreases with an increase in the magnetic field [132]. From the late '90s onwards, mixed-valence manganites are become one of the major research areas due to its high potential in various technological applications. The structures, magnetic and electrical properties of these materials are strongly correlated due to the competing interaction between charge, spin and orbital ordering [133]. $La_{1-x}A'_xMnO_3$ is one of the most studied family among the manganites with A'=Sr having the highest T_C of 370 K at x = 0.33 [134-138]. On the other hand, $Nd_{1-x}A'_xMnO_3$ and $Pr_{1-x}A'_xMnO_3$ families exhibit different magnetic and electrical phenomena from that of $La_{1-x}A'_xMnO_3$ series which is attributed to the weakening of DE interaction by the smaller Nd and Pr ions [139-143]. Substitution of the trivalent rare earth elements (La^{3+}, Nd^{3+}, Pr^{3+} etc.) by monovalent elements (Na^+, K^+ etc.), divalent alkaline earth elements (Ca^{2+}, Sr^{2+}, Ba^{2+}etc.) or tetravalent element produces an inhomogeneous distribution of mixed-valence Mn-ions. The magnetic behaviour of these materials strongly depends on the strength of DE interactions between $Mn^{2+}/Mn^{3+}/Mn^{4+}$ ions resulting from the motion of the e_g electron between the two partially filled d-orbitals. To maintain the charge neutrality, the change in valency at the A-site creates ferromagnetism and conduction in these materials.

Among the $La_{1-x}Sr_xMnO_3$ family, $La_{0.67}Sr_{0.33}MnO_3$ have a $-\Delta S_M$ of 1.55 J kg^{-1} K^{-1} and 5.15 J kg^{-1} K^{-1} under 10 kOe and 50 kOe magnetic field change respectively [144]. But due to its higher T_C value, i.e., 370 K, it is restricted from room temperature magnetic refrigeration applications. In 1996, $-\Delta S_M$ of 1.69 J kg^{-1} K^{-1} at 348 K was reported in $La_{0.67}Sr_{0.33}MnO_3$ under a magnetic field of 50 kOe [135]. Magnetic entropy change of 1.48J kg^{-1} K^{-1} (at 292 K) and 2.06 J kg^{-1} K^{-1} (at 252 K) was reported in $La_{0.67}Ba_{0.33}MnO_3$ and $La_{0.67}Ca_{0.33}MnO_3$ respectively under a magnetic field change of 50 kOe [135]. Liu *et al.* [145] reported a charge ordering phenomena and magnetoresistance in $Nd_{1-x}Ca_xMnO_3$ single crystals due to the reduction in DE interaction. From the crystal structure analysis, they reported that the system undergoes a larger lattice distortion than La/Pr-based system. A charge ordering with an abrupt increase in resistivity is seen over a large composition range, and a metastable first-order phase transition from AFM-semiconductor to FM-metal with the reduction in resistance by several orders at low temperature is seen for a small range of x value of $0.33 \leq x \leq 0.4$. Guo *et al.* [136] found the $-\Delta S_M$ of $La_{0.8}Ca_{0.2}MnO_3$ as 5.5 J kg^{-1} K^{-1} at 230 K under a field change of 15 kOe, which is higher than that of Gd (4.2 J kg^{-1} K^{-1}) under the same magnetic field. Fujiwara *et al.* [146] did a theoretical study on the spin, orbital, and charge ordering in $Nd_{1-x}Sr_xMnO_3$ using local spin density approximation calculations. Tang *et al.* reported a $-\Delta S_M$ of 3.45 J kg^{-1} K^{-1} in $La_{0.8}Ag_{0.2}MnO_3$ at 278 K for a field of 10 kOe [137]. Large value of $-\Delta S_M$ of 7.5 J kg^{-1} K^{-1} was reported in $Nd_{0.5}Sr_{0.5}MnO_3$at 183 K for a field of 10 kOe [143]. A commendable work in this direction was done by Phan *et al.* [147] who reported a large $-\Delta S_M$ value of 2.12 J kg^{-1} K^{-1} in $La_{0.65}Sr_{0.35}MnO_3$ at 305 K under a magnetic field change of 10 kOe. Later, the same group have [148] reported the magnetocaloric properties of $La_{0.7}Ba_{0.3}MnO_3$ polycrystalline material, which undergo a T_C of 336 K with $-\Delta S_M$ of 1.6 J kg^{-1} K^{-1} for field change of 10 kOe. Arroyo *et al.* [149] reported the room-temperature magnetoresistance in $La_{0.5}Ca_{0.5}MnO_3$ manganite. They achieved 50% of Mn^{4+} and a change of state from AFM insulating phase to

FM metallic phase with the creation of cationic vacancies. Szewczyk *et al*. [150] reported the magnetocaloric properties of $La_{1-x}Sr_xMnO_3$ (x= 0.12, 0.135, 0.155, 0.185 and 0.2) manganites. They reported a maximum ΔT_{ad} of 4.15 K for $La_{0.8}Sr_{0.2}MnO_3$ under 70 kOe field change. Luong *et al.* [51] studied the magnetocaloric properties of $La_{1-x}Cd_xMnO_3$ (x = 0.1, 0.2 and 0.3) manganites. They achieved $-\Delta S_M$ of 1.01 J kg^{-1} K^{-1} (150 K) and 2.88 J kg^{-1} K^{-1} (140 K) for $La_{0.8}Cd_{0.2}MnO_3$ and $La_{0.7}Cd_{0.3}MnO_3$ respectively for 13.5 kOe field change. $Pr_{0.68}Ca_{0.32}MnO_3$ and $Pr_{0.63}Sr_{0.37}MnO_3$ compounds were reported as a promising candidates for room temperature applications, and it shows large $-\Delta S_M$ of 24 J kg^{-1} K^{-1} (at 21.5 K) and 8.52 J kg^{-1} K^{-1} (at 300 K) for ΔH of 50 kOe [141, 142]. Later $La_{0.7}Ca_{0.25}K_{0.05}MnO_3$ and $La_{0.7}Ca_{0.25}Sr_{0.05}MnO_3$ were reported to be potential candidates that exhibits $-\Delta S_M$ of 3.95 J kg^{-1} K^{-1} (at 270 K) and 10.5 J kg^{-1} K^{-1} (at 275 K) for 20 kOe and 50 kOe field respectively [152, 153]. Single crystal of $Pr_{0.52}Sr_{0.48}MnO_3$ compound show large $-\Delta S_M$ of 3.8 J kg^{-1} K^{-1} at 275 K and for field change of 50 kOe [154].

Roy *et al*. [155] has experimentally studied the effect of particle size in $Nd_{0.7}Sr_{0.3}MnO_3$ and found that the compound belongs to a magnetic cluster glass system. The resistivity increases with decrease in particle size and the authors correlated the observed electrical transport properties of the compound to the enhancement of grain boundary effect. The same group [156] had reported the magnetic cluster glass behaviour in nanocrystalline $Nd_{0.7}Ba_{0.3}MnO_3$ manganite. They observed that the spin-polarised tunnelling and grain boundary effect influence the magnetic, electrical transport and magnetoresistance properties of the compounds. Colin *et al.* [157] observed a continuous first-order orbital order-disorder transition in $Nd_{1-x}Ca_xMnO_3$ manganite for a doping range of x value of $0 \leq x \leq 0.1$. For a small doping range of $0 \leq x \leq 0.02$, they observed a large temperature range of phase coexistence associated with the first-order transition and the characteristic features of martensitic transition. For higher doping range, phase coexistence associated with the first-order transition phenomena is suppressed. Zemni *et al.* reported a $-\Delta S_M$ of 3.8 J kg^{-1} K^{-1} at 320 K for a field of 25 kOe in polycrystalline $Pr_{0.6}Sr_{0.4}MnO_3$ compound [158]. Hsu *et al.* [159] studied the crystal structural analysis and magnetic phase diagram of $Nd_{1-x}Ca_xMnO_3$ manganites. As the Ca doping concentration increases, they observed a structural change from orthorhombic to pseudo-tetragonal. Moreover, with the increase in Ca doping concentration, they observed a magnetic phase change from FM to AFM with the coexistence of charge ordering and canted AFM. A magnetoresistance of near 100% is obtained for a composition of $Nd_{0.6}Ca_{0.4}MnO_3$ and which is attributed to the instability of AFM-insulator phase under high magnetic fields. Several authors reported the synthesis and properties of $Nd_{0.67}Sr_{0.33}MnO_3$ by various methods such as pulsed laser deposition, solid-state reaction, sol-gel, PVA gel route and pyrophoric reaction process [160-165]. A commendable work in this direction was done by Venkataiah *et al.* [162] who reported the electrical resistivity and magnetoresistance of $Nd_{0.67}Sr_{0.33}MnO_3$ by varying the sintering temperature from 800 °C to 1100 °C. Venkatesh *et al.* reported the critical exponent study combined with MCE and have explained how the PM-FM transition is influenced by the competing order parameters [160]. However, from the literature, it is understood that the magnetic and electrical properties of the materials strongly depend on the crystalline size, which varies with the synthetic routes and annealing conditions. Recently, D.C. Krishna *et al.* reported the non- linear variation of electrical resistivity and magnetic transition temperature of nanocrystalline $Nd_{0.67}A_{0.33}MnO_3$ (A=Ca, Sr, Pb, Ba) based on size variance effect [164]. The authors explained the non-linear variation of electrical and magnetic transition temperatures based on size variance parameter. Among the studied compounds, nanocrystalline $Nd_{0.67}Sr_{0.33}MnO_3$ possesses magnetic anisotropy and a metamagnetic phase, however, $Nd_{0.67}Ca_{0.33}MnO_3$ showed the highest magnetoresistance.

Prasad *et al*. [166] studied the influence of film thickness on the magnetic and electrical transport properties in $Nd_{0.51}Sr_{0.49}MnO_3$ films. From the study, it is evident that the magnetic phase coexistence and electrical transport properties of the compound are severely influenced by the film thickness. The nonlinear properties in $Nd_{0.7}Ba_{0.3}MnO_3$ single crystal were reported by Ryzhov *et al.* [167], and they investigated the PM to FM transition in detail to understand the changes in the metallic ground state of the compound. Later, Lalitha *et al.* [163] presented the low-temperature resistivity anomalies and magnetic field induced metal-insulator transition in $Nd_{0.67}A_{0.33}MnO_3$ (A=Ca, Sr, Ba and Pb) manganites. They found that the field-induced transition due to the response of the FM clusters with the applied magnetic field and the resistivity anomalies due to different interaction mechanism happened at low-temperature. Raju *et al.* [168] reported the structural, magnetic and electrical properties in nanocrystalline $Nd_{1-x}Ca_xMnO_3$ (x=0.2, 0.33, 0.4 and 0.5) manganites. They found that at low temperature, there is a coexistence of charge-ordered AFM and FM metal phases in the system due to the strong interplay between spin, charge and orbital degrees of freedom. In the same year, Lampen *et al.* [169] systematically studied the magnetic, and magnetocaloric properties of amorphous and nanocrystalline $La_{0.4}Ca_{0.6}MnO_{3+\delta}$ manganites. They found that the magnetization and FM ordering increases with increase in particle size while the coercive field decreases with increase in particle size. Thaljaoui *et al.* reported that $Pr_{0.6}Sr_{0.4-x}K_xMnO_3$ exhibit a $-\Delta S_M$ value of 1.95 J kg^{-1} K^{-1} at 310 K and 3.2 J kg^{-1} K^{-1} at 269 K under a field change of 20 kOe for K-content varying from 0 to 0.2 [170]. They further reported a $-\Delta S_M$ value of 1.95 J kg^{-1} K^{-1} at 310 K in bulk $Pr_{0.6}Sr_{0.4}MnO_3$ and 1.84 J kg^{-1} K^{-1} in nanocrystalline $Pr_{0.6}Sr_{0.35}Na_{0.05}MnO_3$ under a field change of 20 kOe [171, 172]. Shaikh *et al.* [173] reported the structural and electrical transport properties of polycrystalline $Pr_{1-x}Sr_xMnO_3$ (x = 0.25, 0.3, 0.35, 0.4) manganites. $La_{0.5}Na_{0.5}MnO_3$ was reported to be a potential candidate for room temperature magnetic refrigeration applications with a $-\Delta S_M$ of 1.5 J kg^{-1} K^{-1} at 290 K under field change 50 kOe [174]. Bhagyashree *et al.* [175] reported that the electron-hole asymmetry in nanocrystalline $Nd_{1-x}Ca_xMnO_3$ manganite is disappeared due to the surface spins and the formation of the FM layer. They confirmed the multiple magnetic phase transitions and charge-ordered transition from the study of magnetization and electron paramagnetic resonance. Arbuzova *et al.* [176] systematically studied the effect of magnetic polarons in $La_{0.7}Ca_{0.3}MnO_3$, $La_{0.7}Ba_{0.3}MnO_3$ and $La_{0.7}Sr_{0.3}MnO_3$ manganites. They found that SE interaction is responsible for arising of polarons, and they developed a correlation between the moments of the polarons with changes in the lattice volume of the studied compounds.

Earlier studies show that substitution of La-site by other RE elements (Nd, Pr, Gd etc.) and Mn-site substitution by other transition elements (Cr, Fe, Ni etc.) leads to tailor the T_C towards room temperature [177-184]. However, to maintain a significant value in T_C, a large drop in ΔS_M was founded and vice versa. Replacing the non-magnetic La^{3+} ($4f^0$) ions by magnetic ions can be expected to show a large magnetic entropy change since the magnetic moment of RE ion is larger than that of La^{3+} ion [185]. Since the ionic radius of other RE ions is less than that of La^{3+}, the substitution leads to decrease the Mn-O bond lengths and Mn-O-Mn bond angles, which in turn lower the exchange interaction between the Mn-ions. As the RE content in the La-site increases, the T_C is found to be decreased due to the crystallographic distortion induced by the different ionic radius between La^{3+} and RE^{3+} ions [186]. Raveau *et al.* studied the changes in the magnetoresistance of manganites by doping various elements at the Mn-site [187]. The author showed that the average cation size of the material is varied with doping elements such as Al, Mg, Ga, In, Ti, Sn, Fe, Cr, Co, Ni etc. and a corresponding change in the magnetoresistance was observed. Chen *et al.* systematically studied the magnetocaloric properties of $(La_{1-x}RE_x)_{2/3}Ca_{1/3}MnO_3$ (RE = Tb, Dy, Gd, Ce) manganites [188]. The T_C of the pristine compound is found to decrease by the partial substitution of RE elements, and the composition with $(La_{0.9}RE_{0.1})_{2/3}Ca_{1/3}MnO_3$ shows highest $-\Delta S_M$ value for 15 kOe field change. The $-\Delta S_M$ value is found to be 4.76 J kg^{-1} K^{-1} (166 K), 6.06 J kg^{-1} K^{-1} (176 K), 5.78 J kg^{-1} K^{-1} (182 K), and 4.53 J kg^{-1} K^{-1} (244 K) for RE = Tb, Dy, Gd and Ce respectively. Chau *et al.* [189] studied the magnetocaloric properties of $La_{0.7}Sr_{0.3}Mn_{1-x}Cu_xO_3$ (x = 0.05 and 0.1) manganites. They achieved $-\Delta S_M$ of 1.96 J kg^{-1} K^{-1} and 2.07 for $La_{0.7}Sr_{0.3}Mn_{o.95}Cu_{0.05}O_3$ and $La_{0.7}Sr_{0.3}Mn_{0.9}Cu_{0.1}O_3$ compounds respectively for ΔH = 13.5 kOe. Kallel *et al.* found that the $-\Delta S_M$ of $La_{0.7}Sr_{0.3}Mn_{0.8}Cr_{0.2}O_3$ as 1.2 J kg^{-1} K^{-1} at 286 K under a field change of 20 kOe [178]. Reshmi *et al.* reported a $-\Delta S_M$ value of 3 J kg^{-1} K^{-1} in $La_{0.67}Sr0_{.33}Mn_{0.9}Ni_{0.1}O_3$ at 290 K under a magnetic field of 50 kOe [179]. Nisha *et al.* [190] investigated the effect of Co substitution in $La_{0.67}Ca_{0.33}MnO_3$ manganites. They presented the critical exponent parameters and magnetocaloric properties by partial Co substitution in $La_{0.67}Ca_{0.33}Mn_{1-x}Co_xO_3$ (x = 0.03, 0.1 and 0.15) manganites. Hcini *et al.* [180] presented the structural and magnetic properties of $Nd_{0.67}Ba_{0.33}Mn_{1-x}Fe_xO_3$ ($0 \leq x \leq 0.1$) manganites. They found that the compounds are ferromagnetic up to doping of x= 0.02 whereas doping of $x \geq 0.05$ shows cluster glass-like behaviour. The critical exponents analysis confirmed that there is a change in the universality class from the 3D-Ising model (x=0) to the mean-field model (x=0.02) due to the doping of Fe. $La_{0.47}Eu_{0.2}Pb_{0.33}MnO_3$ and $La_{0.69}Dy_{0.01}Sr_{0.3}MnO_3$ were reported to be potential candidate exhibits $-\Delta S_M$ of 3.31 J kg^{-1} K^{-1} (at 284 K) and 1.21 J kg^{-1} K^{-1} (at 315 K) under 50 kOe field [182, 183].

Moreover, researchers have tried to tune the T_C and ΔS_M by creating deficiency content at the A and A' sites. Boujelben *et al.* reported the effect of Pr and Sr- deficiency in $Pr_{0.7}Sr_{0.3}MnO_3$ compound and found that Pr-deficiency and Sr-deficiency have different effects on the magnetic properties [191]. They, further reported that the structural and magnetic properties are closely related to the Pr-deficiency created and eventually on the average A-site cationic radius. The effect of La deficiency in $(La_{1-x})_{0.8}Ca_{0.2}MnO_3$ was reported by Phan *et al.* and found that the La-deficient compounds exhibit a large ΔS_M value than that of the pristine compound [192]. Zhong *et al.* [193] studied the effect of oxygen deficiency on the magnetocaloric properties of $La_{2/3}Ba_{1/3}MnO_{3-\delta}$ (δ=0-0.1) and found that the magnetic property reduces with increase in oxygen deficiency. A composition with δ= 0 exhibited a large $-\Delta S_M$ = 2.7 J kg^{-1} K^{-1} at 350 K for 10 kOe field change. Hou *et al.* [194] studied the magnetocaloric properties of La-deficient $La_{0.67-x}Ca_{0.33}MnO_3$ (x = 0, 0.02, 0.06, and 0.1) manganites. The compound $La_{0.65}Ca_{0.33}MnO_3$ was reported the largest $-\Delta S_M$ = 2.78 J kg^{-1} K^{-1} at 277 K for 10 kOe field change. Boujelben *et al.* [195] reported the ferromagnetic behaviour of Nd- deficient $Nd_{0.7-x}\square_x Sr_{0.3}MnO_3$ manganites and found that the T_C of the compounds increases with increase in Nd- deficiency. Zhao *et al.* [196] reported a giant magnetoresistance in Mn-deficient $La_{2/3}Ca_{1/3}Mn_{1-x}O_3$ at the low magnetic field. Chen *et al.* [197] studied the effect of cationic vacancies on the entropy change and transition temperature in $La_{0.67}Ca_{0.33}Mn_{1-x}O_3$ manganites. Ji *et al.* [198] investigated the effect of Mn-site deficiency on the electrical transport of $La_{0.75}Sr_{0.25}Mn_{1-x}O_3$ manganites. They found that the resistivity increases and metal-insulator transition broadened due to the introduction of deficiency at the Mn-site. Na-deficient $La_{0.8}Na_{0.05}\square_{0.15}MnO_3$ and Sr-deficient $La_{0.65}Eu_{0.05}Sr_{0.15}MnO_3$ exhibit $-\Delta S_M$ values of 3.48 J kg^{-1} K^{-1} at 260 K and 4.96 J kg^{-1} K^{-1} at 280 K under a field change of 20 kOe [199, 200]. Estemirova *et al.* [201] observed a co-existence of magnetic phases in Nd-deficient $Nd_{0.95-x}Ca_xMnO_{2.93\pm\delta}$ manganite and found that the transition temperature increases with increasing Ca content. They reported the phase relationship, structural and magnetic properties of the compound in connection with the Nd-deficiency. A tunable transition temperature with a $-\Delta S_M$ value of 3.42 J kg^{-1} K^{-1} (300 K) under 50 kOe field change was reported by Skini *et al.* in K-deficient $La_{0.8}K_{0.1}\square_{0.1}MnO_3$ compound [202]. Marzouki-Ajmi *et al.* [203] reported the effect of deficiency on the structural, magnetic and magnetocaloric properties of $La_{0.65}Ba_{0.35-x}\square_x MnO_3$ ($0\leq x\leq 0.2$)

manganites and found that the magnetocaloric properties improved with Ba-deficiency. Recently, Oumezzine *et al.* [204] reported the effect of Mn-site deficiency on the structural and magnetic properties of nanocrystalline $La_{0.67}Ba_{0.33}Mn_{1-x}O_3$ manganites. They found that deficiency creates more Mn^{4+} ions and decreases the magnetization and T_C of the deficient compounds.

2.7. Concluding remarks

Perovskite manganites are considered as good magnetocaloric materials for magnetic refrigeration applications. It possesses large spontaneous magnetization and shows a sharp drop in magnetization in the vicinity of FM-PM transition. They have some superior features over RE and Tr based alloys, such as

- they are potential candidates for the magnetic refrigeration applications due to its low cost, simple synthesis route, higher chemical stability, small magnetic and thermal hysteresis and low eddy current heating.
- they have a wide range of transition temperature.
- T_C and magnetocaloric properties can be easily tuned in a required range by changing the doping concentration and deficiency content etc.

These superior features make them promising candidate for magnetic refrigeration applications.

Chapter 3

Comparative study of magnetic ordering, magnetocaloric, electrical transport properties in bulk and nanocrystalline $Nd_{0.67}Sr_{0.33}MnO_3$ manganite

This chapter deals with the comparative study of magnetic ordering, magnetocaloric and electrical transport properties in bulk and nanocrystalline $Nd_{0.67}Sr_{0.33}MnO_3$ manganite. It has been found that the long range ferromagnetic ordered state becomes unstable upon the reduction of the sample size down to nanometre scale. DC and AC magnetization studies suggest the frustration of spins in nanocrystalline system, and thereby it could lead into a cluster glass behaviour. The bulk compound shows a T_C of 235 K, and exhibits a $-\Delta S_M$ of 2.68 J kg^{-1} K^{-1} and 7.37 J kg^{-1} K^{-1} under 10 kOe and 50 kOe field change. The $-\Delta S_M$ values are found to be decreased with the reduction in particle size and the bulk $Nd_{0.67}Sr_{0.33}MnO_3$ compound is found to be a promising candidate for magnetic refrigeration applications at sub-room temperatures.

3.1. Introduction

$Nd_{1-x}Sr_xMnO_3$ is reported to be a FM metal for x<0.5 and AFM insulator for x>0.6 whereas the intermediate doping range shows AFM metallic behaviour [7]. Among the $Nd_{1-x}Sr_xMnO_3$ series, x= 0.33 is known as tricritical point, which separates a first-order transition (x= 0.3) from a second-order transition (x= 0.4) [160]. However, from the literature, it is understood that the magnetic and electrical properties of the materials strongly depend on the crystalline size which varies with the synthetic routes and annealing conditions [162-165]. Nanocrystalline manganites show unusual physical properties when compared to its bulk counterparts [205]. Reduction of the particle size enhances the number of grain boundaries which results in structural and magnetic disorders in the grain surfaces and thereby influences various magnetic and electrical phenomena significantly. Magnetic nanoparticle exhibits less value of magnetization and a high value of low field magnetoresistance [156]. It has been reported that spin glasses or cluster glass are the magnetic systems which exhibit a freezing transition temperature (T_f) to a state of order in which spins are aligned in random directions [155]. Moreover, T_C and T_f decrease with the reduction in particle size [155]. In nanocrystalline materials, synthesis is a key factor in controlling morphology, chemical composition, and grain size distribution [206]. These factors deeply influence the physical and chemical properties of the system, and they exhibit interesting phenomena due to small coercivity as well as increased anisotropy [207]. Therefore, in the present chapter, we have prepared bulk and nanocrystalline $Nd_{0.67}Sr_{0.33}MnO_3$ (NSMO) by solid-state and sol-gel routes respectively and done a comparative study on structural, magnetic ordering and magnetocaloric properties in connection with their phase transition behaviour.

3.2. Experiment

Bulk and nanocrystalline NSMO compounds were prepared by the conventional solid-state and sol-gel techniques [208] respectively. For the bulk composition, stoichiometric amount of Nd_2O_3 (Alfa-aesar, 99.9 %), $SrCO_3$ (Sigma-Aldrich, 98 %), $MnCO_3$ (Sigma-Aldrich, 99.9+ %) were mixed in an agate mortar using distilled water for 6h. The resultant slurry was then dried and calcined at 1200 °C for 12h. For the preparation of nanocrystalline NSMO, stoichiometric amount of $Nd(NO_3)_3.6H_2O$ (Alfa-aesar, 99.9%), $Sr(NO_3)_2$ (Sigma-Aldrich, 99%), $Mn(NO_3)_2 \cdot xH_2O$ (Sigma-Aldrich, 98%), were dissolved in deionized water and it is mixed with the solution of citric acid $C_6H_8O_7.H_2O$ (S D Fine-chem limited) and ethylene glycol (Sigma-Aldrich), in the ratio of (0.67 $[Nd^{3+}]$+0.33 $[Sr^{2+}]$+1 $[Mn^{3+}]$) /1.5 [citric acid]/ 2.25 [ethylene glycol]. Ammonia solution was added to the solution until the pH reaches 9. Then heated with constant stirring at 80 °C and converted into a viscous gel. The gel was dried, ground and calcined at 600 °C for 4 h. The granulated powders were pressed uniaxially into cylindrical pellets of appropriate dimension under a pressure of 100 MPa. The pellets were then sintered at 1350 °C for 12h (Bulk) and 750 °C for 4h (Nano) in air and finally cooled to room temperature. The crystal structure and phase purity of the powdered samples were analysed using X-ray diffraction (PAN analytical X'Pert Pro Diffractometer having Ni filtered Cu Kα radiation, Netherlands). Rietveld refinement of the diffraction pattern was carried out using the GSAS software [209], and Crystal structure was carried out using Crystal Maker software (Crystal maker Software limited, Oxfordshire OX5 1PF, UK). Microstructural analysis was conducted using a scanning electron microscope (JEOL-SEM 5601v, Tokyo, Japan). The morphology and size of the nanocrystalline were directly investigated by high-resolution transmission electron microscopy (HR-TEM). Energy-dispersive X-ray analysis (EDAX) was performed for different regions of the samples to confirm their homogeneity and expected stoichiometry. Magnetic and electrical transport measurements of the samples were made as a function of temperature and applied field using a physical property measurement system (PPMS) (Quantum Design Inc., USA).

3.3. Results and discussion

3.3.1. Structural and morphological analysis:

The XRD patterns of both bulk and nanocrystalline NSMO compounds were analysed, and the structural parameters were determined from the Rietveld refinement using GSAS software [209]. The XRD patterns of both the compounds were identified to form a single-phase perovskite structure of orthorhombic crystal symmetry with Pbnm space group. The refined XRD patterns with the crystallographic structure are shown in Fig. 3.1.

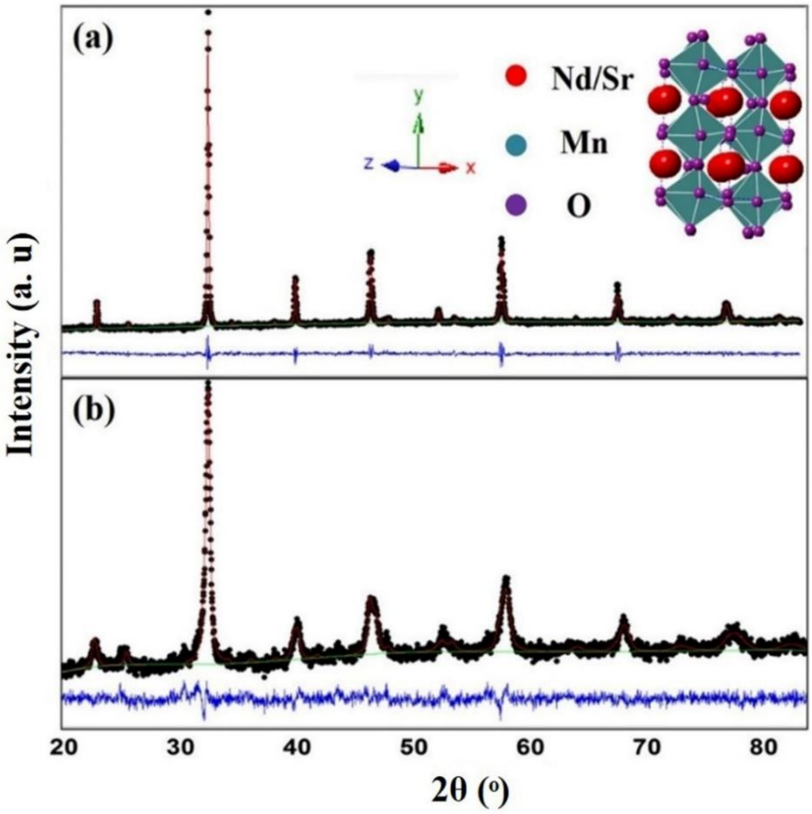

Fig. 3.1. *Rietveld refined XRD patterns of (a) bulk and (b) nanocrystalline NSMO compounds at room temperature. Dotted circles correspond to the XRD data, and the lines are theoretical fits to the observed XRD data. The difference pattern between the observed data and the theoretical fit is shown at the bottom. Inset figure corresponds to the crystallographic structure obtained using crystal maker software*

The refined structural parameters of the same are listed in Table 3.1. From the refinement analysis, it is evident that there is an excellent agreement between the calculated and experimental fits for both the compounds, considered from the small values of residuals for the weighted pattern R_{WP}, pattern R_P and the goodness of fit χ^2. It can be seen from Table 3.1 that the observed Mn-O-Mn bond angle is less than 180° for both compounds and hence deviates from the ideal cubic structure for which the Mn-O-Mn bond angle is 180° [210]. Deviation from the same is an indication of the distortion of the MnO_6 octahedra, which further corroborates the orthorhombic crystal structure.

	NSMO-Bulk	**NSMO-Nanocrystalline**
Cell parameter		
a (Å)	5.4649(2)	5.4672(6)
b (Å)	5.4494(3)	5.4470(5)
c (Å)	7.6984(0)	7.6995(5)
V (Å^3)	229.266	229.290
Positional parameters		
Nd/Sr x	0.4989(17)	0.4925(8)
Nd/Sr y	0.0225(5)	0.0204(5)
O1 x	0.571(4)	0.5736(6)
O1 y	0.5019(35)	0.5050(8)
O2 x	0.231(8)	0.1979(3)
O2 y	0.283(8)	0.2514(5)
O2 z	0.011(5)	0.0122(4)
Occupancy/Atomic displacement parameter		
Nd	0.6692/ 0.0274	0.6689/ 0.0275
Sr	0.3287/ 0.0274	0.3294/ 0.0275
Mn	0.9984/ 0.0223	0.9971/ 0.0044
O1	1.0032/ 0.0049	1.0017/ 0.1477
O2	1.0021/ 0.1073	1.0024/ 0.0900
Bond distance (Å)		
Mn-O1	1.964(4)	1.967(4)
Mn-O2	1.990(5)	2.138(5)
Mn-O2	1.890(5)	1.748(5)
Bond angle (°)		
Mn-O1-Mn	157.2(12)	156.3(8)
Mn-O2-Mn	167.2(19)	166.4(1)
Agreement factors		
R_{WP}	3.41	3.12
R_P	2.43	2.46
χ^2	1.54	1.08

Table. 3.1. *Structural parameters of NSMO obtained from Rietveld refinement*

Magnetic properties of manganites are strongly governed by the grain morphology and grain boundary nature [211]. Fig. 3.2(a) shows the surface microstructure of well densified NSMO bulk compound obtained from the SEM analysis. The polygonal grains are almost uniform in size, and the grain boundaries are visible. The micrograph indicates that the surface of the compound is homogeneous. Fig. 3.2(b) represent the TEM image (inset shows grain size distribution), (c) and (d) represent the EDAX spectrum of bulk and nanocrystalline NSMO compound respectively. The TEM analysis reveals different sized particles with an average particle size of 22 nm. Further, the analysis of chemical composition has been carried out using EDAX at different regions of the sample to confirm the homogeneity. The EDAX analysis shows that the obtained compositions are nearly identical with the nominal one.

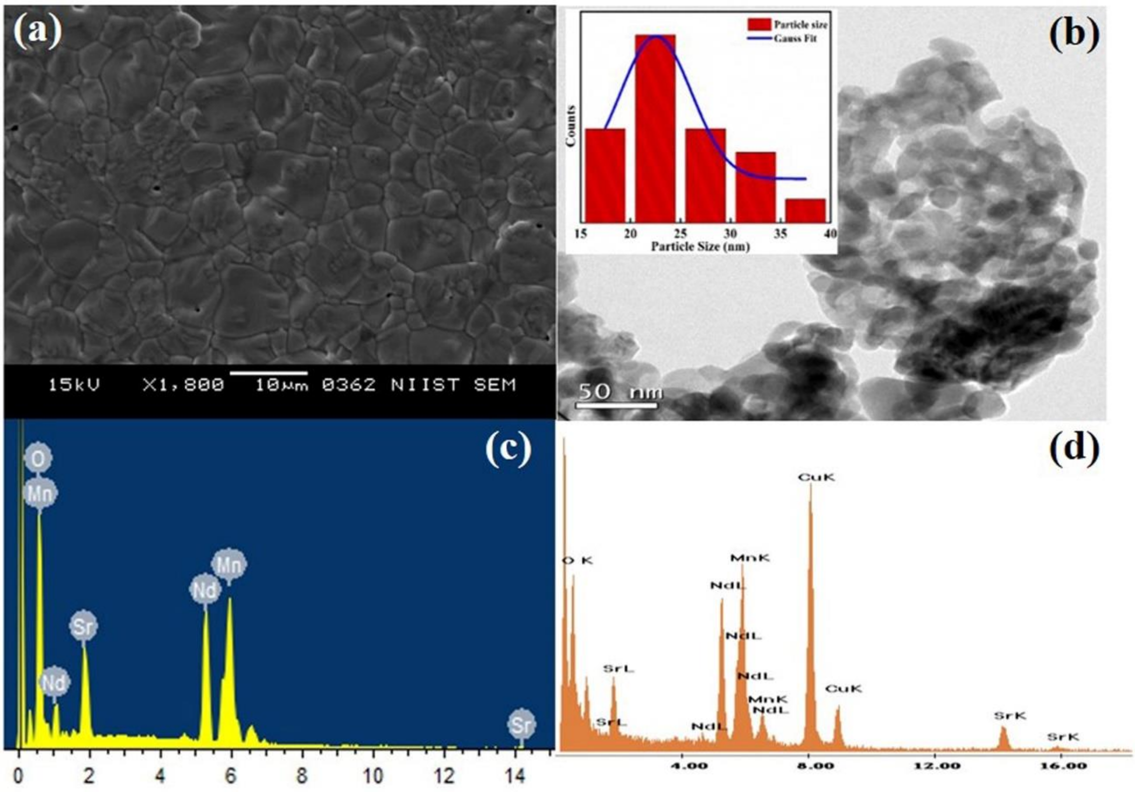

Fig. 3.2. *(a) SEM image of bulk NSMO compound (b) TEM image of nanocrystalline NSMO compound (The inset shows particle size distribution having an average particle size of 22 nm) (c) and (d) EDAX spectrum of bulk and nanocrystalline NSMO compound*

3.3.2. D C magnetic characterization

Temperature variation of magnetization, M(T) of both the compounds has been carried out in zero-field cooled (ZFC), and field cooled (FC) mode from 2-300 K, under an external field of 50 Oe and are depicted in Fig. 3.3 (a). In the ZFC process, the sample was cooled from 300 K to 2 K in the absence of magnetic field, and then the magnetization measurement was performed under 50 Oe during the warming process from 2 to 300 K. In FC process, the magnetization measurement was carried out under the same magnetic field during the cooling from 300 to 2 K. The bulk compound showed a typical PM-FM transition at the intermediate temperatures with a T_C of 235 K. However, in the nanocrystalline compound, the magnetization in the ZFC curve exhibit a broadened transition and a cusp at a particular temperature called blocking temperature, T_B and below which the magnetization decreases abruptly. Here, reduction in the particle size results in degradation of long-range order and suppression of the magnetization value [155]. The blocking temperature, T_B observed in the ZFC curve occurs at slightly lower temperature than the irreversibility temperature, $T_{irr.}$ Due to the particle size distribution, the largest particle initially frozen at temperature T_{irr} and major fraction of the nanoparticles being blocked at $T_{B.}$ Hence this results in broadening of the blocking temperature and thereby large irreversibility in magnetization was observed between ZFC and FC curves at $T_{irr.}$ This irreversibility is due to the spins of each particle tends to align with the easy axis and remain frozen at low temperature with the field direction. However, the bifurcation between the ZFC and FC curves and cusp like character in ZFC magnetization is one of the characteristic features of spin glass, cluster glass or superparamagnetic nature [156]. It is expected that the strong irreversibility between ZFC and FC curves should disappear when the magnetic fields are much higher than the anisotropy field of the nanocrystalline compound.

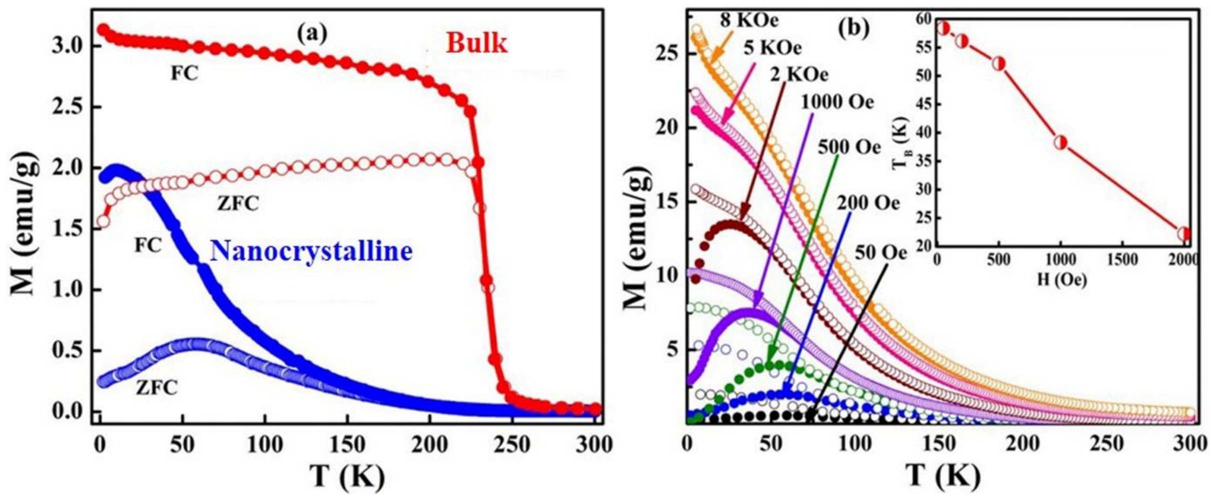

Fig. 3.3. *(a) Temperature dependence of ZFC and FC dc magnetization of bulk and nanocrystalline NSMO compounds measured under a magnetic field of 50 Oe. (b) Temperature dependence of magnetization of nanocrystalline NSMO compound measured under different magnetic field (The inset shows the variation of blocking temperature as a function of the magnetic field)*

Hence we have carried out the ZFC and FC measurements at different magnetic fields for the nanocrystalline compound (shown in Fig. 3.3(b)) and found that the bifurcation is still persisted at higher fields reflecting that part of the total moment cannot be reversed even at such higher fields. However, the cusp is smeared out, and the ZFC overlaps with the FC curve under a high field of 8 kOe. Again, the T_B observed at different temperatures is decaying with the field as shown in the inset of Fig. 3.3(b) and this kind of nature are generally found in the superparamagnetic nanoparticles. However, on a note, a few key qualities essential for superparamagnetic are: (i) A magnetization curve with no hysteresis, (ii) Non-saturating tendency of magnetization even at high field and (iii) Experimental data of different temperature superimpose on to a universal curve of M_S vs. H/T [212] Hence, if the particles are superparamagnetic, the particles should have zero coercivity above T_B and an exponential increase in H_C while lowering the temperature below T_B [213].

However, to confirm the existence of competing magnetic states at low temperature, a detailed magnetization data with the application of magnetic fields is essential, and thus we have carried out the hysteresis loops at various temperature and is shown in Fig. 3.4.

The inset of the figure shows the enlarged view of the hysteresis loops to visualize the hysteresis. At 2 K, the nanocrystalline compound shows a prominent coercivity (H_C). i.e., 2200 Oe. The variation of H_C as a function of temperature is also shown in the inset of Fig. 3.4 and H_C decrease with the increase of temperature. Thus, the prominent H_C above the blocking temperature indicates that the nanocrystalline material is not superparamagnetic. The magnetization values increase rapidly at lower magnetic fields but do not saturate even at applied magnetic fields as high as 90 kOe. This unusual behaviour could be due to the presence of two different magnetic components. i.e., an FM component which gets quickly saturated at lower fields and an AFM component that doesn't saturate even at very high fields. The competing nature of these two components results in such a non-saturating M-H behaviour. It is observed that the non-saturating tendency of magnetization is more prominently seen in the present study, indicating a spin glass/ cluster glass nature [156].

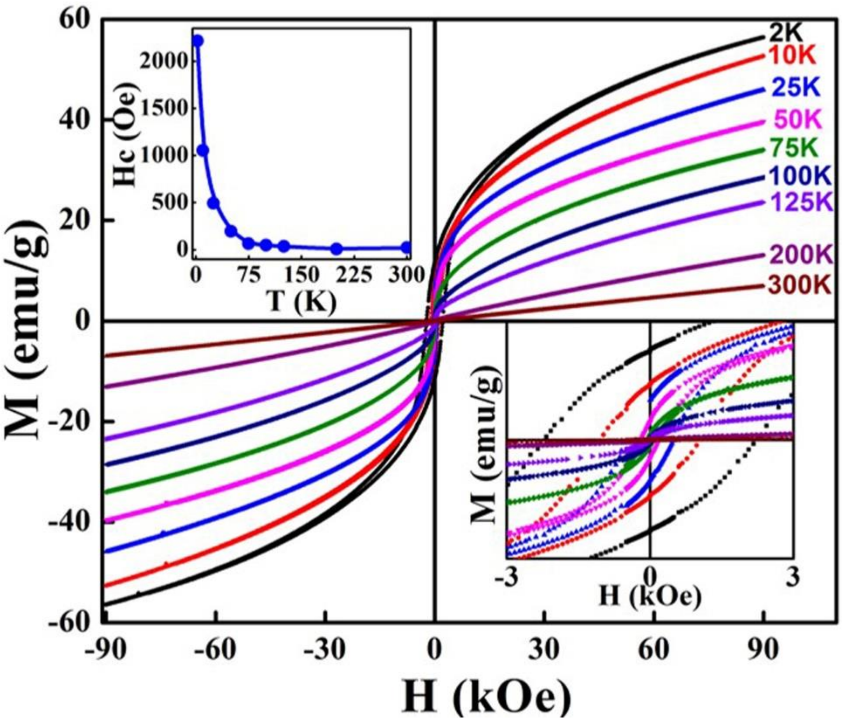

__Fig. 3.4.__ Hysteresis loops in the range of -90 kOe to +90 kOe of nanocrystalline NSMO compound. (Insets: Enlarged view of the hysteresis loops and variation of H_C with temperature)

3.3.3. AC magnetic characterization

To further clarify the spin/cluster glass behaviour, the frequency and field dependence of AC susceptibility as a function of temperature was measured, and it is shown in Fig. 3.5. The measurement was done in an applied field of 1 Oe in the temperature range of 5 to 300 K at frequencies ranging from 3 Hz to 923 Hz, as shown in Fig. 3.5 (a) and (c). Fig. 3.5 (b) and (d) represents the field dependence of the in-phase component (χ'-real part) and the out of phase component (χ''-imaginary part) of the AC susceptibility as a function of temperature. Both real and imaginary parts of the AC susceptibility show characteristic maximum close to the blocking temperature, T_B. The real part of the AC susceptibility is similar to the ZFC of the dc magnetization curve. It can be seen from the figure that the characteristic maximum is obtained around 60 K and this maximum is independent of the change in frequency. The imaginary part (χ'') of the AC susceptibility is frequency-dependent and the peak temperature, i.e., the freezing temperature, T_f shift towards higher temperature with increasing frequency [214]. The magnitude of χ'' decreases with increasing frequency up to 123 Hz and thereafter increases with increasing frequency. But the peak temperature, T_f always shift towards the higher temperature with increasing frequency. This is a clear indication of a slow dynamics system with spin glass or cluster glass nature.

Further, an empirical parameter 'g' can be used as a good criterion to identify the magnetic order of the system, where g is known as the relative shift of the freezing temperature per a frequency decade.

$$\Delta T_f / (T_f \Delta \log f) \tag{3.1}$$

where ΔT_f is the difference in freezing temperature and f is the AC magnetic field frequency. We have obtained a g value of 0.0814, which is more likely to be a cluster glass type system. We used critical slowing down relation for the dynamical scaling analysis [215]

$$\tau/\tau_0 = [(T_f - T_g)/T_g]^{-z\upsilon} \tag{3.2}$$

where τ is the relaxation time. We have plotted τ as a function of reduced temperature (t), where $t = (T_f - T_g)/T_g$. From the analysis, the critical glass transition temperature $T_g = 58.8$ K, the relaxation time $\tau_0 \sim 2\text{x}10^{-4}$, the dynamical critical exponent $z\upsilon = 1.1$ are determined. For the spin-glass system, $\tau_0 = 10^{-13}$ and $z\upsilon$ lies between 4 to 12. The higher value of τ_0 and lower value of $z\upsilon$ shows the presence of some randomly oriented ferromagnetic clusters in the nanocrystalline compound.

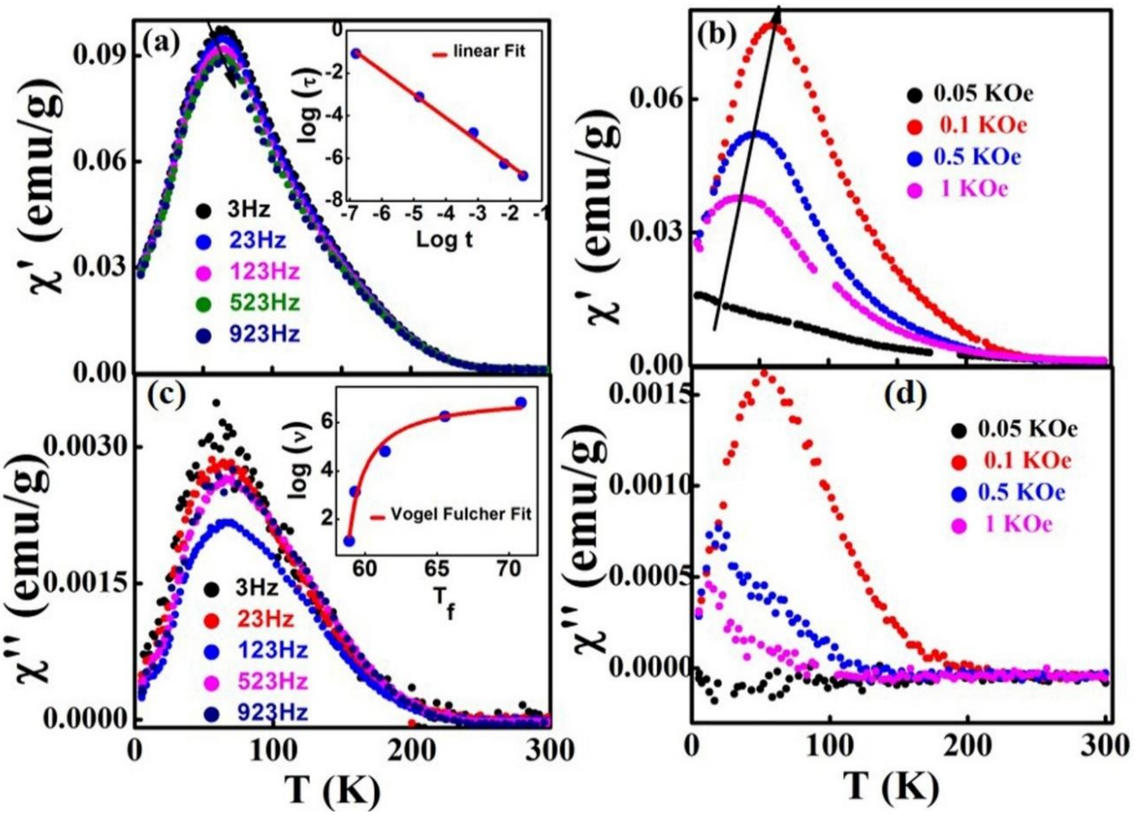

Fig. 3.5. *Frequency dependence of the (a) real and (c) imaginary component, and field dependence of (b) real and (d) imaginary component of the AC-magnetic susceptibility of nanocrystalline NSMO compound*

To further investigation on the cluster nature, the Vogel-Fulcher law is used for the calculation of characteristic frequency and activation energy. The inset of Fig. 3.5 (c) shows the Vogel-Fulcher fit using the equation

$$\upsilon = \upsilon_0 \exp\left[- E_a/k_B (T_f - T_0)\right] \tag{3.3}$$

where υ_0 is the characteristic frequency of the clusters, E_a is the activation energy, T_0 is the Vogel-Fulcher temperature. From the analysis, we obtained $\upsilon_0 = 1.3x10^3$, $E_a/k_B = 7.14$ and $T_0 = 57.7$ K and the excellent agreement of the fit is a clear indication of cluster glass behaviour.

3.3.4. Magnetocaloric properties

Further to analyze the nature of transition and the magnetocaloric properties, isothermal magnetization measurement has been done for every 4 K interval around the T_C and is shown in Fig. 3.6(a) and (b) for the bulk and nanocrystalline compounds. The magnetization increases gradually at lower fields for both the compounds and the magnetization values of the nanocrystalline compound are much lesser than its bulk counterpart. For the bulk compound, the positive slope shown by the Arrott plot, a graph between M^2 and H/M (shown in Fig. 3.6 (c)) confirms that the transition is second-order in nature [216]. The reduction of particle size in the nanocrystalline compound results in the suppression of magnetization and different Arrott plot behaviour due to the grain boundary effect. We have calculated the $-\Delta S_M$ of both the compounds from the isothermal magnetization measurements. Fig. 3.7(a) shows the $-\Delta S_M$ of bulk compound estimated under field change of 10 kOe and 50 kOe. The Bulk compound shows maximum values of 2.68 J kg^{-1} K^{-1} and 7.37 J kg^{-1} K^{-1} at 235 K for 10 kOe and 50 KOe field change respectively. However, the nanocrystalline compound shows a maximum value of 0.88 J kg^{-1} K^{-1} at 68 K for a field change of 50 kOe (shown in Fig. 3.7 (b)). From this result, it is clear that the bulk compound shows a significant ΔS_M and could be a potential candidate for sub-room-temperature magnetic refrigeration applications. It is observed that the ΔS_M value of the nanocrystalline compound is lower than that of its bulk counterpart by one order. The cluster glass nature of the nanocrystalline compound drastically suppresses the ΔS_M value at its transition temperature.

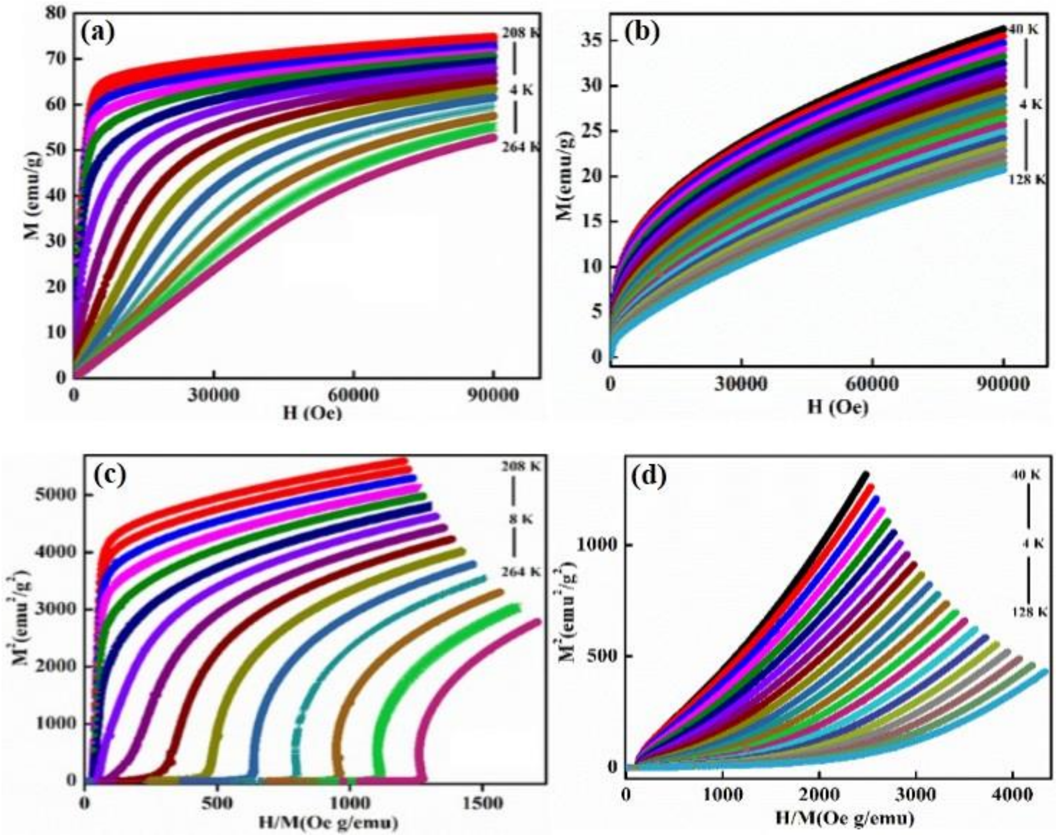

Fig. 3.6. *Isothermal magnetization curves (a) bulk and* (b) nanocrystalline, *Arrott plot of (c) bulk and (d) nanocrystalline compounds respectively*

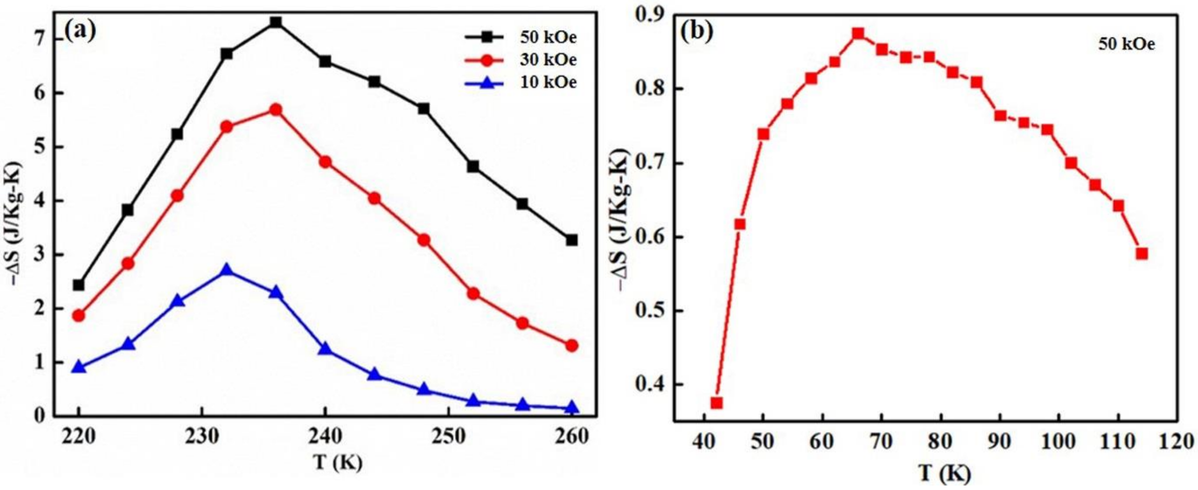

Fig. 3.7. *Magnetic entropy change of (a) bulk and (b) nanocrystalline NSMO compounds*

3.3.5. Electrical transport properties

To understand the transport behaviour with the reduction of crystalline size, we have carried out the temperature dependence of electrical resistivity, ρ(T) under different magnetic fields in the temperature range of 2-300 K (shown in Fig. 3.8 (a) and (b)). From the figure, it can be seen that the reduction in crystalline size results in higher resistivity than that of its bulk counterpart. Further, it is noticed that while lowering the temperatures, the resistivity increases gradually for both the compounds and then decreases by making a maximum (say T_P). Upon further lowering the temperature, the resistivity develops a low-temperature upturn by making a minimum (say T_m) in the ρ(T) curve. In the case of the nanocrystalline compound, the T_P is broader, and the low-temperature upturn is more prominent compared to its bulk compound. Again, the T_P is shifting towards higher temperature with the application of magnetic fields for both the compounds whereas the T_m shifts towards low temperature in case of the nanocrystalline compound, but remains unaltered for the bulk one. The enhancement in resistivity for the nanocrystalline compound may be due to the enhancement of grain boundary effects which decrease the DE interaction between Mn^{3+} and Mn^{4+} due to the breakage of Mn-O-Mn bonds.

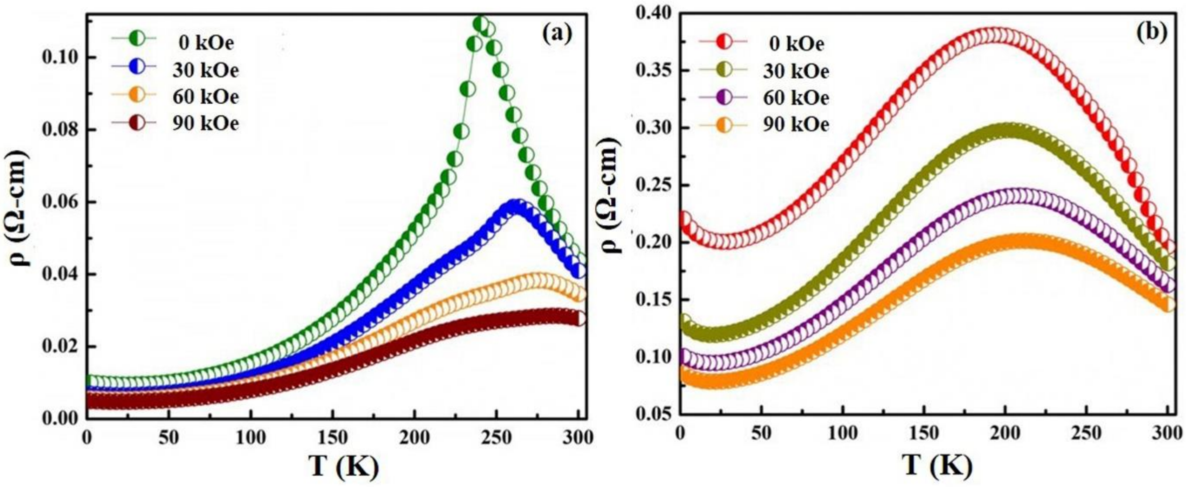

Fig. 3.8. *Variation of electrical resistivity with the temperature of (a) bulk and (b) nanocrystalline NSMO compounds*

Thus the nanocrystalline compound may be considered as a core-shell type structure with a FM metallic core covered by an AFM insulating surface shell. The applied magnetic field delocalizes the charge carriers and causing local ordering of the magnetic spins. Thus the ρ value decreases with increasing magnetic field and T_P shifts towards higher temperature region. Again the T_m in the nanocrystalline compound shifts towards the low-temperature region with the applied magnetic field, which may be due to the suppression of the magnetic spin scattering by the external magnetic field. Further, it is found that the T_C and T_P are almost the same in the case of the bulk compound, whereas the T_P is higher than that of T_C in the case of the nanocrystalline compound. This anomaly may be due to the phase separation phenomenon as mentioned in the earlier report [164]. It is because the nanocrystalline compound consists of FM clusters in the presence of PM matrix, that makes a phase separation and in which the conduction takes place via clusters. Hence these clusters grow and get connected to form conductive paths resulting in the metallic character above T_C. Thus metal-insulator transition temperature is higher than the magnetic transition temperature for the nanocrystalline compound.

3.4. Conclusion

A comprehensive study of magnetic phase transitions and magnetocaloric properties of bulk and nanocrystalline $Nd_{0.67}Sr_{0.33}MnO_3$ manganites has been conducted, and the following observations have been drawn from the study.

- Both the compounds crystallized into an orthorhombic structure with Pbnm space group confirmed from Rietveld refinement of XRD patterns.
- The long-range ferromagnetic ordered state appears to become unstable upon the reduction of the samples dimension down to nanometre scale, and thus the frustration

of spin system happens in the nanocrystalline compound, and thereby lead into a cluster glass-like behaviour.

- The nanocrystalline compound shows an enhancement in resistivity in comparison to its bulk counterpart and a broad metal-insulator transition confirm the presence of ferromagnetic clusters.
- The bulk compound shows a T_C of 235 K, and exhibits a $-\Delta S_M$ of 2.68 J kg^{-1} K^{-1} and 7.37 J kg^{-1} K^{-1} under 10 kOe and 50 kOe field change and could be a potential candidate for sub room-temperature magnetic refrigeration applications, whereas the nanocrystalline compound exhibit a maximum $-\Delta S_M$ value of 0.88 J kg^{-1} K^{-1} at 68 K for a field change of 50 kOe.
- The cluster glass nature drastically suppresses the magnetic ordering and magnetic entropy change of the nanocrystalline compound.

Chapter 4

Effects of transition metal elements substitution at the Mn-site on magnetic ordering and magnetocaloric properties in $Nd_{0.67}Sr_{0.33}MnO_3$ manganite

In this chapter, we have investigated the effects of partial substitution of transition metals (10 at. % of Cr, Fe, Co, Ni and Cu) at the Mn-site in $Nd_{0.67}Sr_{0.33}MnO_3$ manganite. Rietveld refinement confirmed that all the compounds crystallized into an orthorhombic structure. X-ray absorption spectroscopic analysis confirmed minor variations in the Mn^{3+}/Mn^{4+} ratio due to doping with transition metal elements at the Mn site. Substitution of transition elements at the Mn-site in $Nd_{0.67}Sr_{0.33}MnO_3$ has broadened the FM-PM transition leading to the suppression of magnetocaloric effect. The critical behaviour of the system was analysed using the modified Arrott plot method and critical isotherm analysis. The critical exponents β and γ calculated for the parent compound were consistent with the tricritical model, whereas the critical exponents determined for the substituted compounds were close to the mean field model.

4.1. Introduction

Chapter 3 reveals interesting magnetic behaviour and appreciable magnetic entropy change in bulk $Nd_{0.67}Sr_{0.33}MnO_3$ compound. Since the magnetic behaviour of manganites is strongly depends on the strength of the DE interaction between Mn^{3+} and Mn^{4+} ions, it would be of great interest to study the effect of substitution of 3d transition elements at the Mn site. The introduction of other transition elements at the Mn site leads to drastic changes associated with the mismatch in electronic configuration between Mn and the substituted ions and strongly affect the structural and magnetic properties of the compound. Moreover, doping changes the Mn-O bond length and Mn-O-Mn bond angle, which strongly affects the electron hopping process between Mn^{3+} and Mn^{4+} ions. Previous studies have shown the effect of 3d-transition elements substitution at the Mn site in manganites, but most of them are on La-based systems [180, 217-226], and thus only limited details are available regarding the $Nd_{1-x}Sr_xMnO_3$, and properties like magnetic phase transition and therefore magnetocaloric properties in this system need to be explored. The study of magnetocaloric properties in these materials is not only important from the application point of view but also serves as a tool to understand the intrinsic properties of these materials. Therefore, in this chapter, a systematic study of substitution of 10 at. % of 3d transition elements (Tr) at the Mn site in NSMO has been carried out. Structure, magnetic and magnetocaloric properties of $Nd_{0.67}Sr_{0.33}Mn_{0.9}Tr_{0.1}O_3$ (NSMTrO) where Tr= Cr, Fe, Co, Ni and Cu are explored. The values of critical exponents are also calculated for this system in connection with their magnetic transitions behaviour.

4.2. Experimental

All compounds were prepared via conventional solid-state ceramic route. The starting powder reagents Nd_2O_3, $SrCO_3$, $MnCO_3$, CrO_3, Fe_2O_3, Co_3O_4, NiO, CuO, were mixed in stoichiometric proportions using an agate mortar and pestle with distilled water as a medium for 6h. The slurry was then dried and calcined at 1200°C for 12 h, grounded and the granulated powders were pressed uniaxially into cylindrical pellets of appropriate dimension under a pressure of 100 MPa. The pellets were then sintered at 1350°C for 12 h in air and finally cooled to room temperature. The sintered samples were grounded again, and the granulated powders were used for characterization. The phase purity was examined by powder X-ray diffraction (XRD) using a PANalytical X'Pert Pro Diffractometer with Ni-filtered Cu Kα radiation. Rietveld refinement was conducted using GSAS software [209], and the crystallographic structures were prepared with Crystal Maker software (Crystal Maker Software Limited, Oxfordshire, OX5 1PF, UK). Energy-dispersive X-ray analysis (EDAX) was performed for different regions of the samples to confirm the homogeneity and expected stoichiometry. The Mn L-edge and O K-edge X-ray absorption spectra (XAS) were collected using the 20 A beamline at the National Synchrotron Radiation Research Facility, Taiwan. Fine powder samples were used for the measurements. Measurements were acquired at room temperature using the total electron yield mode at a chamber base pressure of ~ 10^{-9} Torr. The cationic compositions were confirmed by X-ray fluorescence spectrometry (EDXRF) analysis (PANalytical Epsilon 3). Magnetic measurements were performed using a vibrating sample magnetometer attached to the physical property measurement system (Quantum Design Inc., USA).

4.3. Results and discussion

4.3.1. Structural analysis

The XRD patterns were analysed for all the compounds, and the structural parameters were determined by Rietveld refinement. The XRD patterns of all the compounds indicated a single-phase orthorhombic crystal structure with the Pbnm space group. The crystallographic structure is shown in Fig. 4.1 and the refined XRD patterns are shown in Fig. 4.2. The refined parameters are listed in Table 4.1. From the refinement analysis, it is evident that there is an excellent agreement between the calculated and experimental fits for all the compounds, considered from the small values of residuals for the weighted pattern R_{WP}, pattern R_P and the goodness of fit χ^2. The observed lattice parameters and cell volume of the substituted compounds can be correlated with the ionic radius of the substituted elements at the Mn site, as seen in Table 4.1.

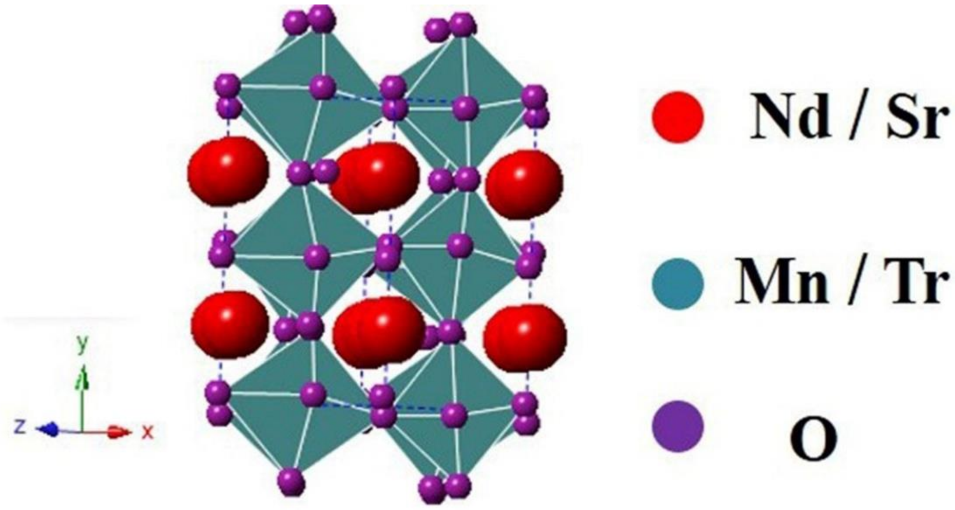

Fig. 4.1. *Crystallographic structure of NSMTrO (Tr= Cr, Fe, Co, Ni and Cu) compounds*

The partial substitution of Mn ions with Tr ions affects the magnetic properties dramatically due to three combinations of bonds that coexist as; Mn-O-Mn, Mn-O-Tr, and Tr-O-Tr. However, the probability of formation of Tr-O-Tr bonds is very less as the substitution is only 10 at. %, whereas the formation of Mn-O-Mn, Mn-O-Tr bonds dominate and thus play a major role in determining the magnetic properties with the substitution of Tr ions.

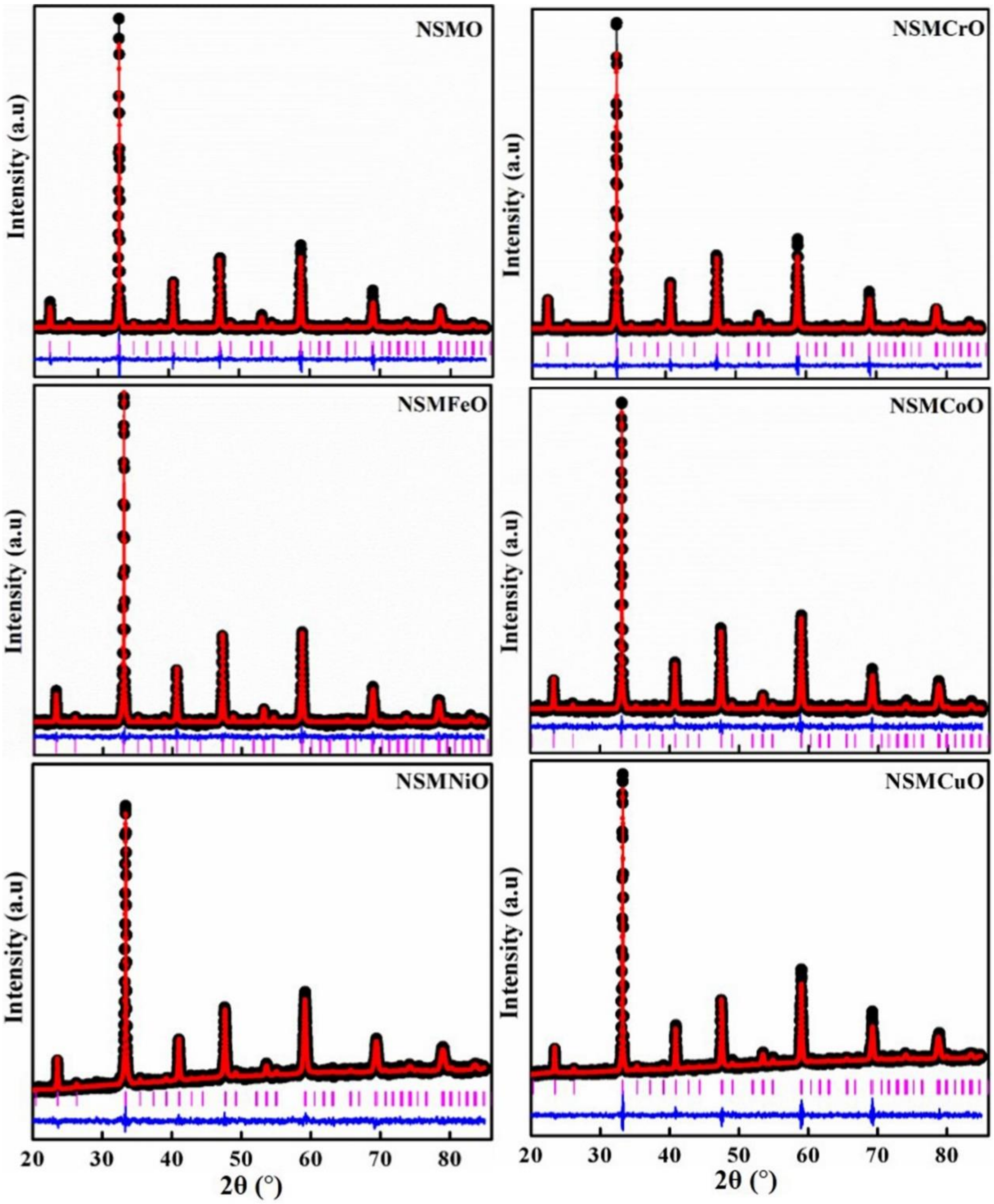

***Fig. 4.2**. Rietveld refined XRD patterns for NSMO and NSMTrO (Tr= Cr, Fe, Co, Ni and Cu) compounds at room temperature. Dotted circles correspond to XRD data, and the lines are the theoretical fits to the observed XRD data. The difference between the observed data and the theoretical fit is shown at the bottom*

It can be seen from Table 4.1 that the Mn-O-Mn bond angle observed is less than 180° for all the compounds and hence deviates from the ideal cubic structure for which the Mn-O-Mn bond angle is 180°. Deviation from the same is an indication of the distortion of the MnO_6 octahedra, which further corroborates the orthorhombic crystal structure.

	NSMCrO	**NSMFeO**	**NSMCoO**	**NSMNiO**	**NSMCuO**
Cell parameters					
a (Å)	5.4648(2)	5.4645(2)	5.4617(9)	5.4463(2)	5.4658(4)
b (Å)	5.4488(2)	5.4499(2)	5.4547(9)	5.4495(3)	5.4488(0)
c (Å)	7.6991(3)	7.6977(3)	7.6962(9)	7.6960(3)	7.6921(5)
V (Å^3)	229.257	229.248	229.285	229.256	229.090
Positional parameters					
Nd/Sr x	0.4987(21)	0.4960(21)	0.4980(5)	0.5006(19)	0.5040(19)
Nd/Sr y	0.0212(5)	0.0220(4)	0.0208(6)	0.0219(5)	0.0205(6)
O1 x	0.5684(34)	0.5690(4)	0.5600(9)	0.5630(6)	0.5780(5)
O1 y	0.4986(31)	0.4992(30)	0.5070(6)	0.5010(5)	0.4970(5)
O2 x	0.2220(6)	0.2470(5)	0.2260(8)	0.2250(6)	0.2290(8)
O2 y	0.2450(6)	0.2940(4)	0.2920(10)	0.2970(7)	0.2200(8)
O2 z	0.0291(29)	0.0233(32)	0.0190(4)	0.0265(33)	0.0160(4)
Occupancy/ Atomic displacement parameter					
Nd	0.6680/ 0.0037	0.6689/ 0.0475	0.6704/ 0.0121	0.6694/ 0.0035	0.6682/ 0.0309
Sr	0.3314/ 0.0037	0.3284/ 0.0475	0.3279/ 0.0121	0.3282/ 0.0035	0.3278/ 0.0309
Mn	0.8990/ 0.0014	0.8985/ 0.0435	0.8992/ 0.0014	0.8982/ 0.0012	0.8988/ 0.0236
Tr	0.0990/ 0.0014	0.0986/ 0.0435	0.0981/ 0.0014	0.0988/ 0.0012	0.0990/ 0.0236
O1	1.0002/ 0.0552	1.0020/ 0.0332	1.0021/ 0.0531	1.0018/ 0.0408	1.0016/ 0.0260
O2	1.0015/ 0.0788	1.0008/ 0.0311	1.0014/ 0.0212	1.0024/ 0.0037	1.0009/ 0.0283
Bond distance (Å)					
Mn-O1	1.961(4)	1.961(4)	1.952(16)	1.955(6)	1.969(6)
Mn-O2	1.817(26)	1.792(22)	1.880(6)	1.88(4)	1.736(22)
Mn-O2	2.071(27)	2.101(22)	2.020(6)	2.03(4)	2.132(23)
Bond angle (°)					
Mn-O1-Mn	158.0(11)	157.9(13)	160.7(28)	159.7(19)	155.1(16)
Mn-O2-Mn	165.8(14)	164.8(13)	162.6(16)	160.1(12)	172.4(18)
Agreement factors					
R_{WP}	3.32	2.75	3.14	3.09	3.65
R_P	2.39	2.16	2.41	2.41	2.67
χ^2	1.51	1.04	1.33	1.24	1.26

Table 4.1. *Structural parameters obtained for* $Nd_{0.67}Sr_{0.33}Mn_{0.9}Tr_{0.1}O_3$ *(Tr= Cr, Fe, Co, Ni and Cu) compounds by Rietveld refinement*

4.3.2. EDAX and EDXRF analysis

NSMTrO (Tr= Cr, Fe and Co) compounds were taken as a representative of the series, and EDAX analysis was conducted in to confirm the homogeneity, which showed that the stoichiometry obtained was nearly identical to the nominal composition.

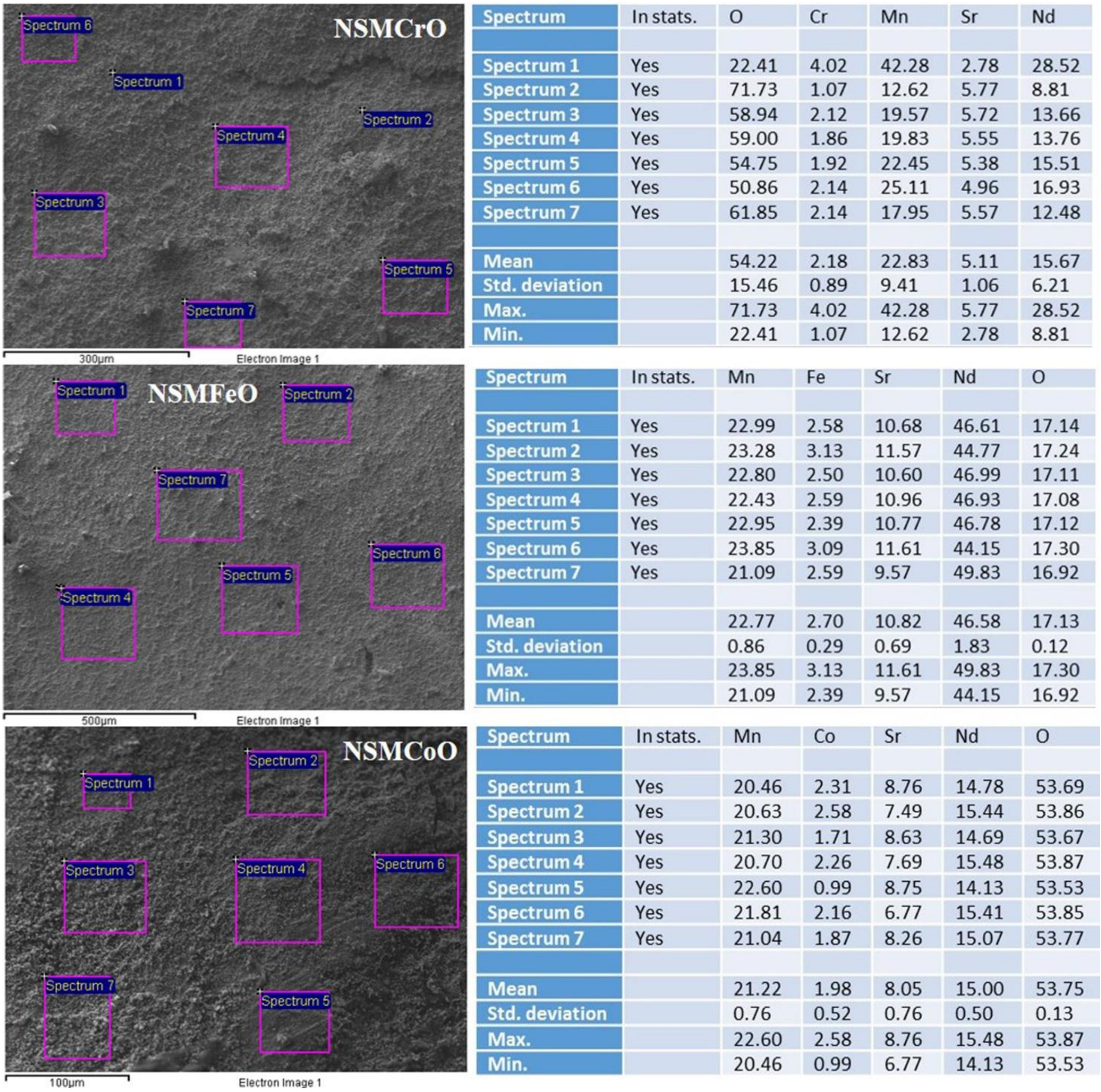

Spectrum	In stats.	O	Cr	Mn	Sr	Nd
Spectrum 1	Yes	22.41	4.02	42.28	2.78	28.52
Spectrum 2	Yes	71.73	1.07	12.62	5.77	8.81
Spectrum 3	Yes	58.94	2.12	19.57	5.72	13.66
Spectrum 4	Yes	59.00	1.86	19.83	5.55	13.76
Spectrum 5	Yes	54.75	1.92	22.45	5.38	15.51
Spectrum 6	Yes	50.86	2.14	25.11	4.96	16.93
Spectrum 7	Yes	61.85	2.14	17.95	5.57	12.48
Mean		54.22	2.18	22.83	5.11	15.67
Std. deviation		15.46	0.89	9.41	1.06	6.21
Max.		71.73	4.02	42.28	5.77	28.52
Min.		22.41	1.07	12.62	2.78	8.81

Spectrum	In stats.	Mn	Fe	Sr	Nd	O
Spectrum 1	Yes	22.99	2.58	10.68	46.61	17.14
Spectrum 2	Yes	23.28	3.13	11.57	44.77	17.24
Spectrum 3	Yes	22.80	2.50	10.60	46.99	17.11
Spectrum 4	Yes	22.43	2.59	10.96	46.93	17.08
Spectrum 5	Yes	22.95	2.39	10.77	46.78	17.12
Spectrum 6	Yes	23.85	3.09	11.61	44.15	17.30
Spectrum 7	Yes	21.09	2.59	9.57	49.83	16.92
Mean		22.77	2.70	10.82	46.58	17.13
Std. deviation		0.86	0.29	0.69	1.83	0.12
Max.		23.85	3.13	11.61	49.83	17.30
Min.		21.09	2.39	9.57	44.15	16.92

Spectrum	In stats.	Mn	Co	Sr	Nd	O
Spectrum 1	Yes	20.46	2.31	8.76	14.78	53.69
Spectrum 2	Yes	20.63	2.58	7.49	15.44	53.86
Spectrum 3	Yes	21.30	1.71	8.63	14.69	53.67
Spectrum 4	Yes	20.70	2.26	7.69	15.48	53.87
Spectrum 5	Yes	22.60	0.99	8.75	14.13	53.53
Spectrum 6	Yes	21.81	2.16	6.77	15.41	53.85
Spectrum 7	Yes	21.04	1.87	8.26	15.07	53.77
Mean		21.22	1.98	8.05	15.00	53.75
Std. deviation		0.76	0.52	0.76	0.50	0.13
Max.		22.60	2.58	8.76	15.48	53.87
Min.		20.46	0.99	6.77	14.13	53.53

Fig. 4.3. *SEM-EDAX and composition of NSMTrO (Tr= Cr, Fe and Co) compounds*

Fig. 4.3 shows the SEM image and the obtained stoichiometry of the studied compounds. Further, the chemical compositions of the elemental oxides present in the compounds were confirmed by EDXRF analysis and shown in Table 4.2, which confirms that the ratios of Nd: Sr and Mn: Tr (Cr, Fe and Co) were close to the nominal compositions within the limits of experimental error.

Compound	**Element oxide**
NSMCrO	49.235% Nd_2O_3 + 16.972% SrO + 28.836% MnO + 4.957% CrO_3
NSMFeO	49.235% Nd_2O_3 + 16.123% SrO + 29.493% MnO + 5.149% Fe_2O_3
NSMCoO	49.234% Nd_2O_3 + 16.632% SrO + 28.420% MnO + 5.714% Co_3O_4

Table 4.2. *Chemical composition of element oxides present in NSMTrO (Tr= Cr, Fe and Co) compounds according to EDXRF analysis*

4.3.3. XAS analysis

Effects of Cr, Fe, Co, Ni and Cu substitutions on the electronic structures and valence states of the Mn ion using XAS at the Mn L-edge and O K-edge have been analysed. Fig. 4.4(a) shows the Mn 2p XAS results for all of the compounds. All the spectra were normalized with respect to the edge step below and above the edge. The standard samples of MnO, Mn_2O_3, and MnO_2 are also plotted in the figure for comparison where the spectra are shifted vertically for clarity. All of the compounds exhibited two broad L_{III} and L_{II} peaks due to spin-orbit coupling. Furthermore, each peak contained multiple structures, which provided information about the local electronic structures for each sample. For all the compounds, the spectral features resembled the superimposition of those for both Mn_2O_3 and MnO_2. Furthermore, the L_{III} peak maximum is between Mn^{3+} and Mn^{4+}, thereby indicating mixed-valence, as shown in previous studies [227]. Both the L_{III} and L_{II} peaks had small hump-like features on the lower energy sides. The change in the spectral shape indicated the variation in the symmetry of the ground state, whereas the chemical shifts of the L_{III} and L_{II} peaks denote changes in the effective ionic valence of the Mn ion. Fig. 4.4(b) shows the O 1s XAS results for all the compounds. The O K-edge spectrum is a unique technique for determining the hybridization of a Tr-element with its surrounding ligand ions. The near edge dipolar allows the O 1s to O 2p transitions to be employed to explore the unoccupied density of states around the O 2p character that hybridizes with transition metal 3d states [228]. In general, the characteristic O K-edge peaks could be split into three types based on their excitation. The first peak at the onset of the edge (~ 528 eV) was assigned to the excitation of the O 1s state to the hybridization of the O 2p-Mn 3d state. Second and third peaks were attributed to the excitation of the O 1s state to the O 2p-Nd 5d (~ 536 eV) and O 2p-Mn 4sp (~ 543 eV) states, respectively [228, 229].

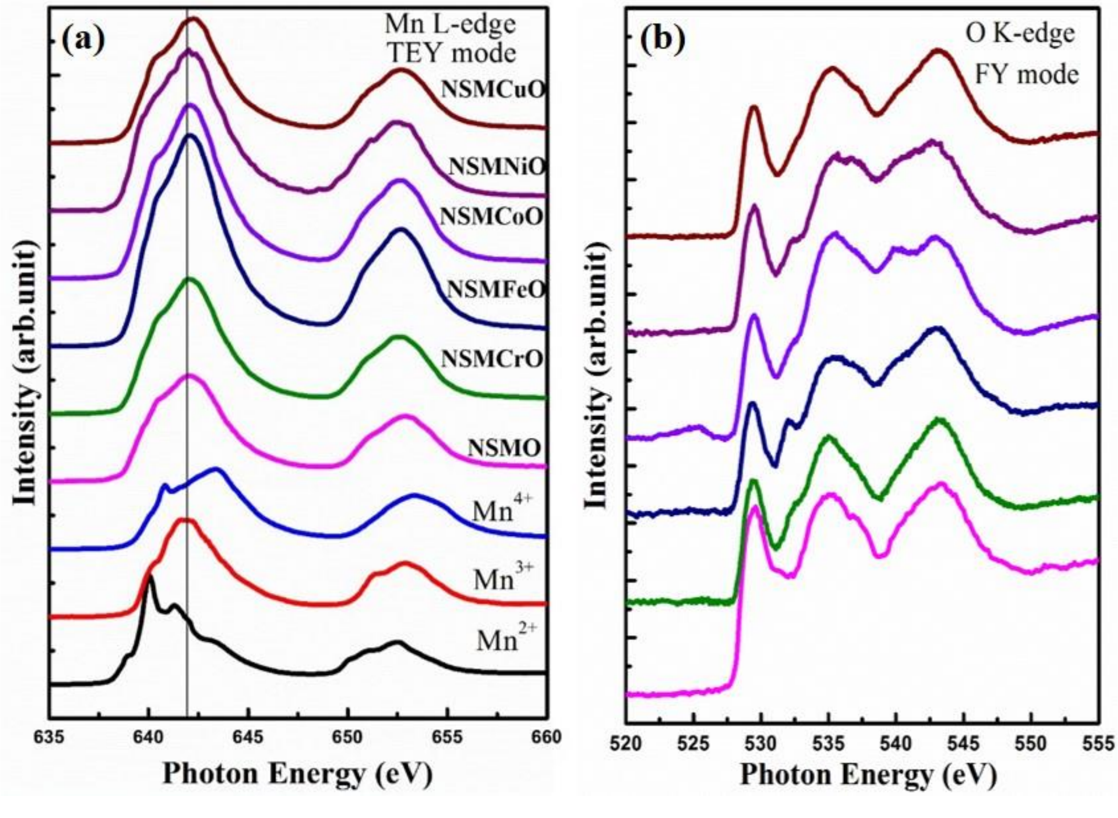

***Fig. 4.4**. X-ray absorption spectroscopic images of NSMO and NSMTrO (Tr= Cr, Fe, Co, Ni and Cu) compounds. (a) Mn 2p XAS for all compounds. (b) Oxygen 1s XAS for all compounds*

According to the XAS data, it is clear that all the Mn ions had mixed valences of Mn^{3+} and Mn^{4+}. In addition, doping with Tr-metals at the Mn site produced very interesting oxidation states, which were highly dependent on the type of Tr-metal dopant. The oxygen spectral features were more or less independent of the dopant elements, and they indicated no change in the oxygen stoichiometry with the dopant elements. The effective Mn ion valence is estimated for all the compounds using the interpolation method, as shown in Fig. 4.5(a). According to Fig. 4.5(a), the photon energy vs. the average Mn valence exhibited linear variation, and the results quantitatively demonstrated that the concentration of Mn^{4+} ions increased slightly in the Fe, Co and Cu-substituted compounds. Furthermore, Fig. 4.5(b–f) confirms the presence of Cr^{3+}, Fe^{3+}, Co^{2+}, Ni^{2+} and Cu^{2+} in the Tr-substituted compounds.

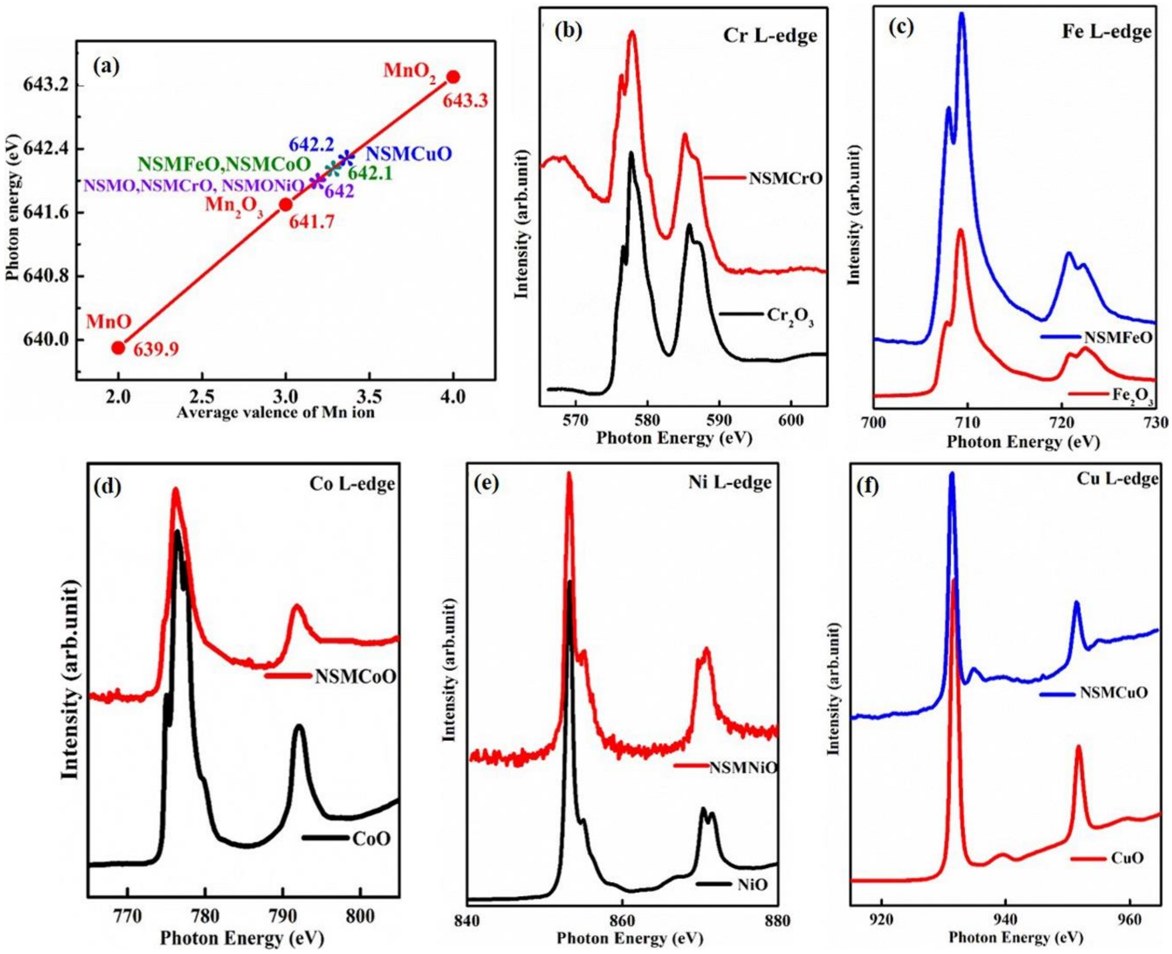

Fig. 4.5*(a) Photon energy vs. Mn valence for all compounds. (b-f) Cr-L, Fe-L, Co-L, Ni-L and Cu-L edges of substituted compounds*

4.3.4. Magnetic characterization

The magnetization as a function of temperature, M(T), was determined for all the compounds in the temperature range from 2-300 K in ZFC and FC modes under 50 Oe, as shown in the insets in Fig. 4.6. The thermo-magnetic irreversibility is witnessed between ZFC and FC is may be due to the magnetic frustration caused by competing magnetic interactions of SE and DE. It can also arise as a consequence of magnetic hysteresis coming from the domain structure. All the compounds show a FM-PM transition at the intermediate temperatures and the magnitude of magnetization was found to increase with the applied magnetic field. The derivative of M (dM/dT) versus Temperature curves for all the compounds was calculated (not shown) and the T_C is determined from the curve where the dM/dT reaches a minimum value. At low magnetic fields (50 Oe) the coexistence of FM/AFM phases eventually lead to the formation of frustrated state and strongly affect the temperature variation of magnetization. We have done the ZFC/FC measurements at 1000 Oe to study the nature of FM/AFM coexisting phases and for better Curie-Weiss fitting parameters. For all the compounds, the T_C is found to increases with the applied magnetic field because of the most stable nature of the FM state at higher magnetic fields. From the M(T) curves, it is found that both NSMNiO and NSMCuO compounds show two consecutive transitions with antiferromagnetic ordering at low temperature. The parent compound shows a T_C around 235 K when measured under for 50 Oe, which decreases with the substitution of transition elements except in the case of NSMCuO compound. The T_C values NSMCrO, NSMFeO, NSMCoO and NSMNiO compounds are found to be 196 K, 92 K, 151 K and 215 K respectively for a field of 50 Oe. The NSMCuO compound is resulting higher T_C (248 K) than that of the parent compound in spite of having the least magnetization values amongst all the studied compounds. For Fe, Ni, Co and Cu substituted compounds, the magnetization in ZFC curve decreases abruptly below a particular temperature, and this may be due to the freezing of moments of randomly distributed clusters [180]. However, NSMCrO had a higher magnetization value in the ZFC curve than its parent because of the increased exchange interaction between Mn and O ions [230].

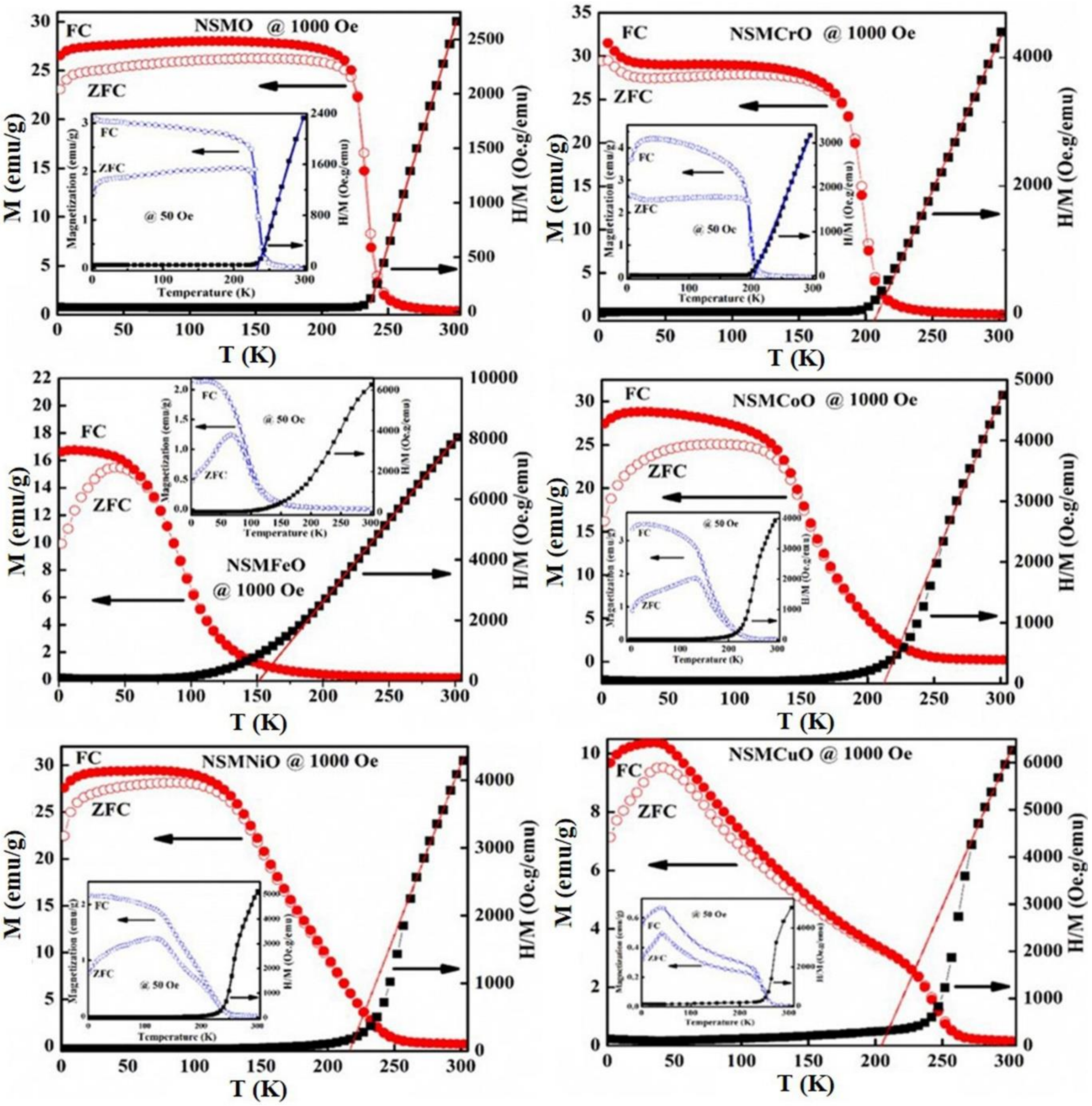

Fig. 4.6. Temperature dependences of ZFC and FC dc magnetization of NSMO and NSMTrO (Tr= Cr, Fe, Co, Ni and Cu) compounds measured under a magnetic field of 1000 Oe, and their inverse susceptibility as well as the linear fit to the Curie–Weiss law in the high-temperature region. Insets of each figure show the M–T curve under a 50 Oe field

The FC magnetization in a FM state is supposed to show either a constant or monotonically increase in the magnetization values while decreasing the temperatures below T_C. A drop in magnetization in the FC curve at low temperature is seen in the case of NSMCoO, NSMNiO and NSMCuO compounds, suggesting the existence of competing magnetic states in these compounds. In NSMFeO compound, the AFM SE interaction will actively suppress the DE interaction between Mn^{3+} and Mn^{4+} ions and leads to a decrease in the transition temperature [180]. The decrease of T_C in NSMCrO compound may be attributed to the replacement of Mn^{3+} ions by the Cr^{3+} ($t_{2g}^3e_g^0$) ions which weakens the Mn^{3+}-O-Mn^{4+} interactions [231]. Here, the Cr^{3+} ions polarize the Mn^{3+} ions. Similarly, Co^{3+} ($t_{2g}^4e_g^2$) and Ni^{2+} ($t_{2g}^5e_g^1$) ions have FM interaction with the surrounding Mn^{4+} ions but AFM interaction with the Mn^{3+} ions. In the case of NSMCuO, the magnetization decreases and the compound enters into the AFM phase at Neel point (T_N) around 50 K.

As from the XAS measurements, it is completely ruled out the possibility of the existence of magnetic impurities in all the compounds. In the substituted compounds, the AFM SE interaction actively suppressed the DE interaction between Mn^{3+} and Mn^{4+} ions due to the replacement of the JT ion (Mn^{3+}) with JT inactive ions which led to a decrease in the transition temperature, as shown in previous studies [180, 218, 232]. Again, the temperature dependence of the inverse susceptibility has been plotted for all the compounds (shown in Fig. 4.6) in order to study the magnetic interaction in the paramagnetic region. Both NSMO and NSMCrO compounds obey the Curie-Weiss law for a field of 50 Oe and show a positive value of paramagnetic Curie temperature, θ_P. For NSMO, θ_P is 235 K, and for NSMCrO, θ_P is 206 K. The positive value of θ_P in these two compounds indicates a decrease in disorder and low magnetic frustration. Rest of the compounds do not obey the Curie-Weiss law even in 1000 Oe applied field and show the presence of some ferromagnetic clusters within the paramagnetic matrix. This inhomogeneous phase above T_C has similar characteristics of Griffiths-like phase seen elsewhere in the literature [233-235]. Thus the deviation of χ^{-1} from the Curie-Weiss law above T_C shows the existence of some FM clusters in the paramagnetic matrix [233].

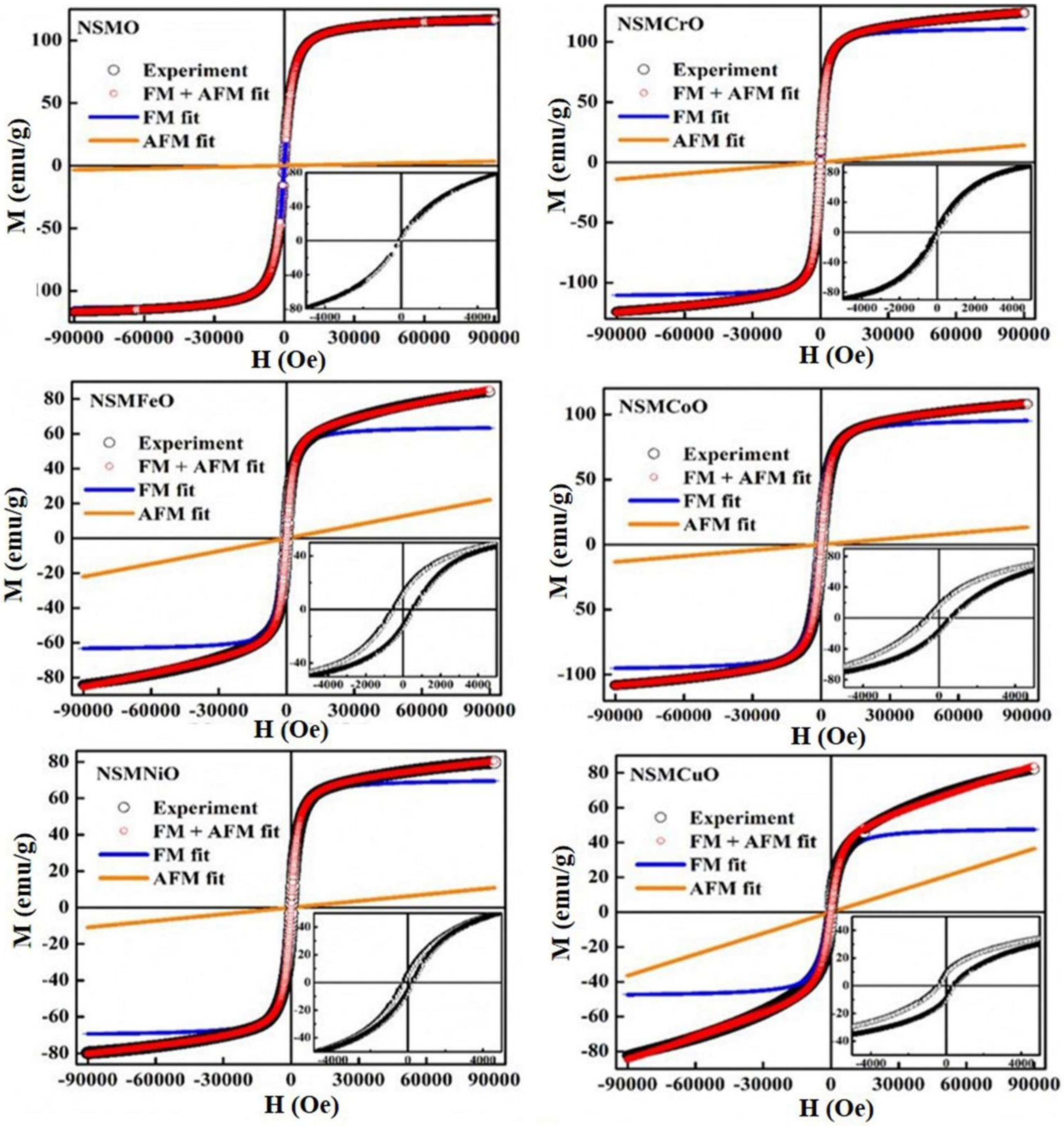

Fig. 4.7. *Isothermal magnetization curves measured at 2 K in the range from –90 kOe to +90 kOe for NSMO and NSMTrO (Tr= Cr, Fe, Co, Ni and Cu) compounds. The red line represents the line fitted using Eq. (4.1) to the experimental data. Insets: close-ups of the hysteresis loops*

However, to confirm the existence of competing magnetic states at low temperature, a detailed magnetization data with the application of magnetic fields is essential, and thus we have carried out the isothermal magnetization at 2 K for all the compounds and are shown in Fig. 4.7. The insets of the figure show the enlarged view of the hysteresis loops in order to visualize the hysteresis. The hysteresis loops show some interesting features as (i) hysteresis is absent for the NSMO compound, whereas all the substituted compounds show a prominent coercivity (H_C). The H_C values of NSMCrO, NSMFeO NSMCoO NSMNiO and NSMCuO are 50 Oe, 524 Oe, 606 Oe, 232 Oe and 440 Oe respectively. (ii) The magnetization values increase rapidly at lower magnetic fields but do not saturate even at applied magnetic fields as high as 90 kOe for all the compounds. This behaviour could be due to the presence of two different magnetic components. i.e., a FM component that gets quickly saturated at lower fields and an AFM component that doesn't saturate even at very high fields. The competing nature of these two components results in such a non-saturating M-H behaviour. It is observed that the non-saturating tendency of magnetization is more prominently seen in the case of NSMCuO compound, indicating an increase in the AFM component. The presence of FM component can be understood due to the DE interaction between Mn^{3+}-O-Mn^{4+}, whereas AFM component is due to the SE interaction, and these results are in agreement with the earlier reports [223]. Presently, no unified model exists to describe the combined FM and AFM magnetization curves obtained in complex magnetic systems. Consequently, we have approached an empirical formula to identify the different magnetic contributions of FM and AFM quantitatively in an expression as [236]

$$M(H) = \frac{2M_S}{\pi} \tan^{-1}\left[\frac{H \pm H_C}{H_C} \tan\left(\frac{\pi Mr}{2M_S}\right)\right] + \chi H \qquad (4.1)$$

where the first term is due to the FM contribution to the total magnetization, as suggested by Stearns and Cheng [237], and the second term has different origins, including the PM phase, surface disorder spins, and non-collinear spin clusters inside the grains, or the AFM component with χ as the magnetic susceptibility. M_S, H_C, and M_r are the saturation magnetization, coercivity, and remanent magnetization, respectively, for the FM contributions. χ is a linear component attributed to the AFM component. Eq. (4.1) yielded reasonably good fits to the experimental data, thereby confirming the existence of FM and AFM components. The solid lines through the data points in Fig. 4.7 are the experimental fits to Eq. (4.1). The FM and AFM contributions are also plotted (using the fitted parameters) in Fig. 4.7 to quantitatively illustrate the fraction of magnetization.

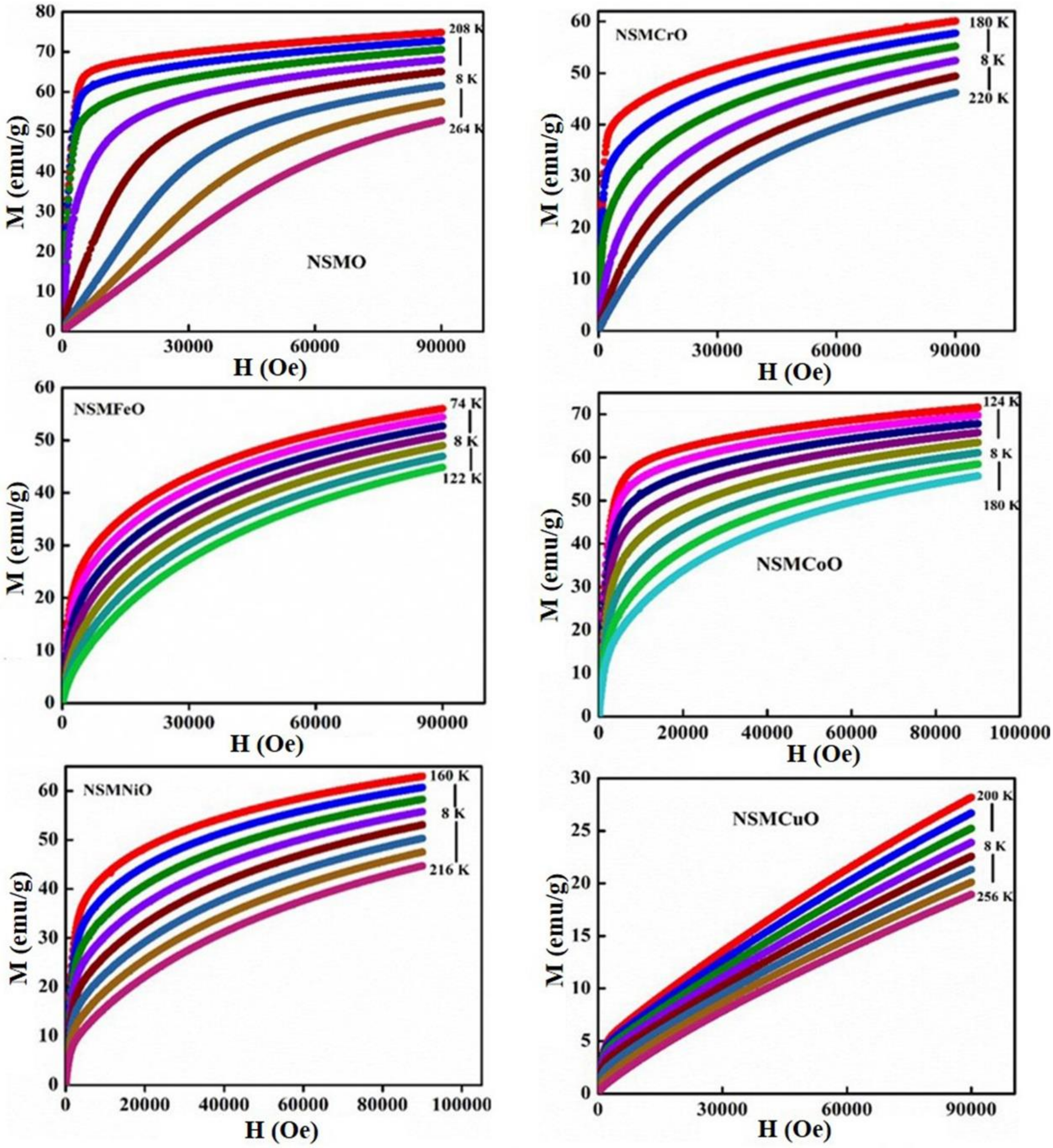

__Fig. 4.8.__ Magnetization as a function of field around T_C for NSMO and NSMTrO (Tr= Cr, Fe, Co, Ni and Cu) compounds

Further to probe the nature of T_C and to calculate the magnetocaloric properties, we have measured the isothermal magnetization of all the compounds in a range of 0-90 kOe with temperature interval of 4 K around T_C. It is to be noted that every second curve is removed from each panel in order to view clear and better way and is depicted in Fig. 4.8. It is observed that there is a gradual change in the M(H) curve at lower fields for all the compounds, making it difficult to extract an accurate value of T_C.

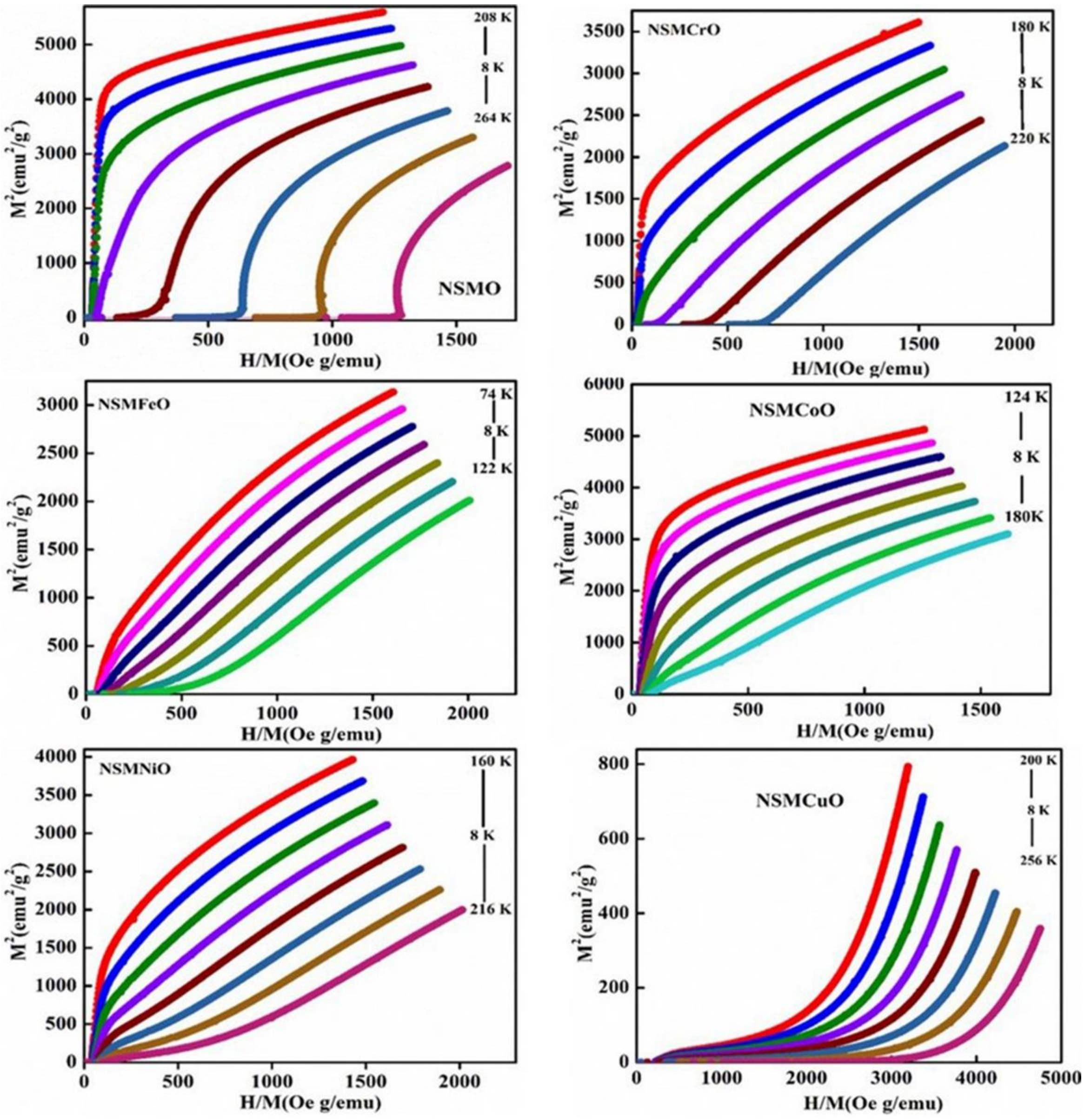

__Fig. 4.9.__ Arrott plots (M^2 Vs H/M) obtained for NSMO and NSMTrO (Tr= Cr, Fe, Co, Ni and Cu) compounds

Further, Arrott plots (M^2 vs. H/M) are plotted and shown in Fig. 4.9. According to the Banerjee criterion [216], the positive slope in the Arrott plots indicates that the transition is second order. It is seen that NSMCuO compound shows a convex curvature nature with H/M and is due to the high AFM nature of the compound.

4.3.5. Magnetocaloric properties

The isothermal magnetization data were used to estimate the ΔS_M values. Temperature variation of ΔS_M under the magnetic fields of 10 kOe has plotted and is shown in Fig. 4.10. All the substituted compounds show a sharp peak at their respective T_C and decrease on either side of the transition temperature. NSMCrO and NSMFeO compounds show $-\Delta S_M$ values of 1.48 J kg^{-1} K^{-1} (196 K) and 0.43 J kg^{-1} K^{-1} (90 K) for 10 kOe field change. NSMCoO and NSMNiO compounds show $-\Delta S_M$ values of 0.69 J kg^{-1} K^{-1} (154 K) and 0.38 J kg^{-1} K^{-1} (150 K) under a field of 10 kOe. NSMCuO compound show $-\Delta S_M$ value of 0.62 J kg^{-1} K^{-1} at 246 K under a field of 10 kOe. It can be seen that the ΔS_M values of the substituted compounds are observed to be lower than that of the pristine compound. Hence, the substitution of different transition elements at the Mn-site leads to a drastic suppression of magnetic entropy change.

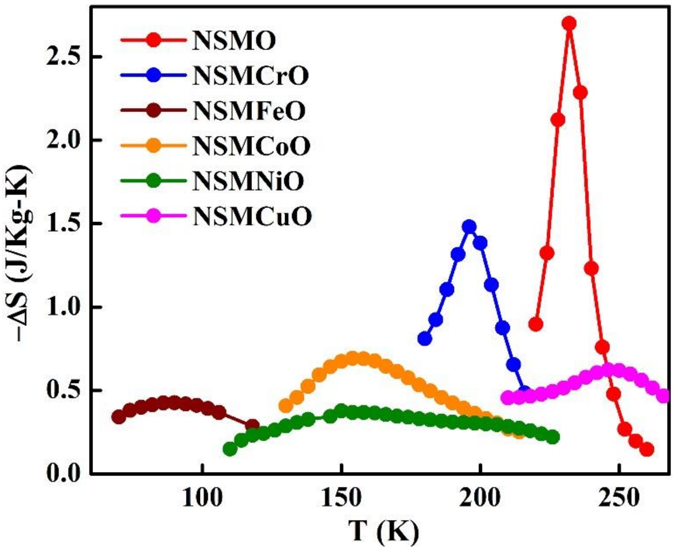

Fig. 4.10. *Magnetic entropy change of NSMTrO (Tr= Cr, Fe, Co, Ni and Cu) compounds under 10 kOe field change*

4.3.6. Critical exponent analysis

The analysis of critical exponent in the vicinity of the magnetic phase transition is a powerful tool to investigate the in-depth mechanisms that are responsible for the magnetic transition [238, 239] and magnetocaloric properties. The critical exponent β is associated with the spontaneous magnetization $M_s(0)$ below T_C, γ is associated with the inverse initial magnetic susceptibility ($\chi_0{}^{-1}$) above T_C and δ is related to the critical magnetization isotherm at T_C [240]. The β describes how the ordered moment grows below T_C and γ describes the divergence of the magnetic susceptibility above T_C. The values of β ranges from 0.25 to 0.5, for the mean-field (β = 0.5), 3D Heisenberg (β = 0.365), 3D Ising (β = 0.325) and tricritical mean-field model (β = 0.25). In the second-order magnetic phase transition near the T_C, the divergence in the correlation length leads to a universal scaling law characterized by a set of interrelated critical exponents comprising β, γ, and δ [241, 242]. According to the mean-field theory, the Arrott plots near T_C should comprise a series of straight lines at different temperatures, and the line that passes through the origin represents T_C. The regular Arrott plot showed that the relationship of M^2 versus H/M was based on the mean-field model of the critical exponents (β = 0.5 and γ = 1.0). According to the scaling hypothesis, the power-law dependences of $M_s(0)$, $\chi_0{}^{-1}$, and H with respect to the critical exponents β, γ, and δ are mathematically related as follows:

$$M_s(0) = m_0|\tau|^{\beta}, \tau < 0, T < T_C \tag{4.2}$$

$$\chi_0{}^{-1} = \left(\frac{h_0}{m_0}\right)|\tau|^{\gamma}, \tau > 0, T > T_C \tag{4.3}$$

$$H = A_0 M^{\delta}, \tau = 0, T = T_C, \tag{4.4}$$

where $\tau = \frac{T - T_C}{T_C}$, is the reduced temperature.

For the parent compound, the curves based on the Arrott plots were nonlinear, thereby indicating that the mean-field theory was not valid. Therefore, the values were determined using the modified Arrott plot (MAP) method, where $M^{1/\beta}$ was plotted against $(H/M)^{1/\gamma}$ [243]. In the MAP method, different values of β and γ were taken as trial exponents from various models, such as 3D-Heisenberg, 3D-Ising, and tricritical mean-field, and the values were fitted to the initial Arrott plot. The values obtained were fitted to the scaling equations (4.2) and (4.3), and the new values were calculated for β and γ. These new values were again used to obtain new MAPs, and this iterative process was continued until it converged to a stable value. The critical exponents calculated for NSMO were β= 0.178, T_C= 242.05 K (derived from Eq. (4.2)), γ= 0.715, and T_C= 242.17 K (derived from Eq. (4.3)), which were consistent with the predictions using the tricritical model. In fact, the critical exponents obtained for NSMTrO (Tr= Cr, Fe, and Co) were close to those obtained using the mean-field model. The MAP method could not apply to NSMNiO and NSMCuO compounds due to their high AFM nature. The spontaneous magnetization, M_s, was determined based on the intersection of the linear extrapolation of the straight line from a high field region toward the $M^{1/\beta}$ axis, and the inverse susceptibility $\chi_0{}^{-1}$ corresponded to the intersection of the linear extrapolation with the $(H/M)^{1/\gamma}$ axis. Fig 4.11 (a) shows the temperature dependence of M_S and $\chi_0{}^{-1}$ along with the power-law fitted to Eqs. (4.2) and (4.3). The value of M_S versus H on a log-log scale was determined based on Eq. (4.4), where it should be a straight line with slope 1/δ. The experimental values of δ were independently determined from the slope of the curve at T= T_C (as shown in Fig. 4.11 (b)). To confirm the consistency of the critical exponents obtained, we also calculated the value of δ using the Widom scaling relation [244]:

$$\delta = 1 + \frac{\gamma}{\beta} \tag{4.5}$$

where the values of β and γ were determined from the MAP and critical isotherm analysis. The calculated values of δ were close to the experimental value, thereby indicating the self-consistency and accuracy of the critical exponents, and thus the values obtained for β and γ appear to be reliable. The critical exponents β and γ calculated for parent compound were consistent with the predictions using the tricritical model, and they were close to the mean-field model for the substituted compounds. The critical exponents, as well as the critical parameters estimated using different models, are listed in Table 4.3. Furthermore, the reliability of the critical exponents can be examined based on the predictions of scaling theory. According to the scaling hypothesis, in the asymptotic critical region, the magnetic equation of state can be written as [245]:

$$M|\tau|^{-\beta} = f_{\pm} H|\tau|^{-(\beta+\gamma)} \tag{4.6}$$

where f_+ for $T > T_C$ and f_- for $T < T_C$ are regular analytical functions. According to Eq. (4.6), all the data points should fall on one of two curves, i.e., $T > T_C$ and $T < T_C$. Thus, the scaled data for the compounds were plotted on a log scale and found that all data points were on either side of the two divisions of the universal curves. Fig.4.11 (c) shows the M-H data points at high magnetic fields belonged to two universal branches for $T > T_C$ and $T < T_C$, respectively. Thus, the results confirmed the correctness of the critical exponents obtained in the present study. According to Oesterreicher *et al*. [246], the field dependence of ΔS_M can be expressed as:

$$\Delta S_{\mathrm{M}} \propto \mathrm{H}^{\mathrm{n}} \tag{4.7}$$

where n is an exponent that depends on the magnetic state of the sample.

For the mean-field model, the field dependence of ΔS_M at T_C corresponds to n = 2/3 [246]. A linear plot of $\ln(\Delta S_M)$ vs. ln(H) at T_C was constructed for all the compounds (shown in Fig. 4.11 (b)), and the value of n at T_C was calculated from the linear fit.

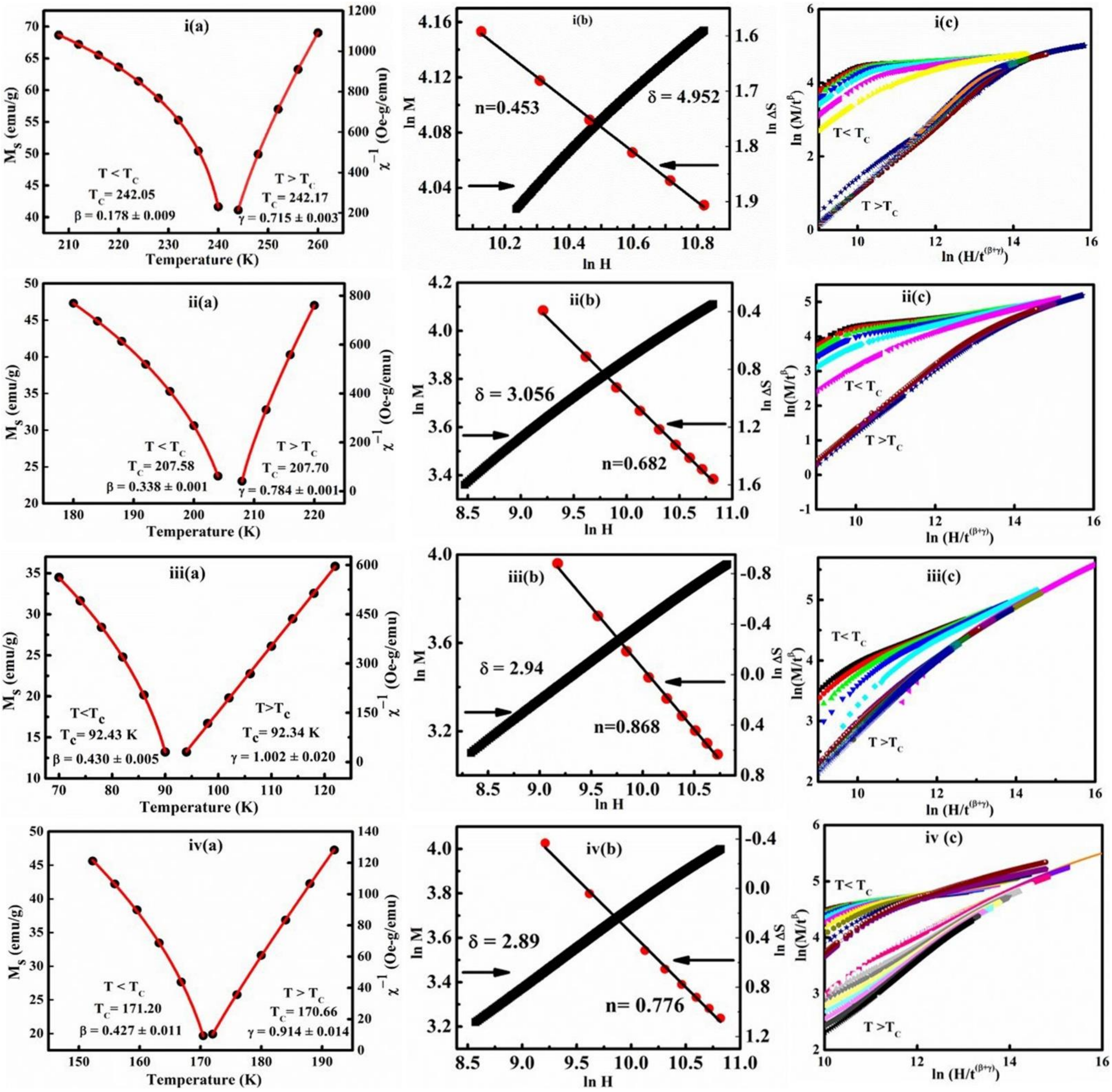

Fig. 4.11. *Compounds in this figure are in the following sequence: (i) NSMO, (ii) NSMCrO, (iii) NSMFeO, and (iv) NSMCoO. (a) Temperature dependence of the spontaneous magnetization* M_S *and the inverse initial susceptibility* χ_0^{-1} *as well as the fitted curves based on Eqs. (4.2) and (4.3). (b) Isothermal ln (M) vs. ln (H) plot at* T_C *and the field dependence of the magnetic entropy change on the ln-ln scale at* T_C *for the compounds. The values of* δ *the graph were obtained from the fitting of the ln (M)-ln (H) data. (c) Scaling plots [*$Mt^{-\beta}$ *vs.* $Ht^{-(\beta+\gamma)}$*] for the compounds below and above* T_C *on the ln-ln scale*

The critical exponents were calculated again using Eq. (4.8) and (4.9) [247], as follows.

$$n = 1 + \frac{1}{\delta}\left(1 - \frac{1}{\beta}\right) \tag{4.8}$$

$$n = 1 + \frac{\beta - 1}{\beta + \gamma} \tag{4.9}$$

The values of β, γ, and δ obtained using the MAP method and critical isotherm analysis were found to be good in agreement with those obtained based on the field dependence of the magnetic entropy change.

Samples		T_C(K)	β	γ	δ	Ref.
NSMO	MAP	242.06	0.176 ± 0.003	0.753 ± 0.006		
	CI (exp)				4.952±0.004	
	CI (cal)				5.278±0.080	This work
	Power law	242.05; 242.17	0.178 ± 0.009	0.715 ± 0.003	5.017±0.020	
NSMCrO	MAP	207.56	0.337 ± 0.002	0.784 ± 0.004		
	CI (exp)				3.185±0.008	
	CI (cal)				3.326±0.018	This work
	Power law	207.58; 207.70	0.338 ± 0.001	0.784 ± 0.001	3.320±0.007	
NSMFeO	MAP	92.19	0.436 ± 0.004	0.940 ± 0.013		
	CI (exp)				2.921±0.003	
	CI (cal)				3.156±0.035	This work
	Power law	92.43;92.34	0.430 ± 0.005	1.002± 0.020	3.330±0.053	
NSMCoO	MAP	170.28	0.431 ± 0.002	0.929 ± 0.006		
	CI (exp)				2.881±0.005	
	CI (cal)				3.155±0.017	This work
	Power law	171.20; 170.66	0.427± 0.011	0.914± 0.014	3.141±0.064	
Mean-field model			0.5	1.0	3.0	Ref. 248
3D Heisenberg model			0.365	1.336	4.80	Ref. 248
3D Ising model			0.325	1.24	4.82	Ref. 248
Tricritical model			0.25	1.0	5.0	Ref. 248

Abbreviation: CI (exp) - δ values obtained by Critical Isotherm fitting; CI (cal) - δ values calculated directly according to the Widom scaling relationship $\delta = 1 + \frac{\gamma}{\beta}$

Table 4.3. *Critical exponents obtained in this study using several methods and comparison with different theoretical models*

4.4. Conclusion

- In this study, we conducted a comprehensive analysis of the magnetic phase transitions and critical behaviour with substitution of 10 at. % of Cr, Fe, Co, Ni and Cu at the Mn site in $Nd_{0.67}Sr_{0.33}MnO_3$, and the following observations are drawn.
- The orthorhombic crystal structure of the parent compound remains unaltered with the substitution, which was confirmed by Rietveld refinement.
- The T_C decreases with the substitution of Tr- elements except in the case of NSMCuO compound. Substitution of Tr-elements has broadened the FM-PM transition leading to the suppression of the magnetocaloric effect.
- The critical exponents of the parent compound were consistent with the predictions of the tricritical model, whereas the critical exponents of Cr-, Fe-, and Co-substituted compounds were close to those with the mean-field model.
- The critical exponents calculated using the MAP method and critical isotherm analysis were in good agreement with those obtained based on the field dependence of ΔS_M.

Chapter 5

Impact of Nd/Sr-site deficiencies on the structural, magnetic and electrical transport properties in $Nd_{0.67}Sr_{0.33}MnO_3$ manganite

Impact of Nd and Sr-site deficiencies on the structural, magnetic and electrical transport properties in bulk $Nd_{0.67-x}Sr_{0.33}MnO_{3-\delta}$ (x = 0.09, 0.17, 0.25, 0.33) and $Nd_{0.67}Sr_{0.33-y}MnO_{3-\delta}$ (y = 0.09, 0.17) manganites were discussed in this chapter. Among the studied compounds, $Nd_{0.67-x}Sr_{0.33}MnO_{3-\delta}$ (x= 0.17) composition shows a significant enhancement in magnetization and decrease in electrical resistivity values than that of its pristine compound. Further, nanocrystalline $Nd_{0.67-x}Sr_{0.33}MnO_{3-\delta}$ (x= 0.17) compound was synthesized, and the structural, magnetic, magnetocaloric properties have been systematically studied and compared with that of its bulk counterpart. The bulk $Nd_{0.67-x}Sr_{0.33}MnO_{3-\delta}$ (x= 0.17) compound shows maximum $-\Delta S_M$ value of 1.65 J kg^{-1} K^{-1} and 4.89 J kg^{-1} K^{-1} at 275 K for 10 kOe and 50 KOe field change, which could be a potential candidate for sub-room temperature applications.

5.1. Introduction

In the recent past, it has been reported that the creation of deficiency at the A and A$'$-sites in mixed-valence manganites alter the ratio of Mn^{3+}/Mn^{4+} and thereby produces significant changes in the magnetic properties [199, 202, 249-256]. In the present chapter, we have studied the effect of Nd and Sr-deficiencies on the structural, magnetic and electrical transport properties of bulk $Nd_{0.67-x}Sr_{0.33}MnO_{3-\delta}$ (x=0.09, 0.17, 0.25, 0.33) and $Nd_{0.67}Sr_{0.33-y}MnO_{3-\delta}$ (y =0.09, 0.17) manganites and their properties are compared. $Nd_{0.67-x}Sr_{0.33}MnO_{3-\delta}$ with x=0.09, 0.17, 0.25, 0.33 and $Nd_{0.67}Sr_{0.33-y}MnO_{3-\delta}$ with y =0.09, 0.17 compounds were synthesized using solid-state route and their magnetic and electric transport properties have been explored. Further, nanocrystalline $Nd_{0.67-x}Sr_{0.33}MnO_{3-\delta}$ (x = 0.17) compound was synthesized by sol-gel route, and the structural, magnetic and magnetocaloric properties have been systematically studied and compared with that of its bulk counterpart.

5.2. Experimental

All the compounds were synthesized using the conventional solid-state method. Compounds such as $Nd_{0.67-x}Sr_{0.33}MnO_{3-\delta}$ (x= 0.09, 0.17, 0.25 and 0.33) are termed as Nd-0.09, Nd-0.17, Nd-0.25, Nd-0.33 respectively. $Nd_{0.67}Sr_{0.33-y}MnO_{3-\delta}$ (y= 0.09 and 0.17) are termed as Sr-0.09 and Sr-0.17 respectively. Later, the nanocrystalline Nd-0.17 compound was prepared using the sol-gel technique. The details of the preparation methods are the same as those mentioned in the previous chapters. The structural analysis was done by XRD technique, and Fullprof software was used for the refinement analysis. The Iodometric titration method was performed to estimate the oxygen stoichiometry [257, 258]. The morphological analysis of bulk and nanocrystalline compounds were investigated by SEM and TEM, and homogeneity was checked by EDAX analysis. The stoichiometry of the compounds was confirmed by EDXRF analysis. The XAS was performed using total electron yield mode under chamber base pressure of ~ 10^{-9} Torr (National Synchrotron Radiation Research facility, Taiwan). Magnetic properties and electrical resistivity were measured using vibrating sample magnetometer and electrical transport option attached to the physical property measurement system.

5.3. Results and discussion

5.3.1. Impact of Nd/Sr-site deficiencies on the structural, magnetic and electrical transport properties in Nd-0.09, Nd-0.17, Nd-0.25, Nd-0.33, Sr-0.09 and Sr-0.17 compounds

5.3.1.1. Structural analysis

The crystal structure and cell parameters of all Nd/Sr- deficient compounds were studied and analyzed by XRD technique. The refined XRD patterns obtained from the Rietveld analysis are shown in Fig. 5.1(a)-(f), and the structural parameters obtained are shown in Table 5.1. The refined patterns confirm that all the compounds belong to the orthorhombic crystal symmetry (Pbnm space group) with an impurity phase of rhombohedral Mn_3O_4 [259]. The secondary phase, Mn_3O_4, is ferrimagnetic and may be formed due to preparation conditions, creation of deficiency etc. From the XRD patterns, it can be seen that the concentration of the secondary phase vary with the deficiency content, but according to reference [260] it does not affect the stoichiometry of the compounds significantly. The refinement of all the compounds was analysed by the quality factor χ^2, where the values are higher than that of the pristine compound due to the presence of the secondary phase. From Table. 5.1, it can be seen that the Nd-deficient compounds have less cell volume, whereas Sr-deficient compounds have greater cell volume than that of the pristine compound. The creation of deficiency at the A-site changes the concentration of Mn^{3+}/Mn^{4+} ions. The concentration of Mn^{4+} increases in the case of Nd-deficient compounds while the concentration of Mn^{3+} increases in case of Sr-deficient compounds. Based on the charge neutrality, the Nd/Sr-deficient compounds can be written as $Nd^{3+}_{0.67-X}\square_X Sr^{2+}_{0.33}\, Mn^{3+}_{0.67-3X} Mn^{4+}_{0.33+3X} O^{2-}_3$ and $Nd^{3+}_{0.67} Sr^{2+}_{0.33-X}\, \square_X Mn^{3+}_{0.67-2X} Mn^{4+}_{0.33+2X} O^{2-}_3$

respectively. Thus in Nd-deficient compounds, the Mn^{3+} content decreases by a factor of (0.67-3X) and Mn^{4+} content increases by a factor of (0.33+3X). Similarly, for Sr-deficient compounds, the Mn^{3+} and Mn^{4+} contents are changed by a factor of (0.67-2X) and (0.33+2X) respectively. The increase in unit cell volume of Sr-deficient compounds cannot be explained based on Mn^{3+}/Mn^{4+} ratio alone, but it may be related to the average ionic radius of the A-site $<r_A>$ and the anionic vacancies. Due to the electrostatic repulsion force, the radius of the Sr-deficient site (1.547 Å) is greater than the radius of the actual Sr-site (1.44 Å), which eventually leads to an increased unit cell volume in case of Sr-deficient compounds.

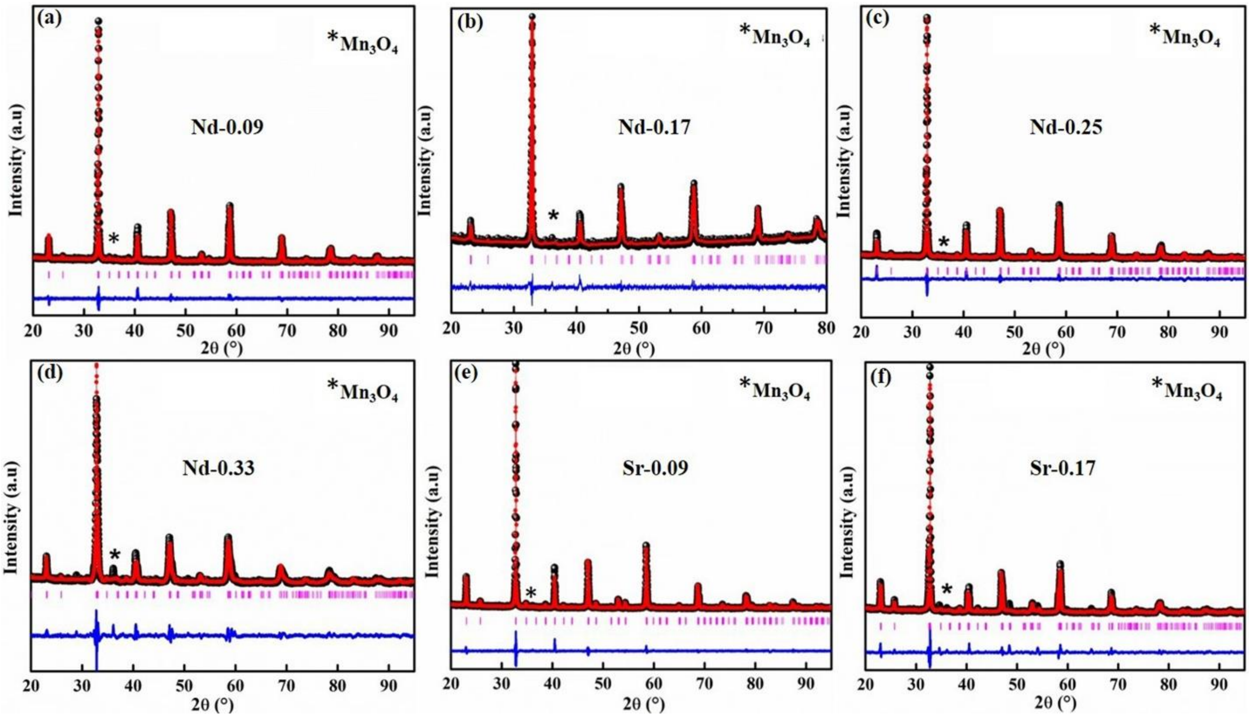

***Fig. 5.1**. Rietveld refined XRD patterns of (a) Nd-0.09, (b) Nd-0.17, (c) Nd-0.25, (d) Nd-0.33,(e) Sr-0.09 and (f) Sr-0.17 compounds*

The amount of oxygen content was estimated from the iodometric titration [257, 258] method. Powders were weighed and dissolved in a mixture of 10 ml of 10 mass % potassium iodide aqueous solution and 2.5 ml of 2 M hydrochloric acid. The iodine liberated in the reaction was titrated against 0.1 N sodium thiosulphate standard volumetric solution, and starch solution (1 mass %) was used as an indicator. The value of α was determined by the iodometric titration method, and the average ratio of Mn^{3+}/Mn^{4+} was calculated for 5 titrations. The amount of oxygen content was estimated from the iodometric titration using the equation as [257, 258]

$$3 \pm \delta = \frac{17+3\alpha}{6} - x \qquad (5.1)$$

The oxygen stoichiometry is found to be 2.94, 2.90, 2.86, 2.82, 2.95 and 2.91 for Nd-0.09, Nd-0.17, Nd-0.25, Nd-0.33, Sr-0.09 and Sr-0.17 compounds respectively within the limits of experimental error.

	Nd-0.09	**Nd-0.17**	**Nd-0.25**	**Nd-0.33**	**Sr-0.09**	**Sr-0.17**
Cell parameters						
a (Å)	5.4669(1)	5.4679(2)	5.4675(1)	5.4123(5)	5.4615(1)	5.4996(2)
b (Å)	5.4413(1)	5.4367(1)	5.4413(2)	5.4626(5)	5.4663(1)	5.1547(2)
c (Å)	7.6873(2)	7.6743(1)	7.6880(2)	7.7227(6)	7.7143(1)	7.7088(3)
V ($Å^3$)	228.67(1)	228.21(2)	228.72(1)	228.32(3)	230.30(1)	231.25(1)
Positional parameters						
Nd/Sr x	0.4977(10)	0.5003(2)	0.4982(9)	0.4991(18)	0.4960(10)	0.5122(6)
Nd/Sr y	0.0176(3)	0.0181(2)	0.0177(3)	0.0230(6)	0.0261(2)	0.0170(5)
O1 x	0.5500(30)	0.5612(6)	0.5534(19)	0.5250(40)	0.5630(40)	0.5030(70)
O1 y	0.5000(20)	0.4988(21)	0.4910(20)	0.5030(20)	0.4905(16)	0.4150(40)
O2 x	0.2140(20)	0.2133(20)	0.2063(19)	0.2140(50)	0.2150(40)	0.2120(20)
O2 y	0.2999(19)	0.2868(11)	0.2930(20)	0.2680(60)	0.2860(40)	0.2640(40)
O2 z	0.0255(0)	0.0258(10)	0.0424(0)	0.0654(12)	0.0323(20)	0.0474(12)
Occupancy/ Atomic displacement parameter						
Nd	0.5782/0.0212	0.4961/0.0149	0.4161/0.0182	0.3321/0.0141	0.6632/0.0421	0.6624/0.0114
Sr	0.3284/ 0.0212	0.3273/0.0149	0.3281/0.0182	0.3206/0.0141	0.2352/0.0421	0.1512/0.0114
Mn	0.9982/0.0327	0.9974/0.0231	0.9971/0.0421	0.9974/0.0253	0.9984/0.0212	0.9974/ 0.0218
.O1	0.9874/0.0021	0.9821/0.0121	0.9784/0.0623	0.9662/0.0134	0.9921/0.0252	0.9832/0.0462
O2	0.9912/0.0141	0.9842/0.0412	0.9821/0.0143	0.9702/0.0562	0.9824/0.0432	0.9846/0.0248
Bond distance (Å)						
Mn-O1	1.941(2)	1.932(2)	1.945(2)	1.935(2)	1.960(4)	1.982(5)
Mn-O2	1.915(11)	1.941(12)	1.980(11)	1.934(30)	1.963(22)	1.889(18)
Mn-O2	2.017(10)	1.987(12)	1.988(10)	2.063(29)	1.971(22)	2.073(16)
Bond angle (°)						
Mn-O1-Mn	157.4(9)	159.6(5)	162.5(9)	171.9(14)	159.5(14)	152.9(25)
Mn-O2-Mn	163.8(12)	160.2(3)	152.8(8)	148.3(24)	158.3(20)	171.5(7)
Agreement factors						
R_{WP}	4.06	4.03	4.48	5.94	3.91	5.65
R_P	3.02	3.14	3.05	4.26	2.83	3.86
χ^2	2.13	1.4	3.9	7.06	2.87	6.00

Table 5.1. *Structural parameters of the deficient compounds obtained from the refinement analysis*

Since the Mn-ionic radius is inversely proportional to the Mn-oxidation state, the unit cell volume increases with increase in oxygen deficiency, and this trend is valid for the Sr-deficient compounds. However, for the Nd-deficient compounds, the unit cell volume shows a decreasing trend up to the Nd-0.17 composition and then increases for Nd-0.25 composition and again decreases with further increase in Nd-deficiency. Due to the smaller ionic radius of Mn^{4+} (0.53 Å) compared to Mn^{3+} (0.645 Å), the decrease in unit cell volume of Nd-deficient compounds may be attributed to the increase in the number of Mn^{4+} ions. However, with the increase of Nd-deficiency, the ratio of the impurity phase of Mn_3O_4 phase is increasing for Nd-0.25 and Nd-0.33 compounds, which can be confirmed from the Rietveld refinement analysis. Since the unit cell of Mn_3O_4 is larger, it would induce the expansion of the neighbouring NSMO cell, resulting in the change of Mn-O bond length, Mn-O-Mn bond angle and hence results in the distortion of the MnO_6 octahedra.

5.3.1.2. XAS analysis

The variation of electronic structure and oxidation states of Mn and oxygen is analysed by Mn L-edge and O K-edge using XAS technique. The room temperature XAS spectra were taken and normalized for comparison and are shown in Fig. 5.2. Fig. 5.2(a) and 5.2 (b) represents the Mn L-edge spectra of Nd-deficient, and Sr-deficient compounds respectively. For better understanding of the valence state of Mn-ions, the spectra are compared with that of the reference samples such as MnO, Mn_2O_3 and MnO_2. Moreover, the presence of multiple peaks indicates the vital information about the local electronic structure of the compounds. The Mn L-edge spectra of all the compounds show two peaks around 642 eV and 653 eV due to the spin-orbit coupling. These peaks are labelled as L_{III} and L_{II} respectively. For MnO, Mn_2O_3 and MnO_2, the maximum of L_{III} peak is located at 639.9 eV, 641.7 eV and 643.3 eV respectively. However, for all the compounds except Sr-0.17, the L_{III} peak falls between 641.7 eV and 643.3 eV, confirm the superposition of Mn^{3+} and Mn^{4+} states [227]. However, for Sr-0.17 compound, the average Mn valence is near to Mn^{3+} state. The effective ionic valence of Mn-ions is calculated via the interpolation method and is depicted in Fig. 5.3. A graph is plotted between the energy of the photon and Mn-oxidation state, and the effective ionic valences of all the deficient compounds are calculated. From the graph, it can be seen that the concentration of Mn^{4+} ions is greater for Nd-0.17 compound while the concentration of Mn^{3+} ions is greater for Sr-0.17 compound. These results are in corroboration with the lattice parameters obtained from the XRD analysis.

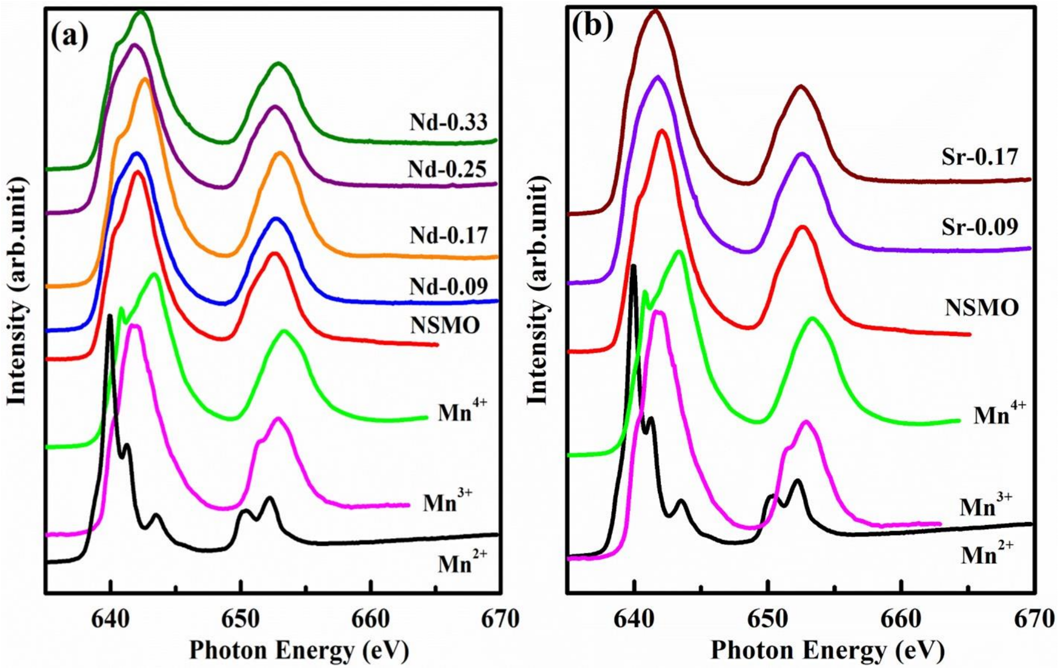

***Fig 5.2**. Mn 2p XAS images of (a) Nd-deficient compounds and (b) Sr-deficient compounds*

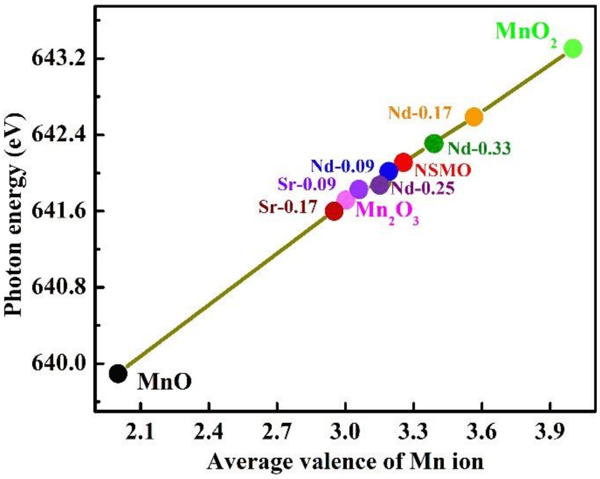

***Fig. 5.3.** Variation of photon energy with an average valence of Mn-ions for the deficient compounds*

5.3.1.3. Surface morphology

To analyse the surface morphology of the Nd/Sr-deficient compounds, the microstructure was studied using SEM and are shown in Fig. 5.4. As a representative of the series, the micrographs of Nd-0.09, Nd-0.25, Sr-0.09 and Sr-0.17 are shown in the figure. The average grain size of Nd-deficient compounds is less than 2 μm, and for Sr-deficient compounds, it is around 2-10 μm range. Moreover, the Sr-deficient compounds are more porous than Nd-deficient compounds. As a representative of the series, the homogeneity of Nd-0.09, Nd-0.25 and Nd-0.33 compounds were analysed using EDAX analysis and shown in Fig. 5.5. The EDAX spectrum shows the signals of Nd, Sr, Mn and O, and no additional peaks were detected which confirm that no extra elements were present in these compounds.

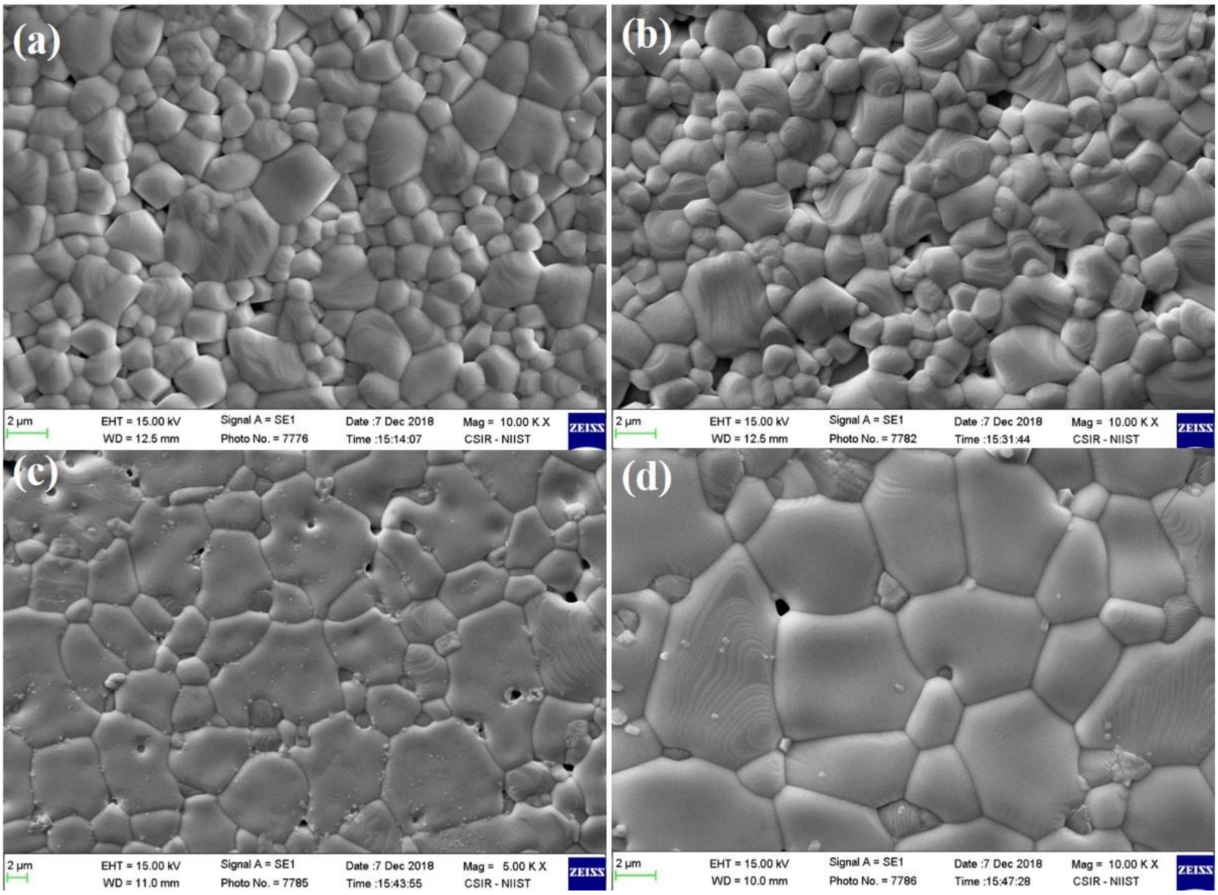

Fig. 5.4. *SEM images (a) Nd-0.09, (b) Nd-0.25, (c) Sr-0.09 and (d) Sr-0.17 compounds*

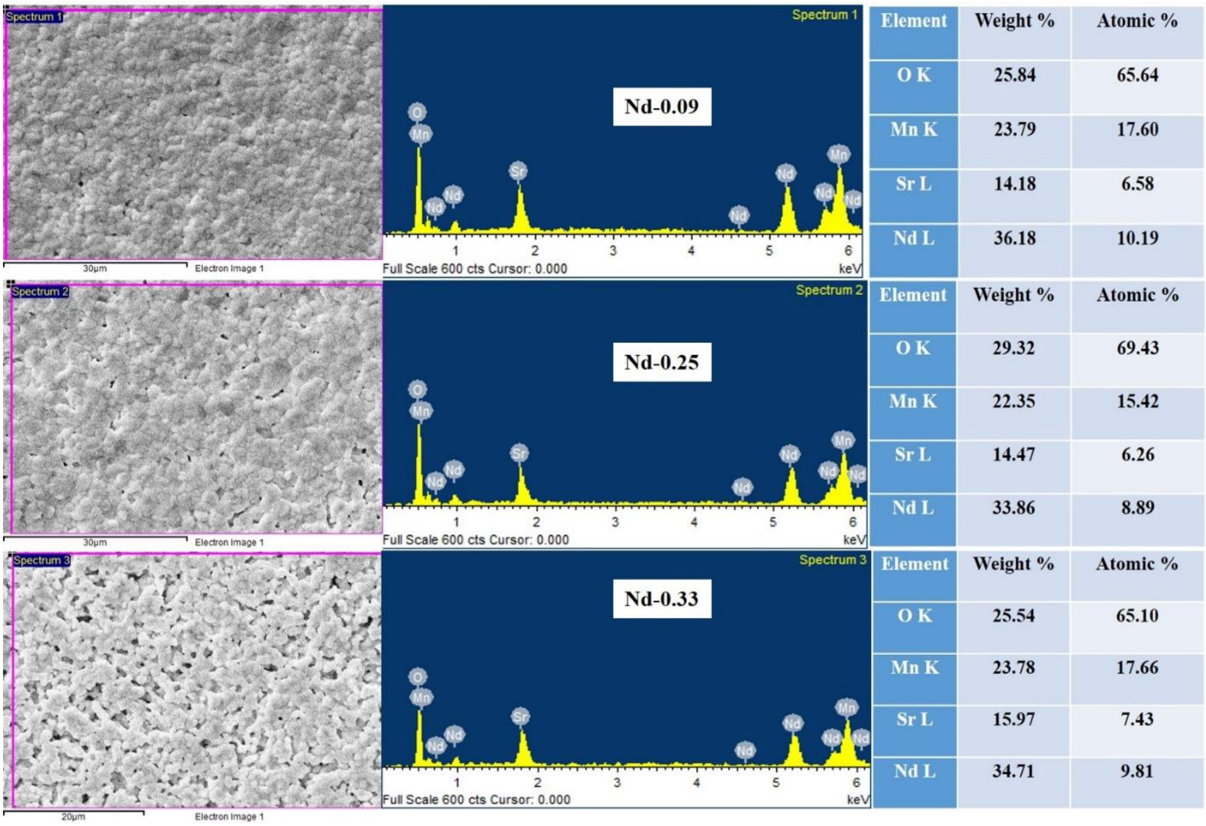

Element	Weight %	Atomic %
O K	25.84	65.64
Mn K	23.79	17.60
Sr L	14.18	6.58
Nd L	36.18	10.19

Element	Weight %	Atomic %
O K	29.32	69.43
Mn K	22.35	15.42
Sr L	14.47	6.26
Nd L	33.86	8.89

Element	Weight %	Atomic %
O K	25.54	65.10
Mn K	23.78	17.66
Sr L	15.97	7.43
Nd L	34.71	9.81

Fig. 5.5. *SEM-EDAX and composition of Nd-0.09, Nd-0.25 and Nd-0.33 compounds*

5.3.1.4. Magnetic characterization

To study the magnetic behaviour with Nd/Sr-deficiency, the temperature dependence of magnetization was measured from 2-300 K in ZFC and FC modes under 50 Oe field. The M(T) curves of Nd-deficient and Sr-deficient compounds are shown in Fig. 5.6(a) and 5.6(b) along with the M(T) curve of pristine compound. It is found that all the deficient compounds undergo a FM-PM transition similar to that of the pristine compound, but with an increase in T_C with the increase in Nd-deficiency and a decrease in T_C with the increase of Sr-deficiency. The variation in T_C of all the deficient compounds is due to the variation in the Goldschmidt tolerance factor and the variation in the DE interactions. The changes in average A-site cationic radius and changes in the B-site cationic radius due to the Mn^{3+}/Mn^{4+} concentration, in turn, affects the tolerance factor.

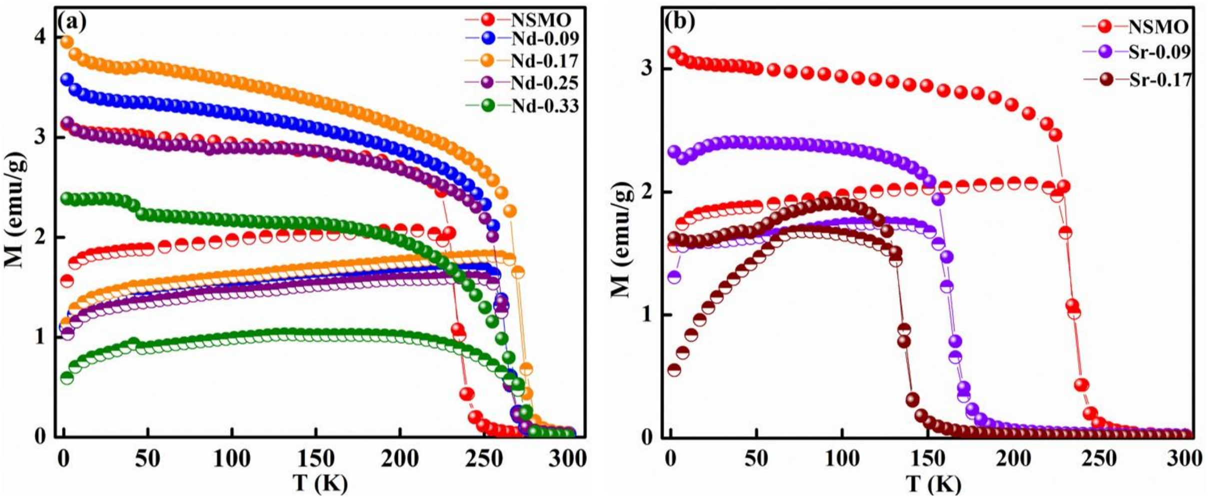

Fig. 5.6. *Temperature variation of magnetization of (a) Nd-deficient compounds and (b) Sr-deficient compounds measured under 50 Oe field*

From Table 5.2, we can see that the average A-site ionic radius and tolerance factor of Nd-deficient compounds decreases while that of Sr-deficient compounds increases with increase in deficiency content. Thus, in Nd-deficient compounds, T_C increases due to the reduction in tolerance factor. However, in Sr-deficient compounds, the average A-site radius and tolerance factor increases due to the increased ionic radius of Sr-deficient site (1.547 Å) and hence Tc decreases. Further, a significant reduction in magnetization values is noted in Sr-deficient compounds, while the magnetization of Nd-deficient compounds shows a parabolic behaviour with maximum magnetization observed for Nd-0.17 compound. For Nd-deficient compounds, the magnetization value increases with increase in deficiency up to Nd-0.17 composition and then decreases further for Nd-0.25 and Nd-0.33 composition. From the XAS analysis, it can be seen that the concentration of Mn^{4+} ions is greater for Nd-0.17 compound. Thus, the increase in the magnetization of Nd-0.17 compound may be attributed to the increase in the DE interaction because of the presence of more number of Mn^{4+} ions in the compound. It is confirmed from the Rietveld refinement that the ratio of the impurity phase of Mn_3O_4 is increases for Nd-0.25 and Nd-0.33 compounds. Since Mn_3O_4 is ferrimagnetic, the net magnetization of the Nd-0.25 and Nd-0.33 compounds decreases. For all the deficient compounds, large thermo-magnetic irreversibility is witnessed between the ZFC and FC curves, which may be attributed to the existence of competing magnetic states in the compounds. All the deficient compounds show a hump-like feature below 50 K, which is due to the ordering of the Mn_3O_4 phase. This ordering is more prominent with the increase in the concentration of deficiency at Nd and Sr-sites due to the increase in the Mn_3O_4 phase, which is in corroboration with the XRD analysis. A graph is plotted between the derivative of M (dM/dT) versus T (not shown) and the T_C of the deficient compounds are calculated from the graph where the peak shows a minimum value.

	Nd-0.09	**Nd-0.17**	**Nd-0.25**	**Nd-0.33**	**Sr-0.09**	**Sr-0.17**
average A-site radius (Å)	1.0453	0.9667	0.8881	0.8094	1.1434	1.520
tolerance factor	0.8750	0.8589	0.8423	0.8252	0.9054	0.9170
μ_{eff}^{theo} (μ_B)	5.12	4.79	4.44	4.07	5.31	5.17
μ_{eff}^{meas} (μ_B)	5.98	5.91	6.64	5.24	7.62	7.50

Table 5.2. *Average A-site ionic radius, tolerance factor, experimental effective magnetic moment* $\mu_{eff,}^{meas}$ *the theoretical effective magnetic moment* μ_{eff}^{th} *of the compounds*

It is being observed that the Nd-deficient compounds show greater values of T_C and the Sr-deficient compounds show smaller T_C values than that of the pristine compound. The T_C values of Nd-0.09, Nd-0.17, Nd-0.25 and Nd-0.33 are 266 K, 275 K, 264 K and 270 K respectively and for Sr-0.09 and Sr-0.17, it is 162 K and 136 K respectively. The increased T_C of the Nd-deficient compounds may be due to the increased FM ordering with the increase in DE interactions due to the presence of increased number of Mn^{4+} ions and the decreased T_C in Sr-deficient compounds may be due to the increase in AFM ordering caused by increased SE interactions due to the presence of more Mn^{3+} ions. Therefore, it is understood that the competing exchange interactions between DE and SE interactions severely affects the magnetic properties in the Nd and Sr-site deficient compounds. The T_C of the deficient compounds is related to the competing interaction between the FM ordering due to DE interaction and AFM ordering due to the SE interaction. Thus the T_C values obtained is in good agreement with the observations from the XAS measurement.

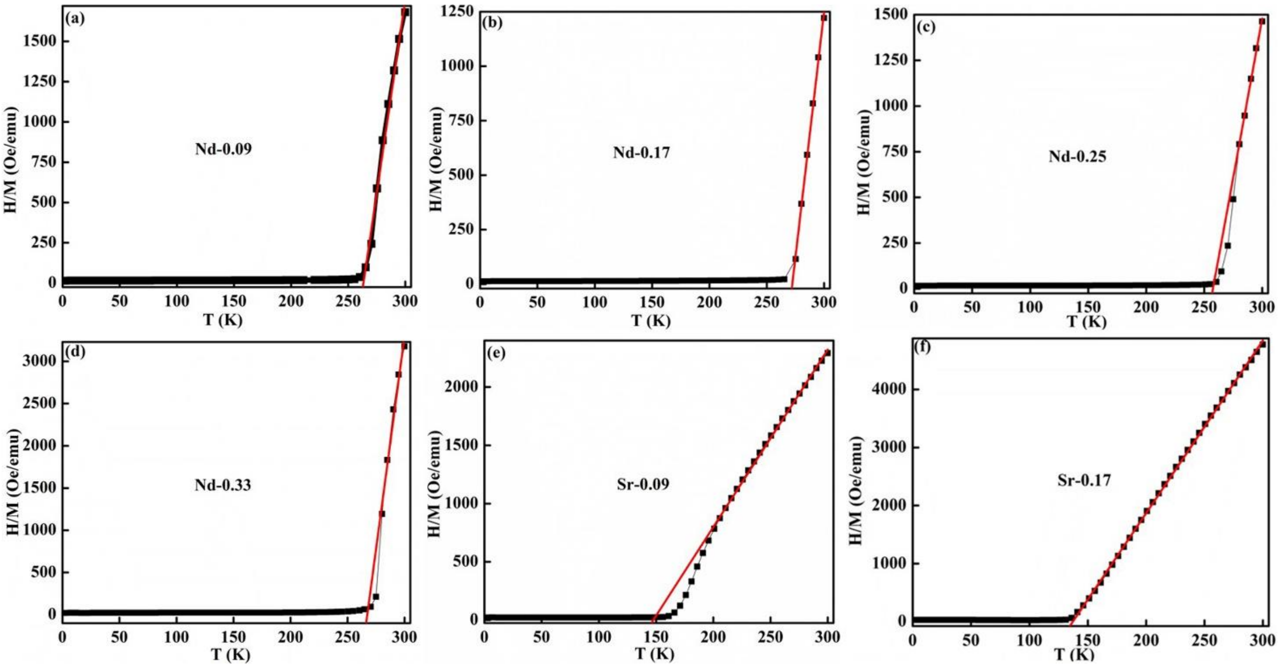

Fig. 5.7. *Inverse magnetic susceptibility along with linear fit to Curie-Weiss law in the high temperature region of (a) Nd-0.09, (b) Nd-0.17, (c) Nd-0.25, (d) Nd-0.33, (e) Sr-0.09 and (f) Sr-0.17 compounds*

The inverse magnetic susceptibility χ^{-1} as a function of temperature was analyzed and is shown in Fig. 5.7. According to the Curie-Weiss law, the magnetic susceptibility should obey the following equation (5.2) for $T > T_C$, and it can be written as [261]

$$\chi = \frac{C}{T-\theta} \tag{5.2}$$

where θ is known as Curie-Weiss temperature and is determined from the point at which χ^{-1} intercepts the temperature axis and C is the Curie constant. After the determination of C, the experimental effective magnetic moment (μ_{eff}^{meas}) is calculated from the equation as follows

$$C = \frac{1}{3k_B}\frac{N_a}{M_m}\mu_{eff}^{meas\,2}\mu_B^2 \tag{5.3}$$

where, k_B is the Boltzmann constant, μ_B is the Bohr magneton, N_a is the Avogadro number and M_m is the molecular formula weight. The theoretical effective magnetic moment μ_{eff}^{th} of Nd-deficient and Sr-deficient compounds is calculated as follows

$$\mu_{eff}^{th}(\mu_B) =$$

$$\sqrt{(0.67\text{-}x)\left[\mu_{eff}^{th}(\mathrm{Nd}^{3+})\right]^2 + (0.67\text{-}3x)\left[\mu_{eff}^{th}(\mathrm{Mn}^{3+})\right]^2 + (0.33 + 3x)\left[\mu_{eff}^{th}(\mathrm{Mn}^{4+})\right]^2}$$

and $\sqrt{(0.67)\left[\mu_{eff}^{th}(\mathrm{Nd}^{3+})\right]^2 + (0.67 - 2x)\left[\mu_{eff}^{th}(Mn^{3+})\right]^2 + (0.33 + 2x)\left[\mu_{eff}^{th}(Mn^{4+})\right]^2}$

(5.4)

with $\mu_{eff}^{th}(\mathrm{Mn}^{3+}) \sim 4.90\mu_B$, $\mu_{eff}^{th}(\mathrm{Mn}^{4+}) \sim 3.87\mu_B$, $\mu_{eff}^{th}(\mathrm{Nd}^{3+}) \sim 3.62\mu_B$ and x is the deficiency at the Nd and Sr-sites. Table. 5.2 shows a comparison of μ_{eff}^{meas} value with μ_{eff}^{th}value for all the deficient compounds and the discrepancy between the values may be due to the presence of FM clusters in the PM matrix. Further, the magnetization as a function of the field at 2 K is measured for all the deficient compounds and is shown in Fig. 5.8. The inset shows the magnified view of the hysteresis loop, and all the compounds show a soft ferromagnetic nature. At lower fields, the magnetization increases abruptly which then increases slowly at higher fields and does not saturate even at fields of 90 KOe. It further confirms the existence of FM and AFM phases in all the compounds, where the FM phases get responses quickly at the lower fields while the AFM phases respond slowly resulting in non-saturating tendency even at such higher fields. The highest magnetization value is observed for Nd-0.17 compound due to increase in DE interactions. Thus, the changes in the relative ratio between $\mathrm{Mn}^{3+}/\mathrm{Mn}^{4+}$ and the competing interactions between the FM and AFM phases with the creation of deficiency, in turn, affects the magnetization values. Even though the Mn^{4+} content is greater for Nd-0.33 compound, the presence of prominent ferrimagnetic Mn_3O_4 secondary phases reduces the magnetization value at 2 K.

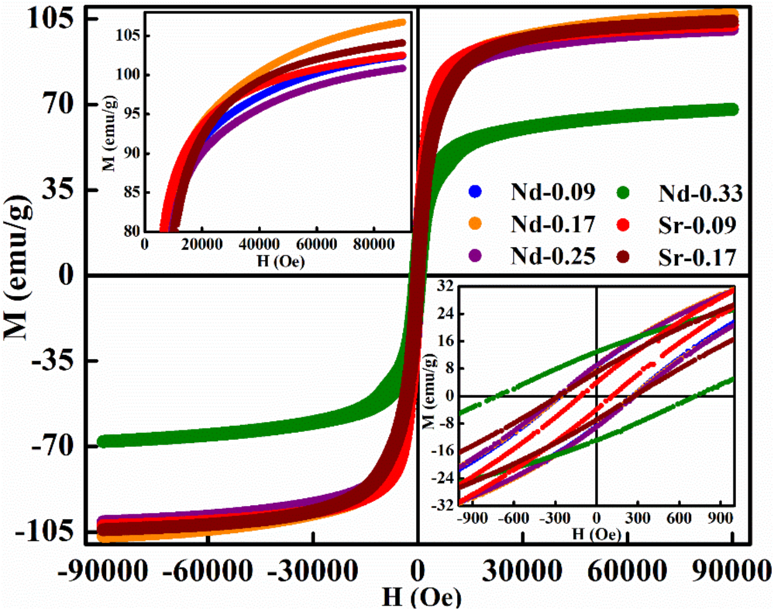

Fig. 5.8. M-H loops of Nd/Sr- deficient compounds at 2 K. The bottom insets show the enlarged view of the H_C, and the upper insets show the enlarged view of variation in magnetization

5.3.1.5. Electrical transport properties

To understand the transport behaviour in the deficient compounds, the temperature variation of electrical resistivity is studied under different magnetic fields and is depicted in Fig. 5.9. The pristine compound shows a sharp metal to insulator transition temperature (T_P) around 243 K, while the Nd-0.09 and Nd-0.17 compounds do not show a sharp metal to insulator transition character, but shows an anomalous double peak behaviour. On lowering the temperature, Nd-0.09 and Nd-0.17 compounds show a sharp peak T_{P1} followed by a broad peak T_{P2} and a low-temperature upturn T_m. The anomalous double peak behaviour witnessed in these Nd-deficient compounds may be due to the coexistence of different phases such as FM metallic (FMM), FM insulator (FMI) and AFM insulator (AFMI) phases [262]. The temperature and magnetic field influence the fraction of each phase [263]. These coexisting phases are induced by the electronic inhomogeneity in the deficient compounds and are more prominent in the absence of magnetic fields. The double peak behaviour in Nd-0.09 and Nd-0.17 compounds could be due to these electronic phase separation. However, Nd-0.09 and Nd-0.17 compounds show broadened transition below T_C due to the increase in the percolation path between FMM phases. Further, at higher fields, the double peak nature weakens and disappears due to the complete transformation of FMI phases into FMM phases.

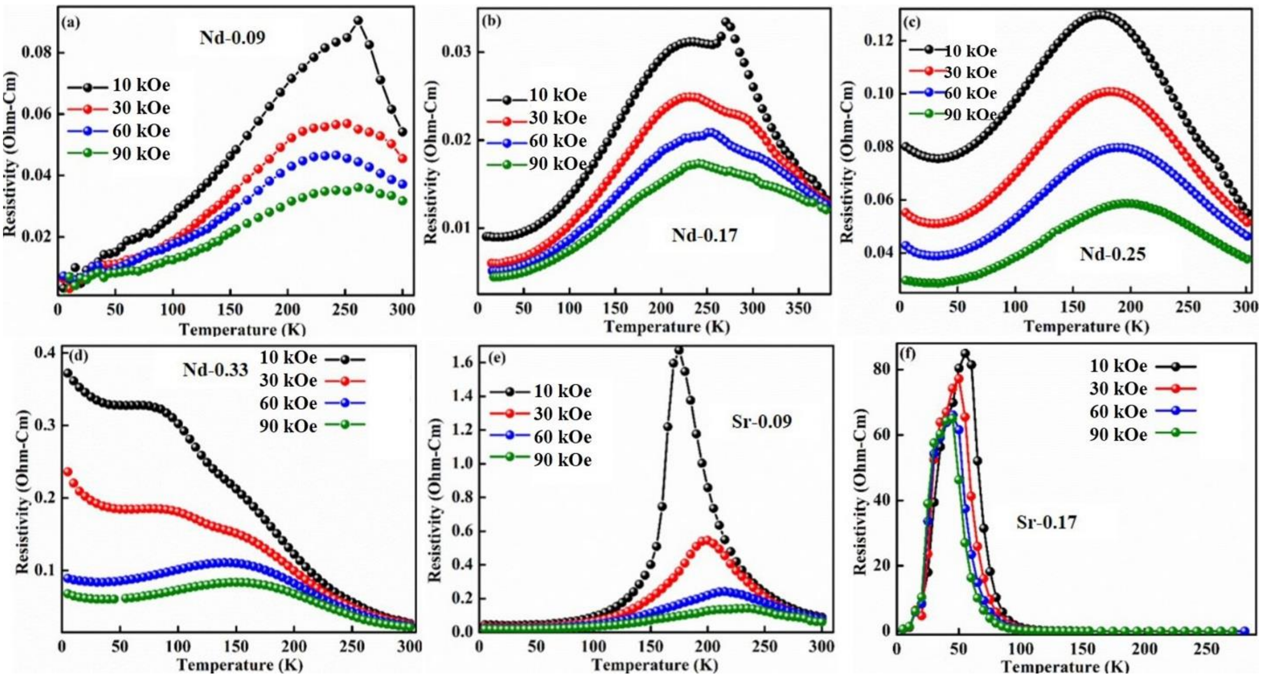

Fig. 5.9. *Temperature variation of electrical resistivity of (a) Nd-0.09, (b) Nd-0.17, (c) Nd-0.25, (d) Nd-0.33, (e) Sr-0.09 and (f) Sr-0.17 compounds measured under different magnetic fields*

The coexisting phases of FMM, FMI and AFMI are not prominent in the remaining compounds due to the less number of trapped mobile electrons at the deficient sites. Hence the double peak is not seen in the metal-insulator transition region of the remaining deficient compounds. The sharp peak at T_{P1} disappears, the broadness of transition temperature increases and more prominent T_m is witnessed for Nd-0.25 compound. However, with further increase in deficiency, the broadness of the peak is reduced for Nd-deficient compounds. The T_P value of the Nd-deficient compounds increases with increase in Nd-deficiency up to Nd-0.17 and decreases thereafter with further increase in Nd-deficiency. Similarly, the T_P value of Sr-0.09 and Sr-0.17 decreases with increase in Sr-deficiency, and the trend is similar to that of the magnetic transition temperature of the Sr-deficient compound. In comparison to the pristine compound, Nd-deficient compounds show a decrease in resistivity up to the concentration of Nd-0.17 and then increases with further increase in the deficiency. The increase in resistivity for higher concentrations of Nd-deficient compounds can be understood due to the increase in Mn_3O_4 concentration which is in corroboration with the XRD data. Thus the electrical resistivity of Nd-deficient compounds follows the same trend as that of the magnetization measurements. On the other hand, the resistivity value of Sr-0.09 is increased by one order and by two orders in case of Sr-0.17 in comparison to the pristine compound. Again, the resistivity value of each compound decreases with the increase in the magnetic field due to the magnetic spin ordering caused by the field. The increase in DE interactions in Nd-0.09 and Nd-0.17 compounds increase the ferromagnetism and electrical conductivity, while the dominance of SE interaction over the DE in rest of the Nd-deficient series decreases the ferromagnetic nature and results in a corresponding increase in the electrical resistivity as evident from the transport properties. Similarly, the increase in SE interactions in Sr-0.09 and Sr-0.17 compounds decreases the ferromagnetism and electrical conductivity.

Hence, from the above results on both Nd and Sr deficiency in $Nd_{0.67-x}Sr_{0.33}MnO_{3-\delta}$ (x=0.09, 0.17, 0.25, 0.33) and $Nd_{0.67}Sr_{0.33-y}MnO_{3-\delta}$ (y =0.09, 0.17) compounds, it is evident that the compound with a deficiency of 0.17 at the Nd-site, i.e., $Nd_{0.67-x}Sr_{0.33}MnO_{3-\delta}$ (x= 0.17) shows the highest value of T_C with significant enhancement in magnetization value.

5.3.2. Comparison between bulk and nanocrystalline $Nd_{0.67-x}Sr_{0.33}MnO_{3-\delta}$ (x= 0.17) compounds

5.3.2.1. Structural analysis

The XRD pattern of nanocrystalline Nd-0.17 compound confirms that it belongs to orthorhombic symmetry with Pbnm space group. The Rietveld refinement of the XRD pattern is shown in Fig. 5.10 and refined structural parameters obtained are listed in Table 5.3. The weighted pattern R_{WP}, pattern R_P and goodness of fit χ^2 show small values indicating good agreement between the calculated and observed XRD data. In the bulk compound, we have found an additional peak around 36° indicates the presence of rhombohedral ferrimagnetic Mn_3O_4 phase. It is to be noted that the nanocrystalline compound didn't show any such impurity phases in the XRD plot.

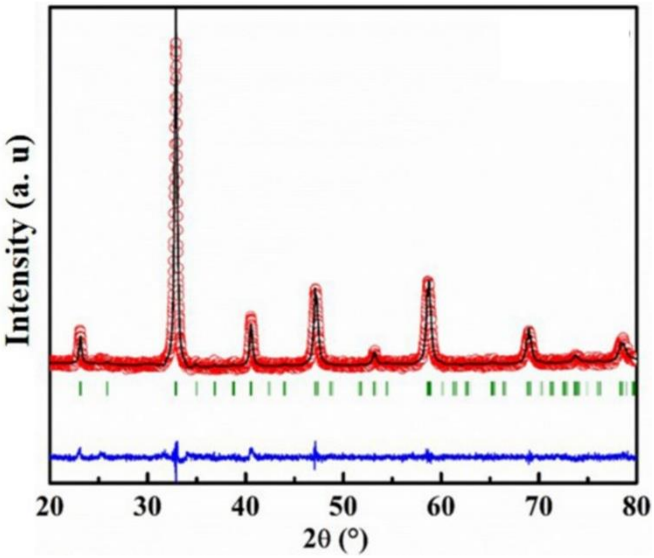

Fig. 5.10. *Refined XRD patterns of nanocrystalline Nd-0.17 compound. The bottom (blue) line represents the difference between the XRD data (red), and calculated fit (black) and the green lines are Bragg positions*

We have carried out the iodometric titration method, and the oxygen stoichiometry is found to be 2.87 with an accuracy of ± 0.02 for the nanocrystalline compound. Thus the nanocrystalline compound contains more oxygen deficiency than that of its bulk counterpart. Hence, the average oxidation state of Mn-ions is expected to decrease and thereby increases the ionic radius results in a corresponding increase in the unit cell volume [264]. Since it is observed that the nanocrystalline compound contains more Mn^{3+} ions than that of bulk counterpart, the former shows greater cell volume (228.45 Å^3) than that of the later (228.21 Å^3). Thus, the change in the lattice parameters and unit cell volume of the bulk and nanocrystalline compounds can be attributed due to the combined effect of the difference in the ionic radius between Mn^{3+}/Mn^{4+} and the presence of vacancies at the oxygen sites.

	Nanocrystalline Nd-0.17 compound
Cell parameters	
a (Å)	5.4590(2)
b (Å)	5.4491(4)
c (Å)	7.6798(2)
V (Å^3)	228.45(3)
Positional parameters	
Nd/Sr x	0.4970(6)
Nd/Sr y	0.0156(8)
O1 x	0.5443(21)
O1 y	0.5132(18)
O2 x	0.1912(20)
O2 y	0.2935(22)
O2 z	0.0308(30)
Occupancy/ Atomic displacement parameter	
Nd	0.4942/ 0.0224
Sr	0.3214/ 0.0144
Mn	0.9962/ 0.0111
O1	0.9824/ 0.0432
O2	0.9782/ 0.0226
Bond distance (Å)	
Mn-O1	1.930(3)
Mn-O2	1.966(8)
Mn-O2	1.982(3)
Bond angle (°)	
Mn-O1-Mn	153.152(6)
Mn-O2-Mn	165.023(1)
Agreement factors	
R_{WP}	2.95
R_P	2.29
χ^2	1.7

Table 5.3. *Refined structural parameters obtained from the Rietveld analysis*

5.3.2.2. XAS analysis

The influence of nanosize effects on the electronic structure and valence states of Mn and O^{2-} ions have been verified with the XAS. Fig. 5.11(a) represents the normalized XAS spectra recorded at 300 K near L-edge of Mn and K-edge of O for both compounds. The spectra of Mn^{2+}, $Mn^{3+}$and Mn^{4+} are plotted in the same figure for the comparison purpose and shifted vertically for clarity. Both compounds showed two broad L_{III} and L_{II} peaks of Mn 2p owing to the spin-orbit coupling. Bulk compound peaks (L_{III} and L_{II}) show pronounced shoulder (marked by an arrow) with well-defined maxima. However, the nanocrystalline compound exhibits a noticeable change in the shape compared to the bulk counterpart. Both L_{III} and L_{II} peaks of the nanocrystalline compound are much broader than its bulk counterpart with hump-like features noticed (shown as arrows in Fig. 5.11(a)) on lower energy sides of both L_{III} and L_{II} peaks. Both compounds show spectra features resemble to superimpose of both Mn^{3+} and Mn^{4+}. The maximum of L_{III} peak falls between Mn^{3+} and Mn^{4+} in accordance with the previous reports on the manganites [227]. But, in the case of the nanocrystalline compound, the peak positions of L_{III} and L_{II} shifted toward the lower energy side in comparison to that of the bulk one. The change in the effective valence state of Mn-ions results in a chemical shift in the $L_{III,}$ and L_{II} peaks and variation in the symmetry of the ground state changes the spectral shape of the compounds. Using the interpolation method, we have calculated the effective oxidation state of Mn-ions and depicted in Fig. 5.11(b). As shown in the figure, the photon energy versus Mn valence exhibit a linear variation. The interpolated average Mn valence from the peak position indicates 3.56 and 3.25 valence states for bulk and nanocrystalline compounds respectively. This result quantitatively demonstrates that Mn^{3+} ions increases in case of the nanocrystalline compound compared to its bulk counterparts. This is because of the broken symmetry at the surface of nanoparticles aid to stabilize more Mn^{3+} ions in the nanocrystalline compound. Fig. 5.11(c) shows the oxygen 1s XAS for both the compounds. The characteristic peaks of oxygen K-edge are used to identify the hybridization between the transition metal ions to the ligand ions, and the spectrum of O K-edge can be split into three types. First and second peaks assigned to the excitation of O 1s state to, O2p- Mn 3d (~ 528 eV) and O2p-Nd5d (~ 536 eV) states respectively. The third peak attribute to the excitation of O 1s state to O2p-Mn4sp state (~ 543 eV) [228, 229]. The octahedral crystal field splitting of e_g and t_{2g} symmetries can be seen from the peaks separation in the shaded area, and the intensity of peak is proportional to the number of unoccupied hybridized density of O2p-Mn3d states [229]. From Fig. 5.11(c), it is clear that the first peak intensities of the nanocrystalline compound are much lower and that signifies the less number of hole doping appeared in the compound. On the other hand, the observed crystal field splitting energy is slightly higher for the nanocrystalline compound, which could be assigned to the presence of more Mn^{3+} ions that lead to large field splitting.

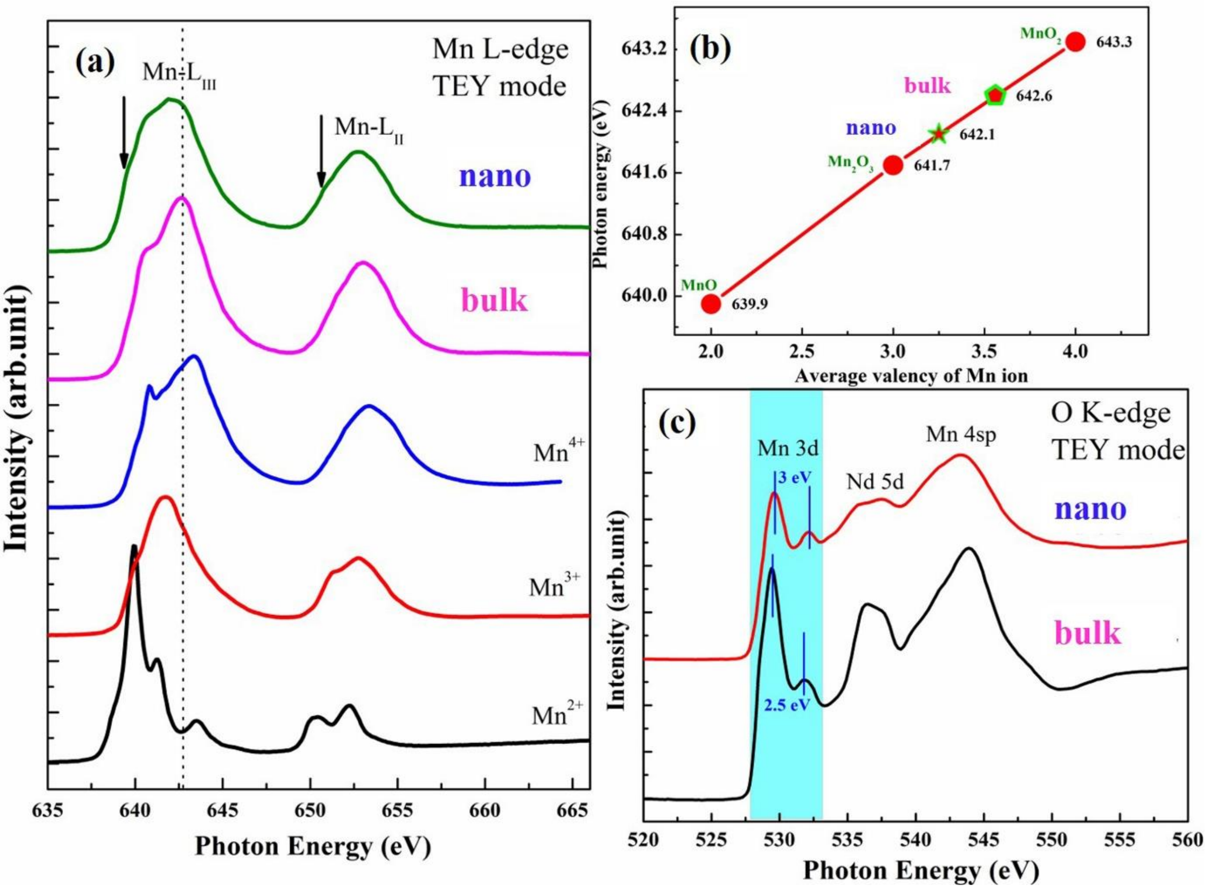

Fig 5.11. *XAS spectra of bulk and nanocrystalline Nd-0.17 compounds. (a) Mn 2p XAS for both the compounds; (b) photo energy versus Mn valence for both the compounds; (c) oxygen 1s XAS for both the compounds*

5.3.2.3. Morphological analysis

Fig. 5.12(a) and 5.12(b) represent the SEM images of highly densified bulk and nanocrystalline compounds with the homogeneous surface.

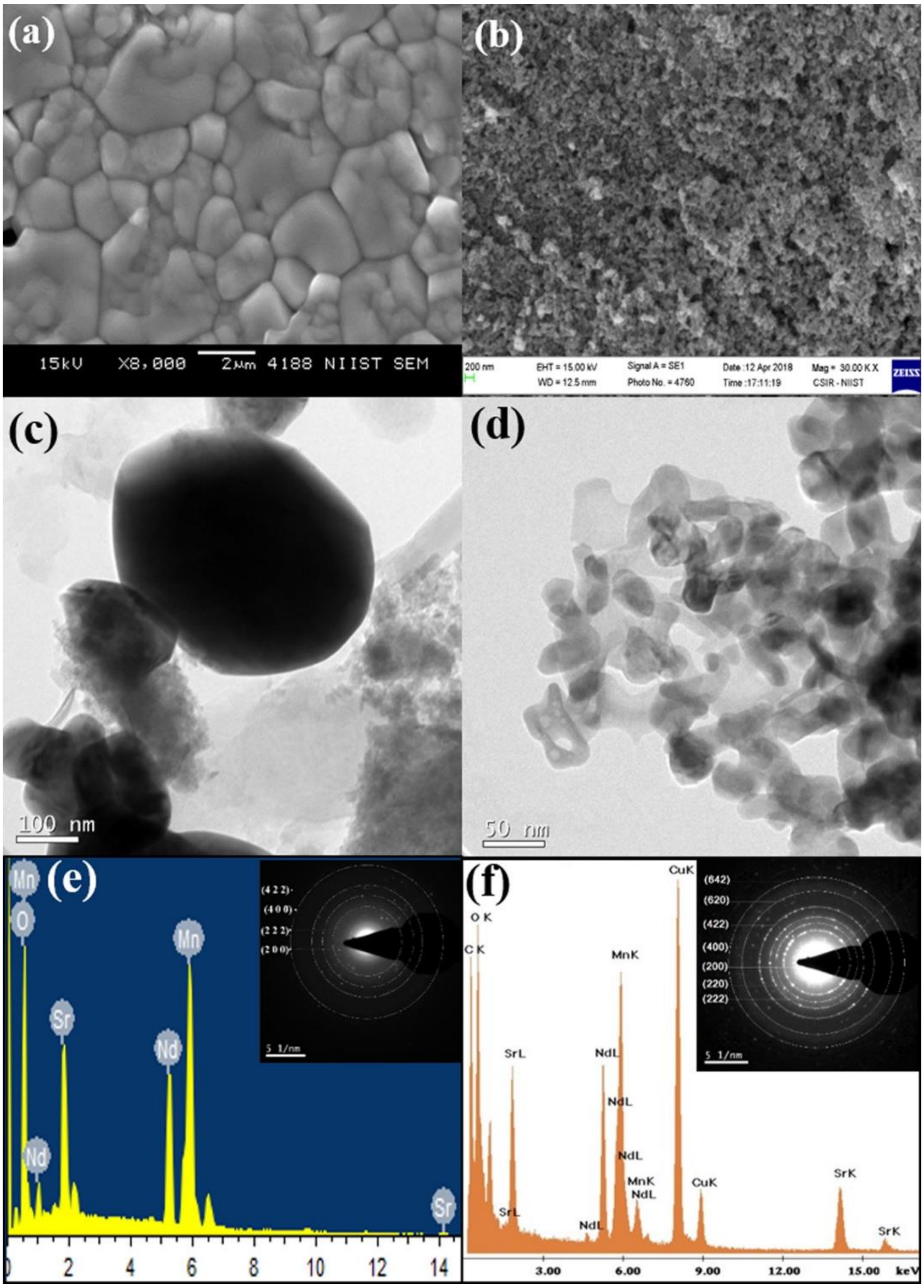

Fig. 5.12. *SEM images of (a) bulk and (b) nanocrystalline Nd-0.17 compounds. TEM images of (c) bulk and (d) nanocrystalline Nd-0.17 compounds. EDAX spectrum of (e) bulk and (f) nanocrystalline Nd-0.17 compounds respectively. SAED patterns are shown in the inset*

Micrometre size grains with grain boundaries are seen in the SEM image of the bulk compound. However, the nanocrystalline compound was taken at 200 nm scale which confirms the nanocrystalline nature of the compound. Fig. 5.12(c) and 5.12(d) represent the TEM images of bulk and nanocrystalline compounds taken at 100 nm and 50 nm scale respectively. The TEM image of nanocrystalline compound reveals particle size of 25-30 nm. Fig. 5.12 (e) and 5.12 (f) represent the EDAX spectrum of bulk and nanocrystalline compounds respectively. The selected area electron diffraction pattern (SAED) is shown in the inset, which confirms the high crystalline nature of the compounds and planes are identified and corroborates with that of its XRD patterns. The EDAX confirm the stoichiometry and homogeneity of the compounds. We have performed EDXRF analysis to determine the stoichiometric composition of both bulk and nanocrystalline compounds. The percentage of elemental oxides observed during the EDXRF analysis are given in Table 5.4. It is clear from the table that the stoichiometric ratio between Nd and Sr are maintained for bulk (0.491: 0.33 with vacancy= 0.179), and nanocrystalline (0.498: 0.33 with vacancy= 0.172) compounds within the limits of experimental error.

Element oxide	**Bulk**	**Nanocrystalline**
Nd_2O_3	44.649	49.371
SrO	18.510	20.129
MnO	36.841	30.500

Table 5.4. *Percentage of element oxide obtained from the EDXRF analysis*

5.3.2.4. Magnetic characterization

Temperature variation of magnetization, M (T), has been carried from 2 K-300 K under 50 Oe and is depicted in Fig. 5.13. There is strong thermo-magnetic irreversibility seen in between the ZFC and FC curves due to the magnetic frustration in the compound [265]. Also, it can be seen that bulk compound show a hump-like character around 46 K and it is due to the ordering of Mn_3O_4, however, we did not observe any such low-temperature transition in the case nanocrystalline compound. The bulk compound shows a sharp transition with a T_C of 275 K and nanocrystalline compound exhibit a broadened transition with a T_C of 242 K. However, it can be seen that both bulk and nanocrystalline Nd-0.17 compounds show higher T_C than its pristine compound $Nd_{0.67}Sr_{0.33}MnO_3$, and it may be due to the increase in DE interaction with the creation of deficiency at the Nd-site. However, from Fig. 5.13, it can be seen that the nanocrystalline compound shows a crossover in FC magnetization curve around 134 K, below which magnetization values are higher for the nanocrystalline compound. This abnormality of change in magnetization is may be due to the temperature dependence of the magnetic anisotropy of the nanocrystalline compound [266, 267]. It is clear from the XAS data that more Mn^{3+} ions exist in the case of the nanocrystalline compound, the more JT distortions exist in the same. The JT effect has a direct dependence on the concentration of Mn^{3+} due to its double orbital degeneracy, and thus it has a strong interplay with DE interactions [268]. Therefore the magnetic properties in the nanocrystalline compound are obviously due to the presence of more JT ions.

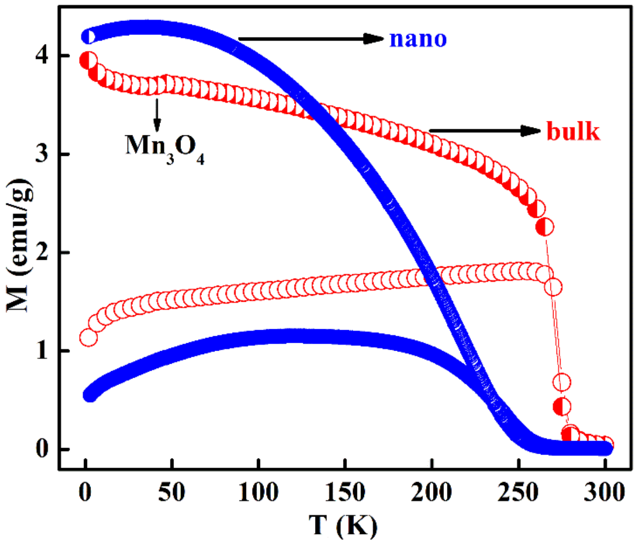

Fig. 5.13. *Temperature variation of magnetization of bulk and nanocrystalline Nd-0.17 compounds*

To further investigate the magnetic behaviour, the magnetization as a function of field is measured at various temperature and are depicted in Fig. 5.14. The magnetization shows a sudden rise at the lower magnetic field but does not saturate even at the higher magnetic field. The magnetization of the nanocrystalline compound shows less value than that of its bulk counterpart at higher fields. It has been observed that the reduction of crystallite size has a strong influence on the magnetic and electric transport properties of nanocrystalline manganites. The observed results suggest that the nanocrystalline compound may form a core-shell structure, where the core is a ferromagnet while the shell behaves like a paramagnet. As the grain size reduces, the surface-to-volume ratio increases and the contribution from the grain boundary effects increases. Thus the core of the nanocrystalline compound has physical properties as same as that of its bulk counterpart while the amorphous outer layer is magnetically disordered due to more oxygen vacancies and crystallographic defects [269]. Thus, due to the high disordered state in the outer shell, the net magnetic moment of this amorphous region becomes zero, which in turn reduces the magnetization. Since the shell behaves more like PM, the magnetization values of the nanocrystalline compound are lesser than that of its bulk counterparts. It is also noticed that the H_C decreases with the increase in temperature for both the compounds.

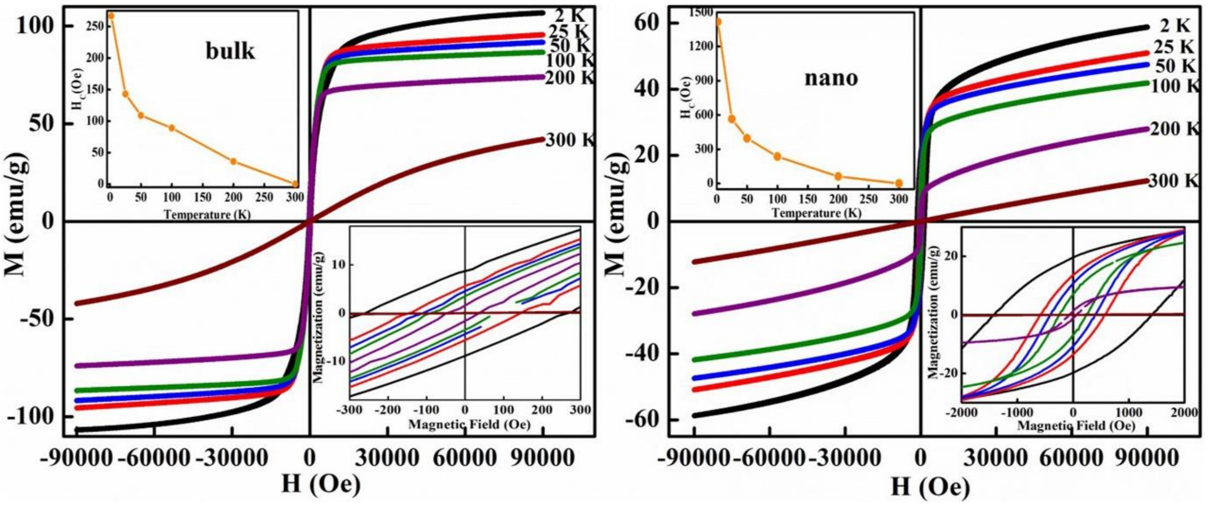

__Fig. 5.14.__ Hysteresis loops of bulk and nanocrystalline Nd-0.17 compounds. Insets show the magnified view of the loop and temperature dependence of the H_C

As the magnetic anisotropy of the compound is proportional to the coercive field, it is evident that the crossover in magnetization in the M-T curve (Fig. 5.13) of the nanocrystalline compound is due to the sudden increase in the coercive field of the nanocrystalline compound while decreasing the temperature. There is a strong exchange coupling takes place between the inner core and outer shell of the nanocrystalline compound. The magnetically disordered state in the outer layer has a surface anisotropy contribution towards the effective anisotropy of the nanocrystalline compound [270]. The effect of the surface anisotropy increases with a decrease in crystallite size [270]. Thus the observed H_C (one order higher) of the nanocrystalline compound is due to the surface anisotropy contribution by the insulating grain boundary growth.

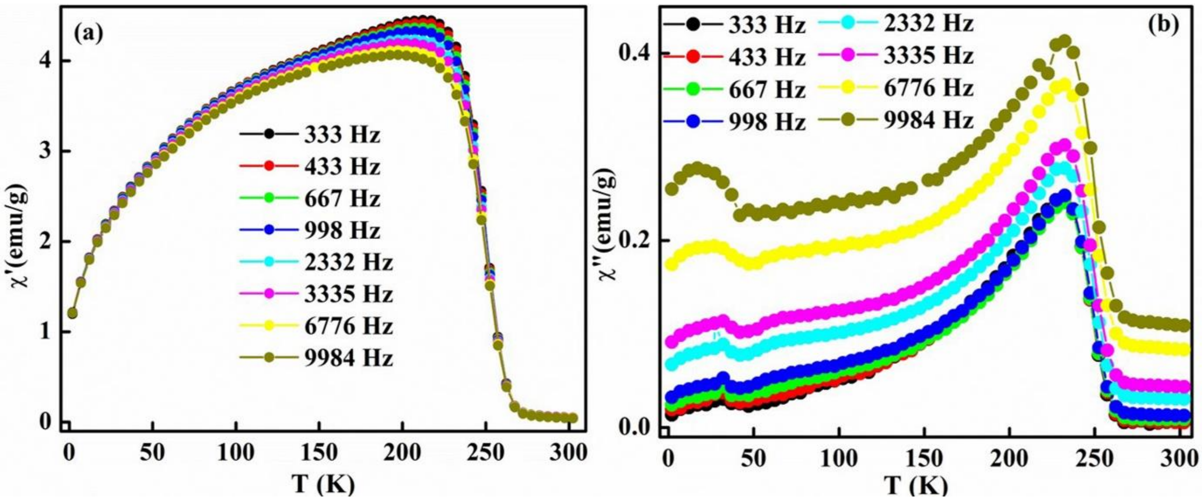

Fig. 5.15. *AC magnetic susceptibility of the nanocrystalline Nd-0.17 compound with (a) real and (b) imaginary parts*

To understand the broad ferromagnetic transition in the nanocrystalline compound, we have further carried out the temperature variation of AC susceptibility from 2 K-300 K under different frequencies vary from 333 Hz to 9984 Hz. Fig. 5.15(a) and 5.15(b) shows the in-phase and out of phase component of susceptibility, and it shows a maximum around T_C, and the obtained maximum is independent on the frequency change. The magnitude of the real part of susceptibility decreases and the imaginary part increases with increasing frequency. The peak temperature is found to be constant with the variation of temperature and frequency. The imaginary part of the ac susceptibility exhibit a low-temperature hump like behaviour around 46 K and this is due to the ordering of Mn_3O_4 secondary phase and which was not seen in the FC curve of dc magnetization in the nanocrystalline compound. It could be because the core is surrounded by a shell which is randomly oriented spins resulting in the suppression of Mn_3O_4 ordering.

The isothermal magnetization measurement has done for every 4 K interval around the T_C for both the compounds and is shown in Fig. 5.16. The magnetization values of the nanocrystalline compound are much lesser than its bulk counterpart. The reduction of particle size in the nanocrystalline compound results in the suppression of magnetization.

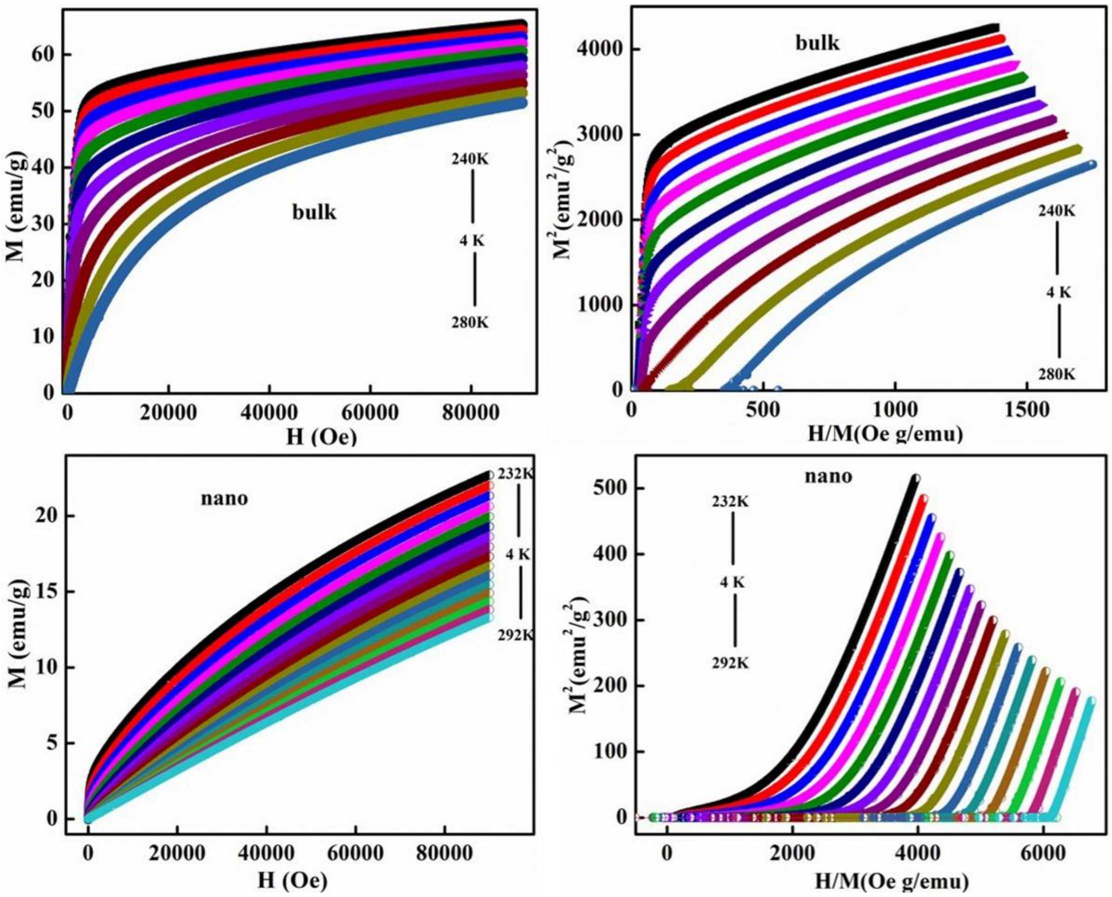

Fig. 5.16. *M-H and Arrott plots of bulk and nanocrystalline Nd- 0.17 compounds*

5.3.2.5. Magnetocaloric properties

We studied the magnetic entropy change of both the compounds using thermodynamic Maxwell relations [148]. Fig. 5.17 shows the -ΔS_M for both the compounds estimated under 10 kOe and 50 kOe. The Bulk compound shows maximum values of 1.65 J kg^{-1} K^{-1} and 4.89 J kg^{-1} K^{-1} at 275 K for 10 kOe and 50 kOe respectively. However, the nanocrystalline compound shows a maximum value of 0.19 J kg^{-1} K^{-1} at 222 K and 0.98 J kg^{-1} K^{-1} at 226 K for fields of 10 kOe and 50 kOe respectively. Thus, it is clear that the bulk compound shows a significant ΔS_M and could be a potential candidate for sub room-temperature magnetic refrigeration applications. It is observed that due to the domain boundary modification, the ΔS_M value of the nanocrystalline compound is lower than that of its bulk counterpart by one order, however, it shows a higher T_C than that of the nanocrystalline pristine compound.

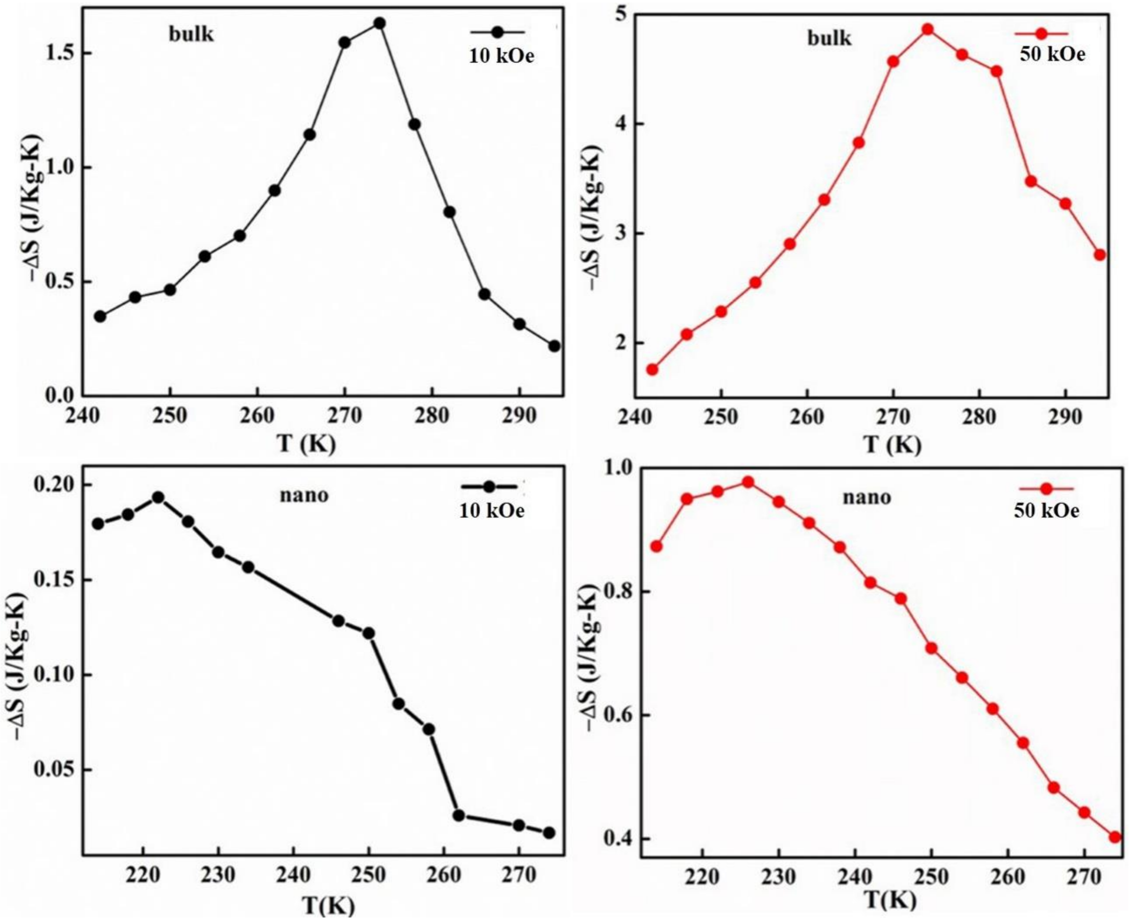

Fig. 5.17. *The magnetic entropy change of bulk and nanocrystalline Nd-0.17 compounds*

5.4. Conclusion

- The Nd/Sr-deficient $Nd_{0.67-x}Sr_{0.33}MnO_{3-\delta}$ (x=0.09, 0.17, 0.25, 0.33) and $Nd_{0.67}Sr_{0.33-y}MnO_{3-\delta}$ (y =0.09, 0.17) compounds were prepared by the solid-state method, and their structural, magnetic and electrical transport properties were investigated. The following conclusion can be drawn from the studies
- The XAS studies confirm that the concentration of Mn^{4+} ions is more with an increase in Nd-deficiency while it decreases with increase in Sr-deficiency.
- The magnetization shows a parabolic trend with the maximum value for $Nd_{0.67-x}Sr_{0.33}MnO_{3-\delta}$ (x= 0.17) compound, while the resistivity shows a hyperbolic trend with minimum resistivity for the same compound. On the other hand, the magnetization decreases and resistivity increase with the increase in Sr-deficiency.
- Both the bulk and nanocrystalline $Nd_{0.67-x}Sr_{0.33}MnO_{3-\delta}$ (x= 0.17) compounds show an enhancement in the magnetic transition temperature than that of its respective stoichiometric $Nd_{0.67}Sr_{0.33}MnO_3$ compound.
- The bulk $Nd_{0.67-x}Sr_{0.33}MnO_{3-\delta}$ (x= 0.17) compound shows $-\Delta S_M$ of 1.65 J kg^{-1} K^{-1} and 4.89 J kg^{-1} K^{-1} at 275 K for 10 kOe and 50 kOe field change and it could be a potential candidate for sub-room temperature applications.

Chapter 6

Impact of La/Sr-site deficiencies on the structural, magnetic and magnetocaloric properties in $La_{0.67}Sr_{0.33}MnO_3$ manganite

Impact of La and Sr-site deficiencies on the structural, magnetic and magnetocaloric properties in $La_{0.67}Sr_{0.33}MnO_3$ manganite are discussed in this chapter. Among the studied compounds, $La_{0.67}Sr_{0.33-y}MnO_{3-\delta}$ (y= 0.09) composition shows the highest $-\Delta S_M$ of 5.08 J kg^{-1} K^{-1} at 352 K for 50 kOe field change with a ΔT_{ad} of 3.48 K, while $La_{0.67}Sr_{0.33}MnO_3$ and $La_{0.67-x}Sr_{0.33}MnO_{3-\delta}$ (x= 0.09) compounds exhibit a $-\Delta S_M$ of 4.78 J kg^{-1} K^{-1} at 364 K and 4.12 J kg^{-1} K^{-1} at 364 K respectively. The Sr-site deficient compound shows a promising behaviour of reduction in the T_C towards room temperature, along with an increase in the ΔS_M values. Thus, higher deficiency at Sr-site in $La_{0.67}Sr_{0.33-y}MnO_{3-\delta}$ (y=0.18 and 0.27) compounds were investigated. Significant $-\Delta S_M$ value of 4.61 J kg^{-1} K^{-1} near room temperature (310 K) was achieved in $La_{0.67}Sr_{0.33-y}MnO_{3-\delta}$ (y= 0.18) compound, and it could be a potential candidate for room temperature magnetic refrigeration applications.

6.1. Introduction

Earlier reports suggest that partial substitution of rare earth elements (Nd, Pr, Gd etc.) at the A-site and partial substitution of transition elements (Cr, Fe, Ni etc.) at the Mn-site leads to tailor the T_C towards room temperature [177-184]. However, to maintain a significant value in T_C, a large drop in ΔS_M was witnessed and vice versa. Recently, many reports have demonstrated that the creation of deficiency at the A-site alters the Mn^{2+}/ Mn^{3+}/ Mn^{4+} ratio which significantly affects the magnetic and magnetocaloric properties [184-186, 199, 202, 249, 251- 253, 256, 271, 277, 278]. As the electron hopping between Mn^{3+} /Mn^{4+} ions are strongly influences by the vacancy creation at the A and A′-sites of the $A_{0.67}A'_{0.33}MnO_3$ composition, one can further enhance the magnetocaloric properties and tune the T_C towards room temperature in the same. Again, the effect of deficiency in these compounds enhances the disorder effect due to the change in $Mn^{2+}/Mn^{3+}/Mn^{4+}$ ratio, which further leads to a change in the magnetic properties. Thus, in the present chapter, we take the opportunity to study the effect of A and A′-sites deficiency (i.e., both La and Sr-deficiency) on the structural, magnetic and magnetocaloric properties in $La_{0.67}Sr_{0.33}MnO_3$ manganite.

6.2. Experimental

The conventional solid-state method is adopted for the preparation of the compounds by taking La_2O_3 (Alfa Aesar, 99 %), $SrCO_3$ (Sigma-Aldrich, 98 %), $MnCO_3$ (Sigma-Aldrich, 99.9+ %) as raw materials. The raw materials were weighed according to the stoichiometry and mixed in an agate mortar using distilled water as a solvent medium for 6h. The homogenous mixture was dried and calcined at 1200 ˚C for 12 h. The grounded powders were pelletized into the cylindrical shape of appropriate dimension, which was then sintered at 1350 ˚C for 12 h. The crystal structure was characterized by XRD techniques, and the Rietveld refinement was done using the FullProf software. The morphological analysis was performed using SEM equipped with EDAX. The oxygen stoichiometry was estimated by iodometric titration method, and the cationic composition was confirmed by EDXRF analysis. XPS measurement was done, and the XPS spectrum was acquired using a PHY 5000 Versa Probe II, ULVAC-PHI, Inc. instrument and an Al Kα X-ray source. The pressure in the XPS chamber during the measurements was 5×10^{-10} mbar and the binding energies were corrected by C 1s as reference energy (C 1s = 284.8 eV). A wide scan was collected to ensure that no foreign materials were present on the sample surface. Magnetic properties, electrical resistivity and specific heat measurements were done using a PPMS.

6.3. Results and discussion

6.3.1. Structural, magnetic and magnetocaloric properties of $La_{0.67-x}Sr_{0.33}MnO_{3-\delta}$ (x= 0 and 0.09) and $La_{0.67}Sr_{0.33-y}MnO_{3-\delta}$ (y= 0.09) manganites

Initially, we have studied the structural, magnetic and magnetocaloric properties of La-deficient compound, i.e., $La_{0.67-x}Sr_{0.33}MnO_{3-\delta}$ (x =0.09), termed as La-0.09 and Sr-deficient compound, i.e., $La_{0.67}Sr_{0.33-y}MnO_{3-\delta}$ (y = 0.09), termed as Sr-0.09 and compared the properties with that of the pristine compound $La_{0.67}Sr_{0.33}MnO_3$ (termed as LSMO).

6.3.1.1. Structural analysis

The structural characterization confirms that all the three compounds belong to rhombohedral crystal symmetry with $R\bar{3}c$ space group. Rietveld refined XRD patterns of all the compounds are shown in Fig. 6.1, and the structural parameters obtained from the same are listed in Table 6.1. From the analysis, it is confirmed that there is an excellent agreement between the observed and calculated XRD pattern. The pristine compound (LSMO) was found to be phase pure, and no trace of secondary phases was detected in the XRD data. However, in the La and Sr-deficient compounds, we have found an additional peak around 36.1° which is marked as * in Fig. 6.1, which indicates the presence of rhombohedral ferrimagnetic Mn_3O_4 phase. In deficient compounds, Mn^{2+}, Mn^{3+} and Mn^{4+} ions are possible [272, 273]. Among these ions, Mn^{3+}/Mn^{4+} ions occupy the B-sites, and Mn^{2+} ions occupy the A-sites along with La^{3+} and Sr^{2+} ions [272]. The effective ionic radius of Mn^{2+} (with coordination number 12) is 1.13 Å. Thus, Mn^{2+} ions are expected to occupy at the A-site, along with La^{3+} (1.36 Å) and Sr^{2+} (1.44 Å) ions [272]. The presence of Mn^{2+} ions in deficient compounds can be attributed due to the charge disproportionation model, suggested by Hundley *et al.* based on the instability of Mn^{3+}-Mn^{3+} state to that of Mn^{2+}-Mn^{4+} state in octahedrally coordinated systems [274]. Thus, due to the charge disproportionation phenomena, the deficient compounds undergo a reaction of $Mn^{3+}+Mn^{3+}\rightarrow Mn^{2+}+Mn^{4+}$ for more stable pairs. Thus in deficient compounds, a portion of the Mn-ions become Mn_3O_4 secondary phase, and another portion occupies at the A-site as Mn^{2+} ions. From Table 6.1, it can be seen that the unit cell volume of La-0.09 is less than that of its stoichiometric compound LSMO. Whereas, Sr-0.09 shows greater unit cell volume than that of LSMO. The decrease in the unit cell volume of La- deficient compound could be due to the presence of more Mn^{4+} content in the compound, which is in agreement with earlier reports about the La/Pr deficient manganites [254, 275, 276]. It is well reported that Nd/La/Pr-deficiency and Sr/Ca/Ba/Na-deficiency have an inverse effect on the unit cell volume of the stoichiometric compounds [254, 275- 278]. Since the ionic radius of Mn^{4+} ions (0.53 Å) is less than that of Mn^{3+} ions (0.645 Å), the increase in the unit cell volume with Sr-deficiency cannot be explained on the basis of amount of Mn^{4+} ions and it is related to the ionic radius of the Sr^{2+} deficient site and anionic vacancies [254]. The radius of Sr^{2+} deficient site (1.547 Å) is approximately 7% greater than that of Sr^{2+} site (1.44 Å), and it is physically acceptable due to the electrostatic repulsion by the nearest O^{2-} ions due to the deficiency of Sr^{2+} ions [279]. Since the change in unit cell volume affects the Mn-O bond lengths and Mn-O-Mn bond angles, the motion of e_g electron between Mn^{3+} and Mn^{4+} ions are strongly influenced by the creation of deficiency at the A-site of manganites.

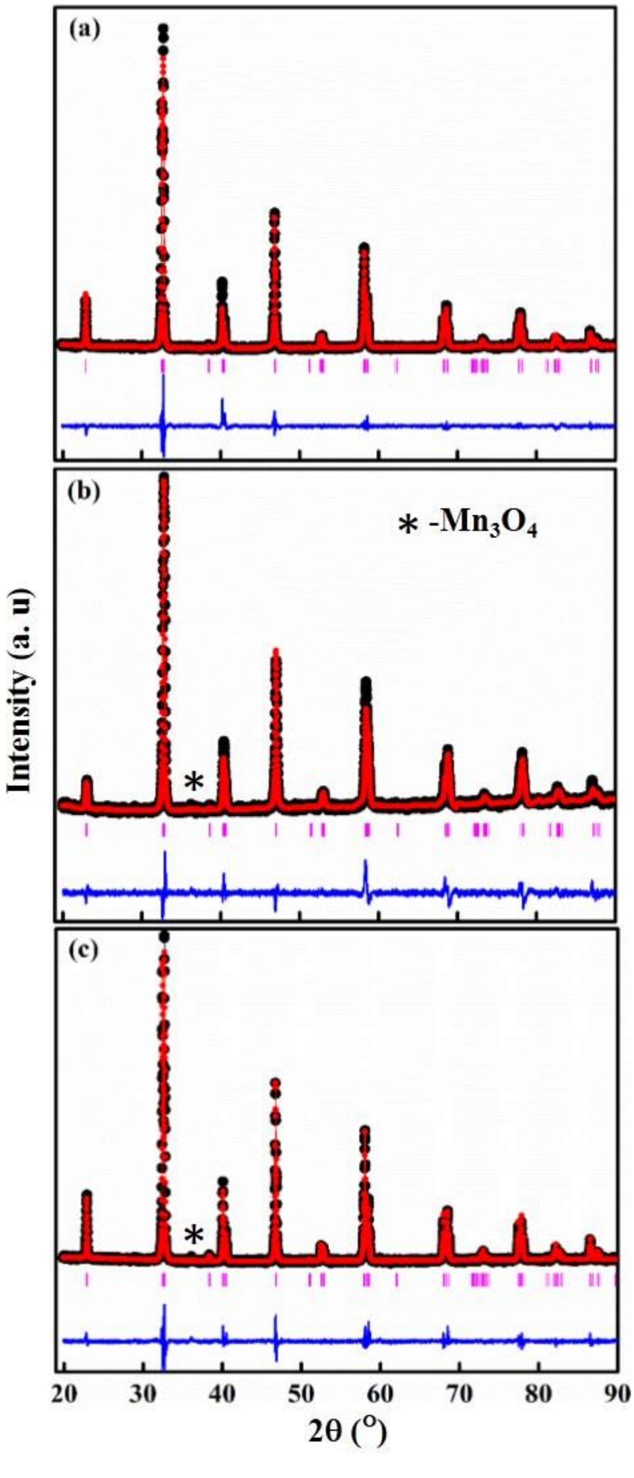

Fig. 6.1. *Rietveld refined XRD patterns of (a) LSMO, (b) La-0.09 and (c) Sr- 0.09 compounds at room temperature. Black lines correspond to the XRD data. Red lines are theoretical fits to the XRD data, and pink lines correspond to Bragg reflection. The difference between the observed data and the theoretical fit is shown at the bottom blue lines*

	LSMO	**La-0.09**	**Sr-0.09**
Cell parameters			
a (Å)	5.4963 (1)	5.4771 (1)	5.5120 (2)
b (Å)	5.4963 (1)	5.4771 (1)	5.5120 (1)
c (Å)	13.3576 (4)	13.3281 (5)	13.3664 (4)
V (Å^3)	349.468 (15)	346.251 (18)	351.686 (12)
Positional parameters			
La/Sr x	0	0	0
La/Sr y	0	0	0
La/Sr z	0.25	0.25	0.25
O x	0.5469	0.5263	0.5489
O y	0	0	0
O z	0.25	0.25	0.25
Occupancy/ Atomic displacement parameter			
La	0.6671/ 0.0424	0.5724/ 0.0148	0.6648/ 0.0164
Sr	0.3242/ 0.0424	0.3238/ 0.0148	0.2314/ 0.0164
Mn	0.9848/0.0262	0.9662/0.0641	0.9821/ 0.0222
O	0.9242/0.0426	0.8848/0.0124	0.8622/ 0.0421
Bond distance (Å)			
$\langle d_{Mn\text{-}O} \rangle$	1.955 (5)	1.938 (1)	1.961 (1)
Bond angle (°)			
Mn-O-Mn	164.8 (5)	171.5 (2)	164.2 (1)
Agreement factors			
R_{WP}	3.80	4.58	3.74
R_P	3.10	3.66	3.04
χ^2	3.09	2.98	2.92

Table 6.1. *Structural parameters of LSMO, La-0.09 and Sr-0.09 compounds obtained from the Rietveld refinement of XRD*

6.3.1.2. XPS analysis

To determine the surface elemental composition and oxidation states, XPS was taken. Fig. 6.2(a) shows the Mn-2p photoelectron spectra of all the three compounds. Two maxima around 641 eV and 653 eV can be seen for LSMO compound which is assigned to be $2P_{3/2}$ and $2P_{1/2}$ states respectively. The La-0.09 and Sr-0.09 compounds also show two maxima, which is slightly shifted towards lower energy side for La-deficiency and a significant shift towards higher energy side is seen for Sr-deficiency. Mn-$2P_{3/2}$ spectra of all the compounds were fitted and analysed using the PEAKFIT 4.1 software and shown in Fig. 6.2(b), (c) and (d). A standard Shirley background is used for the fitting analysis. The multiple peak fitting of Mn-$2P_{3/2}$ spectra of LSMO compound decomposes into two components corresponds to Mn^{3+} and Mn^{4+}.

The peak centres of Mn^{3+} and Mn^{4+} are located at 640.8 eV and 642.8 eV respectively [280]. The percentage of the total area of each component was obtained from the peak fitting, and the ratio of Mn^{3+}/ Mn^{4+} was calculated. The obtained ratio of Mn^{3+}/ Mn^{4+} in LSMO is about 67.9: 32.1, which is nearly equal to the expected value (67: 33). However, the Mn $2P_{3/2}$ spectra of La-0.09 and Sr-0.09 are asymmetric, and the core Mn-2P spectra show satellite peak-like features at higher binding energies, confirmed the presence of Mn^{2+} ions, which is in agreement with the earlier reports [281, 282]. However, the Mn-ions with higher oxidation states do not show this kind of satellite structures at higher binding energies [281, 283].

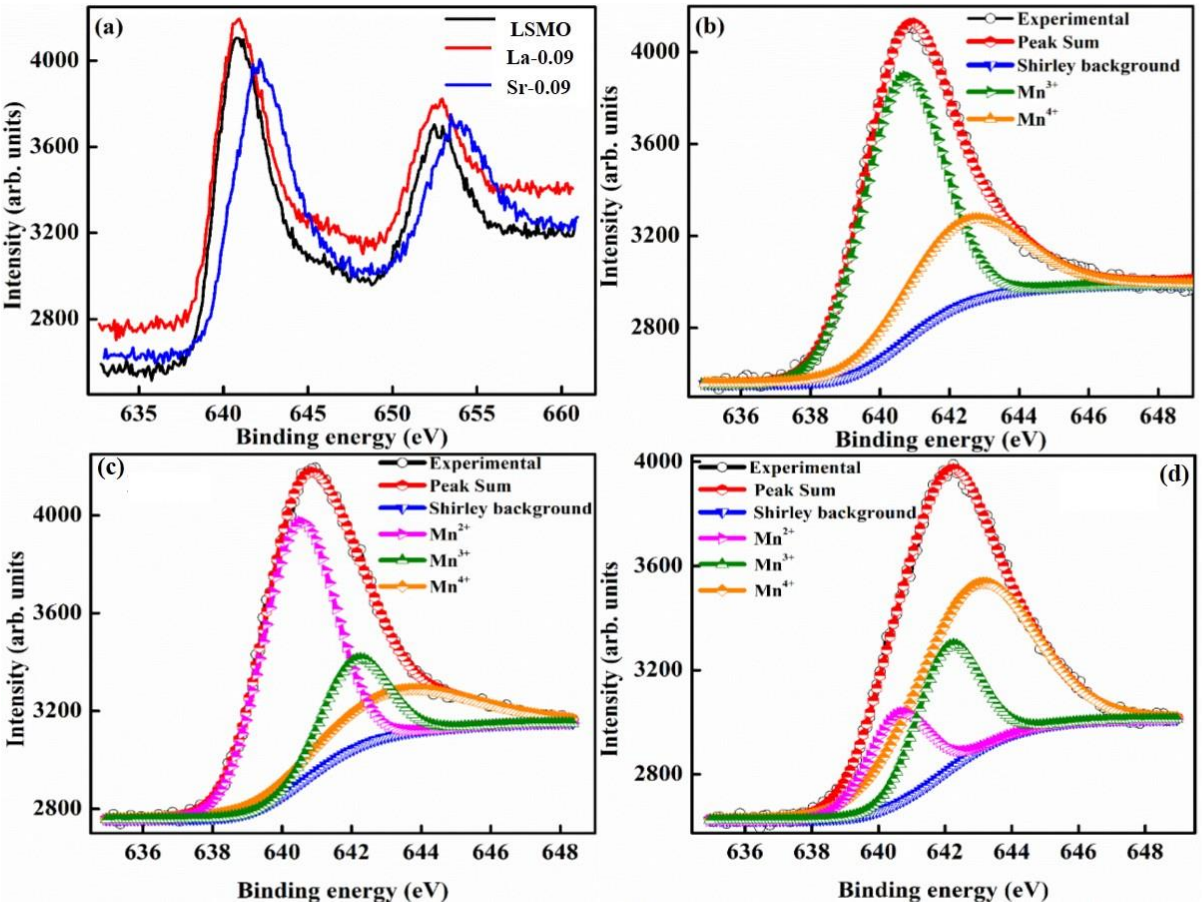

Fig. 6.2. *XPS spectra: (a) Mn-2p photoelectron spectra of all the compounds; (b) Mn-$2P_{3/2}$ spectra of LSMO (c) Mn-$2P_{3/2}$ spectra of La-0.09 and (d) Mn-$2P_{3/2}$ spectra of Sr-0.09*

From the peak fit, the peak centres of Mn^{2+}, Mn^{3+} and Mn^{4+} are located at 640.5 eV, 642.2 eV and 643.8 eV for La-0.09 and 640.7 eV, 642.2 eV and 643.1 eV for Sr-0.09 respectively [280, 284-287]. However, it has also been observed that the number of Mn^{3+} ions undergoes charge disproportionation is different for La- deficiency and Sr-deficiency. Thus, the ratio of Mn^{3+}/Mn^{4+} is different for La-0.09 and Sr-0.09 compounds, which have different effects on the DE interaction and hence the magnetic properties.

6.3.1.3. Surface morphology

The surface microstructure of densified compounds was studied and shown in Fig. 6.3. The microstructure shows well packed polygonal grains with few micrometres in size and grain boundaries are visible. Further, the analysis of chemical composition using EDAX was carried out on several areas, confirmed the homogeneity of the compounds.

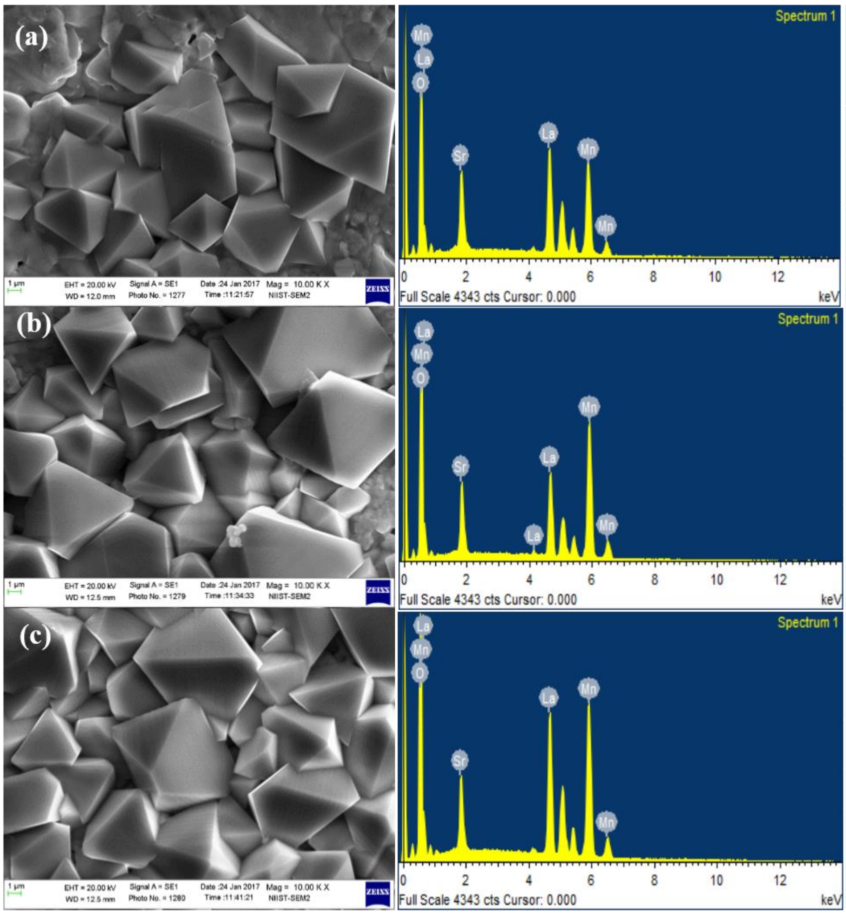

Element	Weight %	Atomic % obtained
O K	25.90	66.32
Mn K	21.33	15.91
Sr L	12.80	5.98
La L	39.96	11.79

Element	Weight %	Atomic % obtained
O K	27.93	66.07
Mn K	30.06	20.71
Sr L	11.14	4.81
La L	30.87	8.41

Element	Weight %	Atomic % obtained
O K	26.33	65.89
Mn K	25.68	18.71
Sr L	9.26	4.23
La L	38.73	11.16

Fig. 6.3. *SEM, EDAX spectrum and composition of (a) LSMO, (b) La-0.09 and (c) Sr-0.09 compounds*

The EDXRF analysis was carried out to estimate the stoichiometry of all the studied compounds and the chemical composition of elemental oxides obtained is shown in Table 6.2.

It is to be noted that La/Sr ratio obtained from the EDXRF analysis was found as same as that of the original stoichiometry within the limits of experimental error. The iodometric titration method was performed to estimate the oxygen stoichiometry of all the studied compounds. Powders were weighed and dissolved in a mixture of 10 ml of 10 mass % potassium iodide aqueous solution and 2.5 ml of 2 M hydrochloric acid. The iodine formed in the reaction was titrated against 0.1 N sodium thiosulphate standard volumetric solution. Starch solution (1 mass %) was used as an indicator. The average value of oxygen content was calculated from 5 titrations. The amount of oxygen content is estimated to be about 2.99, 2.88 and 2.85 for LSMO, La-0.09 and Sr-0.09 respectively with an accuracy of ± 0.02. This is a highly effective and reproducible method and has been reported elsewhere in the literature [257, 258, 288, 289].

Element oxide	**LSMO**	**La-0.09**	**Sr-0.09**
La_2O_3	62.24	58.44	70.57
SrO	16.29	23.47	17.76
MnO	21.47	18.09	11.67

Table 6.2. *Chemical composition of element oxide present LSMO, La-0.09 and Sr-0.09 compounds in according to EDXRF analysis*

6.3.1.4. Magnetic characterization

Fig. 6.4 shows the temperature variation of magnetization from 2-380 K in ZFC and FC modes under 100 Oe field. All the three compounds show significant thermo-magnetic irreversibility between ZFC and FC curves, and it may be due to magnetic frustration exist in the compounds. La-0.09 and Sr-0.09 show higher magnetization values than that of LSMO compound, and this indicates that creating deficiency does not merely destroy the DE interaction but increasing the ferromagnetic nature of the deficient compounds. The Mn^{3+} ions have an electronic configuration of $3d^4$ ($t_{2g}^{3\uparrow}$ $e_g^{\uparrow}$) with S=2 and Mn^{4+} has $3d^3$ ($t_{2g}^{3\uparrow}$) electrons with S=3/2 [124]. The Mn^{2+} ions are very stable and have $3d^5$ ($t_{2g}^{3\uparrow}$ $e_g^{2\uparrow}$) configuration with S=5/2. The spin only magnetic moment of Mn^{2+}, Mn^{3+} and Mn^{4+} ions are $5\mu_B$, $4\mu_B$ and $3\mu_B$ respectively. The Mn^{3+} is a JT ion, and it distorts the octahedral environment due to the strong JT effect. However, Mn^{2+} and Mn^{4+} are JT inactive and do not tend to distort the oxygen octahedra. The exchange coupling between $Mn^{3+}(3d^4)$ and $Mn^{4+}(3d^3)$ ions are highly ferromagnetic, while the coupling between two $Mn^{4+}(3d^3)$ ions are antiferromagnetic [124]. However, in deficient compounds, the Mn^{2+} ions at the La^{3+}-sites are involved in the additional hopping of the electrons. The electronic bands of Mn^{2+} are crossing the Fermi energy level and favour an additional charge hopping through Mn^{3+}-O^{2-}-Mn^{2+}-O^{2-}-Mn^{4+} path and increase the ferromagnetism and conductivity. From the high magnetization value of the deficient compounds, one would expect that the Mn^{2+} ions which are assumed to be at the A-site contribute an additional electron hopping via multiple DE interactions [272].

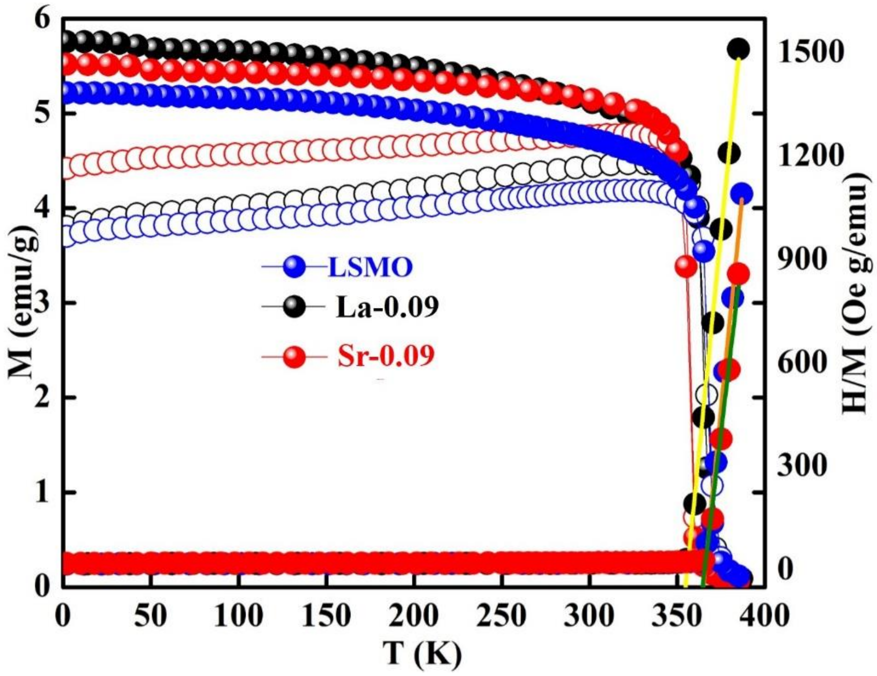

Fig. 6.4. *Temperature dependence of ZFC and FC dc magnetization of LSMO, La-0.09 and Sr-0.09 compounds measured under 100 Oe field. The inverse susceptibility vs. temperature is also shown, and the solid lines represent the Curie-Weiss fits*

Due to the multiple DE interaction, an unconventional charge hopping mechanism through intervening Mn^{2+} ions is taken part and thus enhanced the ferromagnetic nature [272]. This suggests that existence of Mn^{2+} ions in deficient compounds are responsible for the increase in the DE interaction, which is in agreement with the coexistence of mixed-valence states of Mn^{4+}, Mn^{3+} and Mn^{2+} ions in deficient compounds obtained from the XPS analysis.

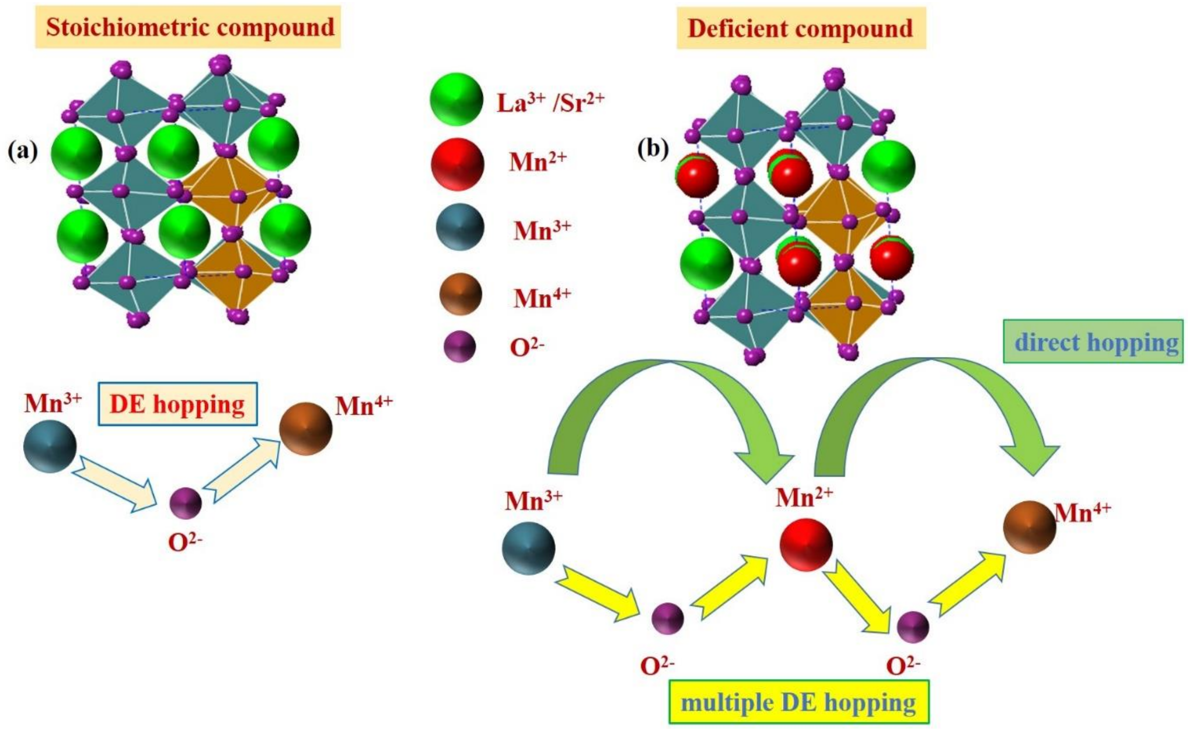

Fig. 6.5. *Schematical representation of DE mechanism: (a) shows the traditional DE hopping mechanism take part in the stoichiometric LSMO compound and (b) shows the multiple DE hopping mechanism through* Mn^{3+}-O^{2-}-Mn^{2+}-O^{2-}-Mn^{4+} *ions and direct hopping between* Mn^{3+}-Mn^{2+}-Mn^{4+} *ions take part in the deficient compounds*

Fig. 6.5(a) shows the traditional DE hopping mechanism take part in the stoichiometric LSMO compound and Fig. 6.5(b) shows the multiple DE hopping mechanism through Mn^{3+}-O^{2-}-Mn^{2+}-O^{2-}-Mn^{4+} ions and direct hopping between Mn^{3+}-Mn^{2+}-Mn^{4+} ions in the La-0.09 and Sr-0.09 compounds. Again, all the compounds undergo a sharp PM to FM transition, and the T_C was determined from the dM/dT curve, which shows a characteristic minimum at their respective transition temperature. In the present case, we obtained a T_C of 365 K for LSMO, a slight increase in T_C is found for La-0.09 (367 K) whereas a significant decrease is found for Sr-0.09 compound (355 K) as shown in Fig.6.4. In La-0.09, tolerance factor decreases due to the reduction in average A-site cationic size and consequently, T_C is slightly increased. On the contrary, in Sr-0.09, due to the Sr-site vacancy, the average A-site cationic radius increases and thereby tolerance factor increases and T_C decreases. The temperature dependence of the inverse susceptibility was plotted in the same graph and found that all the compounds show a similar trend in nature, and it is evident that all compounds obey the Curie-Weiss law above T_C. Thus, it is understood that all the compounds show low magnetic frustration and less disorder.

Further, we have carried out the isothermal hysteresis loops at 2 K and 300 K and is depicted in Fig. 6.6. The insets of Fig. 6.6 show the enlarged view of the hysteresis loops in order to visualize the coercive field. All the compounds show soft ferromagnetic nature with a small coercive field at 2 K, and the hysteresis behaviour of the LSMO is do not destroyed with La and Sr-deficiencies. The magnetization values increased rapidly at very low fields but did not saturate completely at high field. A strong FM component that gets quickly saturated at very low fields and an AFM component that does not saturate even at 90 kOe results in a non-saturating behaviour at 2 K. The relative strength of competing interactions between FM in Mn^{3+}-O^{2-}-Mn^{4+} bonds and AFM in Mn^{4+}-O^{2-}-Mn^{4+} bonds strongly influences the magnetization of LSMO compound. The Sr-0.09 compound shows the highest magnetization value at 2 K due to the increased FM contribution due to the multiple DE interaction via the Mn^{3+}-O^{2-}-Mn^{2+}-O^{2-}-Mn^{4+} path. However, the competing interaction between the FM/AFM components of La-0.09 varies substantially with the change in the Mn^{2+}/ Mn^{3+}/ Mn^{4+} ratio, which in turn reduces the magnetization value at 2 K. Moreover, the non-saturating behaviour is seen even at 300 K, and the magnetization value of all the compounds show a small increment at the high field due to the existence of competing magnetic states.

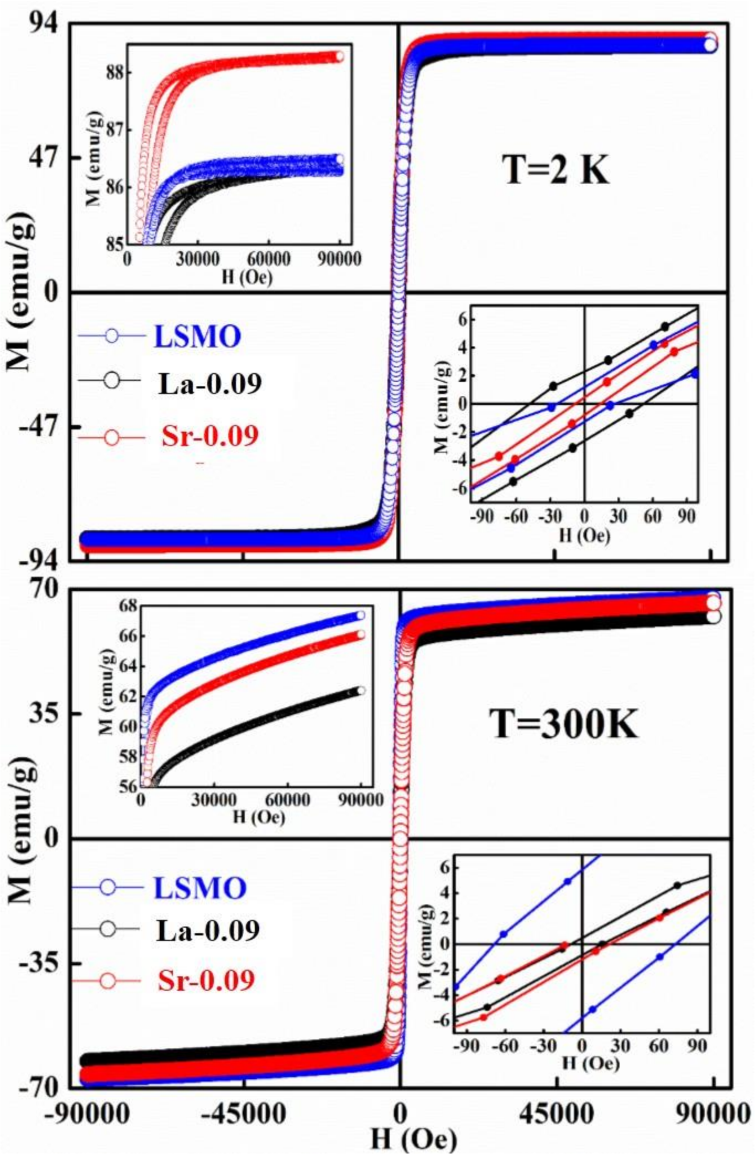

Fig. 6.6. *Hysteresis loops at 2 K and 300 K for LSMO, La-0.09 and Sr-0.09 compounds. The bottom insets show the enlarged view of the hysteresis loops and upper insets show the variation of magnetization as a function of the magnetic field*

6.3.1.5. Magnetocaloric properties

Isothermal magnetization curves around T_C with an interval of every 4 K is measured and is shown in Fig. 6.7(a). For T< T_C, a sharp rise is observed at lower fields and a non-saturating tendency at higher fields, reflecting the ferromagnetic nature. However, for T>$T_{C,}$ magnetization decreases drastically, and almost a linear behaviour is seen indicating the paramagnetic nature of the compounds. Temperature variation of ΔS_M under magnetic fields of 10-50 kOe is shown in Fig. 6.7(b). All the compounds show a maximum ΔS_M at their respective T_C and decrease on either side of it. The position of the peak for LSMO and Sr-0.09 does not shift with higher magnetic fields, however, the peak position of La-0.09 shifts with the increase in magnetic fields. It can be seen that LSMO reaches a maximum $-\Delta S_M$ value of 1.62 J kg^{-1} K^{-1} for 10 kOe and 4.78 J kg^{-1} K^{-1} for 50 kOe field change at 364 K. The La-0.09 compound shows $--\Delta S_M$ values of 1.41 J kg^{-1} K^{-1} (at 360 K), and 4.12 J kg^{-1} K^{-1} (at 364 K) and Sr-0.09 compound shows $-\Delta S_M$ values of 1.78 J kg^{-1} K^{-1} and 5.08 J kg^{-1} K^{-1} at 352 K under field change of 10 kOe and 50 kOe respectively. From Fig. 6.7(b), it can be seen that the T_C of LSMO is tuned from 364 K to 352 K without reducing the ΔS_M value by the introduction of deficiency at the Sr-site. The traditional DE hopping is one of the main reason behind the magnetic entropy change of the LSMO compound. In addition to these hopping mechanism, spin-lattice and spin-orbit coupling are also involved in the ordering process [148]. However, in deficient compounds, the Mn^{2+} ions at the La^{3+}-site induce more distortion in the MnO_6 octahedra due to the change in the average A-site cationic radius. The distortion favours the hopping of the electrons through Mn^{2+} ions and which in turn increases the ΔS_M of the compound. However, from the observed behaviour, it can be understood that the change in the Mn^{2+}/ Mn^{3+}/ Mn^{4+} ratio is the key point in the additional DE interaction through the Mn^{2+} ion and the ΔS_M varies substantially with a change in this ratio. The entropy change obtained in the present investigation is larger than numerous perovskite manganites reported in the past [135, 178, 180, 182-184, 202, 256]. Thus the compounds under present investigation show a significant ΔS_M and could be a potential candidate for the magnetic refrigeration applications.

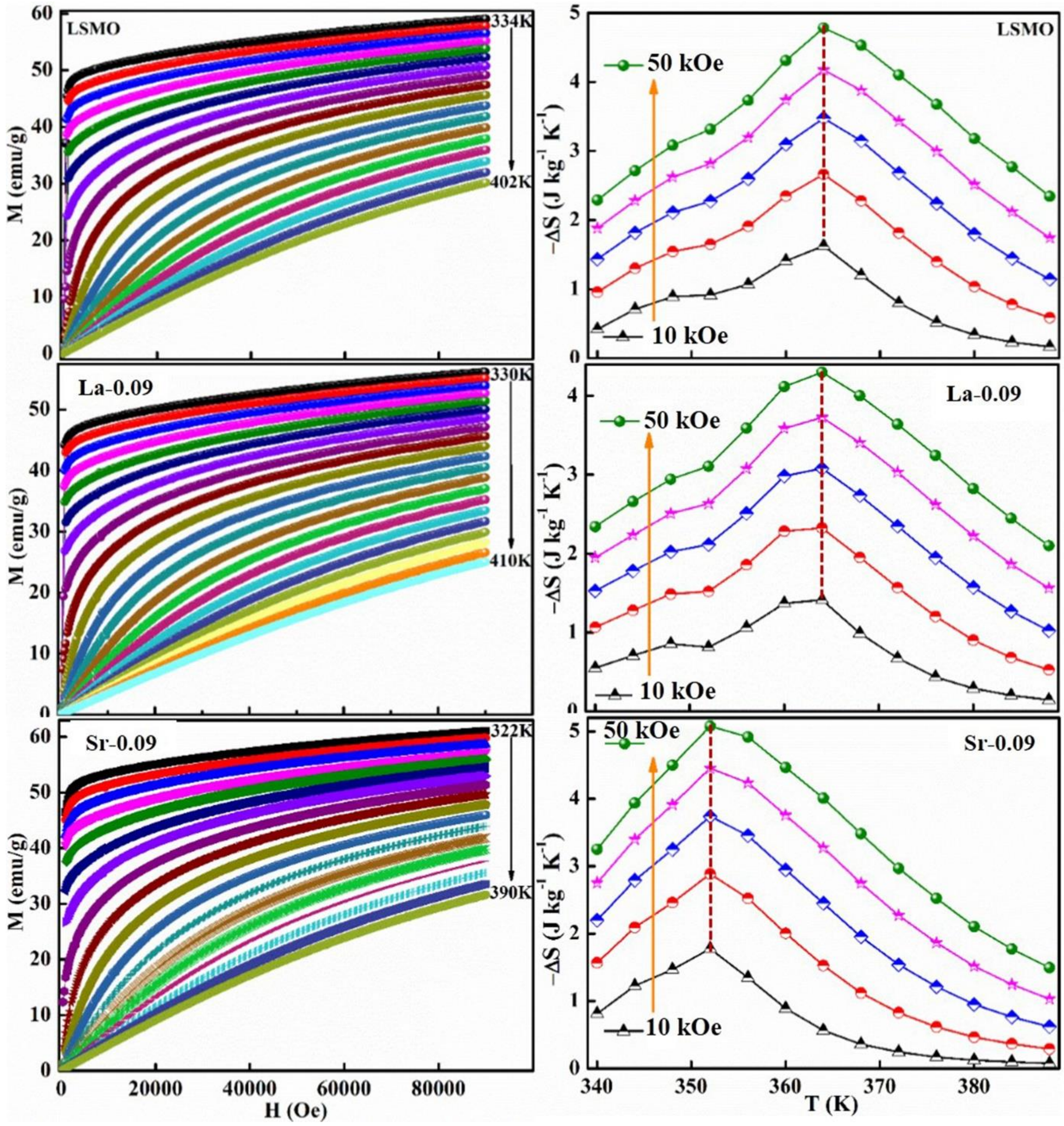

Fig. 6.7. *Isothermal field dependence of magnetization (left panel) and magnetic entropy change (right panel) of LSMO, La-0.09 and Sr-0.09 compounds*

To further attest the ΔS_M values, we have carried out the specific heat capacity (C_P) as a function of temperature from 225 K to 390 K under zero field, 10 kOe and 50 kOe magnetic field and is depicted in Fig. 6.8 (a). It shows that C_P approaches the highest value of 608 J kg^{-1} K^{-1} (at 363 K) for LSMO, 601 J kg^{-1} K^{-1} (at 362 K) for La-0.09 and 589 J kg^{-1} K^{-1} (at 352 K) for Sr-0.09 compounds under zero magnetic field and decreases with increase in the magnetic field. The adiabatic temperature change (ΔT_{ad}) is calculated and shown in Fig. 6.8(b).

The value ΔT_{ad} increases and reaches maximum value of 1.02 K (for 10 kOe) and 3.1 K (for 50 kOe) at 363 K for LSMO and decreases on further increase in temperature. La-0.09 reaches a maximum value of 0.96 K and 2.95 K at 362 K, and Sr-0.09 reaches 1.13 K and 3.48 K at 352 K for 10 kOe and 50 kOe magnetic fields respectively.

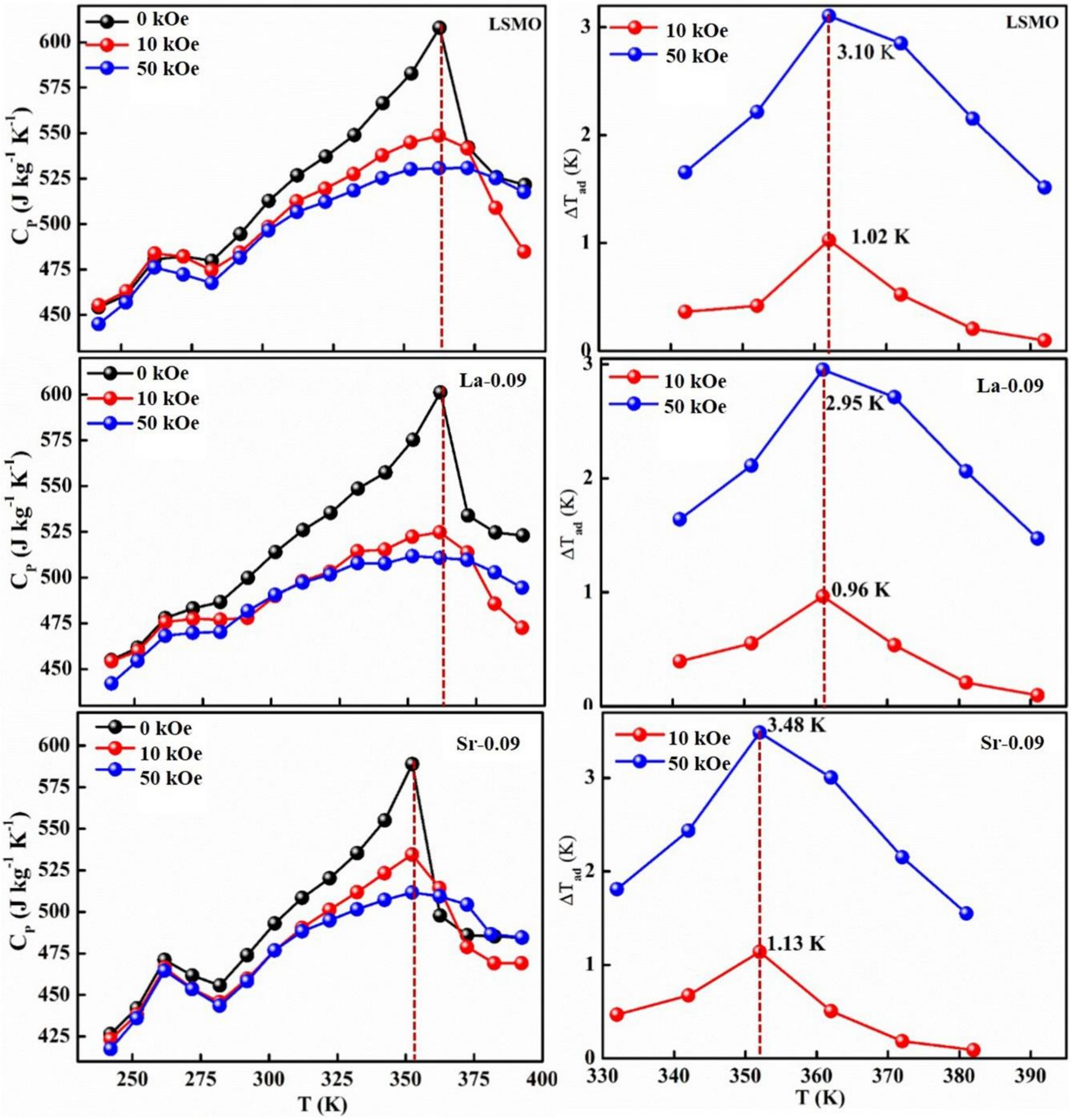

Fig. 6.8. *Specific heat as a function of temperature (left panel) and adiabatic temperature change (right panel) of LSMO, La-0.09 and Sr-0.09 compounds*

6.3.2. Structural, magnetic and magnetocaloric properties of $La_{0.67}Sr_{0.33-y}MnO_{3-\delta}$ (y= 0.18 and 0.27) manganites

It is found that Sr-deficient compound has better magnetocaloric properties than that of the pristine as well as La-deficient compounds. Thus the creation of Sr-deficiency in LSMO exhibits a promising behaviour with significant improvement in magnetocaloric properties with shifting of T_C towards room temperature. Therefore, it is interesting to study the properties with further increase in Sr-deficiency content., Therefore, $La_{0.67}Sr_{0.33-y}MnO_{3-\delta}$ (y = 0.18 and 0.27) compounds which are termed as Sr-0.18 and Sr-0.27 respectively have been prepared and T_C is tuned towards room temperature.

6.3.2.1. Structural analysis

From the Rietveld refinement of the powder XRD patterns, it is confirmed that both the Sr-0.18 and Sr-0.27 compounds belong to rhombohedral structure with $R\bar{3}c$ space group. The refined XRD patterns are shown in Fig. 6.9 and the refined parameters obtained from the Rietveld analysis are shown in Table 6.3.

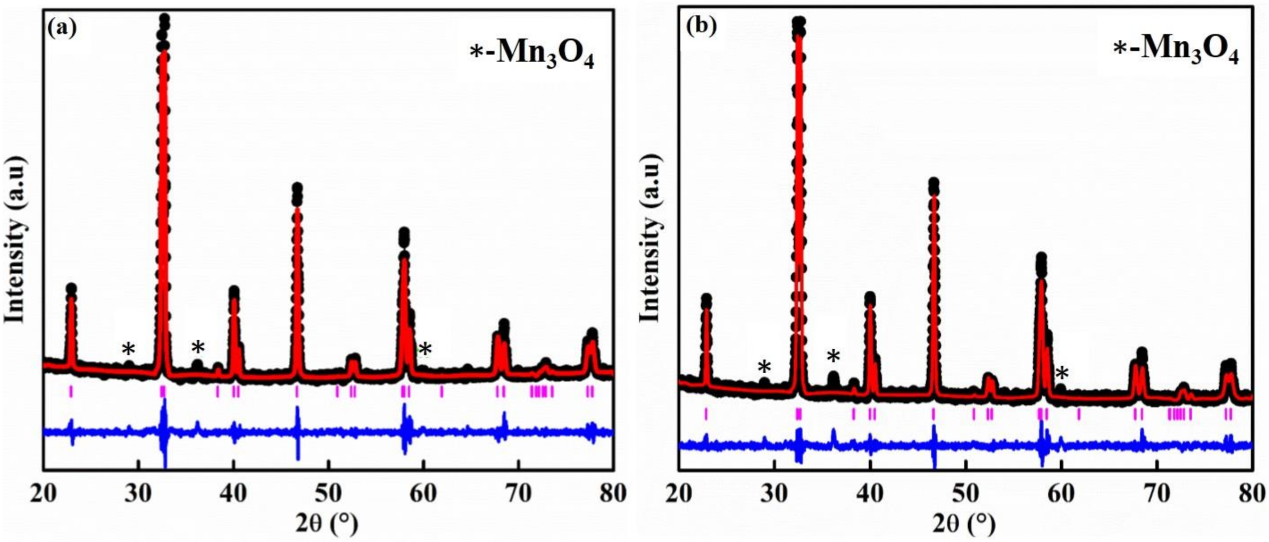

Fig. 6.9. *Rietveld refined XRD patterns of (a) Sr-0.18 and (b) Sr-0.27 compounds. Black colour indicates the experimental data. Red lines are theoretical fits to the XRD data; pink corresponds to the Bragg reflection, and blue lines correspond to the difference between the experimental and the calculated fits*

The experimental XRD patterns are in good agreement with the calculated patterns and show better goodness of fit. It is shown that the Sr-0.09 compound shows an additional peak at 36.1˚ due to the presence of Mn_3O_4 as a secondary phase. However, with further increase in Sr-site deficiency, i.e., Sr-0.18 and Sr-0.27 compounds show some additional secondary peaks at 28.9˚, 36.1˚, 25.9˚etc. due to the prominent presence of Mn_3O_4 phases. Moreover, with the increase in Sr-deficiency, the intensity of the secondary peaks also increases. It indicates that, with the increase in Sr-deficiency content, the percentage of rhombohedral ferrimagnetic Mn_3O_4 secondary phase also increases.

	Sr-0.18	**Sr-0.27**
Cell parameters		
a (Å)	5.4309 (1)	5.5379 (1)
b (Å)	5.5309 (1)	5.5379 (1)
c (Å)	13.3767 (2)	13.3805 (2)
V (Å^3)	354.377 (8)	355.388 (7)
Positional parameters		
La/Sr x	0	0
La/Sr y	0	0
La/Sr z	0.25	0.25
O x	0.546	0.550
O y	0	0
O z	0.25	0.25
Occupancy/ Atomic displacement parameter		
La	0.6624/ 0.0166	0.6668/ 0.0904
Sr	0.1464/ 0.0166	0.0554/ 0.0904
Mn	0.8925/ 0.0377	0.9262/ 0.0631
O	0.7251/ 0.0503	0.7662/ 0.0178
Bond distance (Å)		
$\langle d_{Mn\text{-}O} \rangle$	1.963 (2)	1.968 (2)
Bond angle (°)		
Mn-O-Mn	165.1 (0)	163.8 (0)
Agreement factors		
R_{WP}	5.20	4.77
R_P	3.85	3.59
χ^2	1.84	1.51

Table 6.3. *Structural parameters of Sr-0.18 and Sr-0.27 compounds obtained from the Rietveld refinement of XRD*

From Table 6.3, it can be seen that Sr-0.18 and Sr-0.27 compounds have greater unit cell volume (354.377 Å^3 and 355.388 Å^3 respectively) than that of the pristine (349.468 Å^3) and Sr-0.09 (351.686 Å^3) compounds. The increase in the unit cell volume of the Sr-deficient compounds cannot be explained based on the ionic radius of $Mn^{2+}/Mn^{3+}/Mn^{4+}$ ions or the amount of Mn_3O_4 impurity phase present in the compound. The increase in unit cell volume of Sr-site deficient compounds can be related to the formation of anionic vacancies and the increase in the radius of the Sr- deficient site [290]. Due to the electrostatic repulsion from the neighbour oxygen ions, the radius of the deficient Sr-site (1.547 Å) is increased by 7 % than the actual ionic radius of Sr-site (1.44 Å) [279]. Moreover, the anion ($V^{(a)}$) vacancies at the oxygen sites reduce bonding electrostatic force and eventually leads to the increase of unit cell volume [291]. This will eventually affect the unit cell volume of the Sr-deficient compounds and hence Sr-0.18, and Sr-0.27 compounds exhibit greater unit cell volumes than that of the pristine and Sr-0.09 compounds. As the unit cell volume changes with Sr-deficiency, distortion occurs in the MnO_6 octahedra due to the changes in the Mn-O bond lengths and the Mn-O-Mn bond angles. The JT active ion, Mn^{3+} distorts the MnO_6 octahedra due to the strong JT effect, while Mn^{2+} and Mn^{4+} are JT inactive and do not tend to distort the octahedrally coordinated system. The Iodometric titration method was performed to estimate the stoichiometry of the oxygen ion [292]. The oxygen content decreases with increase in Sr-deficiency, and it is found to be 2.74 and 2.69 for Sr-0.18 and Sr-0.27 compounds respectively with an accuracy of ± 0.03.

6.3.2.2. XPS analysis

To determine the oxidation state of Mn and to identify the elemental composition on the surface, a detailed XPS analysis was performed. The Mn-$2P_{3/2}$ spectra of Sr-0.18 and Sr-0.27 compounds were curve fitted and are shown in Fig. 6.10(a) and (b) respectively. The fitting was done using a standard Shirley background, and the Mn-$2P_{3/2}$ spectra were decomposed into three components for both Sr-0.18 and Sr-0.27 compounds. In Sr-0.18 compound, the three peak centres at 640.9, 642.4 and 643.4 eV corresponds to Mn^{2+}, Mn^{3+} and Mn^{4+} oxidation states respectively [280, 284-287]. In Sr-0.27 compound, the peak centres of Mn^{2+}, Mn^{3+} and Mn^{4+} are at 640.8, 642.3 and 643.2 eV respectively [280, 284-287]. The ratio of $Mn^{2+}/Mn^{3+}/Mn^{4+}$ is calculated from the area of each component obtained from the peak fitting. The ratio of $Mn^{2+}/Mn^{3+}/Mn^{4+}$ is found to be 70.6/6.3/23.1 and 64.7/10.4/24.9 for Sr-0.18 and Sr-0.27 compounds respectively. Hence it is to be noted that the change of state from Mn^{3+} + Mn^{3+} pairs to Mn^{2+} + Mn^{4+} pairs under charge disproportionation phenomena are different for Sr-deficient compounds, and this has been confirmed from XPS analysis. Thus the ratio of $Mn^{2+}/Mn^{3+}/Mn^{4+}$ ions alters with the Sr- deficiency content, which in turn significantly affects the DE interactions and thus the magnetic properties.

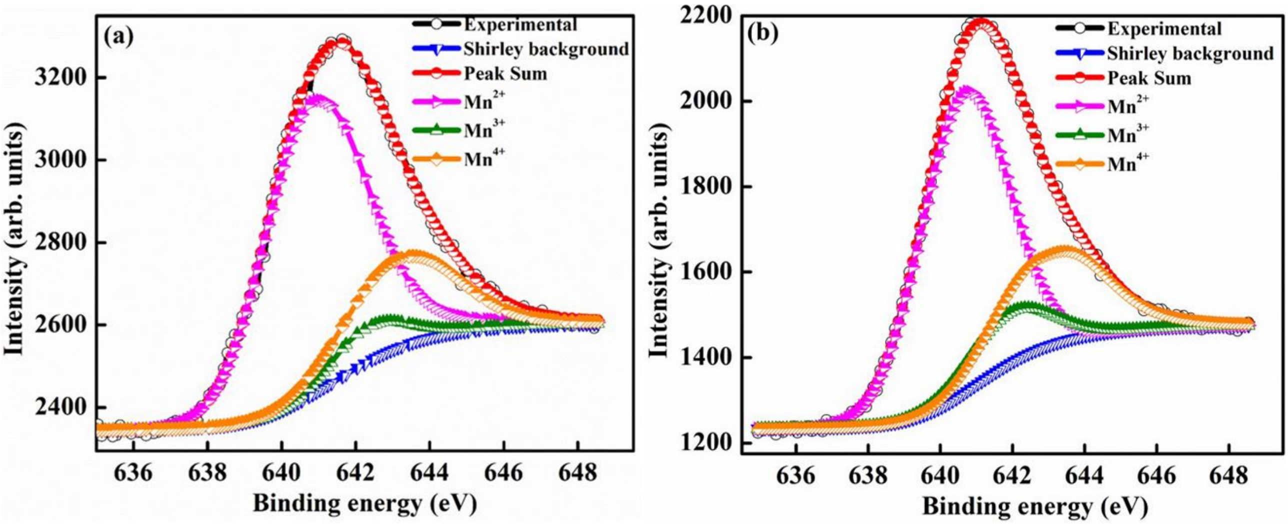

Fig. 6.10. *Mn-2$P_{3/2}$ X- ray photo electron spectra of (a) Sr-0.18 and (b) Sr-0.27 compounds*

6.3.2.3. Magnetic characterization

Fig. 6.11 shows the magnetization as a function of temperature from 2-380 K for both the compounds. The measurement was carried out under 100 Oe field in ZFC and FC modes. Large thermo-magnetic irreversibility is witnessed in both the compounds due to the competing interaction between different magnetic states. Both the compounds show a hump-like feature below 50 K, which was not seen in the magnetization curves of La-0.09 and Sr-0.09

compounds. This low-temperature anomaly is due to the ordering of the ferrimagnetic Mn_3O_4 phase, which is very prominent with the increase in Sr- deficiency, this result corroborates with that obtained from the Rietveld refinement analysis. It was seen that the magnetization of La-0.09 and Sr-0.09 compounds are greater than that of the pristine compound due to the increase in DE interaction. However, the magnetization increases further for Sr-0.18 and then decreases for Sr-0.27, which means that Sr-0.18 compound shows maximum magnetization among all the Sr-deficient compounds. Thus the DE interaction and FM nature of Sr-0.18 and Sr-0.27 compounds do not merely destroy by Sr-deficiency. It can be understood that the high magnetization value of Sr-0.18 and Sr-0.27 compounds compared to that of the pristine compound is due to the multiple DE interaction through intervening Mn^{2+} ions at the A-site. It suggests that the coexistence of $Mn^{2+}/Mn^{3+}/Mn^{4+}$ ions in Sr-0.18 and Sr-0.27 compounds can be corroborated with the result obtained from XPS analysis. However, the unconventional charge hopping mechanism completely depends on the ratio of Mn^{2+}/ Mn^{3+}/ Mn^{4+} ions, the Sr-0.18 compound shows maximum magnetization, and after that decreases for Sr-0.27 compound. It suggests that the existence of Mn^{2+} ions in deficient compounds is responsible for the increase in the DE interaction, which is in agreement with the coexistence of the mixed-valence state of Mn^{2+}/ Mn^{3+}/ Mn^{4+} in deficient compounds as obtained from XPS analysis. It is to be noted that the T_C is tuned from 365 K (pristine) to 355 K for Sr-0.09 compound, however, the same is further tuned down to 314 K and 277 K for Sr-0.18 and Sr-0.27 compounds respectively. The significant reduction in T_C towards room temperature in both the compounds is due to the changes in the average ionic radius and the changes in the Goldschmidt tolerance factor. From the Rietveld refinement analysis, it is evident that the average A-site ionic radius and unit cell volume of both the compounds increases with increase in Sr-deficiency. As the tolerance factor of the compounds is directly proportional to the average

A-site cationic radius, the decrease in T_C with the increase in Sr-deficiency can be related to the increase in tolerance factor.

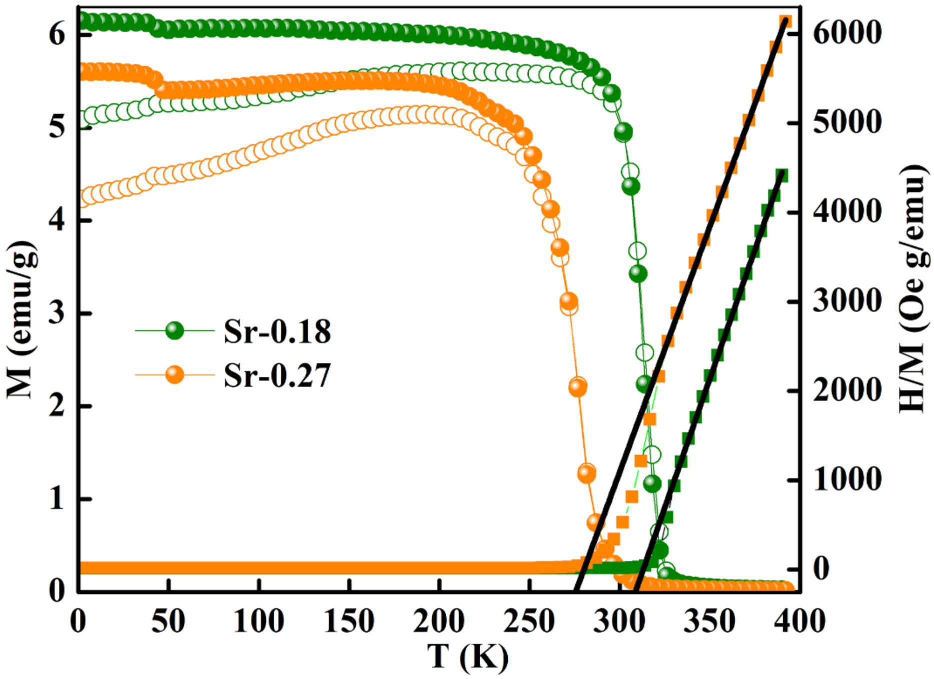

***Fig. 6.11.** Temperature dependence of magnetization of (a) Sr-0.18 and (b) Sr-0.27 compounds under 100 Oe field*

Further, the isothermal magnetization measurement was carried out at 2 K and 300 K and are shown in Fig. 6.12(a) and (b) respectively. Both the compounds show a small coercive field with soft ferromagnetic nature. It can be seen that magnetization increases rapidly at low field and does not saturate even at a field of 90 kOe. The hysteresis loops at 2 K confirm the high FM nature of the compounds, and it is evident that the FM nature is not merely destroyed by the increase in Sr-deficiency. From the hysteresis loop at 300 K, it can be understood that Sr-0.18 compound shows more FM character than that of Sr-0.27 compound, which confirms the room temperature FM behaviour of the former. The competing exchange interaction between DE and SE due to the FM/AFM components vary with the $Mn^{2+}/Mn^{3+}/Mn^{4+}$ ratio, which in turn significantly affects the isothermal magnetization behaviour of the deficient compounds at 2 K and 300 K.

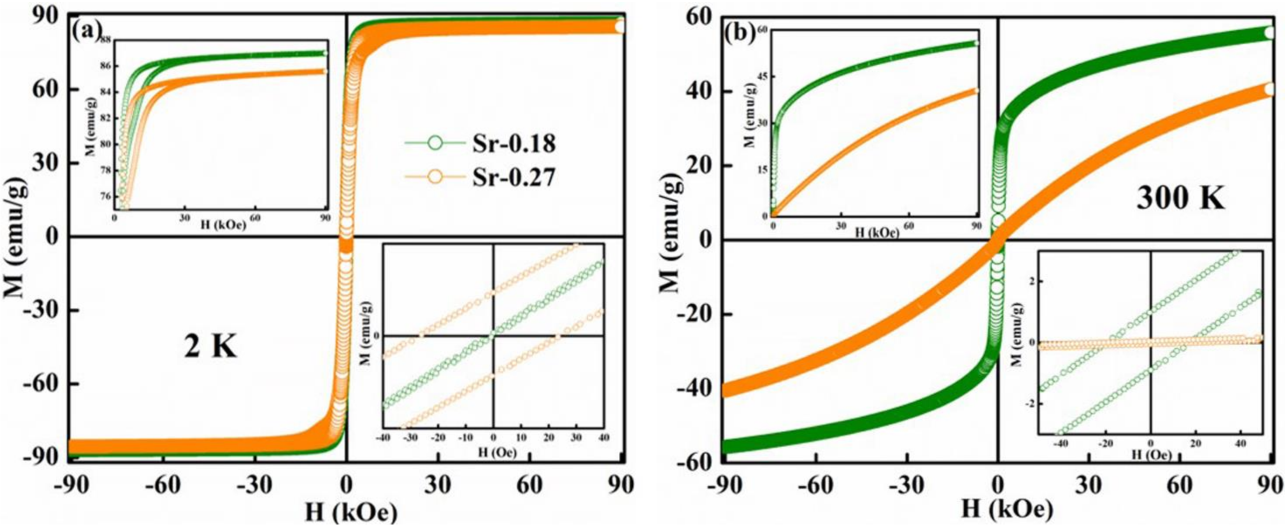

Fig. 6.12. *M-H loops at (a)2 K and (b) 300 K of Sr- 0.18 and Sr-0.27 compounds. The inset shows the enlarged view of the coercive field*

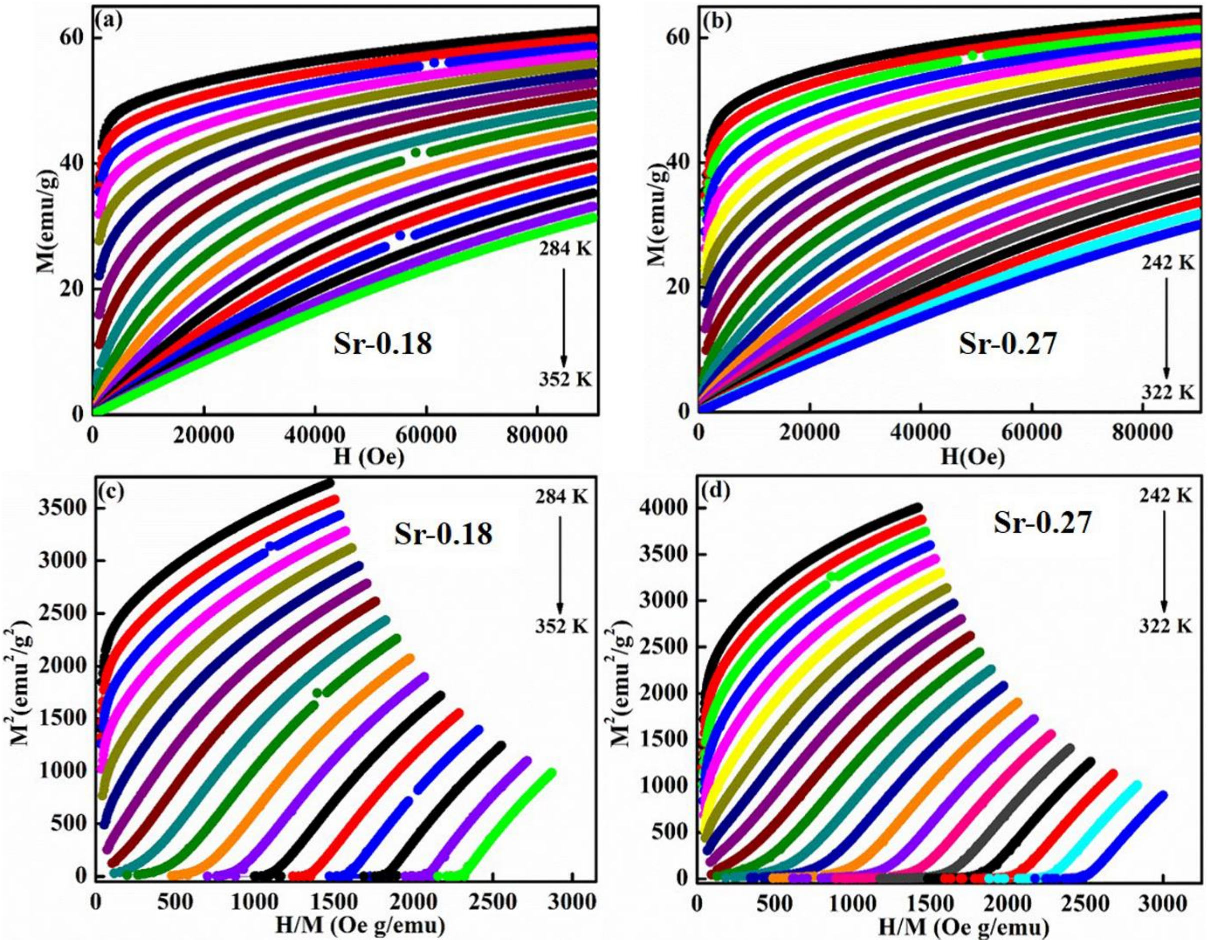

Fig. 6.13. *Isothermal field dependence magnetization of (a) Sr-0.18 and (b) Sr-0.27 and Arrott plot of (c) Sr-0.18 and (d) Sr-0.27 compounds*

Furthermore, the isothermal magnetization measurements around the respective T_C was measured and are shown in Fig. 6.13(a) and (b). The magnetization was measured from 284 K to 354 K for Sr-0.18, and 242 K to 322 K for Sr-0.27 with temperature interval of every 4 K. For $T < T_C$, a FM nature with a non-saturating behaviour at higher fields is seen for both the compounds. However, for $T > T_C$, a PM behaviour with a reduction in magnetization was observed. To further understand the nature of the magnetic transition, Arrott plots were plotted and are shown in Fig. 6.13(c) and (d). The regular Arrott plot between M^2 and H/M indicates that the transition governing the mean field model and the curve that pass through the origin should represent the T_C. Moreover, based on the Banerjee's criterion, a positive slope in the Arrott plot confirms that both the compounds undergo second-order transition [216].

6.3.2.4. Magnetocaloric properties

The ΔS_M is calculated from the isothermal magnetization curves based on the Maxwell relation [148]. The ΔS_M as a function of temperature for 10-50 kOe field is shown in Fig. 6.14. Both the compounds show a maximum $-\Delta S_M$ around T_C, and a reduction is seen on either side of the curve. For a field of 10 kOe, the Sr-0.18 compound exhibit a maximum $-\Delta S_M$ value of 1.40 J kg^{-1} K^{-1} at 306 K, and for Sr-0.27 compound, the $-\Delta S_M$ reaches a maximum value of 1.17 J kg^{-1} K^{-1} at 272 K. It can be seen that with increase in the magnetic field, the maximum $-\Delta S_M$ value is slightly shifted to the high-temperature region for both the compounds. For a field of 50 kOe, the Sr-0.18 compound exhibit a $-\Delta S_M$ value of 4.61 J kg^{-1} K^{-1} at 310 K, and for Sr-0.27 compound, the ΔS_M reaches a maximum value of 4.11 J kg^{-1} K^{-1} at 276 K. Thus, we have achieved a near room temperature (310 K) MCE with a significant $-\Delta S_M$ value of 4.61 J kg^{-1} K^{-1} for Sr-0.18 compound which is larger than that reported for numerous perovskite manganites [178, 180, 184, 202, 256].

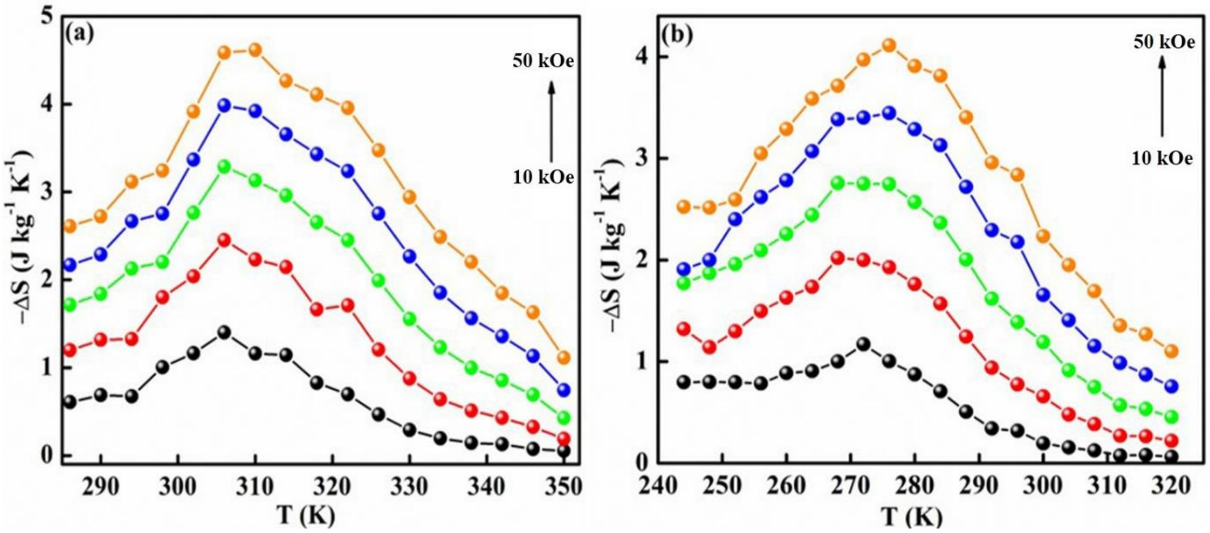

Fig. 6.14. *Magnetic entropy change of (a) Sr-0.18 and (b) Sr- 0.27 compounds*

Apart from the spin, charge and orbital ordering, the conventional DE interaction is the only favourable mechanism behind the entropy change in the pristine compound. However, from the magnetization and magnetocaloric properties, it can be understood that the presence of Mn^{2+} ions in deficient compounds enhances the ferromagnetism and ΔS_M due to the multiple DE interactions via Mn^{3+}-O^{2-}-Mn^{2+}-O^{2-}-Mn^{4+} path. In addition to that, the $Mn^{2+}/Mn^{3+}/Mn^{4+}$ ratio is the key parameter that determines the strength of the multiple DE interactions and hence, the ΔS_M of the deficient compounds. For practical applications at room temperature, the magnetocaloric materials should have a maximum ΔS_M value within the range of $300\ K \leq T \leq 310\ K$. Hence Sr-0.18 compound is found to be an ideal candidate for room temperature magnetocaloric applications. Thus, the present investigation reveals that a significant $-\Delta S_M$ near room temperature can be achieved by the creation of deficiency at the Sr-site in $La_{0.67}Sr_{0.33}MnO_3$ compound and the composition with a deficiency of y= 0.18, i.e., $La_{0.67}Sr_{0.33-y}MnO_{3-\delta}$ (y= 0.18) could be a potential material for room temperature magnetic refrigeration applications.

6.4. Conclusion

- We have studied the effect of both La-deficiency and Sr-deficiency on the structural, magnetic and magnetocaloric properties in $La_{0.67}Sr_{0.33}MnO_3$ and found the following observation.
- Both La/Sr-deficient compounds enhance the ΔS_M values. But, the Sr-site deficient compound shows a promising behaviour of reduction in the T_C towards room temperature.
- $La_{0.67}Sr_{0.33-y}MnO_{3-\delta}$ (y= 0.18) was found to be ferromagnetic at 300 K and exhibit a $-\Delta S_M$ of 4.61 J kg^{-1} K^{-1} at 310 K for a 50 kOe field.
- The present study indicates that the creation of deficiency at the Sr-site of $La_{0.67}Sr_{0.33}MnO_3$ helps to tune the T_C towards room temperature with a significant ΔS_M value and the compound could be a potential candidate for room temperature magnetic refrigeration applications.

Chapter 7

Investigation on structural, magnetic and magnetocaloric properties in $(RE_{MIX})_{0.67}Sr_{0.33}MnO_3$ manganites using different combinations of mixed rare earth oxide precursors

A cost effective precursor material to develop a magnetocaloric material for magnetic refrigeration is discussed in this chapter. A mixed rare earth manganite $(RE_{MIX})_{0.67}Sr_{0.33}MnO_3$ was prepared using a natural mixture of rare earth oxide (RE_2O_3-1), which is a by-product derived from the Indian monazite sand after thorium extraction. The $(RE_{MIX})_{0.67}Sr_{0.33}MnO_3$ compound is found to be ferromagnetic at room temperature and exhibit a $-\Delta S_M$ of 3.28 J kg^{-1}K^{-1} at 310 K under a field change of 50 kOe and makes it a potential candidate for room temperature magnetic refrigeration applications. Further, two different kinds of mixed rare earth oxide (RE_2O_3-2 and RE_2O_3-3) were prepared by commercially available high purity rare earth oxides. The $(RE_{MIX})_{0.67}Sr_{0.33}MnO_3$ composition was again prepared by RE_2O_3-2 and RE_2O_3-3 individually and their structural, magnetic and magnetocaloric properties were studied.

7.1. Introduction

In this chapter, we have used a raw material RE_2O_3-1, which is a mixture of various rare earth oxides, obtained after the removal of radioactive thorium from Indian monazite sand. Indian monazite, a beach placers sand contains up to 60–66 % RE_2O_3-1, 8–10 % ThO_2 and 20–25 % P_2O_5 as major constituents. RE_2O_3-1 contain CeO_2 (47.5%), La_2O_3 (22.0%) as the major components and Pr_6O_{11}, Nd_2O_3 and Sm_2O_3 in appreciable amount (shown in Table 7.1) [293]. To avoid complicated, and expensive separation and purification techniques, the by-product RE_2O_3-1 obtained from the monazite sand has been directly used as a raw material for the preparation of $(RE_{MIX})_{0.67}Sr_{0.33}MnO_3$ (RESMO-1) compound. We are the pioneers in attempting to make the direct use of mixed rare earth oxides (without separation into individual rare earth oxides) as cost-effective and efficient raw materials for the development of rare-earth manganite for the magnetocaloric applications. Even though RE_2O_3-1 is an inexpensive raw material, the major drawback is its impure nature, which in turn may be detrimental to the magnetic and magnetocaloric properties. Therefore, as a continuing effort, we have further used two different kinds of mixed rare earth oxides combination (RE_2O_3-2 and RE_2O_3-3, containing high purity, 99.9 % rare earth oxides) in which RE_2O_3-2 has the same composition as that of RE_2O_3-1 while RE_2O_3-3 is completely free of CeO_2. The chemical composition of RE_2O_3-2 and RE_2O_3-3 is shown in Table 7.1. We have also synthesized $(RE_{MIX})_{0.67}Sr_{0.33}MnO_3$ (RESMO-2) and $(RE_{MIX})_{0.67}Sr_{0.33}MnO_3$ (RESMO-3) compounds using RE_2O_3-2 and RE_2O_3-3 respectively by the conventional solid-state method and have studied the structural, magnetic and magnetocaloric properties of the compounds and compared them with that of RESMO-1 compound.

Composition wt. %	RE_2O_3-1*	RE_2O_3-2	RE_2O_3-3
CeO_2	47.5	47.5	-
La_2O_3	22.0	22.0	32.26
Pr_6O_{11}	7.80	7.80	12.85
Nd_2O_3	17.1	17.1	28.18
Sm_2O_3	3.10	3.10	5.11
Eu_2O_3	0.015	0.015	0.03
Gd_2O_3	1.40	1.40	2.31
Tb_4O_7	0.10	0.10	0.16
Dy_2O_3	0.20	0.20	0.33
Ho_2O_3	0.10	0.10	0.16
Er_2O_3	0.10	0.10	0.16
Y_2O_3	0.40	0.40	0.69

Table 7.1. *Chemical composition of RE_2O_3-1 (natural mixture of rare earth oxides obtained from Indian monazite sand), RE_2O_3-2 and RE_2O_3-3(prepared by high pure oxides)*

7.2. Experiment

RESMO-1 compound was prepared by solid-state reaction method by taking RE_2O_3-1 (Indian Rare Earth Ltd. Kerala, India), $SrCO_3$ (Sigma-Aldrich, 98 %), $MnCO_3$ (Sigma-Aldrich, 99.9+ %) as raw materials. However, high pure La_2O_3, Nd_2O_3, CeO_2, Pr_2O_3 etc. were used as raw materials for the preparation of RESMO-2 and RESMO-3 compounds. The stoichiometric amounts of the same were mixed in an agate mortar for 6 h until the mixture became homogenous. It was then calcined at 1200 °C for 12 h. The powder was pulverized and pelletized in the form of uniform and compact pellets, which were sintered at 1350 °C for 12 h in air. The crystal structure and phase purity of the compounds were analyzed using XRD. Rietveld refinement of the diffraction patterns was carried out using the FullProf software. Microstructural analysis was conducted using a scanning electron microscope.

Magnetic, electrical resistivity and specific heat measurements were made as a function of temperature and applied field using PPMS.

7.3. Results and discussion

7.3.1. Mixed rare earth oxides derived from Indian monazite sand as an inexpensive precursor material for magnetic refrigeration applications

7.3.1.1. Structural analysis

The Rietveld refined XRD patterns of RESMO-1 compound is shown in Fig. 7.1. The recorded diffracted patterns are very likely to be a superimposed pattern of several rare-earth manganites having the same crystal structure. There is one more possibility that different rare-earth cations are likely to be substituted at the A site of $(RE_{MIX})_{0.67}Sr_{0.33}MnO_3$. The compound is crystallized into a mixed phase with a major phase having perovskite structure of orthorhombic crystal symmetry with Pbnm space group, while minor phase has CeO_2 of cubic symmetry with Fm3m space group [294]. The refinement results are shown in Table 7.2.

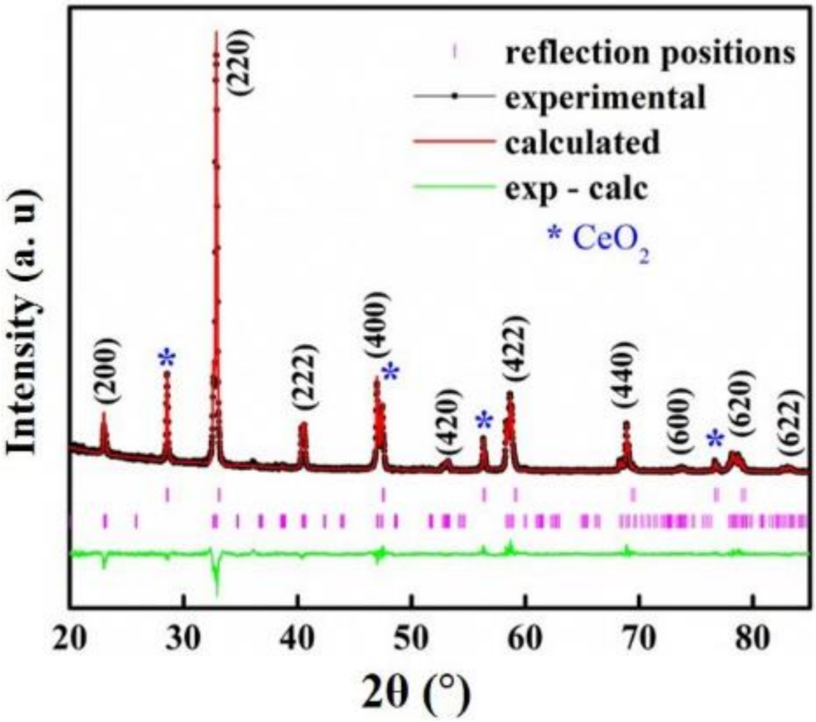

Fig. 7.1. *Rietveld refined XRD patterns of RESMO-1 compound at room temperature. Dotted circles (black) correspond to the XRD data, and the lines (red) are theoretical fits to the observed XRD data. The difference pattern between the observed data and the theoretical fit is shown at the bottom (green)*

(a)	**Primary phase**
Cell parameters	
a (Å)	5.4465(10)
b (Å)	5.4880(8)
c (Å)	7.6771(13)
Positional parameters	
RE/Sr x	0.4965
RE/Sr y	0.0010
O1 x	0.5270
O1 y	0.5401
O2 x	0.2475
O2 y	0.2559
O2 z	0.0102
Occupancy/ Atomic displacement parameter	
RE	0.6522/ 0.0121
Sr	0.3341/ 0.0121
Mn	1.0008/ 0.0252
O1	1.0012/ 0.0126
O2	1.0007/ 0.0117
Agreement factors	
R_{WP}	9.36
R_P	7.62
χ^2	2.09

(b)	**CeO_2**
Cell parameters	
a (Å)	5.4130(5)
b (Å)	5.4130(5)
c (Å)	5.4130(5)
Positional parameters	
Ce x	0
Ce y	0
Ce z	0
O x	0.25
O y	0.25
O z	0.25

Table 7.2(*a). Refinement parameters obtained for rare earth manganite phase (b). Refinement parameters obtained for CeO_2 phase*

7.3.1.2. Surface morphology

The surface microstructure of well densified RESMO-1 compound was shown in Fig. 7.2(a) and (b). The micrographs show grains with two different types of morphology: one is bigger grains with size ranging from 3 μm to 10 μm (area 1) which are in polygonal shape and the other one is smaller grains of sphere-like shape with size varying from 1 μm to 3 μm (area 2). There is a noticeable contrast difference between bigger and smaller grains. The polygonal kind of grains are well packed, and the grain boundaries are visible. Further, the analysis of chemical composition using EDAX on several areas confirmed that the bigger grains correspond to mixed rare earth manganites and smaller grains correspond to CeO_2. It is to be noted that Ce has higher thermal stability and a smaller value of enthalpy of fusion compared to other RE ions, and thereby, rare earth manganite phase does not accept Ce, thus forming the secondary phase of CeO_2 [294]. However, Ce is the most abundant cation in the raw material, some amount of Ce was substituted at the RE site of RESMO-1 which is confirmed via EDAX. Table. 7.3 shows the EDAX analysis of the RESMO-1 compound. From the table, it can be seen that area 1 corresponds to the rare-earth manganite phase, and area 2 corresponds to Ce rich phase which further corroborates with the XRD results.

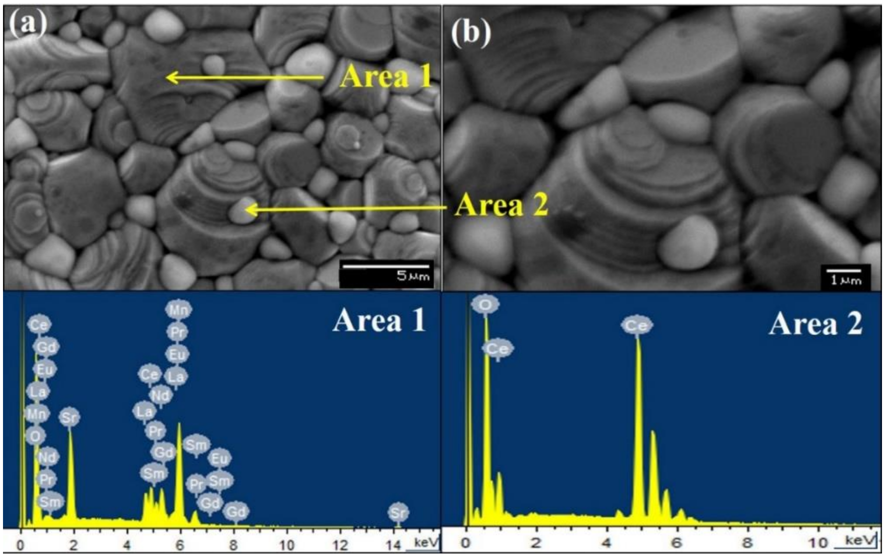

Fig. 7.2. *SEM images: (a) 5 µm and (b) 1 µm scale with EDAX spectrum of area 1 and area 2*

Area 1

Element	wt. %	At. %
O K	25.73	65.84
Mn K	22.11	16.48
Sr L	14.55	6.80
La L	10.42	3.07
Ce L	13.56	3.96
Pr L	2.55	0.74
Nd L	8.67	2.46
Sm L	1.23	0.34
Eu L	0.24	0.07
Gd L	0.94	0.24

Area 2

Element	wt. %	At. %
O K	26.40	75.85
Ce L	73.60	24.15

Table 7.3. *EDAX analysis of RESMO-1 compound*

7.3.1.3. Magnetic characterization

Fig. 7.3. shows the temperature variation of magnetization, M(T), carried out in ZFC and FC modes from 2-380 K, under an external field of 50 Oe. The compound undergoes a sharp T_C around 310 K, and it remains ferromagnetic down to 42 K, and then magnetization decreases. Further, the temperature dependence of the inverse susceptibility of the compound has been plotted. From Fig. 7.3, it is clear that the compound obeys the Curie- Weiss law above T_C which indicates a decrease in disorder and low magnetic frustration of the compound. A drop in magnetization observed at lower temperatures indicate the existence of AFM coupling due to the presence of CeO_2 [295]. The bifurcation in the M-T curve is due to the magnetic frustration between the competing magnetic exchange interactions [296-298]. The irreversibility can also arise as a result of magnetic hysteresis contributed by the domain structure.

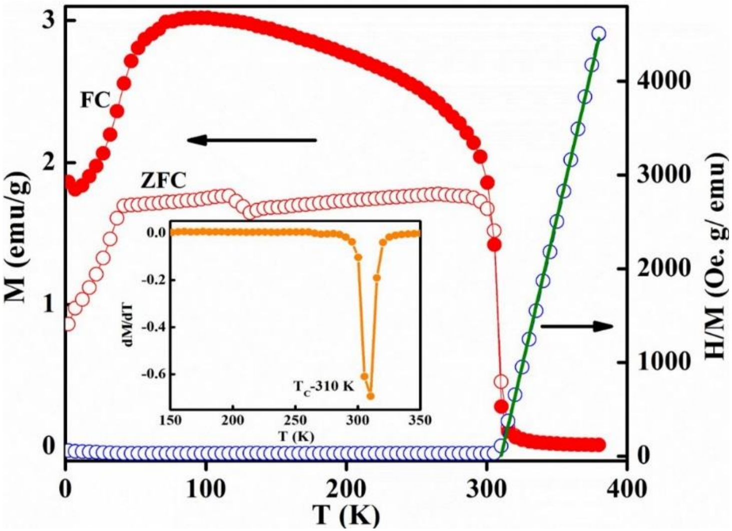

Fig. 7.3. *Temperature dependence of zero-field-cooled (ZFC) and field-cooled (FC) dc magnetization of* $(RE_{MIX})_{0.67}Sr_{0.33}MnO_3$ *compound measured under the magnetic field of 50 Oe and their inverse susceptibility along with linear fit to Curie-Weiss law. The inset figure shows the derivative of magnetization (dM/dT) versus Temperature curve*

However, the variation of magnetization with the applied magnetic field is essential to confirm the existence of competing magnetic states. Thus, we have carried out the isothermal magnetization at 2 K and is shown in Fig. 7.4(a). It shows a typical hysteresis with a small coercive field of 266 Oe, indicates that the compound having soft FM nature. Again, the magnetization values increase rapidly at lower magnetic fields but do not saturate even at applied magnetic fields as high as 90 kOe. This behaviour could be due to the presence of two different magnetic components, a FM component that gets quickly saturated at lower fields and an AFM component that doesn't saturate even at very high fields. The competing nature of these two components results in such a non-saturating behaviour. The presence of FM component can be understood due to the DE interaction between Mn^{3+}-O-Mn^{4+}, whereas AFM component is due to the SE interaction, and these results are in agreement with the earlier reports in conventional manganites [223].

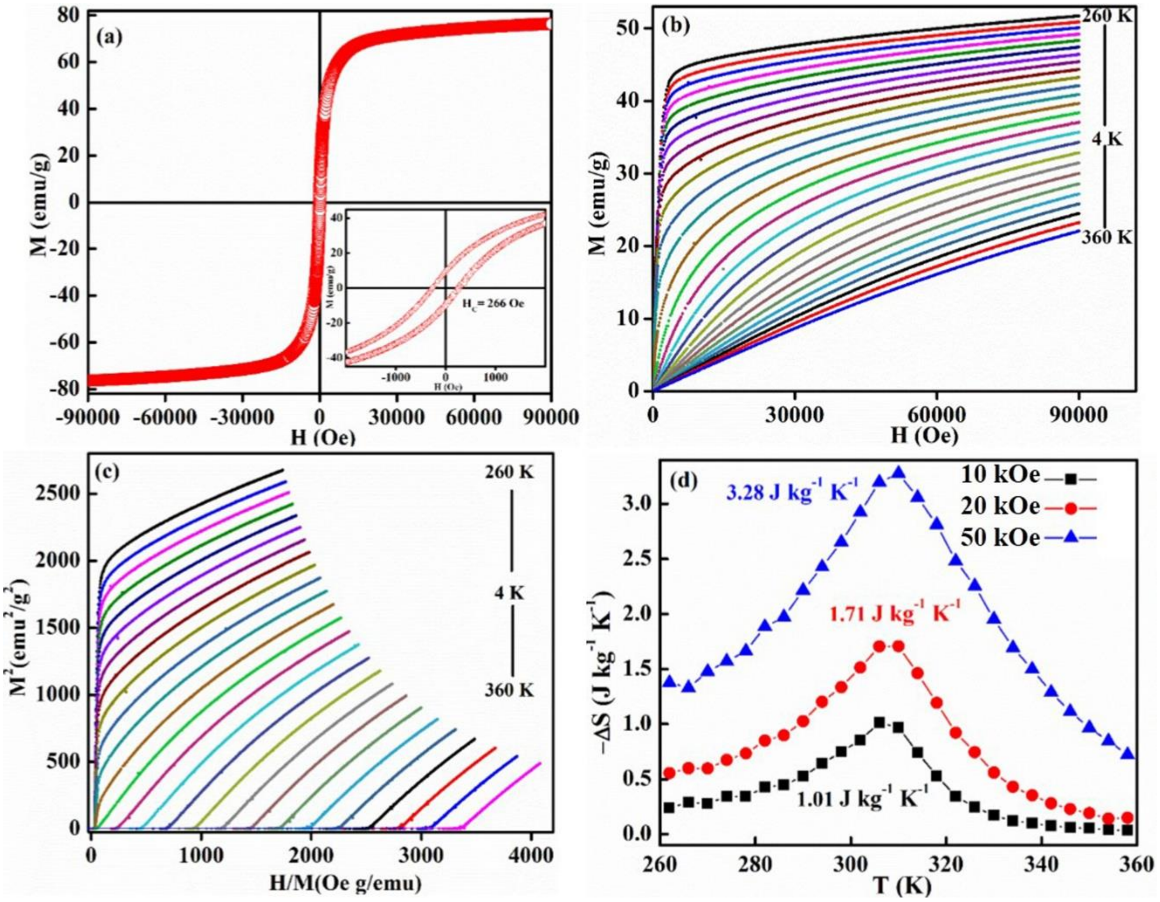

Fig. 7.4. *(a) Hysteresis loop at 2 K, Inset: Enlarged view of the hysteresis loop, (b) Isothermal field dependence of magnetization of the compound, (c) Arrott plots (M^2 Vs H/M), (d) The magnetic entropy change at 10 kOe, 20 kOe and 50 kOe magnetic fields*

To determine the magnetic phase transitions precisely, we have measured a series of isothermal magnetization curves M(H) at different temperatures around T_C with an interval of 4 K and the same is shown in Fig. 7.4(b). It is noticed that the M(H) curves below T_C, show a non-linear behaviour with a sharp rise at lower fields and it is not saturated even at a field of 90 kOe, reflecting the FM nature of the compound. However, for temperatures above $T_{C,}$ the magnetization decreases drastically, and the curves show almost linear behaviour indicating the PM nature. We have performed Arrott plots of M^2 vs. H/M in the vicinity of T_C (shown in Fig. 7.4(c)), and according to Banerjee's criterion [216], the positive slope in the Arrott plot indicates that the phase transition is of second order in nature.

7.3.1.4. Magnetocaloric properties

The variation of magnetization near the T_C results in a significant effect in ΔS_M. We have plotted the temperature variation of $-\Delta S_M$ under the magnetic fields of 10 kOe, 20 kOe and 50 kOe is shown in Fig. 7.4(d). We obtained a $-\Delta S_M$ value of 1.01 J kg^{-1} K^{-1} and 1.71 J kg^{-1} K^{-1} under 10 kOe and 20 kOe magnetic field change respectively. It can be seen that the $-\Delta S_M$ reaches a maximum value of 3.28 J kg^{-1} K^{-1} at 310 K for 50 kOe field change. Further, we have carried out the temperature variation of C_P from 200 K to 380 K under 10 kOe and 50 kOe magnetic field to measure the ΔT_{ad}**.** The C_P as a function of temperature is depicted in Fig. 7.5 (a). From the figure, it can be seen that the C_P approached the highest value of 538 J kg^{-1} K^{-1} at 300 K for zero magnetic field. It is also observed that C_P decreases with the increase in the magnetic field. The ΔT_{ad} is calculated from the C_P value, which is plotted as a function of temperature under 10 kOe and 50 kOe magnetic fields and shown in Fig. 7.5(b). The ΔT_{ad} increases with increase in temperature and reaches a maximum value of 0.62 K under 10 kOe and 2.11 K under 50 kOe at 310 K and decreases there after as evident from Fig. 7.5(b). The behaviour of ΔT_{ad} indicate that the compound is a good candidate for room temperature magnetic refrigeration applications.

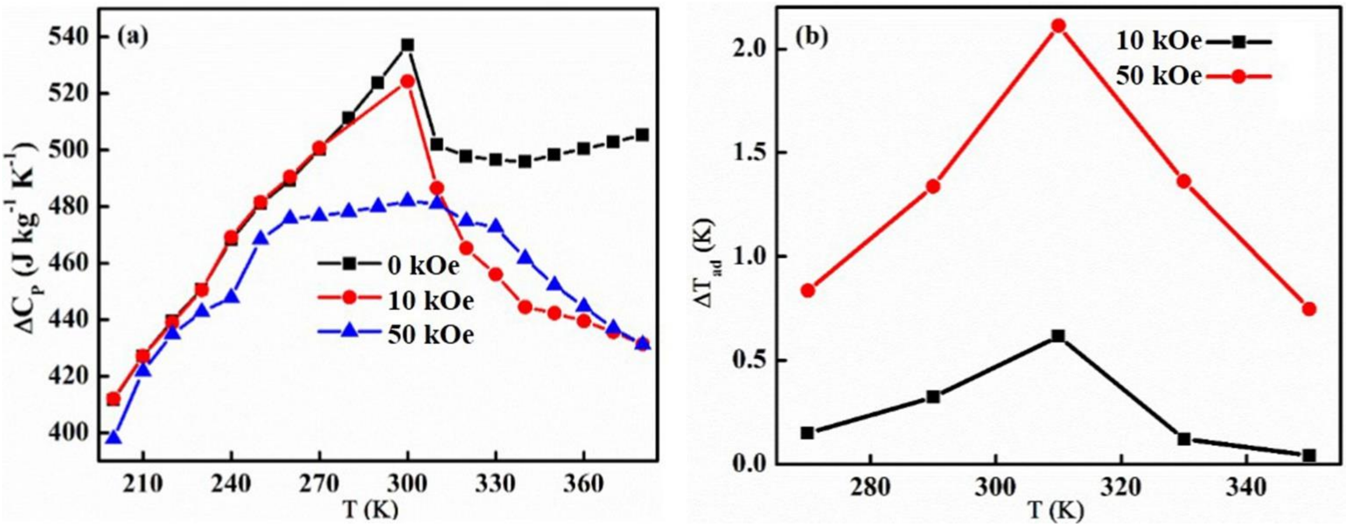

Fig. 7.5. (a) Specific heat of RESMO-1 as a function of temperature, **(b)** Adiabatic temperature change of RESMO-1 as a function of temperature

7.3.1.5. Electrical transport properties

To understand the electrical transport behaviour of the compound, we have carried out the variation of ρ(T), in the range of 2-300 K with and without the application of magnetic fields and is shown in Fig. 7.6. While lowering the temperature, ρ(T) increases gradually and then decreases by making a broad maximum around 180 K, indicating a metal to insulator transition. The resistivity is found to decrease upon the application of the magnetic field (90 kOe), and the T_P is shifted to higher temperatures. It is interesting to notice that the absolute value of ρ (T) and the behaviour of ρ (T) are similar to those $RE_{0.67}Sr_{0.33}MnO_3$ (RE = La, Pr, Nd) manganites as reported in the literature [225, 299]. The compound exhibits an improvement in $-\Delta S_M$ and ΔT_{ad} values at the room temperature without affecting its electrical transport behaviour, which is a challenging move towards the development of cost-effective room temperature magnetocaloric materials.

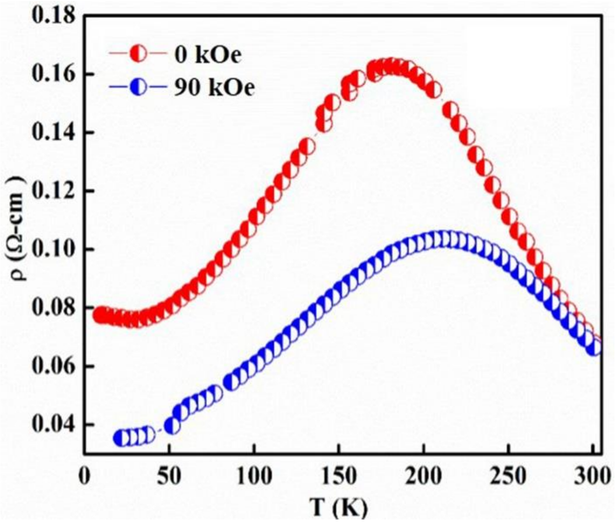

Fig. 7.6. *Temperature variation of electrical resistivity of RESMO-1 compound measured with and without the presence of magnetic field*

7.3.2. Magnetocaloric properties of $(RE_{MIX})_{0.67}Sr_{0.33}MnO_3$ manganites using different combination of mixed rare earth oxide precursors

We have synthesized RESMO-2, and RESMO-3 compounds using precursors RE_2O_3-2 and RE_2O_3-3 respectively and have studied the structural, magnetic and magnetocaloric properties.

7.3.2.1. Structural analysis

The X-ray powder diffraction patterns confirm that both the RESMO-2 and RESMO-3 compounds belong to orthorhombic crystal symmetry with Pbnm space group. The Rietveld refinement of both the compounds is done based on the assumption that the compounds are more likely to be a solid solution of different rare-earth cations based on the concentration of oxides given in Table. 7.1. The refined XRD patterns obtained from the Rietveld analysis are shown in Fig. 7.7, and the structural parameters obtained are shown in Table 7.4. The experimental patterns of the compounds are in good agreement with the calculated XRD patterns, and the refinement confirms the presence of secondary phases in both the compounds. In RESMO-2, we have found some additional peaks at 28.55° and 56.36° due to the presence of CeO_2 as secondary phase (marked by * in Fig. 7.7(a)). Thus the Rietveld refinement result of RESMO-2 resembles that of RESMO-1[300]. Due to the prominent presence of CeO_2 in RESMO-2, we couldn't achieve better goodness of fit since the number of parameters to be refined is greater. The presence of CeO_2 is very prominent in RESMO-2, and this could affect the structural, magnetic and electrical transport properties. The RESMO-3 compound is completely free of CeO_2, however, it contains some additional peaks at 27.83°, 28.84° and 49.82° due to the presence of La_2O_3 as secondary phase (marked by * in Fig. 7.7(b)). Even though the secondary phase of La_2O_3 is present is in RESMO-3, it is not as prominent as compared to the secondary phase observed in RESMO-2. Thus RESMO-3 shows better goodness of fit and less χ^2 value than that of RESMO-2. It is confirmed that the major phase of both the compounds is a mixture of various rare-earth manganites having orthorhombic crystal symmetry with Pbnm space group. However, the secondary phases such as CeO_2 belongs to cubic symmetry with Fm-3m space group, and La_2O_3 belongs to hexagonal symmetry with $R\overline{3}c$ space group. From the refinement analysis, we do not find any additional peaks for Mn_3O_4 phase, since the formation of this ferrimagnetic rhombohedral phase depends on the formation conditions [259].

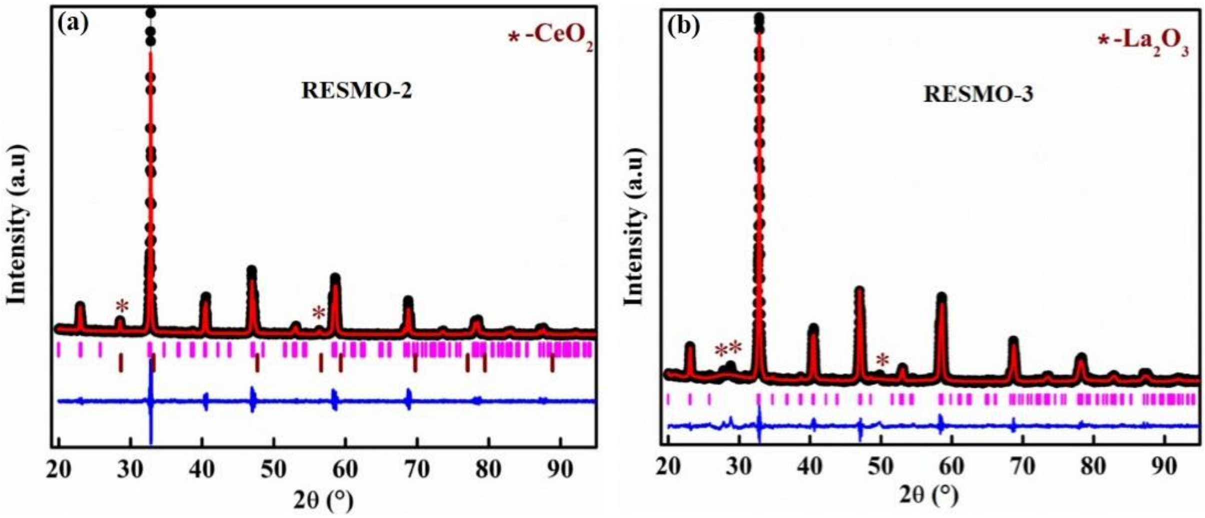

Fig. 7.7. *Rietveld refined XRD patterns of (a) RESMO-2 and (b) RESMO-3 compounds. Black colour indicates the experimental data. Red lines are theoretical fits to the XRD data; pink and green lines correspond to the Bragg reflection. The bottom blue lines correspond to the difference between the experimental and the theoretical fits*

	RESMO-2	**RESMO-3**
Cell parameters		
a (Å)	5.4530(1)	5.427(1)
b (Å)	5.4922(1)	5.4788(2)
c (Å)	7.7001(2)	7.6900(1)
V ($Å^3$)	230.61(1)	228.72(1)
Positional parameters		
RE/Sr x	0.4977(7)	0.4971(5)
RE/Sr y	0.0084(9)	0.0098(7)
O1 x	0.5391(6)	0.5589(29)
O1 y	0.5260(7)	0.4850(5)
O2 x	0.237(4)	0.2203(1)
O2 y	0.2130(5)	0.2814(4)
O2 z	0.0233(27)	0.0294(9)
Occupancy/ Atomic displacement parameter		
RE	0.6513 0.0067	0.6620/ 0.0238
Sr	0.3312/ 0.0067	0.3313/ 0.0238
Mn	0.9984/ 0.0060	0.9822/ 0.0261
O1	1.1503/ 0.0317	1.1320/ 0.0250
O2	1.0329/ 0.0123	1.1323/ 0.0222
Bond distance (Å)		
Mn-O1	1.942(4)	1.950(2)
Mn-O2	1.751(25)	1.966(0)
Mn-O2	2.140(25)	1.950(0)
Bond angle (°)		
Mn-O1-Mn	164.9(19)	160.5(9)
Mn-O2-Mn	167.9(13)	160.75(0)
Agreement factors		
R_{WP}	6.01	4.55
R_P	3.92	3.40
χ^2	4.9	2.6

Table 7.4. *Structural parameters of RESMO-2 and RESMO-3 compounds obtained from the Rietveld refinement of XRD*

7.3.2.2. Surface morphology

The microstructure of both the compounds are analysed and is shown in Fig. 7.8. From the well-densified microstructure, it is clear that RESMO-2 contain two different types of grains, indicating the presence of a prominent secondary phase. The bigger polygonal type of grains corresponds to the rare earth manganite phase, and the smaller sphere-like grains corresponds to the fluorite CeO_2 phase. Thus it is confirmed from the microstructure analysis that the presence of CeO_2 is very prominent in RESMO-2, which corroborates the result obtained from refinement analysis. Moreover, the microstructure of RESMO-2 resembles that of RESMO-1. However, such kind of grain differences could not be seen in RESMO-3 compound. Moreover, the grain boundaries are visible. Thus, it is confirmed that the secondary phase such as La_2O_3 is not prominent in RESMO-3 which corroborates the result obtained from the refinement analysis.

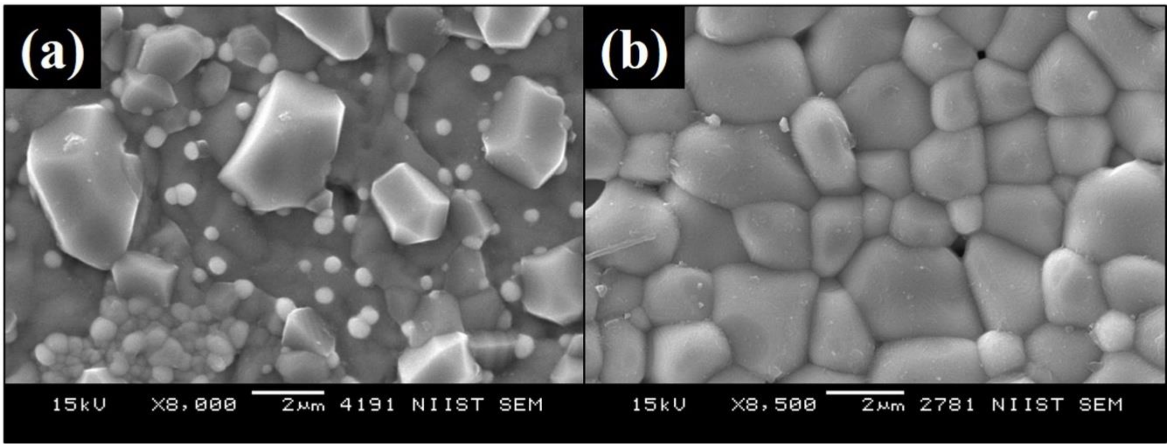

Fig. 7.8. *SEM images (a) RESMO-2 and (b) RESMO-3 compounds*

7.3.2.3. Magnetic characterization

Fig. 7.9 shows the variation of magnetization with temperature from 2-380 K under 50 Oe magnetic field. Large thermo-magnetic irreversibility has been witnessed for both the compounds due to the existing magnetic frustration in the compounds. Both the compounds show a sharp FM to PM transition at their respective T_C. In RESMO-2 compound, an AFM ordering is seen below 50 K, and this may be due to the presence of CeO_2 secondary phase, which is in corroboration with RESMO-1 [300]. However, in RESMO-3, CeO_2 is not used for the preparation of mixed rare earth oxide, and hence such a low-temperature ordering is not seen. Also, the magnetization value of the RESMO-3 compound is greater than that of RESMO-2, which suggest that the presence of CeO_2 destroys the FM interaction at low temperature and thereby decreases the magnetic moment due to the co-existence of FM and AFM interactions. From the dM/dT curve, we obtained a T_C of 306 K and 302 K for RESMO-2 and RESMO-3 compounds as shown in the inset of Fig.7.9. The inverse susceptibility as a function of temperature has also been plotted and is shown in Fig. 7.9. The RESMO-2 compound obeys the Curie-Weiss law above T_C. However, RESMO-3 is slightly disobeying the Curie-Weiss law above T_C, and this may be due to the high magnetic frustration present in the compound. It shows that RESMO-3 is not purely paramagnetic above T_C, which confirm the existence of some FM clusters in the PM matrix.

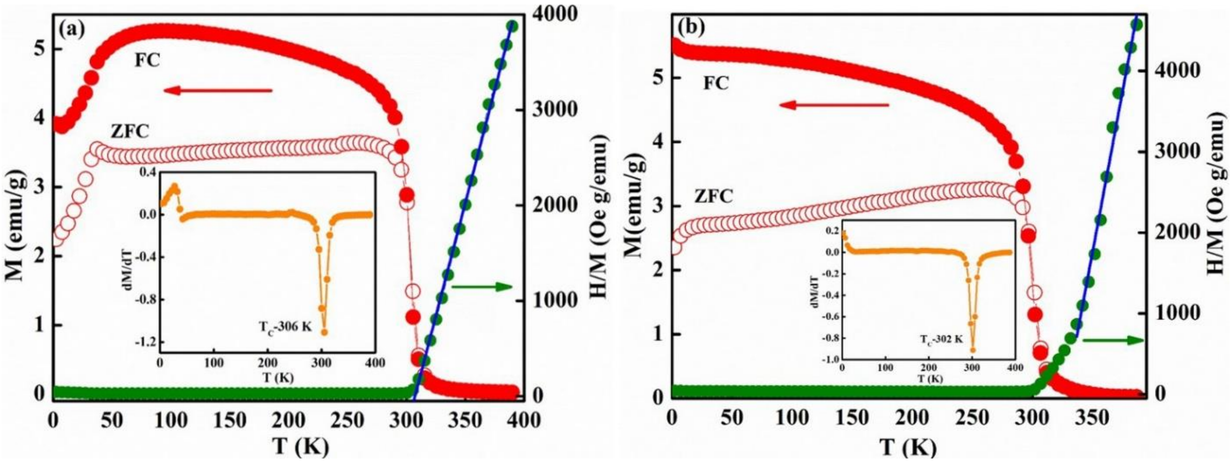

Fig. 7.9. Magnetization as a function of the temperature of (a) RESMO-2 and (b) RESMO-3 compounds under 50 Oe field

The isothermal magnetization measurements were carried out at 2 K for both the compounds and is shown in Fig. 7.10. The inset shows the enlarged view of the coercive field. From the hysteresis loop, a soft FM nature has been witnessed for both the compounds, having a coercive field of 196 Oe and 170 Oe for RESMO-2 and RESMO-3 respectively. The magnetization increases rapidly at lower magnetic fields and does not completely saturate even for a field of 90 kOe due to the competing exchange interaction between FM/AFM components.

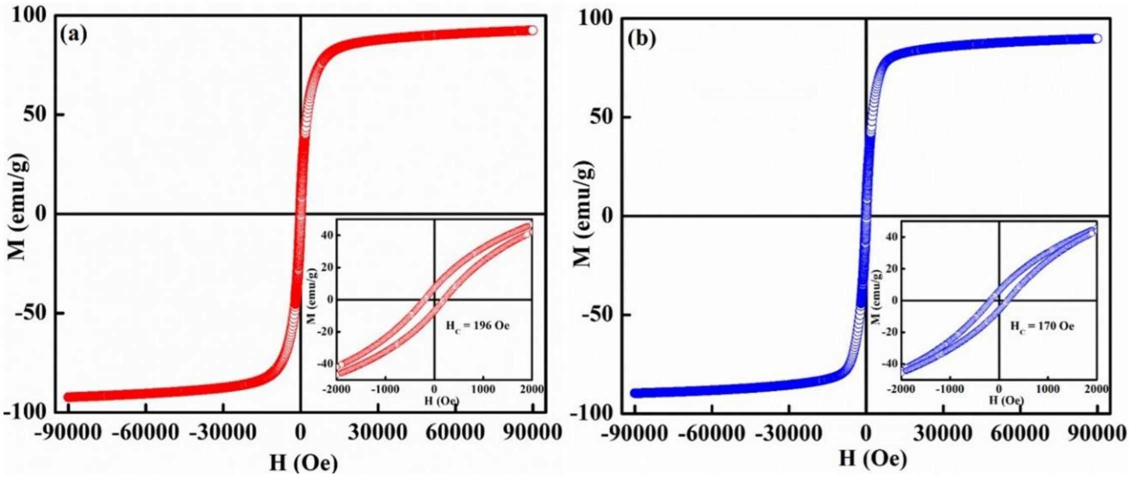

Fig. 7.10. M-H loop at 2 K of (a) RESMO-2 and (b) RESMO-3 compounds. The inset shows the enlarged view of the coercive field

Also, isothermal magnetization curves have been measured around T_C with 4 K interval for both the compounds and are shown in Fig. 7.11(a) and (b) respectively. For temperatures less than T_C, the compounds show FM nature, and for temperatures above T_C, PM behaviour is observed. According to the Banerjee's criterion [216], the positive slope in the Arrott plot of M^2 versus H/M indicates that the transition is of second order in nature. According to the mean field theory, the Arrott plots near T_C should show a series of straight lines and the line that passes through the origin represents the T_C.

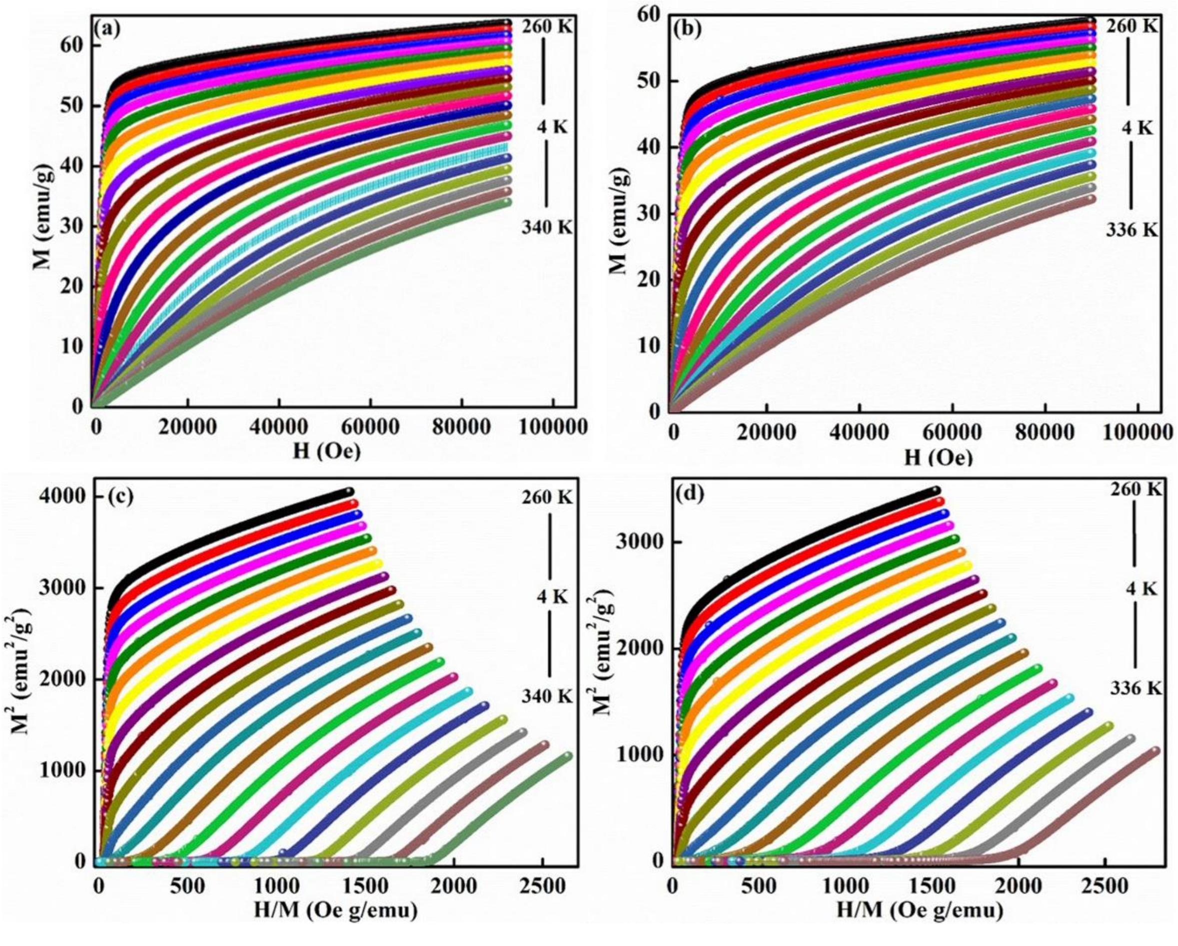

Fig. 7.11. Isothermal field dependence magnetization plots (a) RESMO-2, (b) RESMO-3 and Arrott plot of (c) RESMO-2 and (d) RESMO-3 compounds

7.3.2.4. Magnetocaloric properties

The variation of ΔS_M as a function of temperature for 10-50 kOe field change is shown in Fig. 7.12(a) and (b) for RESMO-2 and RESMO-3 respectively. Both the compounds show a maximum ΔS_M at their respective T_C, which decrease symmetrically on either side of the ΔS_M

curve. The RESMO-2 compound shows -ΔS_M values of 1.26 J kg^{-1} K^{-1} and 4.22 J kg^{-1} K^{-1} (at 302 K) for10 kOe and 50 kOe respectively, while RESMO-3 compound show -ΔS_M values of 1.08 J kg^{-1} K^{-1} (at 298 K) and 3.81 J kg^{-1} K^{-1} (at 302 K) for 10 kOe and 50 kOe respectively. The value of ΔS_M for both the compounds has enhanced compared to that of RESMO-1. The temperature variation of C_P from 200 K-380 K is measured for both the compounds under zero, 10 kOe and 50 kOe fields and is shown in Fig. 7.13. In the absence of magnetic field, the C_P approaches a maximum value of 550 J kg^{-1} K^{-1} (at 302 K) for RESMO-2 and 720 J kg^{-1} K^{-1} (at 300 K) for RESMO-3 respectively and decreases for higher magnetic fields.

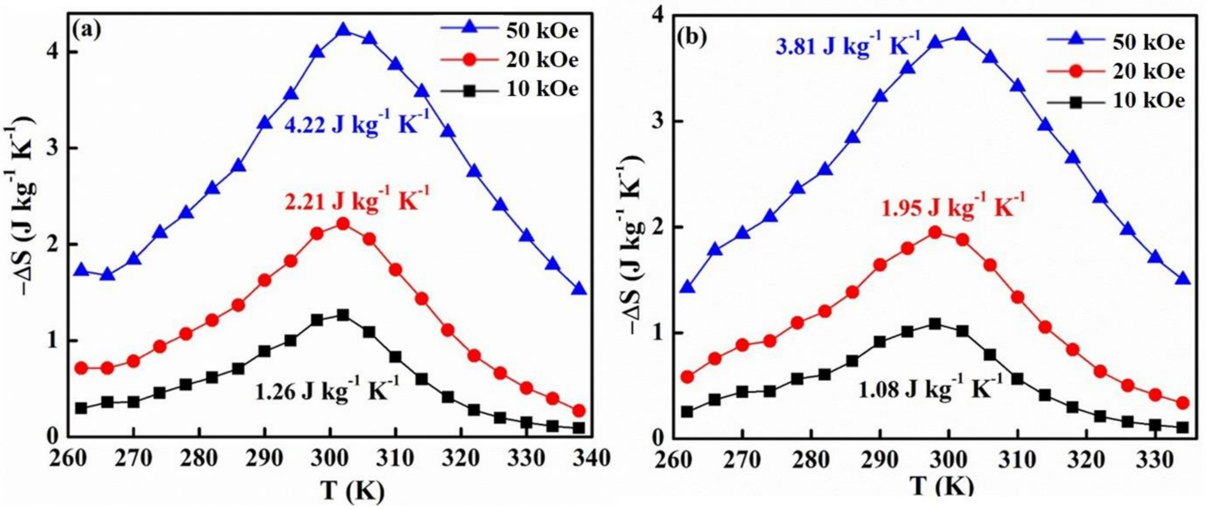

Fig. 7.12. *Magnetic entropy change of (a) RESMO-2 and (b) RESMO-3 compounds*

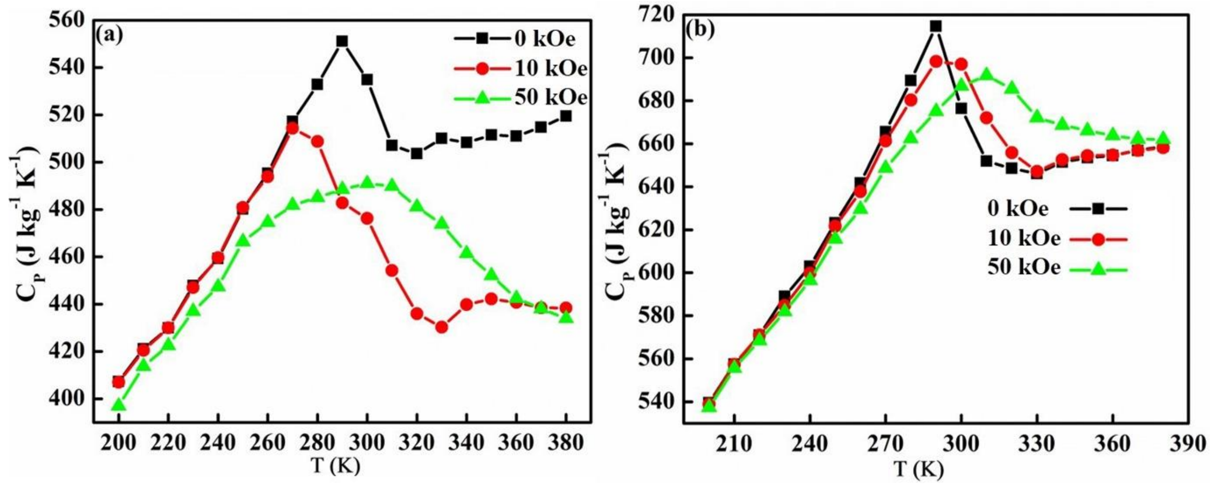

Fig. 7.13. *Variation of specific heat with the temperature of (a) RESMO-2 and (b) RESMO-3 compounds*

From Fig. 7.14, we can see that the value of ΔT_{ad} increases and reaches a maximum of 2.4 K for 50 kOe at 302 K for RESMO-2 and decreases with further increase in temperature. RESMO-3 exhibits a maximum ΔT_{ad} value of 1.5 K at 300 K for 50 kOe magnetic field. It could be seen that the value of ΔT_{ad} is enhanced for RESMO-2 but lowered for RESMO-3 in comparison to RESMO-1 [300]. This indicates that the presence of CeO_2 is merely helpful in enhancing the magnetocaloric properties even though it destroys the FM ordering at low temperature up to an extent. Moreover, the purity of the raw materials used also plays a prominent role in enhancing the magnetocaloric properties and tuning of the T_C towards room temperature.

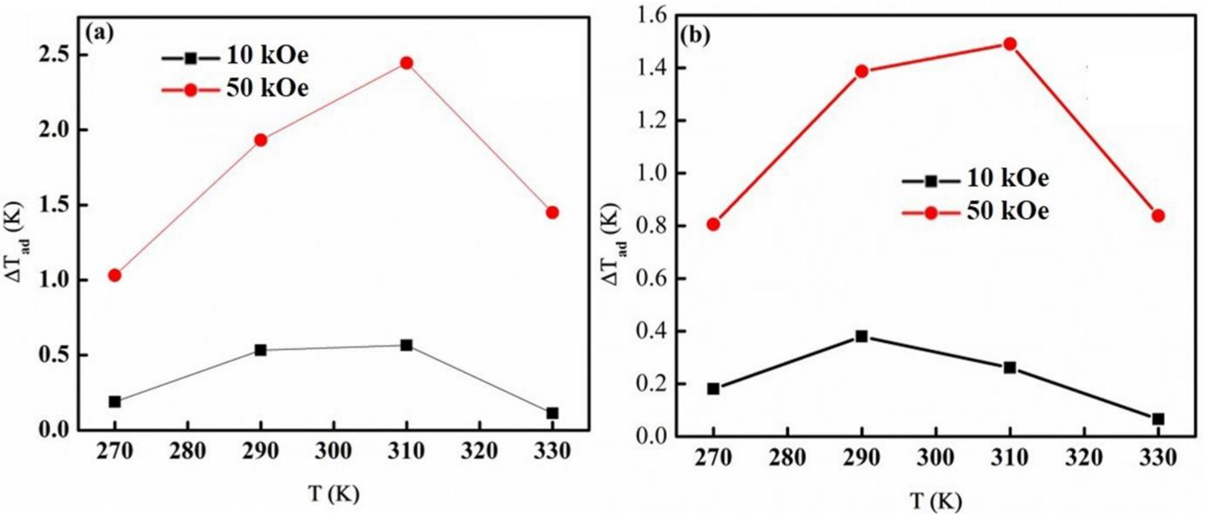

Fig. 7.14. *The adiabatic temperature change of (a) RESMO-2 and (b) RESMO-3 compounds*

7.3.2.5. Electrical transport properties

Further, to study the electrical transport behaviour, we have measured the electrical resistivity as a function of temperature in the absence and presence of magnetic field for both the compounds and the plots are shown in Fig. 7.15. The electrical resistivity values of RESMO-2 are found to be similar to that of RESMO-1, but it is one order less for RESMO-3 compound. The RESMO-2 compound shows a broad metal to insulator transition with a maximum around 300 K. However, RESMO-3 compound does not show a complete metal-insulator transition due to the presence of anomalous double peaks in the resistivity curve. From the Curie-Weiss fitting of the inverse susceptibility plot, it has also been confirmed that RESMO-3 is disobeying the Curie-Weiss law near T_C, due to the presence of magnetic frustration in the compound. Thus RESMO-3 shows some electronic inhomogeneity near the transition region due to the existence of FM clusters in the PM matrix. Thus the anomalous peak in RESMO-3 may be due to the coexistence of FMM, FMI and AFMI phases [262]. These coexisting phases have been mainly induced by electronic inhomogeneity, which is more prominent at zero field. The FMM, FMI and AFMI phases are not prominent in RESMO-2 due to less electronic inhomogeneity, and the anomalous behaviour is not seen in the resistivity curve.

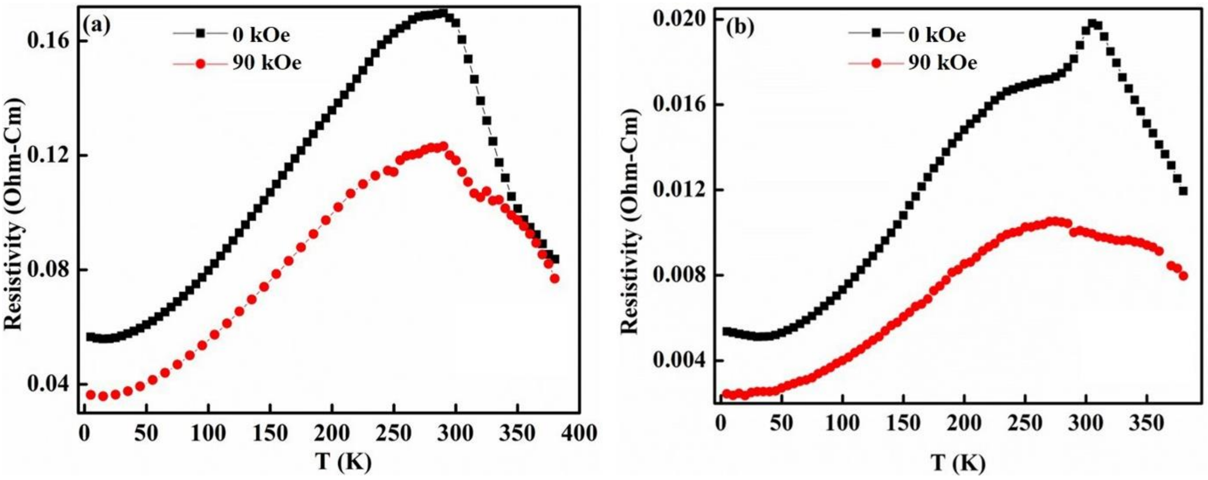

Fig. 7.15. *Temperature variation of electrical resistivity of (a) RESMO-2 and (b) RESMO-3 compounds*

At 90 kOe magnetic field, the ordering of the magnetic spins takes place due to the delocalization of charge carriers and the resistivity of both of the compound decreases. At higher magnetic fields, the peaks shift towards higher temperature, and the broadness of the peak increases with the increase in magnetic fields. Also, with increasing field, the anomalous peak behaviour is weakened, and it completely disappears in RESMO-3 due to the complete transformation of FMI phases into FMM phases.

7.4. Conclusion

- We have synthesized an inexpensive $(RE_{MIX})_{0.67}Sr_{0.33}MnO_3$ compound using mixed rare earth oxides precursors derived from monazite sand using solid-state technique and studied the magnetic and magnetocaloric properties. Then the same composition is again prepared by two different combinations of commercially available high purity rare earth oxides, and the following observations are witnessed.
- Rietveld refinement of X-ray powder diffraction patterns confirms that both RESMO-1 and RESMO-2 contain CeO_2 as secondary phase, while RESMO-3 contains La_2O_3 as the secondary phase.
- The RESMO-1 compound exhibits a $-\Delta S_M$ of 3.28 J kg^{-1} K^{-1} and ΔT_{ad} of 2.11 K at 310 K under 50 kOe field.
- The RESMO-2 compound shows $-\Delta S_M$ of 4.22 J kg^{-1} K^{-1} and ΔT_{ad} of 2.4 K (at 302 K) for 50 kOe, while RESMO-3 show $-\Delta S_M$ values of 3.81 J kg^{-1} K^{-1} (at 302 K) and ΔT_{ad} of 1.5 K (at 300 K) for 50 kOe respectively.
- The high purity of the raw materials enhanced the $\Delta S_{M,}$ and the presence of CeO_2 is merely helpful in enhancing the magnetocaloric properties.
- The enhanced value of ΔS_M near 300 K makes these compounds, as potential candidates for room temperature magnetic refrigeration applications.

Chapter 8

Summary and scope for future work

This chapter provides a brief summary of the observations made during the investigation and scope for the future work. The significant results of the investigation are also highlighted in this chapter.

8.1. Summary

This thesis presents a detailed study of structural, electrical transport, magnetic phase transitions and magnetocaloric properties of several perovskite-type rare-earth manganites. The studies carried out in the present work have revealed various interesting aspects, providing considerable insight into the magnetic and magnetocaloric properties of rare-earth manganites. Summary of these investigations along with the important conclusions drawn thereby are given below. In the end, a brief description of the possible future work in this area are also included.

- Chapter 1 provides an introduction and motivation of the present work.
- Chapter 2 deals with the detailed literature review of mixed-valence manganites. The theoretical aspects of MCE and the important features that are determining the electronic and magnetic properties of manganites were pointed out in this chapter.
- In chapter 3, bulk and nanocrystalline $Nd_{0.67}Sr_{0.33}MnO_3$ were prepared by solid-state and sol-gel routes respectively and a comparative study on structural, magnetic ordering and magnetocaloric properties in connection with their phase transition behaviour were studied. The magnetocaloric properties of the nanocrystalline compound are found to be less due to the reduction in particle size, however, the bulk $Nd_{0.67}Sr_{0.33}MnO_3$ manganite shows $-\Delta S_M$ value of 7.37 J kg^{-1} K^{-1} under 50 kOe field change at 235 K and could be a potential candidate for magnetic refrigeration at sub-room temperatures.
- In chapter 4, the effects of substitution of 10 at. % of Cr, Fe, Co, Ni and Cu at the Mn-site in $Nd_{0.67}Sr_{0.33}MnO_3$ manganite were studied. Substitution of transition elements has broadened the FM-PM transition leading to the suppression of the magnetocaloric effect. The critical exponents calculated were in good agreement with those obtained based on the field dependence of ΔS_M.

- In Chapter 5, Impact of Nd/Sr-site deficiencies on the structural, magnetic and electrical transport properties in $Nd_{0.67}Sr_{0.33}MnO_3$ compound was studied. Among all the deficient compounds, $Nd_{0.67-x}Sr_{0.33}MnO_{3-\delta}$ (x= 0.17) composition shows a significant enhancement in magnetization and decrease in electrical resistivity values than that of $Nd_{0.67}Sr_{0.33}MnO_3$ compound. The bulk $Nd_{0.67-x}Sr_{0.33}MnO_{3-\delta}$ (x= 0.17) compound shows maximum $-\Delta S_M$ value of 1.65 J kg^{-1} K^{-1} and 4.89 J kg^{-1} K^{-1} at 275 K for 10 kOe and 50 KOe field change, and it could be a potential candidate for sub-room temperature applications.
- Chapter 6 describes the Impact of La/Sr-site deficiencies on the structural, magnetic and magnetocaloric properties in $La_{0.67}Sr_{0.33}MnO_3$ manganite. Among the studied compounds, the Sr-site deficient compound shows a promising behaviour of reduction in the T_C towards room temperature, along with an increase in the ΔS_M values. Significant $-\Delta S_M$ value of 4.61 J kg^{-1} K^{-1} at 310 K was achieved in $La_{0.67}Sr_{0.33-y}MnO_{3-\delta}$ (y= 0.18) compound, and it could be a potential candidate for room temperature magnetic refrigeration applications.
- Chapter 7 illustrates the development of $(RE_{MIX})_{0.67}Sr_{0.33}MnO_3$ manganites using different combination of mixed rare earth oxide precursors. Initially, rare earth oxides derived from monazite sand was used as a precursor and later, the same compound was prepared by two different combinations of commercially available high purity rare earth oxides. The significant value of ΔS_M near 300 K make all the compounds as potential candidates for room temperature magnetic refrigeration applications

8.2. Scope for the future work

Although the present dissertation reports a detailed investigation on the structural, magnetic and magnetocaloric properties of several rare-earth manganites, the following investigations can be undertaken as a continuation of the present dissertation work.

- Direct measurement of adiabatic temperature can provide more information about the magnetocaloric properties of the studied compounds.
- Magnetocaloric studies of field pressed samples, and the variation of magnetic properties with the application of pressure can provide more information about the magnetic phase and magnetic ordering of these compounds.
- Temperature variation of Mossbauer spectra can provide further information about the competing exchange interaction between different magnetic phases in the compounds.
- Neutron diffraction experiments can provide more information about the magnetic phase unit cell structure of the studied compounds.

List of Publications

1. **B. Arun**, V.R. Akshay and M. Vasundhara, "Observation of enhanced magnetic entropy change near room temperature in Sr-site deficient $La_{0.67}Sr_{0.33}MnO_3$ manganite" *RSC Adv. 9 (2019) 23598-23606.*
2. **B. Arun**, V.R. Akshay, K. D. Chandrasekhar and M. Vasundhara, "Impact of Nd and Sr-site deficiencies on the structural, magnetic and electrical transport properties in $Nd_{0.67-x}Sr_{0.33}MnO_{3-\delta}$ (x=0.09, 0.17, 0.25, 0.33) and $Nd_{0.67}Sr_{0.33-y}MnO_{3-\delta}$ (y=0.09, 0.17) manganites", *J. Magn. Magn. Mater. 489 (2019) 165418.*
3. **B. Arun**, V. R. Akshay, K. D. Chandrasekhar, Geeta R. Mutta and M. Vasundhara, "Comparison of structural, magnetic and electrical transport behavior in bulk and nanocrystalline Nd-lacunar $Nd_{0.67}Sr_{0.33}MnO_3$ manganites", *J. Magn. Magn. Mater. 472 (2019) 74-85.*
4. **B. Arun**, V. R. Akshay and M.Vasundhara, "Observation of enhanced magnetocaloric properties with A-site deficiency in $La_{0.67}Sr_{0.33}MnO_3$ manganite", *Dalton Trans.* ***.*** *47 (2018) 15512.*
5. **B. Arun**, M.V.Suneesh, B Sudakshina, V. R. Akshay, K. D. Chandrasekhar and M.Vasundhara, "Effect of Mn-site substitution on magnetic ordering and critical behavior in $Nd_{0.67}Sr_{0.33}MnO_3$ manganite", *J. Phys. Chem. Solids 123 (2018) 327-335.*
6. **B. Arun**, M. Athira, V.R. Akshay, B. Sudakshina, Geeta. R. Mutta and M. Vasundhara, "Investigation on the structural, magnetic and magnetocaloric properties of nanocrystalline Pr-deficient $Pr_{1-x}Sr_xMnO_{3-\delta}$ manganites", *J. Magn. Magn. Mater. 448 (2018) 322–331.*
7. **B. Arun**, B. Sudakshina, V. R. Akshay, K. D. Chandrasekhar, H. D. Yang and M. Vasundhara, "Structural and magnetic behavior of (Ni, Cu) substituted $Nd_{0.67}Sr_{0.33}MnO_3$ perovskite compounds", *AIP Conf. Proc. 1953 (2018) 120016.*
8. **B. Arun**, V.R. Akshay, Geeta R. Mutta, Ch. Venkatesh and M. Vasundhara, "Mixed rare earth oxides derived from monazite sand as an inexpensive precursor material for room temperature magnetic refrigeration applications", *Mater. Research. Bullt. 94 (2017) 537–543.*

9. **B. Arun**, M.V. Suneesh and M. Vasundhara, “Comparative Study of Magnetic Ordering and Electrical Transport in Bulk and Nano-Grained $Nd_{0.67}Sr_{0.33}MnO_3$ Manganites”, *J. Magn. Magn. Mater. 418 (2016) 265–272.*

10. **B. Arun**, V.R. Akshay and M. Vasundhara, “Investigation on structural, magnetic and magnetocaloric properties in $(RE_{MIX})_{0.67}Sr_{0.33}MnO_3$ manganites using different combination of mixed rare earth oxide precursors*”* (Manuscript under review) .

11. V. R. Akshay, **B. Arun**, Guruprasad Mandal and M.Vasundhara, “Impact of Mn-Dopant Concentration in Observing Narrowing of Band-Gap, Urbach tail and Paramagnetism in Anatase TiO_2 Nanocrystals”, *New. J. Chem. 43 (2019) 14786-14799.*

12. V. R. Akshay, **B. Arun**, Guruprasad Mandal and M.Vasundhara, “Visible Range Optical Absorption, Urbach Energy Estimation and Paramagnetic Response in Cr-Doped TiO_2 Nanocrystals Derived by Sol-Gel Method”, *Phys. Chem. Chem. Phys. 21 (2019) 12991-13004.*

13. V. R. Akshay, **B. Arun**, Guruprasad Mandal, Anupama Chanda and M.Vasundhara, “Significant Reduction in the Optical Band-gap and Defect Assisted Magnetic Response in Fe-Doped Anatase TiO_2 Nanocrystals as Dilute Magnetic Semiconductors”, *New. J. Chem. 43 (2019) 6048-6062.*

14. V. R. Akshay, **B. Arun**, Guruprasad Mandal and M.Vasundhara, “Structural, Optical and Magnetic Behavior of Sol-Gel Derived Ni- Doped Dilute Magnetic Semiconductor TiO_2 Nanocrystals for Advanced Functional Applications”, *Phys. Chem. Chem. Phys. 21 (2019) 2519-2532.*

15. M. Mukesh, K. K. Thejas, V. R. Akshay, **B. Arun** and M. Vasundhara, “Effect of annealing conditions on particle size, magnetic and optical properties of Gd_2O_3 nanoparticles”, *AIP Conf. Proc. 2162 (2019) 020091.*

16. V. R. Akshay, **B. Arun**, Shubhra Dash, Ajit Patra, Guruprasad Mandal, Geeta R Mutta, Anupama Chanda and M.Vasundhara, “Defect Mediated Mechanism in Undoped, Cu and Zn-Doped TiO_2 Nanocrystals for Tailoring the Band gap and Magnetic Properties”, *RSC Adv. 8 (2018) 41994-42008.*

17. V. R. Akshay, **B. Arun**, Guruprasad Mandal, Geeta R Mutta, Anupama Chanda and M.Vasundhara, “Observation of Optical Band-gap Narrowing and Enhanced

Magnetization in Co-doped Sol-gel derived Anatase TiO_2 Nanocrystals", *J. Phys. Chem. C 122 (2018) 26592-26604.*

18. V. R. Akshay, **B. Arun**, B, M. V. Suneesh and M. Vasundhara, "Surfactant Induced Structural Phase Transitions and Enhanced Room Temperature Thermoelectric Performance in n-Type Bi_2Te_3 Nanostructures Synthesized via Chemical Route", *ACS Appl. Nano Mater. 1 (2018), 3236-3250.*

19. B. Sudakshina**, B. Arun**, K. D. Chandrasekhar, H.D. Yang and M. Vasundhara, "Structural and magnetic properties of $Nd_{0.67}Ba_{0.33}MnO_3$ manganites with partial replacement of Fe and Cu at Mn-site", *Phy. B: Cond. Matter 539 (2018) 14–20.*

20. B. Sudakshina, **B. Arun** and M. Vasundhara, "Electrical, magnetic, and magnetotransport behavior of inhomogeneous $Nd_{1-x}Ca_xMnO_3$ ($0.0 \leq x \leq 0.8$) manganites", *J. Magn. Magn. Mater. 448 (2018) 250–256.*

21. B. Sudakshina, **B. Arun**, K. Devi Chandrasekhar, H. D. Yang and M. Vasundhara, "Magnetically induced electrical transport and dielectric properties of 3d transition elemental substitution at the Mn-site in $Nd_{0.67}Ba_{0.33}MnO_3$ manganites", *AIP Conf. Proc. 1953 (2018) 120051.*

22. **B. Arun**, J. Varghese, K. P. Surendran and M. T. Sebastian, "Microwave dielectric and thermal properties of mixed rare earth orthophosphate [$RE_{mix}PO_4$]", *Ceram. Inter. 40 (2014) 13075-13081.*

23. **B. Arun**, K. M. Manu and M. T. Sebastian, "Tailoring the Microwave Dielectric Properties of Alkaline Earth Gehlenite type Ceramic", *Int. J. Mod. Phy.: Conf. Ser. 22 (2013) 173-178*

24. B. Sudakshina, **B. Arun**, and M. Vasundhara, "Structural, Magnetic, and Magneto-Caloric Properties of Cu-Substituted $Nd_{0.67}Ba_{0.33}MnO_3$ Manganites", J. Phys. Solid. State, 2019 (accepted)

25. V.R. Akshay, **B. Arun**, and M. Vasundhara, "Tailoring the NIR Range Optical Absorption, Band-gap Narrowing and Ferromagnetic Response in Defect Modulated TiO2 Nanocrystals by Varying the Annealing Conditions" (Manuscript under review)

Papers presented in Conferences:

Contributory Talks:

1. **B. Arun** and M. Vasundhara, “Mixed rare earth oxides derived from monazite sand as an inexpensive precursor material for room temperature magnetic refrigeration applications" *Research Scholars Symposium on Materials Science and Engineering, Indian Institute of Metals (IIM) Trivandrum chapter, CSIR-National Institute for Interdisciplinary Science and Technology, Thiruvananthapuram, December 20, 2016*
2. **B. Arun**, and M. Vasundhara, “Comparative Study of Magnetic Ordering and Electrical Transport in Bulk and Nano-Grained $Nd_{0.67}Sr_{0.33}MnO_3$ Manganites”, *International Conference on Magnetic Materials and Applications (ICMAGMA-2015) in association with Magnetics Society of India, VIT University, Vellore, December 02-04, 2015.*

Poster Presentation:

3. **B. Arun**, B. Sudakshina, V. R. Akshay, K. D. Chandrasekhar, H. D. Yang and M. Vasundhara, “Structural and magnetic behavior of (Ni, Cu) substituted $Nd_{0.67}Sr_{0.33}MnO_3$ perovskite Compounds”, *2nd International Conference on Condensed Matter & Applied Physics (ICC-2017), Bikaner, Rajasthan, November 24-25, 2017.*
4. **B. Arun**, M. Athira, V.R. Akshay, B. Sudakshina, Geeta. R. Mutta, M. Vasundhara, “Investigation on the structural, magnetic and magnetocaloric properties of nanocrystalline Pr-deficient $Pr_{1-x}Sr_xMnO_{3-\delta}$ manganites”, *International Conference on Magnetic Materials and Applications (ICMAGMA-2017) in association with Magnetics Society of India, Defence Metallurgical Research Laboratory (DMRL), Hyderabad, February 01-03, 2017.*
5. **B. Arun** and M. Vasundhara, “Inexpensive manganite compound using mixed rare earth oxides derived from monazite sand for the room temperature magnetocaloric effect”, *National Conference on Materials Science and Technology (NCMST- 2016), IIST, Trivandrum, July 12-14, 2016.*
6. **B. Arun** and M. Vasundhara, “Study on critical exponents behavior and magnetocaloric effect of $Nd_{0.67}Sr_{0.33}Mn_{0.9}Tr_{0.1}O_3$ (Tr = Cr, Fe, Co, Ni and Cu) perovskite manganites” *International Conference on Science, Technology and Applications of Rare Earths (STAR 2015), Trivandrum, April 23-25, 2015.*

References

[1] K. Gschneidner Jr and V. K. Pecharsky, *Annu. Rev. Mater. Sci.*, 2000, **30**, 387.

[2] K. A. GschneidnerJr, V. Pecharsky and A. Tsokol, *Rep. Prog. Phys.*, 2005, **68**, 1479.

[3] A. Tishin, *Handb. Magn. Mater.*, 1999, **12**, 395.

[4] S. L. Russek and C. B. Zimm, *Int. J. Refrig.*, 2006, **29**, 1366.

[5] E. Brück, *J. Phys. D: Appl. Phys.*, 2005, **38**, R381.

[6] M. Jachtenfuchs, *J. Common Mkt. Stud.*, 1989, **28**, 261.

[7] F. X. Hu, B. G. Shen, J. R. Sun, Z. H. Cheng, G. H. Rao and X. X. Zhang, *Appl. Phys. Lett.*, 2001, **78**, 3675.

[8] F. X. Hu, B. G. Shen, J. R. Sun and G. H. Wu, *Phys. Rev. B*, 2001, **64**, 132412.

[9] T. Krenke, E. Duman, M. Acet, E. F. Wassermann, X. Moya, L. Mañosa and A. Planes, *Nat. Mater.*, 2005, **4**, 450.

[10] O. Tegus, E. Brück, K. Buschow and F. De Boer, *Nature*, 2002, **415**, 150.

[11] E. Brück, M. Ilyn, A. Tishin and O. Tegus, *J. Magn. Magn. Mater.*, 2005, **290**, 8.

[12] L. Zhang, O. Može, K. Prokeš, O. Tegus and E. Brück, *J. Magn. Magn. Mater.*, 2005, **290**, 679.

[13] A. Bezaguet, J. Casas-Cubillos, A. Cyvoct, P. Lebrun, R. Losserand-Madoux, M. Marquet and M. Schmidt, *IEEE Trans. Magn.*, 1994, **30**, 2138.

[14] C. Zimm, A. Jastrab, A. Sternberg, V. Pecharsky, K. Gschneidner, M. Osborne and I. Anderson, *Adv. Cryog. Engin 1998*, ***43***, 1759.

[15] E. Warburg, *Ann. Phys*, 1881, **13**, 141.

[16] P. Weiss and A. Piccard, *J. Phys. Theor. Appl*, 1917, **7**, 103.

[17] P. Debye, *Ann. Phys.*, 1926, **386**, 1154.

[18] W. Giauque, *J. Am. Chem. Soc*, 1927, **49**, 1864.

[19] W. Giauque and D. MacDougall, *Phys. Rev.*, 1933, **43**, 768.

[20] G. Brown, *J. Appl. Phys.*, 1976, **47**, 3673.

[21] V. K. Pecharsky and K. A. Gschneidner Jr, *Phys. Rev. Lett.*, 1997, **78**, 4494.

[22] O. Tegus, E. Brück, L. Zhang, K. Buschow and F. De Boer, *Phys. B*, 2002, **319**, 174.

[23] L. D. Kirol and M. W. Dacus, *Adv. Cryog. Eng.*, 1988, **33**, 757.

[24] F. Allab, Design and implementation of a magnetic refrigeration device based on the magnetocaloric effect and dedicated to automotive air conditioning, PhD thesis, Grenoble, National Polytechnic Institute of Grenoble (2008).

[25] T. Okamura, K. Yamada, N. Hirano and S. Nagaya, *Int. J. Refrig.*, 2006, **29**, 1327.

[26] C. Zimm, J. Auringer, A. Boeder, J. Chells, S. Russek and A. Sternberg, Design and initial performance of a magnetic refrigerator with a rotating permanent magnet, *Proceedings of the Second International Conference on Magnetic Refrigeration at Room Temperature*, Portoroz, Slovenia, 2007, 341.

[27] A. Tura and A. Rowe, Design and testing of a permanent magnet magnetic refrigerator, *Proceedings of the Second International Conference on Magnetic Refrigeration at Room Temperature*, Portoroz, Slovenia, 2007, 363.

[28] C. Vasile and C. Muller, A new system for a magnetocaloric refrigerator, *Proceedings of First International Conference on Magnetic Refrigeration at Room Temperature*, Montreux, Switzerland, 2005, 357-366.

[29] C. Muller, L. Bour and C. Vasile, Study of the efficiency of a magnetothermal system according to the permeability of the magnetocaloric material around its Curie temperature. *Proceedings of the Second International Conference on Magnetic Refrigeration at Room Temperature*, Portoroz, Slovenia, 2007, 323.

[30] B. Yu, M. Liu, P. W. Egolf and A. Kitanovski, I*nt. J. Refrig*., 2010, **33**, 1029.

[31] P. Clot, D. Viallet, F. Allab, A. Kedous-Lebouc, J. M. Fournier, J. P. Yonnet, *IEEE Trans. Magn.*, 2003, **39**, 3349.

[32] *H. R. E. H.* Bouchekara, *Research* on *magnetic* refrigeration *systems*. *Numerical modeling*, *design* and *optimization*, PhD *thesis, Grenoble*, *National Polytechnic Institute* of *Grenoble (2008).*

[33] C. Dupuis, Materials with giant magnetocaloric effect and magnetic refrigeration systems, PhD *thesis, Grenoble*, *National Polytechnic Institute* of *Grenoble (2009).*

[34] B. Ponomarev, *J. Magn. Magn. Mater.*, 1986, **61**, 129.

[35] B. Gopal, R. Chahine and T. Bose, *Rev. Sci. Instrum.*, 1997, **68**, 1818.

[36] B. Gopal, R. Chahine, M. Földeàki and T. Bose, *Rev. Sci. Instrum.*, 1995, **66**, 232.

[37] A. H. Morrish, The Physical Principles of Magnetism, John Wiley & Sons, Inc., New York (1965).

[38] L. Tocado, E. Palacios and R. Burriel, *J. Magn. Magn. Mater.*, 2005, **290**, 719.

[39] J. Y. Law, V. Franco and R. V. Ramanujan, *J. Appl. Phys.*, 2011, **110**, 023907.

[40] V. Basso, M. Kuepferling, C. P. Sasso and L. Giudici, *Rev. Sci. Instrum.* 2008, **79**, 063907

[41] M. Pasquale, C. P. Sasso, L. Lewis, L. Giudici, T. Lograsso and D. Schlagel, *Phys. Rev. B*, 2005, **72**, 094435.

[42] V. Khovaylo, K. Skokov, Y. S. Koshkidko, V. Koledov, V. Shavrov, V. Buchelnikov, S. Taskaev, H. Miki, T. Takagi and A. Vasiliev, *Phys. Rev. B*, 2008, **78**, 060403.

[43] S. Y. Dankov, A. Tishin, V. Pecharsky and K. Gschneidner Jr, *Rev. Sci. Instrum.*, 1997, **68**, 2432.

[44] A. Dinesen, S. Linderoth and S. Mørup, *J. Phys.: Condens. Matter*, 2005, **17**, 6257.

[45] S. Jeppesen, S. Linderoth, N. Pryds, L. T. Kuhn and J. B. Jensen, *Rev. Sci. Instrum.*, 2008, **79**, 083901.

[46] K. Gschneidner Jr and V. Pecharsky, *J. Appl. Phy*, 1999, **85**, 5365.

[47] X. Niu, K. Gschneidner Jr, A. Pecharsky and V. Pecharsky, *J. Magn. Magn. Mater.*, 2001, **234**, 193.

[48] C. B. Zimm, P. M. Ratzmann, J. A. Barclay, G. F. Green and J. N. Chafe, Adv. Cryog. Eng., 1990, **36**, 763.

[49] C.B. Zimm, S. L. Kral, J. A. Barclay, G. F. Green, and G. Patton, The Magnetocaloric Effect in Erbium, Proceedings of 5th International Cryocooler Conference, Dayton, Ohio, 1988, 49.

[50] C. Zimm, J. Barclay, H. Harkness, G. Green and W. Patton, *Cryogenics*, 1989, **29**, 937.

[51] T. V. Jayaraman, L. Boone and J. E. Shield, *J. Alloys Compd.*, 2011, **509**, 1411.

[52] T. V. Jayaraman, L. Boone and J. E. Shield, *J. Magn. Magn. Mater.*, 2013, **345**, 153.

[53] V. K. Pecharsky and K. A. Gschneidner Jr, *J. Magn. Magn. Mater.*, 1999, **200**, 44.

[54] Q. Zhang, J. Cho, B. Li, W. Hu and Z. Zhang, *Appl. Phys. Lett.*, 2009, **94**, 182501.

[55] M. Ujihara, G. P. Carman and D.-G. Lee, *Appl. Phys. Lett.*, 2007, **91**, 093508.

[56] J. Chen, B. Shen, Q. Dong, F. Hu and J. Sun, *Appl. Phys. Lett.*, 2010, **96**, 152501.

[57] B. Shen, J. Sun, F. Hu, H. Zhang and Z. Cheng, *Adv. Mater.*, 2009, **21**, 4545.

[58] F. X. Hu, B. G. Shen, J. R. Sun, Z. H. Cheng and X. X. Zhang, *J. Phys.: Condens. Matter*, 2000, **12**, L691.

[59] V. Pecharsky, K. Gschneidner Jr, Y. Mudryk and D. Paudyal, *J. Magn. Magn. Mater.*, 2009, **321**, 3541.

[60] R. D. Shull, V. Provenzano, A. J. Shapiro, A. Fu, M. W. Lufaso, J. Karapetrova, G. Kletetschka and V. Mikula, *J. Appl. Phy.*, 2006, **99**, 08K908.

[61] J. Li, W. Sun, Y. Jian, Y. Zhuang, W. Huang and J. Liang, *J. Appl. phy.*, 2006, **100**, 073904.

[62] V. Provenzano, T. Zhang, A. Shapiro, Y. Chen and R. D. Shull, *IEEE Trans. Magn.*, 2008, **44**, 3048.

[63] E. Yüzüak, I. Dincer and Y. Elerman, *J. Rare Earths*, 2010, **28**, 477.

[64] E. Yüzüak, I. Dincer and Y. Elerman, *Chin. Phys. B*, 2010, **19**, 037502.

[65] K. Prabahar, D. R. Kumar, M. M. Raja, M. Palit and V. Chandrasekaran, *Mater. Sci. Eng.*, 2010, **172**, 294.

[66] K. Prabahar, D. R. Kumar, M. M. Raja and V. Chandrasekaran, *J. Magn. Magn. Mater.*, 2011, **323**, 1755.

[67] P. Gorria, P. Álvarez, J. S. Marcos, J. L. S. Llamazares, M. J. Pérez and J. A. Blanco, *Acta. Mater.*, 2009, **57**, 1724.

[68] K. Mandal, A. Yan, P. Kerschl, A. Handstein, O. Gutfleisch and K. Müller, *J. Phys. D: Appl. Phys.*, 2004, **37**, 2628.

[69] P. Alvarez, P. Gorria, J. L. S. Llamazares, M. J. Perez, V. Franco, M. Reiffers, I. Curlik, E. Gazo, J. Kovac and J. A. Blanco, *Intermetallics*, 2011, **19**, 982.

[70] S. Tripathy, K. Suresh and A. Nigam, *J. Magn. Magn. Mater.*, 2006, **306**, 24.

[71] P. Kumar, K. Suresh and A. Nigam, *J. Appl. Phy.*, 2011, **109**, 07A909.

[72] B. Li, J. Du, W. Ren, W. Hu, Q. Zhang, D. Li and Z. Zhang, *Appl. Phys. Lett.*, 2008, **92**, 242504.

[73] C. Zhang, D. Wang, Z. Han, S. Tang, B. Gu and Y. Du, *Appl. Phys. Lett.*, 2006, **89**, 122503.

[74] W. Fang, S. Bao-Gen, Z. Jian, S. Ji-Rong, M. Fan-Bin and L. Yang-Xian, *Chin. Phys. B*, 2010, **19**, 067501.

[75] J. Marcos, A. Planes, L. Mañosa, F. Casanova, X. Batlle, A. Labarta and B. Martinez, *Phys. Rev. B*, 2002, **66**, 224413.

[76] Z. Han, D. Wang, C. Zhang, H. Xuan, B. Gu and Y. Du, *Appl. Phys. Lett.*, 2007, **90**, 042507.

[77] R. Kainuma, Y. Imano, W. Ito, Y. Sutou, H. Morito, S. Okamoto, O. Kitakami, K. Oikawa, A. Fujita and T. Kanomata, *Nature*, 2006, **439**, 957.

[78] A. K. Pathak, M. Khan, I. Dubenko, S. Stadler and N. Ali, *Appl. Phys. Lett.*, 2007, **90**, 262504.

[79] N. Trung, L. Zhang, L. Caron, K. Buschow and E. Brück, *Appl. Phys. Lett.*, 2010, **96**, 172504.

[80] C. Zhang, D. Wang, Q. Cao, Z. Han, H. Xuan and Y. Du, *J. Phys. D: Appl. Phys.*, 2008, **42**, 015007.

[81] O. Tegus, E. Brück, F. De Boer and K. Buschow, *J. Alloys Compd*., 2002, **337**, 269.

[82] Z. Xie, D. Geng and Z. Zhang, *Appl. Phys. Lett*., 2010, **97**, 202504.

[83] H. Wada and Y. Tanabe, *Appl. Phys. Lett*., 2001, **79**, 3302.

[84] D. Cam Thanh, E. Bruck, O. Tegus, J. Klaasse, T. Gortenmulder and K. Buschow, *J. Appl. Phys*, 2006, **99**, 08Q107.

[85] D. Cam Thanh, E. Bruck, N. Trung, J. Klaasse, K. Buschow, Z. Ou, O. Tegus and L. Caron, *J. Appl.Phys.*, 2008, **103**, 07B318.

[86] M. Annaorazov, K. Asatryan, G. Myalikgulyev, S. Nikitin, A. Tishin and A. Tyurin, *Cryogenics*, 1992, **32**, 867.

[87] M. Manekar and S. Roy, *J. Phys. D: Appl. Phys.*, 2008, **41**, 192004.

[88] C. B. Rong and J. P. Liu, *Appl. Phys. Lett*., 2007, **90**, 222504.

[89] T. Tohei, H. Wada and T. Kanomata, *J. Appl. Phy.*, 2003, **94**, 1800.

[90] E. V. Gopalan, I. Al-Omari, D. S. Kumar, Y. Yoshida, P. Joy and M. Anantharaman, *Appl. Phys. A*, 2010, **99**, 497.

[91] Y. Tokura and Y. Tomioka, *J. Magn. Magn. Mater*., 1999, **200**, 1.

[92] A. Bhalla, R. Guo and R. Roy, *Mater. Res. Innovations*, 2000, **4**, 3.

[93] J. B. Goodenough and J.-S. Zhou, *J. Mater. Chem*., 2007, **17**, 2394.

[94] Perovskite mineral data, http://webmineral.com/data/Perovskite

[95] H. R. Wenk and A. Bulakh, Minerals: their constitution and origin, Cambridge University Press (2016).

[96] V. M. Goldschmidt, *Naturwiss*., 1926, **14**, 477.

[97] H. D. Megaw, *Nature*, 1945, **155**, 484.

[98] H. Hwang, S-W. Cheong, N. P. Ong and B. Batlogg, *Phys. Rev. Lett*., 1996, **77**, 2041.

[99] M. Mochizuki, N. Furukawa and N. Nagaosa, *Phys. Rev. Lett*., 2010, **105**, 037205.

[100] P. Raychaudhuri, C. Mitra, A. Paramekanti, R. Pinto, A. Nigam and S. Dhar, *J. Phys.: Condens. Matter*, 1998, **10**, L191.

[101] P. Mandal and S. Das, *Phys. Rev. B*, 1997, **56**, 15073.

[102] C. Y. Kwan, “All-oxide Giant Magneto resistive Devices” PhD thesis The Hong Kong Polytechnic University (Aug. 2008).

[103] C. Zener, *Phys. Rev*, 1951, **81**, 440.

[104] J. B. Goodenough and A. L. Loeb, *Phys. Rev*., 1955, **98**, 391.

[105] J. B. Goodenough, *Rep. Prog. Phys*., 2004, **67,** 1915.

[106] J. B. Goodenough, *Aust. J. Phys*., 1999, **52**, 155.

[107] G. van Tendeloo, O. I. Lebedev, M. Hervieu, and B. Raveau, *Rep. Prog. Phys*., 2004, **67,** 1315.

[108] V. M. Goldschmidt, Geochemistry, Oxford: Oxford University Press) (1958).

[109] J. B. Goodenough, J.A. Kafalas and J.M. Longo, Preparation Methods in Solid State Chemistry, (edited by P. Hagenmuller) New York: Academic press (1972).

[110] A. M. Moustafa, I. S Ahmed Farag and L. M. Salah, *Egypt. J. Solids*, 2004, **27**, 213.

[111] D. G. Kuberkar, D. S. Rana, C. M. Thaker, K. R. Mavani, Darshan C. Kundaliya and S. K. Malik, *J. Magn. Mater*. 2004, **272**, 1823.

[112] J. B Goodenough, Magnetism and the Chemical Bond, John Wiley and Sons, United states (1963).

[113] K. I. Kugel and D. I. Khomskii, *Phys. Usp.*, 1982, **25** 231.

[114] N. A. Spaldin, Magnetic Materials: Fundamentals and Applications, 2nd edition, Cambridge University Press, New York (2011).

[115] P. A. Cox, Transition Metal oxides, Clarendon Press, Oxford University press, U. K. (1995).

[116] E. Pollert, S. Krupicka and E. Kuzwicova, *J. Phys. Chem. Solids*, 1982, **43**, 1137.

[117] H. Jahn and E. Teller, *Proc. Royal Soc. Lond. A Mat*., 1937, **161** (905), 220.

[118] R. Janes and A. Elaine Moore, Metal-ligand bonding. Royal Society of Chemistry (2004).

[119] J. D. Dunitz and L. E. Orgel, *J. Phys. Chem. Solids*., 1957, **3**, 20.

[120] D. S. McClure, *J. Phys. Chem. Solids*., 1957, **3**, 311.

[121] J. Kanamori, *J. Appl. Phys*., 1960, **31**, S14.

[122] G. A. Gehring and K. A. Gehring, *Rep. Prog. Phys*., 1975, **38**, 1.

[123] S. J. Blundell, Magnetism in Condensed Matter, Oxford University Press (2001).

[124] C. Zener, Phys. Rev., 1951, **82**, 403.

[125] P. G. de Gennzst, Phys. Rev., 1960, **118**, 141.

[126] P. W. Anderson, *Phys. Rev.*, 1950, **79**, 350.

[127] J. B. Goodenough, Phys. Rev., 1955, **100**, 564.

[128] J. Kanamori, *J. Phys. Chem. Solids*., 1958, **10**, 87.

[129] P. W. Anderson, in Magnetism, edited by G. T. Rado and H. Suhl, Academic Press, New York and London (1963).

[130] G. H. Jonker and J. H. van Santen, *Physica (Amsterdam)*, 1950, **16**, 337.

[131] J. H. van Santen and G. H. Jonker, *Physica (The Hague)*, 1950, **16**, 599.

[132] J. Volger, *Physica* 1954, **20**, 49.

[133] R. von Helmolt, J. Wecker, B. Holzapfel, L. Schultz, and K. Samwer, *Phys. Rev. Lett.,* 1993, **71**, 2331.

[134] W. Zhong, W. Cheng, W.P. Ding, N. Zhang, Y.W. Du and Q.J. Yan, *Solid State Commun.,* 1998, **106**, 55.

[135] D. T. Morelli, A.M. Mance, J. V. Mantese and A.L. Micheli, *J. Appl. Phys.*, 1996, **79**, 373.

[136] Z.B. Guo, Y.W. Du, J.S. Zhu, H. Huang, W.P. Ding and D. Feng, *Phys. Rev. Lett*., 1997, **78,** 1142.

[137] T. Tang, K. M. Gu, Q. Q. Cao, D. H. Wang, S. Y. Wang, S. Y. Zhang and Y. W. Du, *J. Magn. Magn*. Mater. 2000, **222**, 110.

[138] J. Mira, J. Rivas, L.E. Hueso, F. Rivadulla, M.A. Lopez Quintela, J. Appl. Phys., 2002, **91**, 8903.

[139] P. Sande, L.E. Hueso, D.R. Miguens, J. Rivas, F. Rivadulla and M.A. Lopez-Quintela, *Appl. Phys. Lett.* 2001, **79,** 2040.

[140] M.S. Reis, A.M. Gomes, J.P. Araujo, J.S. Amaral, P.B. Tavares, I.S. Oliveira and V.S. Amaral, *J. Magn. Magn. Mater*. 2005, **697**, 290.

[141] M.H. Phan, H.X. Peng and S.C. Yu, *J. Appl. Phys.*, 2005, **97**, 10M306.

[142] A.M. Gomes, F. Garcia, A.P. Guimaraes, M.S. Reis, V.S. Amaral and P.B. Tavares, J. *Magn. Magn. Mater.* 2005, **694**, 290.

[143] P. Chen, Y.W. Du, and Chin. *J. Phys.*, 2001, **39**, 357.

[144] A. Rostamnejadi, M. Venkatesan, P. Kameli, H. Salamati-and J. M. D. Coey, *J. Magn. Magn. Mater.*, 2011, **323**, 2214.

[145] Liu K, Wu X W, Ahn K H, Sulchek T, Chien C L and Xiao J Q, *Phys. Rev. B*, 1996, **54**, 3007.

[146] Fujiwara T and Korotin M, *Phys. Rev. B*, 1999, **59**, 9903.

[147] M.H. Phan, S.B. Tian, D.Q. Hoang, S.C. Yu, C. Nguyen and A.N. Ulyanov, *J. Magn. Magn. Mater*. , 2003, **309**, 258.

[148] M. H. Phan, S.B. Tian, S.C. Yu and A.N. Ulyanov, *J. Magn. Magn. Mater*. , 2003, **256**, 306.

[149] Arroyo A, Alonso J, Cortés-Gil R, González-Calbet J, Hernando A, Rojo J and Vallet-Regí M, *J. Magn. Magn. Mater*., 2004, **272,** 1748.

[150] A. Szewczyk, M. Gutowska, B. Dabrowski, T. Plackowski, N. P. Danilova and Y.P. Gaidukov, *Phys. Rev*. B, 2005, **71**, 224.

[151] N.H. Luong, D.T. Hanh, N. Chau, N.D. Tho and T.D. Hiep, *J. Magn. Magn. Mater.*, 2005, **290–291**, 690.

[152] M. Bejar, R. Dhahri, E. Dhahri, M. Balli and E.K. Hlil, *J. Alloys Compd*., 2007, **442**, 136.

[153] M.H. Phan, S.C. Yu and N.H. Hur, Appl. Phys. Lett., 2005, **86**, 072504.

[154] M. Patra, S. Majumdar, S. Giri, G.N. Iles, and T. Chatterji, *J. Appl. Phys.*, 2010, **107**, 076101.

[155] B. Roy, A. Poddar and S. Das, *J. Appl.Phys.* 2006, **100** 104318.

[156] B. Roy and S. Das, *J. Appl.Phys.* 2008, **104** 103915.

[157] C. V. Colin, A. J. C, Buurma, M. v Zimmermann and T. T. M. Palstra, *J. Phys: Condens. Matter*, 2008, **20** 434223.

[158**]** S. Zemni, M. Baazaoui, J.R. Dhahri, H. Vincent and B.M. Oumezzine, Mater. Lett., 2009, **63**, 489.

[159**]** D. Hsu, Y. Shih, W. Wang and J. Lin, *IEEE Trans. Magn.*, 2009. **45,** 4345.

[160] R. Venkatesh, M. Pattabiraman, K. Sethupathi, G. Rangarajan, S. Angappane and J.G. Park, *J. Appl. Phys.*, 2008, **103**, 07B319.

[161] Y. I. Chang and C. K. Ong, *J. Appl. Phys. A*, 2004, **79**, 2103.

[162] G. Venkataiah and P. V. Reddy, *J. Mag. Mag. Mater.*, 2005, **285**, 343.

[163] G. Lalitha and P. Venugopal Reddy, *Phys. Scr.*, 2010, **82**, 045704.

[164] D. C. Krishna, Y. K. Lakshmi, B. Sreedhar and P. V. Reddy, *Solid State Sci.*, 2009, **11**, 1312.

[165] S. Paul and T. K. Nath, *Mater. Res. Soc. Symp. Proc.*, 20009, **1118**-K05-03.

[166] R. Prasad, M. Singh, P. Siwach, A. Kaur, P. Fournier and H. Singh, *Appl. Phys. A*, 2010, **99**, 823.

[167] V. A. Ryzhov, P. L. Molkanov, A. V. Lazuta, V. V. Runov, V. P. Khavronin, I. O. Troyanchuk, Bull. Russ. Acad. Sci: Phys., 2010, **74**, 1477.

[168] **K.** Raju, K. V. Sivakumar and P. V. Reddy, *J. Phys. Chem. Solids*, 2012, **73,** 430.

[169**]** P. Lampen, A. Puri, M. H. Phan and H. Srikanth, *J. Alloys Compd.*, 2012, **512,** 94.

[170**]** R. Thaljaoui, W. Boujelben, M. Pekala, K. Pekala, J.-F. Fagnard, P. Vanderbemden, M. Donten and A. Cheikhrouhou, *J. Magn. Magn. Mater.*, 2014, **352**, 6.

[171**]** R. Thaljaoui, W. Boujelben, K. Pekala, M. Pekala, W. Cheikhrouhou-Koubaa and A. Cheikhrouhou, *J. Mater. Sci*., 2013, **48**, 3894.

[172**]** R. Thaljaoui, W. Boujelben, M. Pekała, D. Pociecha, J. Szydlowska, A. Cheikhrouhou, *J. Alloys Compd*., 2012, **530**, 138.

[173] M. Shaikh and D.Varshney, *Mater. Sci. Semicond. Process*., 2014, **27**, 418.

[174**]** D. V. M. Repaka, M. Aparnadevi, Pawan Kumar, T. S. Tripathi and R. Mahendiran, *J. Appl. Phys.*, 2013, **113**, 17A906.

[175] K. S. Bhagyashree and S. V. Bhat, *J. Appl. Phys.*, 2015, **117**, 17D514.

[176] T. I. Arbuzova and S. V. Naumov, JETP lett., 2015, **101**, 760.

[177] M. Oumezzine, A. C. Galca, I. Pasuk, C. F. Chiril, A. Leca, V. Kuncser, L. C. Tanase, A. Kuncser, C. Ghica and M. Oumezzine, *Dalton Trans.*, 2016, **45**, 15034.

[178] N. Kallel, S. Kallel, A. Hagaza and M. Oumezzine, *Physica B*, 2009, **404**, 285.

[179] C.P. Reshmi, S. S. Pillai, K.G. Suresh, M. R. Varma, *Solid State Sci.*, 2013, **19**, 130.

[180] S. Hcini, M. Boudard, S. Zemni and M. Oumezzine, *Ceram. Inter.*, 2014, **40**, 16041.

[181] M. A. Zaidi, J. Dhahri, I. Zeydi, T. Alharbi and H. Belmabrouk, *RSC Adv.*, 2017, **7**, 43590.

[182] A. B. Hassine, A. Dhahri, M. L. Bouazizi, M. Oumezzine and E. K. Hlil, *Ceram. Inter.*, 2017, **43**, 1390.

[183] I. Sfifir, A. Ezaami, W. Cheikhrouhou-Koubaa and A. Cheikhrouhou, *J. Alloys. Compd*., 2017, **696**, 760.

[184] M. Chebaane, R. Bellouz, Ma. Oumezzine, E. K. Hlil and A. Fouzri, *RSC Adv*., 2018, **8**, 7186.

[185] Y. Sun, W. Tong, N. Liu and Y. Zhang, *J. Magn. Magn. Mater*., 2002, **238**, 25.

[186] Z. Juan and W. Gui, *J. Magn. Magn. Mater*., 2009, **321**, 2977.

[187] B. Raveau, C. Martin and A. Maignan, *J. Alloys Compd.*, 1998, **275–277**, 461.

[188] H. Chen, C. Lin and D.S. Dai, *J. Magn. Magn. Mater*., 2003, **257**, 254.

[189] N. Chau, P.Q. Niem, H.N. Nhat, N.H. Luong and N.D. Tho, *Physica B: Condens. Matter*, 2003, **327**, 214.

[190] P. Nisha, S. S. Pillai, M. R. Varma and K. Suresh, *J. Magn. Magn. Mater*., 2013, **327**, 189.

[191] W. Boujelben, A. Cheikh-Rouhou, J.C. Joubert, *Eur. Phys. J. B,* 2001, **24**, 419.

[192] M. H. Phan, S. C. Yu and N. H. Hur, *J. Magn. Magn. Mater*., 2003, **262**, 407.

[193] W. Zhong, W. Cheng, C.T. Au and Y.W. Du, *J. Magn. Magn. Mater*., 2003, **261**, 238.

[194] D.L. Hou, Y. Bai, J. Xu, G.D. Tang, X.F. Nie, *J. Alloys Compd.*, 2004, **384,** 62.

[195] W. Boujelben, A. Cheikh-Rouhou and H. Roussel, *J. Magn. Magn. Mater*., 2005, **290**, 952.

[196] L-F. Zhao, W. Chen, J-L. Shang, L. Chen, S. Liu, Z-C. Xia and S-L. Yuan, *J. Phy. D: Appl. Phys.*, 2005, **38**, 2480.

[197] W**.** Chen, L. Nie, X. Zhao, W. Zhong, G. Tang, A. Li, J. Hu and Y. Tian, *Solid. State. Commun*., 2006, **138** 165.

[198] D. Ji, G. Tang, Z. Li, Q. Han, X. Hou, R. Bian and S. Liu, *J. Appl. Phys.*, 2012, **111**, 113902.

[199] M. Wali, R. Skini, M. Khlifi, E. Dhahri and E. K. Hlil, *Dalton Trans*., 2015, **44**, 12796.

[200] R. Bellouz, M. Oumezzine, A. Dinia, G. Schmerber, E.K. Hlil and M. Oumezzine, *RSC Adv.*, 2015, **5**, 64557.

[201**]** S. Estemirova, V. Mitrofanov, G. Kozhina and A. Fetisov, *J. Mag. Mag. Mater*., 2016, **399,** 32.

[202**]** R. Skini, M. Khlifi and E.K. Hlil, *RSC Adv*., 2016, **6**, 34271.

[203] A. Marzouki-Ajmi, H. Omrani, W. Cheikhrouhou-Koubaa, M. Koubaa and A. Cheikhrouhou, *J. Alloys Compd.*, 2017, **690,** 403.

[204**]** M. Oumezzine, O. Hassayoun, R. Bellouz and H. B. Sales, *J. Alloys Compd.*, 2017, **729,** 156.

[205] M. H. Ehsani, P. Kameli, M. E. Ghazi, and F. S. Razavi, *Adv. Mater. Res.*, 2013, **829**, 712.

[206] A. K. Pradhan, R. Bah, R. B. Konda, R. Mundle, H. Mustafa, O. Bamiduro and D. J. Sellmyer, *J. Appl. Phy.* 2008, **103**, 07F704.

[207] J. L. Dormann, D. Fiorani and E. Tronc, *J. Mag. Mag. Mater*., 1999, **202**, 251.

[208] M. Gupta, P. Yadav, W. Khan, A. Azam, A. H. Naqvi and R.K. Kotnala, *Adv. Mat. Lett.*, 2012, **3**, 220.

[209] A. C. Larson, R. B. Von Dreele, General Structure Analysis System (GSAS), Los Alamos National Laboratory Report LAUR, New Mexico, 2004, 86.

[210] M. Johnsson and P. Lemmens, Crystallography and Chemistry of Perovskites, in Handbook of Magnetism and Advanced Magnetic Media, Edited by H. Kronmuller., John Wiley & Sons, New York, 2006, 2098.

[211] A. Gaur and G.D. Varma, *J. Phys. Condens. Matter*, 2006, **18**, 8837.

[212] A. Jordan, R. Scholz, P. Wust, H. Fahling and R. Felix, *J. Mag. Mag. Mater*., 1999, **201**, 413.

[213] E. C. Stoner and E. P. Wohlfarth, *Philos. Trans. R. Soc. London, Ser. A, 1948,* **240**, 599.

[214] C. A. M. Mulder, A. J. V. Duyneveldt and J. A. Mydosh, *Phy. Rev. B*, 1981, **23**, 1384.

[215] J. A. Mydosh, *J. Mag. Mag. Mater*., 1996, **157-158**, 606.

[216] B.K. Banerjee, *Phys. Lett.*, 1964, **12**, 16.

[217] S. L. Young, Y. C. Chen, H. Z. Chen, L. Horng and J. F. Hsueh, *J. Appl. Phys.*, 2002, **91**, 8915.

[218] N. Gayathri, A. K. Raychaudhuri, S. K. Tiwary, R. Gundakaram, A. Arulraj and C. N. R. Rao, *Phys. Rev. B*, 1997, **56**, 1345.

[219] Y. Sun, W. Tong, X. Xu and Y. Zhang, *Appl. Phys. Lett*., 2001, **78**, 643.

[220] Y. L. Chang, Q. Huang and C. K. Ong, *J. Appl. Phys.*, 2002, **91**, 789.

[221] X. H. Li, Y. H. Huang, C. H. Yan, Z. M. Wang and C. S. Liao, *J. Phys. Condens. Matter*, 2002, **14**, L177.

[222] C. P. Reshmi, S. S. Pillai, M. Vasundhara, G. R. Raji, K. G. Suresh and M. R. Varma, *J. Appl. Phys.*, 2013, **114**, 033904.

[223] S. Asthana, A. K. Nigam and D. Bahadur, *J. Appl. Phys*., 2005, **97**, 10C101.

[224] M. H. Phan, N. D. Tho, N. Chau, S. C. Yu and M. Kurisu, *J. Appl. Phys.*, 2005, **97**, 103901.

[225] L. Chen, J. H. He, Y. Mei, Y. Z. Cao and B. Q. Liu, *J. Appl. Phys*., 2009, **105**, 123910.

[226] S. Mnefgui, N. Zaidi, A. Dhahri, E. K. Hlil and J. Dhahri, *J. Solid State Chem*., 2014, **215**, 193.

[227] H. Terashita, J. C. Cezar, F. M. Ardito, L. F. Bufaical and E. Granado, *Phys. Rev. B.*, 2012, 85, 104401.

[228] J. Suntivich, W. T. Hong, Y. L. Lee, J. M. Rondinelli, W. Yang, J. B. Goodenough, B. Dabrowski, J. W. Freeland and Y. Shao-Horn, *J. Phy. Chem. C*, 2014, 118, 1856.

[229] M. Abbate, F. M. F. de Groot, J. C. Fuggle, A. Fujimori, O. Strebel, F. Lopez, M. Domke, G. Kaindl, G. A. Sawatzky, M. Takano, Y. Takeda, H. Eisaki and S. Uchida, *Phys. Rev. B*, 1992, **46**, 4511.

[230] P. W. Anderson and H. Hasegawa, *Phys. Rev.*, 1955, 100, 675.

[231] P. Nisha, S. S. Pillai, M. R. Varma and K.G. Suresh, *Solid State Sci*., 2012, **14**, 40.

[232] Y. Sun, W. Tong and Y. H. Zhang, *J. Magn. Magn. Mater.*, 2001, **232**, 205.

[233] A. K. Pramanik and A. Banerjee, Phy. Rev. B, 2010, **81**, 024431.

[234] A. J. Bray, *Phy. Rev. Lett*., 1987, **59**, 586.

[235] W. Jiang, X. Zhou, G. Williams, Y. Mukovskii and K. Glazyrin, *Phy. Rev. Lett*., 2007, **99**, 177203.

[236] M. Vasundhara, V. Srinivas and V. V. Rao, *Phy. Rev. B*, 2008, **78**, 064401.

[237] M. B. Stearns and Y. Cheng, *J. Appl. Phys*., 1994, **75**, 6894.

[238] R. Cabassi, F. Bolzoni, A. Gauzzi and F. Licci, *Phys. Rev. B: Condens. Matter*, 2006, **74**, 184425.

[239] M. Fahnle, W.U. Kellner and H. Kronmuller, *Phys. Rev. B: Condens. Matter*, 1987, **35**, 3640.

[240] H. E. Stanley, Introduction to Phase Transitions and Critical Phenomena, Oxford University Press, London, 1971.

[241] B. M. Wang, L. Wang, Y. Liu and B. C. Zhao, *J. Appl. Phys*., 2009, **105**, 023913.

[242] J. Fan, L. Ling, B. Hong, L. Zhang, L. Pi and Y. Zhang, *Phys. Rev. B*, 2009, **81**, 144426.

[243] A. Arrott and J. E. Noakes, Phys. Rev. Lett. 19 (1967) 786.

[244] B. Widom, *J. Chem. Phys*., 1964, **41**, 1633.

[245] H. E. Stanley, *Rev. Mod. Phys*., 1999, **71**, S358.

[246] H. Oesterreicher and F. T. Parker, *J. Appl. Phys*., 1984, **55**, 4334.

[247] V. Franco, J. S. Blazquez, and A. Conde, *Appl. Phys. Lett.*, 2006, **89**, 222512.

[248] M. Seeger, S. N. Kaul, H. Kronmuller and R. Reisser, *Phys. Rev. B*, 1995, **51**, 12585.

[249] W. Boujelben, A. Cheikh-Rouhou, J. Pierre and J.C. Joubert, *Physica B*, 2002, **321**, 37.

[250] M. Ellouze, W. Boujelben, A. Cheikhrouhou, H. Fuess and R. Madar, *J. Alloys Compd.*, 2003, **325**, 41.

[251] M. Khlifi, A. Tozri, M. Bejar, E. Dhahri and E.K. Hlil, *J. Magn. Magn. Mater.*, 2012, **324**, 2142.

[252] W. Cheikh-Rouhou Koubaa, M. Koubaa, A. Cheikh-Rouhou, W. Boujelben and A. M. Haghiri-Gosnet, *J. Alloys Compd.*, 2008, **455**, 67.

[253] L. Malavasi, *J. Mater. Chem.*, 2008, **18**, 3295.

[254] F. Elleuch, M. Triki, M. Bekri, E. Dhahri and E.K. Hlil, *J. Alloys Compd.*, 2015, **620**, 249.

[255] J. Makni-Chakroun, I. Sfifir, W. Cheikhrouhou-Koubaa, M. Koubaa and A. Cheikhrouhou, *J. Magn. Magn. Mater.*, 2017, **432**, 484.

[256] S. Choura-Maatar, R. Mnassri, W. Cheikhrouhou-Koubaa, M. Koubaa, A. Cheikhrouhou, and E. K. Hlil, *RSC Adv.*, 2017, **7**, 50347.

[257] C. Vazquez-Vazquez, M. C. Blanco, M. A. Lopez-Quintela, R. D. Sanchez, J. Rivas and S. B. Oseroff, *J. Mater. Chem.*, 1998, **8**, 991.

[258] J. Spooren, R. I. Walton and F. Millange, *J. Mater. Chem.*, 2005, **15**, 1542.

[259] R. Skini, A. Omri, M. Khlifi, E. Dhahri and E.K. Hlil, *J. Magn. Magn. Mater.*, 2014, **364**, 5.

[260] B. Vertruyen, J.-F. Fagnard, Ph. Vanderbemden, M. Ausloos, A. Rulmont and R. Cloots, *J. Eur. Ceram. Soc.*, 2007, **27**, 3923.

[261] C. Kittel, Introduction to Solid state Physics, sixth edition, Wiley, NewYork, 1986, 404.

[262] M. Uehara, S. Mori, C.H. Chen and S.-W. Cheong, *Nature,* 1999, **399**, 560.

[263] A. Krichene, W. Boujelben, S. Mukherjee, N. A. Shah and P. S. Solanki, *Phys. Chem. Chem. Phys.*, 2018, **20**, 12608.

[264] M. Wali, R. Skini, M. Khlifi, E. Dhahri and E.K. Hlil, *J. Magn. Magn. Mater.*, 2015, **394**, 207.

[265] B. Sudakshina, K. D. Chandrasekhar, H. D. Yang and M. Vasundhara, J. Phys. D. Appl. Phys., 2017, **50**, 065004.

[266] C. Antoniak, J. Lindner and M. Farle, *Europhys. Lett*, 2005, **70**, 250.

[267] S. S. Rao and S. V. Bhat, *J. Phys. D: Appl. Phys*., 2009, 42, 075004.

[268] A. J. Millis, B. I. Shraiman and R.Muller, *Phys. Rev. Lett.*, 1996, **77**, 175.

[269] P. Dey, T. K. Nath, P. K. Manna and S. M. Yusuf, *J. Appl. Phys*., 2008, **104**, 103907.

[270] V. Dyakonov, A. Slawska-Waniewska, N. Nedelko, E. Zubov, V. Mikhaylov, K. Piotrowski, A. Szytula, S. Baran, W. Bazela, Z. Kravchenko, P. Aleshkevich, A. Pashchenko, K. Dyakonov, V. Varyukhin and H. Szymczak, *J. Magn. Magn. Mater*., 2010, **322**, 3072.

[271] M. Ellouze, W. Boujelben, A. Cheikhrouhou, H. Fuess and R. Madar, *J. Alloys Compd.* 2003, **352**, 41.

[272] P. Orgiani, A. Galdi, C. Aruta, V. Cataudella, G. De Filippis, C. A. Perroni, V. Marigliano, Ramaglia, R. Ciancio, N. B. Brookes, M. Moretti Sala, G. Ghiringhelli and L. Maritato, *Phys. Rev. B*, 2010, **82**, 205122.

[273] D. Abou-Ras, W. Boujelben, A. Cheikh-Rouhou, J. Pierre, J.-P. Renard, L. Reversat and K. Shimizu, *J. Magn. Magn. Mater*., 2001, **233**, 147.

[274] M. F. Hundley and J. J. Neumeier, *Phys. Rev. B.*, 1997, **55**, 11511.

[275] B. Arun, M. Athira, V. R. Akshay, B. Sudakshina, G. R. Mutta and M. Vasundhara, *J. Magn. Magn. Mater.*, 2018, **448**, 322.

[276] R. Skini, M. Khlifi, M. Jemmali, E. Dhahri and E.K. Hlil, *Phys. B*, 2015, **457**, 314.

[277] B. Arun, V. R. Akshay, K. D. Chandrasekhar, Geeta R. Mutta and M. Vasundhara, *J. Magn. Magn. Mater.*, 2019, **472**, 74.

[278] B. Arun, V.R. Akshay, D Chandrasekhar Kakarla and M. Vasundhara, *J. Magn. Magn. Mater*., 2019, **489**, 165418.

[279] A. Tkach, A. Almeida, J. Agostinho Moreira, T. M. Correia, M. R. Chaves, O. Okhay, P. M. Vilarinho, I. Gregora, and J. Petzelt, *Appl. Phys. Lett.*, 2011, **98**, 052903.

[280] M. C. Biesinger, B. P. Payne, A. P. Grosvenor, L.W.M. Lau, A. R. Gerson and R. St.C. Smart, Appl. Surf. Sci., 2011, **257**, 2717.

[281] J. van Elp, R. H. Potze, H. Eskes, R. Berger and G. A. Sawatzky, *Phys. Rev. B*, 1991, **44**, 1530.

[282] G. N. Rao G and J. W. Chen, Effect of Mo doping for the Mn site in the ferromagnetic manganite $La_{0.7}Ca_{0.3}MnO_3$, 2007, arXiv:0705.3080v1 [cond-mat.str-el].

[283] M. Oku, K. Hirokawa and S. Ikeda, *J. Electron Spectrosc. Relat. Phenom*., 1975, **7**, 465.

[284] D. R. Baer, D. L. Blanchard, M. H. Engelhard and J. M. Zachara, *Surf. Interface Anal.*, 1991, **17**, 25.

[285] C. Doroftei and L. Leontie, *RSC Adv.*, 2017, **7**, 27863.

[286] X. Xie, M. Chen, T. Liu, H. Jiang, H. Zhang and A. Chang, *J. Mater. Sci. - Mater. Electron*., 2017, **28**, 8655.

[287] R. Natarajan, N. Palaniswamy, M. Natesan and V.S. Muralidharan, *Open. Corros. J.*, 2009, **2**, 114.

[288] B. Arun, V. R. Akshay and M. Vasundhara, *Dalton Trans*., 2018, **47**, 15512.

[289] B. Arun, V. R. Akshay and M. Vasundhara, *RSC Adv*., 2019, **9**, 23598.

[290] A. V. Pashchenko, V. P. Pashchenko, V. K. Prokopenko, Yu. F. Revenko, Yu. S. Prylipko, N. A. Ledenev, G. G. Levchenko, V. P. Dyakonov and H. Szymczak, *Acta Materialia*, 2014, **70**, 218.

[291] K. Guidara, N. Abdelmoula, J. Dhahri and E. Dhahri, *Phase Trans.*, 2000, **70**, 243.

[292] N.A. Liedienov, A.V. Pashchenko, V.A. Turchenko, V. Ya. Sycheva, A. V. Voznyak, V. P. Kladko, A. I. Gudimenko, D. D. Tatarchuk, Y. V. Didenko, I. V. Fesych, I. I. Makoed, A. T. Kozakov and G. G. Levchenko, *Ceram. Int.*, 2019, **45**, 14873.

[293] B. Arun, J. Varghese, K. P. Surendran and M. T. Sebastian, *Ceram. Inter.*, 2014, **40**, 13075.

[294] R. Ganguly, I. K. Gopalakrishnan and J. V. Yakhmi, *J. Phys. Condens. Matter*, 2000, **12**, L719.

[295] J. Hemberger, S. Lobina, H.-A. Krug von Nidda, N. Tristan, V. Y. Ivanov, A. A. Mukhin, A. M. Balbashov and A. Loidl, *Phys. Rev. B,* 2004, **70**, 024414.

[296] J. Yang, W.H. Song, Y.Q. Ma, R.L. Zhang, B.C. Zhao, Z.G. Sheng, J.M. Dai and Y.P. Sun, *Phys. Rev. B,* 2004, **70**, 92504.

[297] B. Arun, M.V. Suneesh and M. Vasundhara, *J. Magn. Magn. Mater.*, 2016, **418**, 265.

[298] B. Arun, M. V. Suneesh, B. Sudakshina, V. R. Akshay, K. D. Chandrasekhar and M. Vasundhara, *J. Phys. Chem. Solids*, 2018, **123**, 327.

[299] R. Choithrani, M. A. Bhat and N. K. Gaur, *J. Magn. Magn. Mater.*, 2014, **361**, 19.

[300] B. Arun, V. R. Akshay, Geeta R. Mutta, Ch. Venkatesh and M. Vasundhara, *Mater. Research. Bullt.*, 2017, **94**, 537.